

# When size does matter: Dimensional metrology of nanostructured layers and surfaces using X-rays

vorgelegt von  
Diplom-Physiker  
Jan Wernecke  
geboren in Strausberg

Von der Fakultät II - Mathematik und Naturwissenschaften  
der Technischen Universität Berlin  
zur Erlangung des akademischen Grades

Doktor der Naturwissenschaften  
- Dr. rer. nat. -

genehmigte Dissertation

Promotionsausschuss:

Vorsitzender: Prof. Dr. Norbert Esser  
Gutachter: Prof. Dr. Stefan Eisebitt  
Gutachterin: Dr. Franziska Emmerling  
Gutachter: Prof. Dr. Mathias Richter

Tag der wissenschaftlichen Aussprache: 15. April 2015

Berlin 2015



## Abstract

Modern nanotechnology includes the measurement of vertical and lateral length parameters of structured surfaces and sub-surface structures in the nanometre range, which is the field of dimensional nanometrology. Grazing incidence small-angle X-ray scattering (GISAXS) provides non-destructive measurements, access to buried structures, and in-situ measurement capabilities, which can hardly be provided by microscopy techniques. This work describes the measurements and analysis of GISAXS data obtained from surface gratings with structure sizes in different regimes, from almost  $1\ \mu\text{m}$  down to 25 nm. Different 'direct' data analysis methods were implemented to determine structural parameters such as grating pitch, critical dimension, groove width, and line height directly from the data, i.e. without numerical modelling. In this way, the traceability of GISAXS measurements is established by determining the value and uncertainty of the pitch of a self-assembled polymer grating of  $(24.83 \pm 0.09)$  nm, i.e. with an uncertainty below 0.1 nm, by tracing all input parameter uncertainties. A structural parameter value obtained by such direct data analysis provides information on the generally achievable measurement accuracy in any GISAXS experiment and it can serve as a reference value for modelling-based data analysis.

Besides traceability, another aspect in dimensional nanometrology is the availability of suitable instrumentation and measurement techniques. Tender X-rays are required for element-sensitive studies of structural features in copolymer thin films by using anomalous scattering techniques. The development and operation of an in-vacuum PILATUS 1M hybrid pixel detector that provides access to imaging at photon energies below 5 keV is described in this work. The determined quantum efficiency of the detector is higher than 80% above 3.6 keV and is sufficient for imaging down to 1.75 keV. The extended capabilities of the detector are used for depth-resolved GISAXS measurements at the silicon K-edge at 1.84 keV on untreated and annealed block copolymer thin films. With this method it is possible to resolve the onset and progress of a thermally treated PS-*b*-P2VP thin film along the depth of the film, which has not been observed previously.

# Zusammenfassung

Ein Gebiet der Nanotechnologie ist die dimensionelle Nanometrologie, die sich mit der Messung von Längen in vertikale und laterale Richtung im nm-Bereich befasst. Messungen der Röntgenkleinwinkelstreuung unter streifendem Einfall (GISAXS) sind zerstörungsfrei, bedürfen keiner Probenpräparation, bieten Mittelung über einen makroskopischen Bereich und liefern tiefenaufgelöste Information von vergrabenen Nanostrukturen. In dieser Arbeit sind GISAXS-Messungen an Reflektionsgittern mit Strukturgrößen von fast  $1\ \mu\text{m}$  bis  $25\ \text{nm}$  gezeigt. Verschiedene „direkte“ Methoden der Datenanalyse werden zur Bestimmung von Gitterparametern wie Periode, Linienbreite, -höhe und Grabenbreite implementiert. Dies ermöglicht die Rückführung von GISAXS-Messungen einer Gitterperiode von  $(24.83 \pm 0.09)\ \text{nm}$ , d.h. mit einer Unsicherheit unter  $0.1\ \text{nm}$ . Die Umsetzung solcher rückgeführter GISAXS-Messungen ermöglichen die Bestimmung der allgemein erwartbaren Unsicherheiten einer GISAXS-Messung und liefern einen Referenzwert für modellbasierte Analysemethoden.

Ein anderer Aspekt der dimensionellen Nanometrologie ist die Verfügbarkeit von Instrumentierung und Messmethoden. Röntgenstreuung bei Photonenenergien zwischen  $1.5\ \text{keV}$  und  $5\ \text{keV}$  bietet die Möglichkeit, die tiefenaufgelöste Verteilung der verschiedenen Komponenten anhand der anomalen Streuung an Absorptionskanten der enthaltenen leichten Elemente (z.B. P, S, Cl, Ca) zu unterscheiden. Während dieser Arbeit ist im Rahmen einer Kooperation ein vakuum-kompatibler PILATUS 1M Hybridpixel-Detektor entwickelt und in Betrieb genommen worden. Dieser Detektor erweitert den zugänglichen Messbereich auf Photonenenergien unter  $5\ \text{keV}$  und bietet somit Zugang zu den erwähnten Absorptionskanten. Der Detektor wurde ausführlich charakterisiert, die Quanteneffizienz oberhalb von  $3.6\ \text{keV}$  ist höher als  $80\ \%$  und ausreichend für Streumessungen bis hinunter zu  $1.75\ \text{keV}$ . Dies ermöglicht die Anwendung vorher unzugänglicher Streumethoden wie tiefenaufgelöste GISAXS-Messungen an Polymerfilmen auf Silizium mit der Minimierung des Streukontrastes zwischen Polymer und Silizium bei einer Photonenergie nahe der Silizium K-Kante bei  $1.84\ \text{keV}$ . Kontrastminimierung bietet die Möglichkeit, die strukturellen Änderungen im Film unabhängig von überlagernden Interferenzen vom Substrat-Interface zu bestimmen. Diese Methode wurde zur Untersuchung von thermisch behandelten PS-*b*-P2VP Block-Copolymerfilmen angewandt. Nach der thermischen Behandlung kommt es zu Strukturänderungen an der Oberfläche und nahe darunter, die Morphologie in größerer Tiefe bleibt jedoch erhalten. Dies liefert neue Erkenntnisse über Selbstorganisationsprozesse in Polymerfilmen und konnte so bisher noch mit keiner anderen Methode gezeigt werden.

# Contents

<b>1</b>	<b>Introduction</b>	<b>1</b>
<b>2</b>	<b>Fundamentals</b>	<b>5</b>
2.1	Interaction of X-rays with matter	5
2.1.1	X-rays	5
2.1.2	Interactions with matter	6
2.2	Crystal lattices and X-ray scattering	12
2.3	Specular X-ray reflectivity	15
2.4	Diffuse small-angle X-ray scattering	19
2.5	GISAXS on nanostructured films and surfaces	24
2.6	Direct data analysis and numerical simulation	26
2.7	Dimensional nanometrology	31
2.7.1	Terminology	32
2.7.2	Microscopy methods	33
2.7.3	Other indirect methods	36
<b>3</b>	<b>Experimental setup and new instrumentation</b>	<b>39</b>
3.1	Synchrotron radiation	40
3.2	Four-crystal monochromator beamline	44
3.3	UHV measurement chamber	46
3.4	HZB SAXS instrument	47
3.5	The new in-vacuum PILATUS 1M detector	48
3.5.1	Operation principle of PILATUS detectors	49
3.5.2	Development of a vacuum-compatible PILATUS 1M	50
3.5.3	Characterisation of the in-vacuum PILATUS 1M	54
3.6	Summary	59
<b>4</b>	<b>Dimensional nanometrology of surface gratings using GISAXS</b>	<b>61</b>
4.1	Large pitches: Discrete Fourier transform	62
4.1.1	Materials and methods	63
4.1.2	Determining the capping layer thickness using XRR	64

## Contents

4.1.3	GISAXS in perpendicular orientation	64
4.1.4	Discrete Fourier analysis of GISAXS in parallel orientation	66
4.1.5	Validation by simulation using IsGISAXS	69
4.1.6	Energy series from 4.5 keV to 9 keV	69
4.1.7	Rotation around the surface normal vector	71
4.2	Intermediate pitches: Fourier amplitude fitting	73
4.2.1	Project framework and samples	74
4.2.2	GISAXS data analysis	75
4.2.3	XRR results of line height and capping layer thickness	76
4.2.4	GISAXS grating parameter determination	76
4.2.5	Stitching period of electron beam lithography	80
4.2.6	Outlook: FEM reconstruction	82
4.3	Small pitches: GTR distances	83
4.3.1	Analysis method and validity	83
4.3.2	Materials and methods	84
4.3.3	Establishing traceability of the input parameters	85
4.3.4	Traceable pitch determination	91
4.4	Summary	92
<b>5</b>	<b>Depth-resolved GISAXS using contrast-matching at the Si K-edge</b>	<b>95</b>
5.1	Introduction	95
5.2	Materials and methods	96
5.3	Results	97
5.3.1	XRR measurements	97
5.3.2	GISAXS contrast matching	100
5.3.3	Depth-resolved GISAXS using contrast matching	102
5.3.4	AFM results	104
5.4	Proposed depth structure	106
5.5	Summary	107
<b>6</b>	<b>Dimensional nanometrology of organic thin film layers using XRR</b>	<b>109</b>
6.1	Materials and methods	110
6.2	Results of the PSD peak analysis	111
6.3	Traceability and Uncertainties	114
6.4	Comparison and validation of PSD peak positions with model data	114
6.4.1	Refraction correction	114
6.4.2	Recommended settings	118
6.5	Summary	119
<b>7</b>	<b>Summary and Outlook</b>	<b>121</b>
	<b>References</b>	<b>125</b>

# List of Figures

2.1	Refractive index components $\delta$ and $\beta$ for titanium. . . . .	7
2.2	Illustrations of effects taking place after the photoionisation. . . . .	9
2.3	Scattering of a incident plane wave by a particle. . . . .	10
2.4	Definition of scattering angles in reflection geometry. . . . .	11
2.5	Anomalous scattering correction terms $f'$ and $f''$ of sulphur. . . . .	12
2.6	A plane wave X-ray beam impinges under an incidence angle of $\alpha_i$ on a set of parallel crystal planes separated by $d_{(hkl)}$ . . . . .	13
2.7	Ewald construction to determine the scattering angles of constructive interference. . . . .	14
2.8	Reflection and refraction of an incident electromagnetic wave impinging at a grazing angle on a smooth surface. . . . .	16
2.9	Fresnel reflectance of a smooth layer. . . . .	17
2.10	Propagation scheme of reflected and refracted waves in a multilayer system with $N$ different layers. . . . .	18
2.11	Reflectance curve calculated using IMD and corresponding PSD. . . . .	20
2.12	The four scattering terms in the DWBA form factor. . . . .	21
2.13	Schematic cross-section of a surface grating in real space and reciprocal space. . . . .	25
2.14	Intersection of GTRs and Ewald sphere in reciprocal space reconstruction. . . . .	26
2.15	Two common windows in signal processing. . . . .	29
2.16	A typical L-curve of a Tikhonov regularisation. . . . .	31
2.17	Schematic measuring principle of atomic force microscopy. . . . .	34
2.18	Schematic representation of a transmission electron microscope. . . . .	35
2.19	Schematic representation of a scanning electron microscope. . . . .	35
2.20	Scattering geometry in CD-SAXS. . . . .	37
2.21	Schematic setup of an ellipsometry measurement. . . . .	38
3.1	Calculated radiant power of radiation sources. . . . .	41
3.2	Average spectral brilliance vs. photon energy of different light sources. . . . .	42
3.3	The beamlines of the PTB laboratory at BESSY II. . . . .	44
3.4	Scheme of the optical elements of the FCM beamline. . . . .	44
3.5	Detectors and axes in the UHV measurement chamber. . . . .	46
3.6	Motor axes of the SAXS instrument. . . . .	48
3.7	The in-vacuum PILATUS 1M detector. . . . .	49
3.8	Schematic representation of the PILATUS hybrid pixel principle. . . . .	50

## List of Figures

3.9	Experimental setups for in-vacuum measurements using a 100k PILATUS test module. . . . .	51
3.10	Point spread function measurement at 3.3 keV using a 20 $\mu\text{m}$ pinhole. . .	52
3.11	Components of the in-vacuum PILATUS 1M before assembly. . . . .	53
3.12	Technical drawings of the in-vacuum PILATUS 1M. . . . .	53
3.13	Registered counts per second along the direct beam. . . . .	55
3.14	Quantum efficiency of the in-vacuum PILATUS 1M detector. . . . .	56
3.15	Homogeneity of the detector. . . . .	57
3.16	Pixel size determination using a SAXS pattern. . . . .	58
3.17	GISAXS measurements to determine the detector module alignment. . . .	59
4.1	XRR data and curve fit. . . . .	64
4.2	GISAXS in perpendicular orientation of incident beam and grating lines. .	65
4.3	GISAXS DFT-PSD analysis method. . . . .	67
4.4	PSD versus correlation length of various grating fields. . . . .	68
4.5	Simulation of scattering by a grating structure using IsGISAXS. . . . .	70
4.6	Test data and PSD for photon energies from 4.5 keV to 9 keV. . . . .	71
4.7	GISAXS of the azimuthally rotated grating close to parallel orientation . .	72
4.8	Scheme of the sample layout. . . . .	75
4.9	XRR measurements on and off the grating lines. . . . .	77
4.10	GISAXS images of the P100/CD50 and the P250/CD100 grating. . . . .	78
4.11	Fourier analysis of the P100/CD35 grating. . . . .	79
4.12	Fourier analysis of the P250/CD100 grating. . . . .	80
4.13	$q_x$ - $q_y$ plot of a typical GISAXS $q_z$ - $q_y$ map. . . . .	81
4.14	Typical mesh layout used for FEM simulation. . . . .	82
4.15	Modified vertical GISAXS scattering geometry. . . . .	84
4.16	Traceable sample-detector distance determination. . . . .	85
4.17	GISAXS pattern in parallel alignment and GTR boxes. . . . .	86
4.18	Evaluating the misalignment from parallel orientation of incident beam and grating lines. . . . .	87
4.19	Pixel size determination. . . . .	89
4.20	Asymmetric shape of a GTR maximum. . . . .	90
5.1	XRR at different energies close to the contrast matching energy. . . . .	99
5.2	Normalised $\chi^2$ goodness-of-fit values. . . . .	100
5.3	$\delta$ and $\beta$ of the complex refractive indices of silicon and PS- <i>b</i> -P2VP. . . .	100
5.4	GISAXS pattern of the as spun sample. . . . .	101
5.5	Calculated scattering depth in PS- <i>b</i> -P2VP at 1827 eV. . . . .	102
5.6	GISAXS $q_y$ profiles of as spun and annealed sample. . . . .	103
5.7	AFM amplitude and phase images of as spun and the annealed sample. .	105
5.8	Schematic representation of the proposed depth structure. . . . .	106
6.1	XRR profiles of sample A and B measured at 1841 eV. . . . .	111
6.2	PSDs of the organic layer systems A-D. . . . .	112
6.3	Calculated XRR and PSD for validation. . . . .	116
6.4	Relative thickness deviation of the PSD analysis. . . . .	116
6.5	Relative thickness deviation upon variation of $\delta$ and $\beta$ . . . . .	117

# List of Tables

3.1	Basic properties of BESSY II. . . . .	42
3.2	Parameters and specifications of the FCM beamline. . . . .	45
3.3	Technical specifications of axes and diodes in the sample chamber. . . . .	46
3.4	Technical specifications of the in-vacuum PILATUS 1M detector. . . . .	54
4.1	Parameters of XRR fitting. . . . .	64
4.2	Mean grating parameters obtained from different PSDs. . . . .	68
4.3	Vertical detector displacement positions. . . . .	88
4.4	Weighted mean distances and weighted standard deviations of the GTRs. . . . .	91
4.5	GISAXS pitch measurement uncertainty budget. . . . .	92
6.1	PSD peak positions of reflectance data of sample B. . . . .	113
6.2	Layer thicknesses determined by XRR-PSD analysis and by ellipsometry. . . . .	113
6.3	Uncertainty budget of the Irganox layer on sample A. . . . .	114
6.4	Parameter variation ranges and standard values for XRR model curves. . . . .	115



# Abbreviations

**AFM** atomic force microscopy.

**BCP** block copolymer.

**BESSY II** electron storage ring for synchrotron radiation.

**CD** critical dimension.

**DFT** discrete Fourier transform.

**DUV** deep ultraviolet.

**DWBA** distorted wave Born approximation.

**EMRP** European Metrology Research Programme.

**EUV** extreme ultraviolet.

**FCM** four-crystal monochromator.

**FEL** free electron laser.

**FEM** finite element method.

**GISANS** grazing incidence small-angle neutron scattering.

**GISAXS** grazing incidence small-angle X-ray scattering.

**GTR** grating truncation rod.

**GUM** *Guide to the Expression of Uncertainty in Measurement*.

**HZB** Helmholtz-Zentrum Berlin.

**ITRS** International Technology Roadmap for Semiconductors.

**NIST** National Institute for Standards and Technology.

**NPL** National Physical Laboratory.

**PS-*b*-P2VP** polystyrene-*block*-poly(2-vinylpyridine).

## Abbreviations

**PSD** power spectral density.

**PSF** point spread function.

**PTB** Physikalisch-Technische Bundesanstalt.

**RDS** resonant diffuse scattering.

**SAXS** small-angle X-ray scattering.

**SDD** silicon drift detector.

**SEM** scanning electron microscope.

**SI system** International System of Units.

**TEM** transmission electron microscope.

**UHV** ultra high vacuum.

**XRR** X-ray reflectometry.

# Symbols

$\alpha_c$	critical angle of total external refraction.
$\alpha_i$	vertical grazing incidence angle of the X-ray beam.
$\beta$	imaginary part of the refractive index, $\beta = \Im(\hat{n})$ .
$c$	vacuum speed of light, $c = 299\,792\,458\text{ m s}^{-1}$ .
$CD$	critical dimension (grating line width).
$\delta$	component of the real part of the refractive index, $\delta = \Re(\hat{n}) - 1$ .
$\mathcal{F}_{\text{DFT}}(k)$	discrete Fourier transform of the sequence of values $x_0, \dots, x_{N-1}$ .
$\frac{d\sigma}{d\Omega}$	differential scattering cross section.
$e$	elementary charge, $e = (1.602\,176\,565 \pm 0.000\,000\,035) \times 10^{-19}\text{ A s}$ .
$E_{\text{match}}$	photon energy scattering contrast matching of two materials.
$E_{\text{ph}}$	photon energy of the monochromatic X-ray beam.
$\epsilon_0$	electric constant (dielectric permittivity of the vacuum), $\epsilon_0 = 1/\mu_0 c^2 = 8.854\,187\,8 \dots \times 10^{-12}\text{ F m}^{-1}$ .
$E_{\text{thresh}}$	energy threshold setting of the PILATUS 1M detector, typically $E_{\text{thresh}} = 1/2 E_{\text{ph}}$ .
$\omega$	photon frequency.
$w_{\text{fwhm}}$	Bragg peak width.
$G$	grating groove width.
$\gamma$	width of the Kaiser window.
$H$	grating line height.
$h$	Planck constant, $h = (6.626\,069\,57 \pm 0.000\,000\,29) \times 10^{-34}\text{ J s}$ .
$h_{\text{T}}$	Tikhonov regularisation parameter.
$\vec{k}$	wave number vector, $ \vec{k}  = k = 2\pi/\lambda$ .
$\Lambda$	scattering depth.

## Symbols

$L_{\text{px}}$	detector pixel pitch.
$L_s$	sample-detector distance.
$m_e$	electron rest mass, $m_e = (9.109\,832\,91 \pm 0.000\,000\,40) \times 10^{-31} \text{ m s}^{-1}$ .
$\mu_0$	magnetic constant (magnetic permeability of the vacuum), $\mu_0 = 4\pi \times 10^{-7} \text{ N A}^{-2}$ .
$\hat{n}$	complex refractive index, $\hat{n} = (1 - \delta) + i\beta$ .
$N_A$	Avogadro constant, $N_A = (6.022\,141\,29 \pm 0.000\,000\,27) \times 10^{23} \text{ mol}^{-1}$ .
$P$	grating period length (pitch).
$\varphi_{\text{phase}}$	phase of electromagnetic wave.
$\vec{q}$	scattering vector / reciprocal space vector, $\vec{q} = (q_x, q_y, q_z)^T$ .
$q_c$	$q$ -coordinate at $\alpha_f = \alpha_c$ and/or $\alpha_i = \alpha_c$ .
$QE$	detector quantum efficiency, $QE = \frac{\text{incoming photons}}{\text{registered photons}}$ .
$q_r$	$q$ at specular condition, $q_r = q_z _{\alpha_f = \alpha_i}$ .
$R$	(specular) reflectance.
$r_0$	classical electron radius, $r_0 = (2.817\,940\,326\,7 \pm 0.000\,000\,002\,7) \times 10^{-15} \text{ m}$ .
$R_F$	Fresnel reflectance.
$\rho$	mass density in $\text{kg m}^{-3}$ .
$\rho_e$	electron density, i.e. electrons per unit volume, in $\text{cm}^{-3}$ .
$\sigma_{\text{rms}}$	root-mean-square interface roughness.
$S(\vec{q})$	structure factor (interference function).
$\lambda$	wavelength.
$W(\vec{q})$	effective average particle form factor.

# 1

## Introduction

In 1959, Richard P. Feynman stated in one of his famous lectures\* that “there’s plenty of room at the bottom.” What he was referring to was the enormous potential for technological applications in the nanometre regime and even below, down to ‘atomic machines’. During the decades that followed up to the present day, the emerging field of nanotechnology has claimed more and more of this room. Today, microprocessors using nm-sized functional elements,<sup>[13]</sup> organic photovoltaic devices,<sup>[28]</sup> bioactive nanoparticles,<sup>[116]</sup> or carbon nanotubes for energy storage<sup>[36,66]</sup> are nanotechnological applications within reach or already in industrial production. However, the field of applications is exciting, but it is only one side of the coin. The flip side is the ability to perform useful and accurate measurements of relevant physical properties in the nanometre regime. Any technological advancement requires appropriate tools to understand, monitor, and make use of the underlying principles. The science of size and structure measurements in the nm range this is the field of dimensional nanometrology.

This work contributes to two aspects that follow directly from Feynman’s statement and involves both of the above-mentioned mentioned fields of nanotechnology – metrology and applications:

- (i) How can we measure dimensional parameters on nanostructured surfaces and within layers? How is a measured value evaluated in terms of accuracy, precision, and uncertainty?
- (ii) How can a nanometrological technique be developed further to offer new and extended insights into materials and structures relevant to current applications?

The first aspect is closely related to metrology. Metrology is the primary field of interest for national metrology institutes (NMIs) worldwide, such as the National Institute for Standards and Technology (NIST) in the USA or the Physikalisch-Technische Bundesanstalt (PTB) in Germany, where the present thesis work was performed. In metrology, the uncertainties, the sensitivities, and the range of validity associated with a measurement are studied. A central term is ‘traceability’ which means the ability to relate a measured value to a base unit definition of the International System of Units (SI system). This

\* <http://www.its.caltech.edu/~feynman/plenty.html>

## INTRODUCTION

has high relevance, because only the statement of an uncertainty along with a measurement value determined using a certain method allows for the evaluation of the method in an objective way, and for comparing the results and the performance of different measurement methods.

The second aspect mentioned focusses on the availability of suitable tools – in the context of this work – in terms of dimensional nanometrology. A wide range of different methods exist that probe the real space or, equivalently, the reciprocal space, each with specific advantages and drawbacks. However, only a few of them are traceable, which is necessary in order to assess the quality of the measurement results obtained and to compare and validate different methods. One of these tools is grazing incidence small-angle X-ray scattering (GISAXS), a scattering technique that is used to probe lateral and vertical structure size features on surfaces and within films and layers in the nm to  $\mu\text{m}$  range. GISAXS can be seen as a combination of X-ray reflectometry (XRR), which is sensitive to vertical density variations in a material, and small-angle X-ray scattering (SAXS), which is used to determine the shape and size of nanoparticles in transmission geometry. GISAXS is a widely used scattering technique for surface and sub-surface structures in functional polymer films for photovoltaics, organic electronics, and chemical functionalisation, as well as in lithographic nanopatterning and multilayer optics characterisation. GISAXS offers a range of appealing properties, such as non-contact and non-destructive measurements, depth-sensitivity, and *in-situ* measurement capabilities. Using X-ray synchrotron radiation allows advanced scattering techniques such as chemical element sensitivity by anomalous scattering at photon energies close to an absorption edge.

Traceability of GISAXS would be highly desirable especially for nanoscopic reference measurements in microelectronics and semiconductors industry and for absolute size measurements of nanostructures. However, traceable GISAXS measurements have not been presented to date for different reasons: First, calibrated instrumentation is needed to establish the traceability of each experimental input parameter, but it is rarely available at a typical X-ray scattering beamline or laboratory setup. Second, GISAXS – as any conventional X-ray scattering technique – is subject to the phase problem, which means the loss of the phases in the measured scattering pattern. This prevents the direct inversion of the scattering data to real space lengths. Instead, the data needs to be numerically simulated using appropriate models. But modelling is a complex process in data analysis that is very difficult to include in an uncertainty analysis. In this work, the traceability of a GISAXS measurement is established. This is realised by direct Fourier analysis of the scattering data, that is, circumventing the need for the selection of appropriate models for their complex numerical simulation. In this way, it is possible to evaluate the general uncertainties of a GISAXS measurement without the additional influence of the model selection itself. Suitable sample systems for such type of metrologic investigations are surface gratings with structure sizes in the sub- $\mu\text{m}$  and nm regime. Gratings are highly ordered model systems because they can be produced with great accuracy using current technology. Moreover, nanoscopic grating structures have a high practical relevance, e.g. in next-generation photolithography, in block copolymer lithography, and as high-quality optical elements in the wavelength regime below 20 nm.

The other aspect necessary for the advancement of nanotechnology is suitable instrumentation. In particular, small-angle X-ray scattering measurements are lacking area detectors suitable for the tender X-ray range, which is roughly between 1.5 keV and 5 keV. This is inconvenient because a number of K-absorption edges of biologically and

technologically relevant elements such as silicon, phosphorus, sulphur, calcium, and chlorine are found in this range and could be used for anomalous scattering techniques such as element-specific scattering contrast tuning. X-ray scattering imaging in this photon energy range can therefore provide new insights and extended measurement capabilities in thin film science and respective application fields. A vacuum-compatible large area hybrid pixel detector capable of imaging down to 1.75 keV, the in-vacuum PILATUS 1M, was developed in cooperation of PTB and Dectris Ltd. during the course of this work. The detector was metrologically characterised with respect to its geometrical and radiometrical properties. When the detector went into service in July 2012, it was the first digital detector of this size (1 Mpixel) to offer such extended imaging capabilities in the tender X-ray regime. The capability of GISAXS measurements in the tender X-ray regime triggered a number of ongoing and perspective collaborations with groups from TU Munich, Lawrence Berkeley National Laboratory, University of Kyoto and Stanford University on different application areas, such as organic photovoltaics, thermoelectric polymer films, and fuel cell membranes.

This work is structured in the following way: The fundamentals of the X-ray scattering experiments that were performed in the PTB laboratory at the Berlin electron storage ring for synchrotron radiation (BESSY II) are presented in Chapter 2. Moreover, Chapter 2 covers the mathematical principles of the analysis methods used as well as the technical basics of other nanometrological measurement techniques relevant for this work. The development and characterisation of the in-vacuum PILATUS 1M detector is described in Chapter 3. Chapter 4 is dedicated to the nanometrology and traceability of GISAXS measurements on grating structures in different size regimes, from large structures up to almost 1  $\mu\text{m}$  down to structure sizes of 25 nm. Chapters 5 and 6 are centred around related areas of current research and application, polymer thin films, and layer systems, respectively. In Chapter 5, the measurement capabilities of the in-vacuum PILATUS 1M in the tender X-ray range are used to match the scattering contrast between a nanostructured block copolymer film and the silicon substrate at photon energies close to the silicon K-absorption edge at 1.84 keV. This allows to study the depth-dependent structure and ordering along the thickness of the film, which is hardly possible with any other measurement method. The so far open scientific question behind the investigation is: How does re-structuring of the vertically ordered block copolymer film change on the surface and along the depth of the film after thermal annealing? Other polymer sample systems are single layers and multilayers of different organic materials, which are investigated in terms of layer thickness using XRR in Chapter 6. The scientific scope in this chapter is strongly driven by metrology as it is challenging to perform traceable thickness measurements on organic thin film layers due to the poorly known optical constants, the pronounced interface roughness, and the weak optical contrast between the different, but very similar, organic materials. Traceable thickness measurements using XRR were performed on several different layer systems by implementing a direct analysis method and maximising the scattering contrast.

Extensive parts of the work presented in Chapters 3 to 6 have been published in peer-reviewed journals.<sup>[224,225,250–254]</sup> Annotations in each (sub-)chapter indicate which publications correspond to the presented results.



# 2

## Fundamentals

This chapter covers the fundamentals of the investigations that follow in the later chapters. Since the focus of this work is on synchrotron radiation X-ray scattering techniques, the basic principles of X-ray interaction with matter are discussed first. Then, different theoretical frameworks of scattering theory, in particular for reflection geometry, are presented, before specular and diffuse scattering is discussed. This sets the transition to recent trends and applications of grazing incidence small-angle X-ray scattering (GISAXS) experiments and to the field of dimensional nanometrology.

### 2.1 Interaction of X-rays with matter

#### 2.1.1 X-rays

X-rays are electromagnetic radiation with typical wavelengths of 0.01 nm to 10 nm, corresponding to photon energies of around 0.1 keV to 100 keV. Different names exist for different ranges of the X-ray spectrum throughout the scientific community, depending on the field of application. In this work, the photon energy range below around 1.5 keV is referred to as the soft X-ray range. The term tender X-ray regime that became popular in the soft matter thin film community is used for photon energies between 1.5 keV to around 5 keV. X-rays above 10 keV are referred to as hard X-rays.

Due to the quantum-mechanical concept of wave-particle duality, X-rays possess a wave nature as well as a particle nature, which are both required to explain the entirety of observations made on the absorption and emission of electromagnetic radiation. Electromagnetic waves are fundamentally characterised by Maxwell's equations, which describe the generation, propagation and interaction of electric and magnetic fields,  $\vec{E}$  and  $\vec{B}$ , respectively, by partial differential equations.\* In vacuum and in the absence of

---

\* Details can be found in many standard text book on electrodynamics, for example in Jackson [106].

electric charges and currents, Maxwell's equations are

$$\begin{aligned}\nabla \cdot \vec{E} &= 0, & \nabla \cdot \vec{B} &= 0 \\ \nabla \times \vec{E} &= -\frac{\partial \vec{B}}{\partial t}, & \nabla \times \vec{B} &= \frac{1}{c^2} \frac{\partial \vec{E}}{\partial t}.\end{aligned}$$

By taking the curl of these equations and after some rearrangements, the homogeneous wave equations

$$\left(\Delta - \frac{1}{c^2} \frac{\partial^2}{\partial t^2}\right) \vec{E}(\vec{r}, t) = \vec{0}, \quad \left(\Delta - \frac{1}{c^2} \frac{\partial^2}{\partial t^2}\right) \vec{B}(\vec{r}, t) = \vec{0} \quad (2.1)$$

are obtained. Two possible solutions of these wave equations are monochromatic plane waves ( $\vec{\psi}$  can be  $\vec{B}$  or  $\vec{E}$ ):

$$\begin{aligned}\vec{\psi}(\vec{r}, t) &= \vec{\psi}_0 \exp(i(\omega t - \vec{k} \cdot \vec{r}) + \varphi_{\text{phase}}), \\ \vec{\psi}(\vec{r}, t) &= \vec{\psi}_0(\vec{r}, t) \cos(\omega t - \vec{k} \cdot \vec{r} + \varphi_{\text{phase}}),\end{aligned} \quad (2.2)$$

with the wave number  $|\vec{k}| = k = 2\pi/\lambda$ , the wavelength  $\lambda$  and the wave frequency  $\omega = 2\pi f$ . The particle nature is accounted for by a quantisation of the energy of the radiation into multiples of discrete units, the photons. Electromagnetic radiation is described as an ensemble of photons. The photon energy  $E_{\text{ph}}$  is given by the wavelength  $\lambda$  or, equivalently, frequency  $\omega$  (speed of light  $c$ , Planck's constant  $h$ ) as

$$E_{\text{ph}} = \frac{hc}{\lambda} = \frac{h}{2\pi} \omega. \quad (2.3)$$

It is common to express the photon energy in units of the elementary charge  $e$ , which is indicated by the unit electron volt (eV).

## 2.1.2 Interactions with matter

In vacuum, the phase velocity of the propagating wave is simply the scalar  $v = c = \sqrt{\epsilon_0 \mu_0} = \omega/k$  with the dielectric permittivity  $\epsilon_0$  and the magnetic permeability  $\mu_0$ . When passing through a medium, the phase velocity becomes a function of the wavelength, which is called *dispersion*. The phase velocity in this case is the vacuum speed of light  $c$  divided by the wavelength dependent refractive index  $\hat{n}(\lambda)$ . The refractive index is usually expressed as a complex-valued parameter, the real part and the imaginary part are connected by the Kramers-Kronig relation and are related to refraction and attenuation, respectively.<sup>[26]</sup> In the X-ray regime, the refractive index  $\hat{n}$  of a material is usually expressed as

$$\hat{n} = (1 - \delta) + i\beta \quad \text{with } \delta > 0, \beta > 0. \quad (2.4)$$

The convention accounts for the fact that the real part  $\Re(\hat{n}) = 1 - \delta$  is slightly less than unity, i.e. typically in the range of  $\delta \approx 10^{-6}$  to  $10^{-2}$ . Consequently, the wave phase velocity in most media is larger than the vacuum phase velocity for X-rays.

In the absence of absorption, the refraction related real part can be written as<sup>[46]</sup>

$$\delta = \frac{r_0}{2\pi} \lambda^2 \rho_e(\vec{r}) \quad (2.5)$$

with the classical electron radius  $r_0$ , the electron density  $\rho_e(\vec{r})$ , and the wavelength  $\lambda$ . The electron density  $\rho_e$  in units of  $\text{m}^{-3}$  of an element is related to the mass density  $\rho$  in units of  $\text{kg m}^{-3}$  by

$$\rho_e = \frac{Z}{A} N_A \rho \quad (2.6)$$

with the mass number  $A$ , the atomic number  $Z$  and the Avogadro number  $N_A$ . The imaginary part of  $\hat{n}$  is related to the linear absorption coefficient  $\mu(\vec{r})$  (Lambert-Beer law) by<sup>[63,120]</sup>

$$\beta = \frac{\lambda}{4\pi} \mu(\vec{r}) . \quad (2.7)$$

Displayed in Fig. 2.1 are  $\delta$  and  $\beta$  for titanium that both clearly show the  $K$  and  $L_3$  absorption edges.

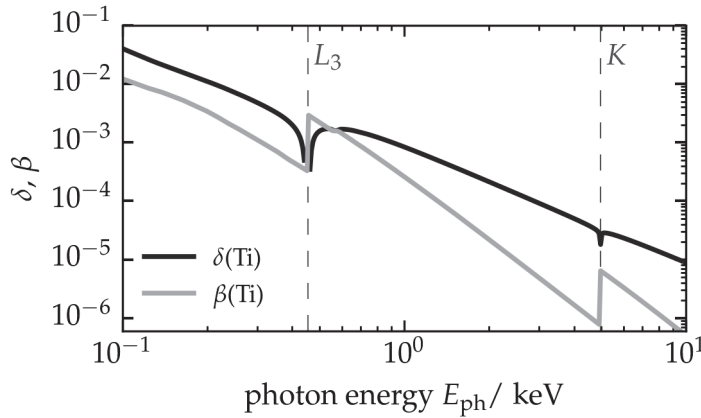


**Figure 2.1** | Refractive index components  $\delta$  and  $\beta$  for titanium.<sup>[90]</sup>

A consequence of the real part of the refractive index being smaller than unity is the occurrence of total external reflection at glancing angles lower than a critical angle at the interface to a denser material, in particular at the vacuum-material-interface. The critical angle for total reflection can be derived from the Snell-Descartes' law using the condition  $\cos \alpha_t = 1$  for the transmission angle  $\alpha_t$  and yields

$$\cos \alpha_c \stackrel{!}{=} \Re(\hat{n}) = 1 - \delta \quad (2.8)$$

The Taylor series of the  $\cos$  term can be aborted after the quadratic term because  $\delta$  is in the order of  $10^{-2}$  or below for X-rays, which yields an approximation for small gracing incidence angles of

$$\alpha_c = \sqrt{2\delta} . \quad (2.9)$$

Combining Eqs. (2.5), (2.6) and (2.9) shows the direct connection of the measurable critical angle  $\alpha_c$  and the mass density  $\rho$  of a material. Thus,  $\rho$  can be derived by determining  $\alpha_c$ , and vice versa, provided that the absorption is negligible, i.e. for photon energies far away from absorption edges.

An X-ray photon interacts with valence and core electrons by three different mechanisms: Photoelectric absorption (also called photoeffect or photoionisation), elastic scattering (Thomson and Rayleigh scattering) and inelastic scattering (Compton and Raman scattering). There exists also the mechanism of pair generation, where a pair of an elementary particle and its anti-particle (electron-positron pairs in most cases) is created in the vicinity of a nucleus. But since the X-ray photon requires a photon energy of at least 1.022 MeV to create an electron-positron pair, it is a high-energy effect that can be completely neglected here.

### Photoelectric absorption

The X-ray photon is completely absorbed by a core electron of an atom, i.e. it does not exist any more after the interaction. If the binding energy of the electron  $E_b$  is smaller than the X-ray photon energy  $E_{ph}$ , this photoelectron is emitted with a kinetic energy of  $E_{ph} - E_b$ , see Fig. 2.2. Detailed information on the internal binding states and composition of the material can be drawn by analysing absorption edges and the kinetic energy distribution of the emitted electrons. This is the field of *photoelectron spectroscopy*.

After emission of a photoelectron, the atom is ionised and is in an energetically excited state. It returns to the ground state by one of the following processes:

- (i) An electron from an outer shell, i.e. of lower binding energy, changes into the energetically more favourable vacancy closer to the core by emitting a fluorescence photon with a characteristic wavelength (Fig. 2.2a). The wavelength of the fluorescence photon is precisely determined by the energetic difference between the two energy levels, which allows to perform detailed elemental analysis (*X-ray fluorescence analysis*). The same process can, of course, occur again with the new vacancy, which eventually results in a cascade of emitted fluorescence photons with decreasing photon energy that are specific for the given chemical element.
- (ii) Instead of emitting a characteristic photon, the energy of the outer shell electron transiting to the inner shell vacancy may also be transferred to another electron on a higher energy level by non-radiative energy transfer. The second electron, the Auger electron, is ejected from the atomic compound and has a kinetic energy equal to the energy difference of the transition energy from the outer to the inner shell and the binding energy of the Auger electron (Fig. 2.2b). In *Auger electron spectroscopy*, the kinetic distribution of Auger electrons can be measured to draw conclusions on the chemical and elemental composition and binding states in the material as well.

Also, subsequent collisions of the primary photoelectron with other electrons occur, resulting in inelastic scattering and the generation of secondary electrons.

The photoabsorption cross-section of any material<sup>[90]</sup> in the photon energy range of eV to keV exhibits sharp drops, so called absorption edges, which occur when the photon energy is equal to the binding energy of electrons in the K, L, M, ... shell of the atom.

The advent of soft X-ray free electron lasers (FELs) with their ultra-high photon intensities and pulse lengths in the fs range allows completely new studies of photon-matter interactions. One example is a non-linear photoionisation process, the multiphoton ionisation of rare gas atoms by soft X-ray FEL pulses.<sup>[69,195,227]</sup> In the ultra-high photon energy flux density of an FEL of  $10^{11}$  W cm<sup>-2</sup> to  $10^{16}$  W cm<sup>-2</sup>, multiple photoionisation of an atom is found at X-ray energies below the ionisation energy. This can only be explained by multiphoton absorption processes such as sequential, simultaneous and resonant ionisation via resonant and virtual energy states.<sup>[147,195,227]</sup>

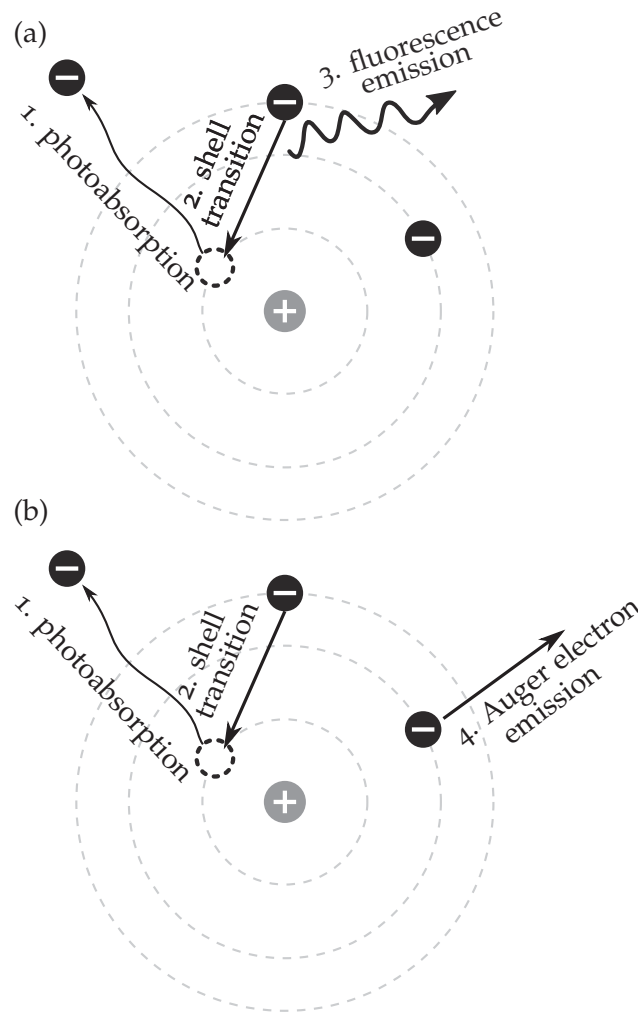


**Figure 2.2** | Illustrations of effects taking place after the photoionisation. (a) fluorescence emission, (b) Auger electron emission. 1. Emission of a photoelectron from an inner energy level, 2. Transition of an outer shell electron to the vacant position, 3. Emission of a fluorescence photon, 4. Emission of an Auger electron.

### Compton scattering

Compton scattering denotes the inelastic scattering of X-ray photons on loosely bound outer shell electrons, that is, the change of photon energy and propagation direction under conservation of total energy and total momentum. Part of the photon energy is transferred to the electron, which is then either in an excited state or released into the continuum in the case of ionisation. The increase in the wavelength of the scattered photon  $\lambda' - \lambda$  can be derived<sup>[42]</sup> from the conservation of energy and momentum and yields

$$\lambda' - \lambda = \frac{h}{m_e c} (1 - \cos 2\theta), \quad (2.10)$$

with the electron rest mass  $m_e$  and the angle  $2\theta$  between the propagation direction of the incident and the scattered X-ray photon.

A related effect is the *Raman effect*, where the inelastic scattering of a photon results in the excitation of an atom without causing ionisation.

### Thomson scattering: Elastic scattering by a free electron

Thomson scattering in this context is the elastic scattering of a monochromatic X-ray photon on a free electron. The incoming plane wave, Eq. (2.2), with the wave vector  $\vec{k}_i$  is elastically scattered by the particle into another direction. This results in a scattered wave with a wave vector  $\vec{k}_f$  ( $|\vec{k}_f| = |\vec{k}_i|$ ) as illustrated in Fig. 2.3. The differential scattering cross section  $\frac{d\sigma}{d\Omega}$  is defined as the number of scattered photons  $dn$  within a certain solid angle  $d\Omega$  divided by the radiant power  $\Phi$  per unit area and per unit time,

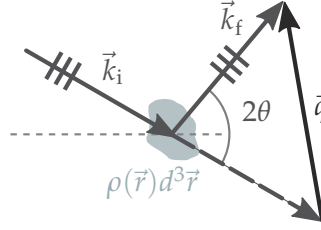
$$\frac{d\sigma}{d\Omega} = \frac{dn/d\Omega}{\Phi} . \quad (2.11)$$

For an unpolarized X-ray beam, the scattering cross section yields

$$\frac{d\sigma}{d\Omega} = \left( \underbrace{\frac{e^2}{4\pi\epsilon_0 m_e c^2}}_{r_0} \right)^2 \frac{1 + \cos^2 2\theta}{2} , \quad (2.12)$$

with the scattering angle  $2\theta$  between  $\vec{k}_i$  and  $\vec{k}_f$  and the classical electron radius  $r_0$ .

**Figure 2.3** | Scattering of an incident plane wave  $\vec{k}_i$  by a particle  $\rho(\vec{r})d^3\vec{r}$  at a scattering angle  $2\theta$  between incident wave  $\vec{k}_i$  and scattered wave  $\vec{k}_f$ .



### Rayleigh scattering: Elastic scattering by ensembles of electrons

In terms of X-ray scattering, an atom corresponds to an ensemble of weakly bound valence electrons, which are assumed to be free. Consequently, the atomic scattering amplitude is the sum of the Thomson scattering amplitudes of each electron, their spatial distribution is accounted for by their phase relation. In transmission geometry, an incident plane wave  $\vec{k}_i$  is scattered coherently by electrons in an ensemble of scatterers  $\rho(\vec{r})d^3\vec{r}$ , e.g. a particle with a mass density  $\rho$ , at an angle  $2\theta$  (Fig. 2.3). The scattering vector  $\vec{q}$ , also called momentum transfer vector, is defined as

$$\vec{q} = \vec{k}_f - \vec{k}_i , \quad (2.13)$$

the modulus is derived from Fig. 2.3 as

$$|\vec{q}| \equiv q = \frac{4\pi}{\lambda} \sin(\theta) = \frac{4\pi}{hc} E_{\text{ph}} \sin(\theta) . \quad (2.14)$$

The components of  $\vec{q}$  in reflection geometry are related to the angles of incidence and scattering as shown in Fig. 2.4 according to

$$\begin{aligned} q_x &= k (\cos \theta_f \cos \alpha_f - \cos \alpha_i) \\ q_y &= k (\sin \theta_f \cos \alpha_f) \\ q_z &= k (\sin \alpha_i + \sin \alpha_f) , \end{aligned} \quad (2.15)$$

with the wave number  $k = 2\pi/\lambda$ . Summation over the entire volume  $V$  of the ensemble of scatterers yields the scattering amplitude

$$f(\vec{q}) = D_e \int_V \rho(\vec{r}) \exp(i\vec{q} \cdot \vec{r}) d^3\vec{r}, \quad (2.16)$$

where the argument  $i\vec{q} \cdot \vec{r}$  of the exponential function accounts for the phase relation between all pairs of scatterers in the volume and  $D_e$  denotes the Thomson scattering amplitude, which is the square root of Eq. (2.12) in the case of unpolarised X-rays. Integration of Eq. (2.16) over the volume of an atom yields the definition of the *atomic form factor*  $f_a(\vec{q}) = f(\vec{q})|_{V_{\text{atom}}} / D_e$ .

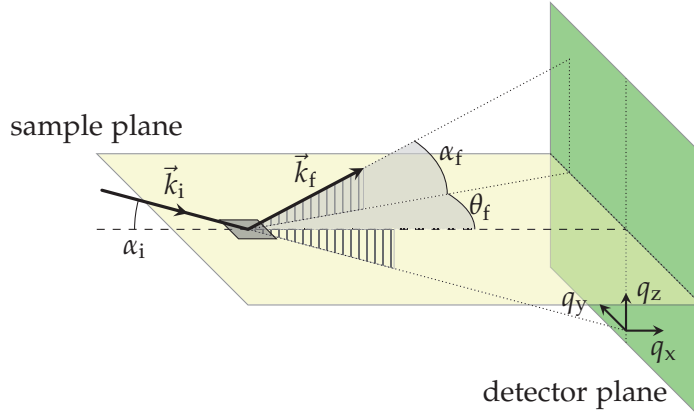


**Figure 2.4** | Definition of scattering angles in reflection geometry. An incident X-ray beam  $\vec{k}_i$  impinges on the sample and is scattered along  $\vec{k}_f$ .

### Anomalous scattering

If the X-ray photon energy is close to the binding energy of electrons within an atom, i.e. close to an absorption edge, *anomalous scattering* by anomalous dispersion becomes significant. The atomic form factor, Eq. (2.16), then becomes a complex-valued parameter of the shape<sup>[258]</sup>

$$f(E_{\text{ph}}) = f_0 + f'(E_{\text{ph}}) + if''(E_{\text{ph}}). \quad (2.17)$$

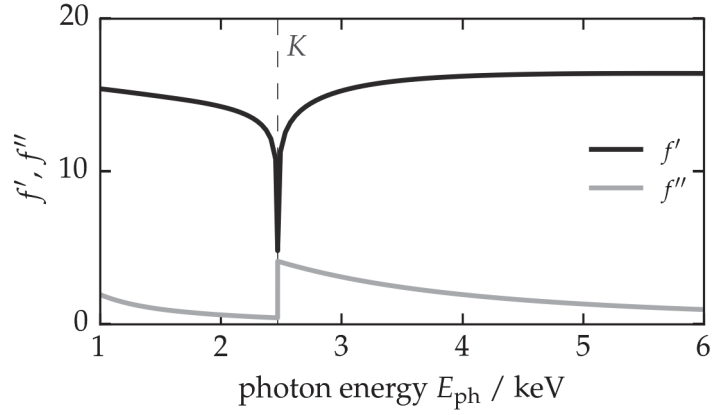
The parameter  $f_0$  denotes the normal Thomson atomic scattering amplitude as defined in Eq. (2.16), while  $f'$  and  $f''$  represent the real part and the imaginary part of the anomalous dispersion correction.  $f'$  and  $f''$  are connected by a Kramers-Kronig relation and vary rapidly with the photon energy close to an absorption edge, which can be seen in Fig. 2.5. The real part component  $\delta$  and the imaginary part  $\beta$  of  $\hat{n}$  are proportional to  $f'$  and  $f''$ , respectively.<sup>[107]</sup> Consequently, the scattering amplitude of a specific element with respect to the scattering amplitude of another element in a multi-component material can be tuned by selecting a photon energy close to an absorption edge of one of the elements.

In X-ray scattering, this effect is known as the *contrast variation* technique, which allows to maximise the scattering contrast between two elements, e.g. to determine the element-specific distribution within the probed volume.<sup>[4,126,174,177,230,232]</sup> In some cases, contrast matching is also applied to minimise the scattering contrast between two elements, e.g. to make an interface virtually 'invisible' for X-ray scattering.<sup>[121,175,252]</sup>

The penetration depth  $\Lambda$ , i.e. the depth where the penetrating evanescent wave is attenuated to  $\exp(-1)$ , is the reciprocal of the linear absorption coefficient  $\mu$  and can be derived<sup>[46]</sup> from the complex refractive index  $\hat{n}$ ,

$$\Lambda = \left[ 2k^2 \left( \sqrt{(\alpha_i^2 - \alpha_c^2)^2 + 4\beta^2} - (\alpha_i^2 - \alpha_c^2) \right) \right]^{-\frac{1}{2}}. \quad (2.18)$$

**Figure 2.5** | Anomalous scattering correction terms  $f'$  and  $f''$  of sulphur.<sup>[90]</sup> Pronounced changes are visible at the sulphur K-edge at 2472 eV.



It is thus possible to tune the penetration depth  $\Lambda$  of the X-ray beam by varying  $\alpha_i$  around  $\alpha_c$ . Consequently, this measures the averaged scattering from the sample surface down to the penetration depth. In other words, the detected signal contains the average structure of the film weighted by an exponential damping factor of this penetration depth. For this reason, Eq. (2.18) is sometimes<sup>[162,164,165]</sup> also referred to as the scattering depth.

## 2.2 Crystal lattices and X-ray scattering

Any material is composed of atoms, which are arranged in a certain way. The highest degree of order is found in crystals, where the basic constituents (atoms, molecules, ions, compounds, etc.) are arranged at well defined positions, i.e. in a crystal lattice. A crystal lattice is composed of elementary building blocks, the unit cells, which are stacked in all directions. Unit cells are described by the lattice parameters (base vectors)  $\vec{a}_1, \vec{a}_2, \vec{a}_3$  along the edges of the unit cell.<sup>[118]</sup> Hence, translational symmetry exists in a lattice with respect to a translation vector  $\vec{T}$  defined as

$$\vec{T} = A_1 \vec{a}_1 + A_2 \vec{a}_2 + A_3 \vec{a}_3, \quad (2.19)$$

with  $A_1, A_2, A_3$  being integer numbers. In three dimensions, there are 7 lattice systems and 14 Bravais lattices which are distinguished by the length of the unit cell base vectors and the angles between them.

It is often more convenient to express a periodic structure such as a lattice or a grating not in real space, but in reciprocal space, especially in regard of X-ray diffraction and scattering. The reciprocal lattice base vectors are derived from the real space lattice base vectors as defined above by

$$\vec{b}_1 = 2\pi \frac{\vec{a}_2 \times \vec{a}_3}{\vec{a}_1 \cdot \vec{a}_2 \times \vec{a}_3} \quad (2.20a)$$

$$\vec{b}_2 = 2\pi \frac{\vec{a}_3 \times \vec{a}_1}{\vec{a}_1 \cdot \vec{a}_2 \times \vec{a}_3} \quad (2.20b)$$

$$\vec{b}_3 = 2\pi \frac{\vec{a}_1 \times \vec{a}_2}{\vec{a}_1 \cdot \vec{a}_2 \times \vec{a}_3}. \quad (2.20c)$$

Any position in the reciprocal lattice can be expressed by the reciprocal translation vector  $\vec{G}$  by

$$\vec{G} = h\vec{b}_1 + k\vec{b}_2 + l\vec{b}_3. \quad (2.21)$$

Mathematically, the transition from real space to reciprocal space corresponds to a Fourier transform of a plane wave function  $\exp(i\vec{G}\cdot\vec{r})$ . The reciprocal lattice is the entirety of all vectors  $\vec{G}$  that satisfy the translational symmetry condition

$$\begin{aligned} \vec{T}\cdot\vec{G} &= 2\pi \times m \quad (m \in \mathbb{Z}) \\ \rightarrow \exp(i\vec{T}\cdot\vec{G}) &= 1. \end{aligned} \quad (2.22)$$

The X-ray scattering amplitude in Eq. (2.16) has the same form, it is the Fourier transform of the spatial distribution of scatterers  $\rho_e(\vec{r})$ . If the scattering object is a lattice, then  $\rho_e(\vec{r})$  can be expressed as a Fourier series and inserted in Eq. (2.16). It can be shown<sup>[118]</sup> that the scattering amplitude is large if the scattering vector  $\vec{q}$  equals a reciprocal space vector

$$\vec{q} = \vec{G}, \quad (2.23)$$

and is negligible otherwise. This is the central result of elastic X-ray scattering theory as it relates the position of scattering maxima directly to the reciprocal grating vectors. Consequently, X-ray scattering directly provides information on the reciprocal space representation of an ensemble of scatterers such as a lattice, a grating or an ensemble of particles.

Equation (2.23) is known as the *Laue condition* for constructive interference in reciprocal space. Combining Eqs. (2.21) to (2.23) yields the Laue equations in real space

$$\vec{a}_1 \cdot \vec{q} = 2\pi h, \quad (2.24a)$$

$$\vec{a}_2 \cdot \vec{q} = 2\pi k, \quad (2.24b)$$

$$\vec{a}_3 \cdot \vec{q} = 2\pi l. \quad (2.24c)$$

A fully equivalent formulation of Eq. (2.23) is the Bragg equation for constructive interference, also called Bragg's law,

$$m \lambda = 2 d_{(hkl)} \sin(\alpha_i) \quad (m \in \mathbb{Z}). \quad (2.25)$$

Bragg's law is a very intuitive approach to X-ray scattering by parallel crystal planes separated by the distance  $d_{(hkl)}$ . In this picture, the plane wave impinges under an incidence angle  $\alpha_i$  on the parallel lattice planes and interacts by Rayleigh scattering, Eq. (2.16), with the valence electrons of the lattice atoms as depicted in Fig. 2.6. The

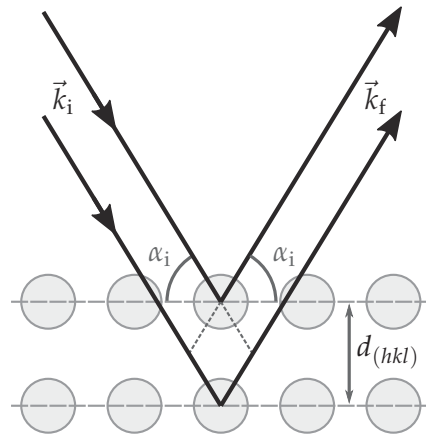


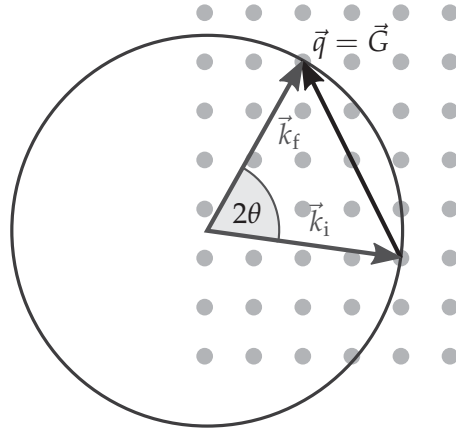
**Figure 2.6** | A plane wave X-ray beam impinges under an incidence angle of  $\alpha_i$  on a set of parallel crystal planes separated by  $d_{(hkl)}$ .

coherently scattered waves interfere. It can be directly seen from the geometry that

constructive interference occurs when the path difference  $2d_{(hkl)} \sin(\alpha_i)$  is equal to an integer multiple of the wavelength  $m\lambda$ .

A very elegant and helpful visualisation of Eq. (2.23) is the *Ewald construction*, as shown in Fig. 2.7, which is used to determine the angles  $2\theta$  and/or wavelengths  $\lambda$  where a scattering spot appears. In the three dimensional case, the Ewald sphere denotes the spherical surface on which the incident wave vector  $\vec{k}_i$  and the scattered wave vector  $\vec{k}_f$  lie. The vector  $\vec{k}_i$  points to an arbitrary point of the reciprocal lattice (dots in Fig. 2.7). The radius  $2\pi/\lambda$  of the Ewald sphere is fixed for a given wavelength and Eq. (2.23) must be fulfilled in order to produce a significant scattering amplitude. Consequently, scattering spots appear only at scattering angles  $2\theta$ , i.e.  $(\alpha_f, \theta_f)$  in three dimensions, Eq. (2.15), where a reciprocal lattice point intersects the surface of the Ewald sphere. The concept of Ewald construction, also called reciprocal space reconstruction, is not restricted to X-ray diffraction on lattices, it can also be used to describe the small-angle scattering of gratings with structure sizes in the sub- $\mu\text{m}$  regime.

**Figure 2.7** | Ewald construction to determine the scattering angles  $2\theta$  of constructive interference in 2D-space. The end point of the incident wave  $\vec{k}_i$  points to an arbitrary reciprocal lattice point (grey dots). The vector is then taken as the radius vector of the Ewald circle. Scattering peaks appear at intersection points of the Ewald circle and the reciprocal lattice points.



### Structure factor

In order to determine the scattering amplitude of a perfect crystal composed of  $N$  unit cells with one atom per unit cell and the lattice vectors  $\vec{a}_j$ , the condition for constructive interference, Eq. (2.23), is combined with the equation of the atomic form factor, Eq. (2.16), as

$$F = \sum_{j=1}^N f_a(\vec{G}) \exp(i\vec{q} \cdot \vec{a}_j) = S_{\vec{G}}. \quad (2.26)$$

$S_{\vec{G}}$  is the *structure factor* of the lattice unit cell. The summation accounts for the atomic form factor contribution from each occupied position in the unit cell. This concept can be generalised<sup>[120]</sup> to the case of a continuous electron density distribution in the unit cell, contrary to a discrete distribution of atoms, just as it was done for an atom in Eq. (2.16) as

$$S(\vec{G}) = \int_V \rho_e(\vec{r}) \exp(i\vec{G} \cdot \vec{r}) d^3\vec{r}. \quad (2.27)$$

The unit cell structure factor is thus the Fourier transform of the periodic electron density distribution.

One remark regarding the terminology should be made: Historically, the elastic scattering theory described above was developed in the first years of the 20<sup>th</sup> century

mainly by Max von Laue, Paul Peter Ewald, William Lawrence, and William Henry Bragg under the term of X-ray diffraction or X-ray crystallography. However, it remains pure convention if the fundamental elastic interaction process is called diffraction, scattering or reflection, which becomes also obvious from the different experimental and theoretical approaches (Thomson scattering, Bragg reflection, Laue diffraction) that describe the same physical mechanism. The terminology used in this work follows one of the wide-spread conventions to regard scattering as the basic interaction process. The terms ‘diffraction’ and ‘reflection’ are used to put emphasis on the scattering geometry: Diffraction is used for large scattering angles of tens of degree, reflection indicates that not the transmitted, but the reflected scattering distribution is observed. In addition, the quote ‘Throughout this work the terms scattering and reflecting are used interchangeably’ from Wu [259] is also valid for this work.

## 2.3 Specular X-ray reflectivity

In this section, the reflection, refraction, and transmission of X-rays by surfaces and layers is described.<sup>[46,120,190]</sup> The basis are the solutions of the Helmholtz wave equation, Eq. (2.2), for the incident wave  $\vec{k}_i$ , the transmitted wave  $\vec{k}_t$ , and the reflected wave  $\vec{k}_r$ .

In reflection geometry, Fig. 2.4, observing the specular component of the elastic scattering means to probe the  $q_z$  axis, i.e.  $q_x = 0 \text{ nm}^{-1}$  and  $q_y = 0 \text{ nm}^{-1}$ . Using the specular condition  $\alpha_f = \alpha_i$ , the scattering vector equation for  $q_z$  simplifies to

$$q_r(\alpha_i) \equiv q_z|_{\alpha_f=\alpha_i} = \frac{4\pi}{\lambda} \sin(\alpha_i) . \quad (2.28)$$

The  $q_r$  value at the critical angle of total refraction  $\alpha_c$  is defined according to Eq. (2.28) as

$$q_c \equiv q_r(\alpha_i = \alpha_c) = \frac{4\pi}{\lambda} \sin(\alpha_c) . \quad (2.29)$$

Another consequence of measuring only along the  $q_z$  axis is that the probed volume of the structure factor, Eq. (2.27), is mainly varied along the  $z$  axis, i.e. perpendicular to the sample surface, disregarding lateral variations along the beam footprint. Hence, reflectivity measurements are sensitive to vertical sample features of layers and multilayer structures such as thickness, interface roughness or roughness correlations.

The experimental technique of reflectivity measurements is X-ray reflectometry (XRR). In X-ray reflectometry (XRR),  $\alpha_i$  is varied in small steps (typically a hundredth to a thousandth of a degree) from  $0^\circ$  to several (tens of) degrees. The specular reflection intensity is measured at each position using a photodiode that is rotated around the same axis as  $\alpha_i$  and positioned at an angle of  $2\alpha_i$ .

### Fresnel reflectance of a smooth surface

An electromagnetic plane wave  $\vec{E}_i(\vec{r}) = \psi_i \exp(i\vec{k}_i \cdot \vec{r})\vec{e}_y$  propagating through vacuum along the unit vector  $\vec{e}_y$  impinges on a smooth surface with a refractive index  $\hat{n}$  as depicted in Fig. 2.8. At the surface, i.e.  $z = 0$ , the wave is reflected and refracted due to the refractive index change according to the Snell-Descartes law. The reflected and refracted partial waves are plane waves of the form

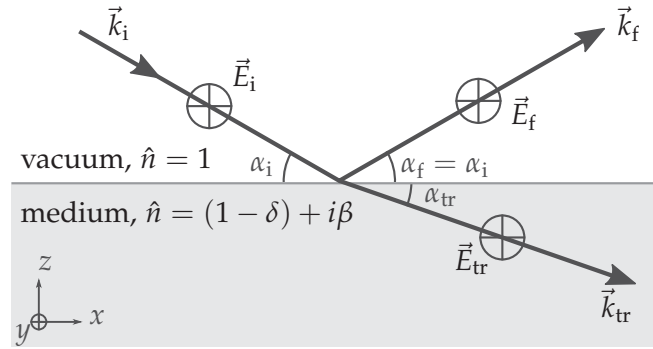
$$\vec{E}_f(\vec{r}) = \psi_f \exp(i\vec{k}_f \cdot \vec{r})\vec{e}_y, \quad (2.30a)$$

$$\vec{E}_t(\vec{r}) = \psi_{tr} \exp(i\vec{k}_{tr} \cdot \vec{r})\vec{e}_y. \quad (2.30b)$$

By applying the boundary condition  $\psi_i + \psi_f = \psi_{tr}$  and assuming that the refracted beam is completely absorbed in the layer, the reflection coefficient  $r_s$  as a function of incidence angle  $\alpha_i$  and critical angle  $\alpha_c$  is obtained as<sup>[46]</sup>

$$r_s = \frac{\psi_f}{\psi_i} = \frac{\alpha_i - \sqrt{\alpha_i^2 - \alpha_c^2}}{\alpha_i + \sqrt{\alpha_i^2 - \alpha_c^2}}. \quad (2.31)$$

**Figure 2.8** | Reflection and refraction of an incident electromagnetic wave  $\vec{E}_i$  (wave vector  $\vec{k}_i$ ) impinging at a grazing angle of  $\alpha_i$  on a smooth surface with a refractive index  $\hat{n}$ .



The term *reflectance* is defined as the ratio of the incidence angle dependent reflected intensity to the incident intensity by

$$R(\alpha_i) = \frac{I(\alpha_i)}{I_0}. \quad (2.32)$$

In order to obtain the intensity-related reflectance from the wave amplitude-related reflection coefficient, the modulus square of Eq. (2.31) has to be taken. For a negligible absorption coefficient  $\mu(\vec{r})$ , this yields the *Fresnel reflectance*  $R_F$  as a function of incidence angle  $\alpha_i$  and critical angle  $\alpha_c$ , or equivalently  $q_r$  and  $q_c$ :

$$R_F(\alpha_i) = r_s r_s^* = \left| \frac{\alpha_i - \sqrt{\alpha_i^2 - \alpha_c^2}}{\alpha_i + \sqrt{\alpha_i^2 - \alpha_c^2}} \right|^2, \quad (2.33)$$

$$R_F(q_r) = \left| \frac{q_r - \sqrt{q_r^2 - q_c^2}}{q_r + \sqrt{q_r^2 - q_c^2}} \right|^2.$$

When absorption is accounted for, the Fresnel reflectance is written as<sup>[46]</sup>

$$R_F(\alpha_i) = \left| \frac{\alpha_i - \sqrt{\alpha_i^2 - \alpha_c^2 - 2i\beta}}{\alpha_i + \sqrt{\alpha_i^2 - \alpha_c^2 - 2i\beta}} \right|^2, \quad (2.34)$$

$$R_F(q_r) = \left| \frac{q_r - \sqrt{q_r^2 - q_c^2 - \frac{32i\pi^2\beta}{\lambda^2}}}{q_r + \sqrt{q_r^2 - q_c^2 - \frac{32i\pi^2\beta}{\lambda^2}}} \right|^2.$$

For large scattering vectors, i.e.  $q_r \gtrsim 3q_c$ , Eqs. (2.5), (2.9) and (2.29) can be combined with Eq. (2.33). This yields the asymptotic behaviour of the Fresnel reflectance

$$R_F(q_r) = \frac{q_c^4}{16q_r^4} = \frac{(4\pi r_0 Q_e(z))^2}{q_r^4}, \quad (2.35)$$

which can be seen in a plot of  $R_F$  for a smooth semi-infinite substrate with a critical angle of  $0.5^\circ$  as shown in Fig. 2.9.

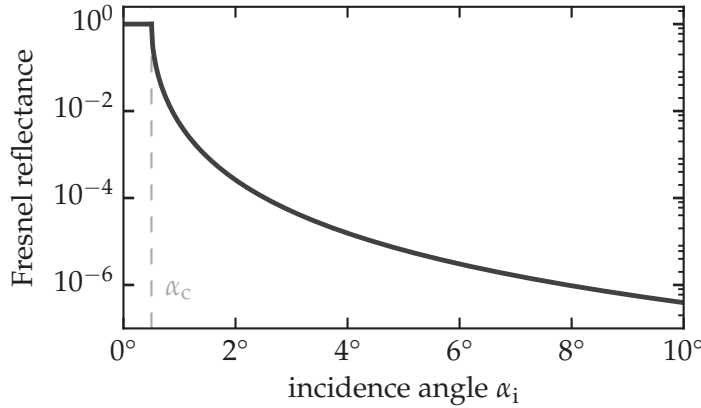


**Figure 2.9** | Fresnel reflectance of a smooth layer with a critical angle of  $\alpha_c = 0.5^\circ$  (dashed line).

### Dynamic and kinematic reflectivity of layered samples

XRR is frequently used to determine thicknesses in multilayer systems or stratified media. For such systems, the individual boundary conditions as well as the transmission and reflection coefficients at each interface have to be taken into account. Furthermore, interfaces are generally not perfectly smooth and sharp, but are rough and can extend in  $z$ . Thus, the reflected intensity deviates from the Fresnel reflectance.

Figure 2.10 shows a scheme of a multilayer system with  $N$  different layers, each layer  $j$  has a thickness  $d_j$ . The incident beam  $\vec{k}_i$  propagates from vacuum into the first layer of the sample. The wave is partially transmitted and partially reflected in accordance with the boundary conditions, the wave amplitudes are denoted as  $T_1$  and  $R_1$ , respectively. At the same time, the reflected wave from the interface between layer 1 and 2 also propagates through layer 1. The ratio of the amplitudes of reflected wave and transmitted wave in the  $j$ -th layer  $L_j$  can be obtained by a recursion formula, known as the Parratt formalism,<sup>[182]</sup> by

$$L_j = \frac{R_j}{T_j} = \frac{L_{(j+1)} \exp(-2ik_{z,j+1}z_j) + r_{(j,j+1)}}{L_{(j+1)} \exp(-2ik_{z,j+1}z_j)r_{(j,j+1)} + 1} \quad (2.36)$$

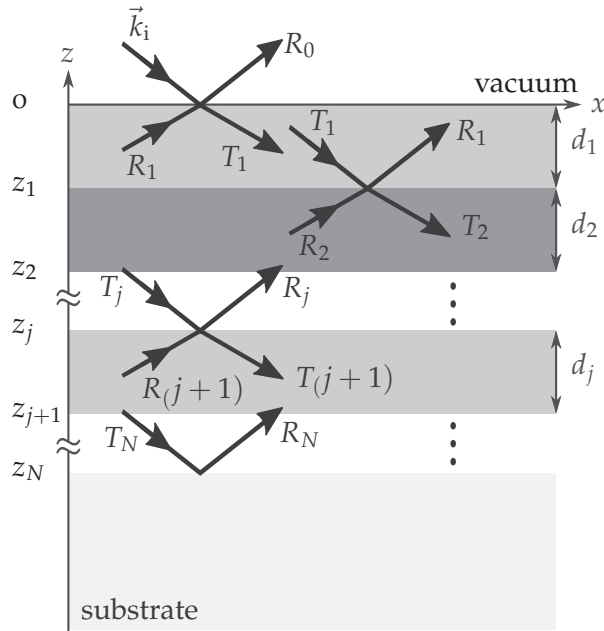
with the reflection coefficient, analogous to Eq. (2.31), of

$$r_{(j,j+1)} = \frac{k_{z,j} - k_{z,j+1}}{k_{z,j} + k_{z,j+1}}.$$

The recursion is carried out from the substrate at the bottom, where  $R_{N+1} = T_{N+1} = 0$ , to the surface of the multilayer system and yields the specular reflectance  $R$  after  $N$  iterations.

Another way of calculating the transmitted and reflected intensities is given in the matrix method<sup>[26,203]</sup> which is closely related to the Parratt formalism. The recursion is implemented by constructing transfer matrices of incoming and outgoing wave amplitudes in each layer, which is often easier to implement in a numerical simulation. Both methods take multiple reflections into account, which is known as the *dynamic* theory of scattering. Different software packages are available, such as IMD<sup>[257]</sup> or GenX,<sup>[20]</sup> that can be used to calculate reflectance curves for a broad range of multilayer systems in the framework of dynamic scattering theory.

**Figure 2.10** | Propagation scheme of reflected and refracted waves in a multilayer system with  $N$  different layers, each layer  $j$  with a reflected wave amplitude  $R_j$ , a transmitted wave amplitude  $T_j$  and a thickness  $z_j$ . The substrate at the bottom is sufficiently thick to fully absorb the transmitted wave.<sup>a</sup>



<sup>a</sup> Figure analogous to Daillant and Gibaud [46].

The dynamic theory of scattering is accurate for the full  $q_r$  range, in particular at  $q_r < q_c$ , but does not illustrate the physics of the scattering process. The reflection coefficient of a single layer with a thickness  $d$  in dynamic scattering theory in accordance with Eq. (2.36) is

$$r \equiv L_1 = \frac{r_{(1,2)} \exp(-2ik_{z,1}d) + r_{(0,1)}}{1 + r_{(0,1)}r_{(1,2)} \exp(-2ik_{z,1}d) - r_{(0,1)}} \quad (2.37)$$

with the reflection coefficients at the vacuum interface  $r_{(0,1)}$ , and at the substrate interface  $r_{(1,2)}$ , respectively.

Kinematic scattering theory, also called Born approximation, is the most widely used simplification of the dynamic scattering theory of Eq. (2.36).<sup>[46,83,94,203]</sup> The transition from dynamic to kinematic scattering theory requires some approximations, which are (i) neglecting multiple scattering by neglecting the phase shift  $-2k_{z,1}d$ , (ii) neglecting refraction and absorption in the material and (iii) assuming a proportionality between the change of reflection coefficient and electron density at each interface. Then, the

reflectance in kinematic scattering theory follows to<sup>[46,203]</sup>

$$R(q_r) = \frac{(4\pi r_0)^2}{q_r^4} \left| \int_{-\infty}^{+\infty} \frac{d\rho_e(z)}{dz} \exp(iq_r z) dz \right|^2 = R_F(q_r) \left| \int_{-\infty}^{+\infty} \frac{d\rho_e(z)}{dz} \exp(iq_r z) dz \right|^2. \quad (2.38)$$

The integral in Eq. (2.38) is obviously the definition of the Fourier transform of the vertical layer electron density gradient  $d\rho_e(z)/dz = \rho_e'(z)$ .<sup>\*</sup> Hence, by definition,  $R/R_F$  is the power spectral density (PSD) or, equivalently, the autocorrelation function of  $\rho_e(z)$ .<sup>[41,46,221]</sup>

This shall be briefly illustrated by examining the reflectance of a homogeneous layer on a semi-infinite substrate. Figure 2.11a shows an XRR profile of a layer of palladium with a thickness  $d = 10$  nm on silicon substrate, calculated using IMD<sup>[257]</sup> in dynamic theory. The density profile has the simple form of a Heavyside function, i.e.

$$\rho_e(z) = \begin{cases} 0 & z > 0, \\ \rho_{e,\text{Pd}} & -d \leq z \leq 0, \\ \rho_{e,\text{Si}} & z < -d. \end{cases} \quad (2.39)$$

The first derivative of  $\rho_e(z)$  consists of two Dirac functions  $\delta_{\text{Dirac}}$ ,

$$\frac{d\rho_e(z)}{dz} = (\rho_{e,\text{Pd}} - \rho_{e,\text{Si}})\delta_{\text{Dirac}}(z - d) - \rho_{e,\text{Pd}}\delta_{\text{Dirac}}(z). \quad (2.40)$$

Carrying out the integration of Eq. (2.38) after inserting Eq. (2.40) yields

$$R(q_r) = R_F(q_r) [\rho_{e,\text{Pd}}^2 + (\rho_{e,\text{Pd}} - \rho_{e,\text{Si}})^2 - 2\rho_{e,\text{Pd}}\rho_{e,\text{Si}}(\rho_{e,\text{Pd}} - \rho_{e,\text{Si}}) \cos(\Delta q_r)] . \quad (2.41)$$

It can be immediately seen from Eq. (2.41) that the smooth  $q_r^{-4}$  decay of the Fresnel reflectance is modulated by a cosine oscillation with the period length of  $\Delta q_r = 2\pi/d$ . The oscillations are also apparent in the reflectance curve (Fig. 2.11a). The PSD of the reflectance curve shown in Fig. 2.11b feature a single peak at a correlation length of 10 nm. Thus, by determining the period lengths of the reflectance oscillations, frequently called *Kiessig fringes*, it is possible to determine the thickness of one or several layers in the framework of kinematic scattering directly from the XRR data, without the need of material properties for full dynamic modelling.

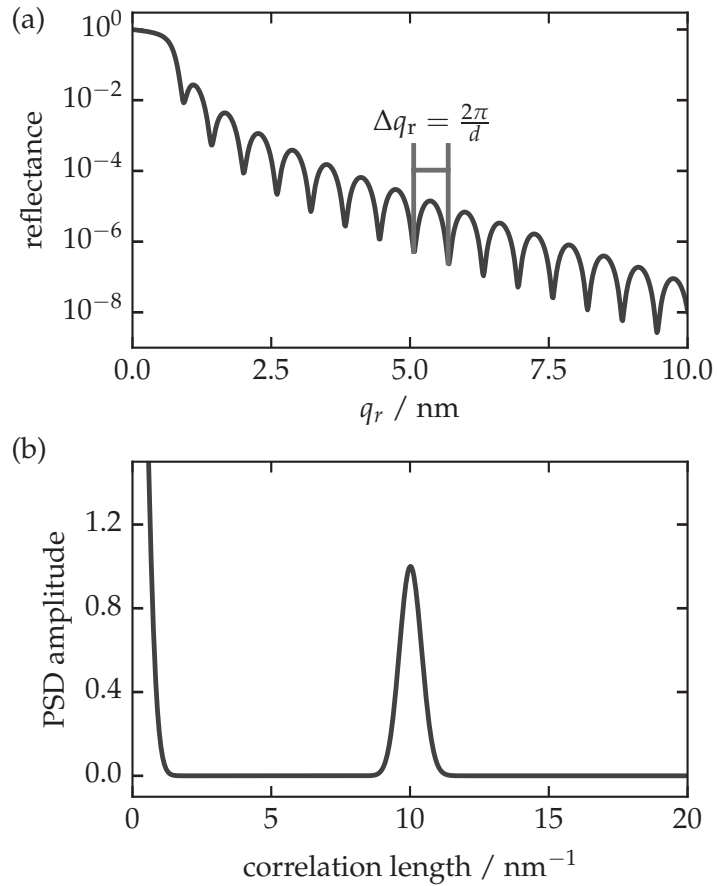
## 2.4 Diffuse small-angle X-ray scattering

In reflection geometry, diffuse scattering, also named non-specular scattering, is any scattering that appears at  $\alpha_f \neq \alpha_i$ . Any diffuse scattering vector  $\vec{q}$  has not only a component in  $q_z$ , but also in  $q_x$  and/or  $q_y$ , see Eq. (2.15) and Fig. 2.4. The  $\vec{q}$ -components parallel to the sample plane, i.e.  $q_x$  and  $q_y$ , are frequently expressed as  $\vec{q}_{\parallel} = (q_x, q_y, 0)^T$  and the perpendicular component accordingly as  $\vec{q}_{\perp} = (0, 0, q_z)^T$ . Consequently, the distribution of diffuse scattering yields information on lateral and vertical structure features of a sample system.

In the following, the angles  $\alpha_i$ ,  $\alpha_f$ , and  $\theta_f$  are restricted to small angles up to only a few degrees, which is the domain of small-angle scattering. Consequently, the accessible feature sizes increase according to  $2\pi/q_{\text{max}}$  from 0.1 nm in X-ray crystallography to larger dimensions in the nanometre regime. The fundamental principles of small-angle X-ray

<sup>\*</sup> As a reminder,  $\rho_e$  can be converted to the mass density  $\rho$  by Eq. (2.6).

**Figure 2.11** | (a) XRR profile calculated by dynamic theory using IMD<sup>[257]</sup> for a layer of palladium (Pd) with a thickness of  $d = 10$  nm on silicon substrate. (b) PSD of the above XRR profile.



scattering (SAXS), the theoretical framework of kinematic scattering in transmission geometry, was introduced in the 1930s by A. Guinier and further developed by him, O. Kratky, G. Porod, and others in the following decades. Nowadays, SAXS is a widely used experimental technique, especially at synchrotron radiation facilities, to determine the size, distribution, and detailed morphology of nano-sized objects. The perhaps most notable application of SAXS can be found in the field of biological macromolecules such as proteins, lipids, and colloids.<sup>[64,73]</sup>

The focus of this work is on nanostructured surfaces and layers. This requires a reflection geometry and is the domain of GISAXS,<sup>[45,94,132,138,159,194]</sup> which can be seen as the combination of SAXS and XRR.\* The geometry of GISAXS and the definition of the scattering vector is already shown in Fig. 2.4. A monochromatic X-ray beam  $\vec{k}_i$  impinges on a sample surface at a grazing incidence angle  $\alpha_i$ , which is kept fixed at around or below  $1^\circ$ . Instead of a point detector placed at  $\alpha_f = \alpha_i$  as in XRR, the scattering intensity is measured by a two-dimensional area detector placed several metres behind the sample. Hence, the probed  $q_x$  component is usually very small and the detector plane is nearly congruent with the  $q_y$ - $q_z$  plane, i.e.  $q_{\parallel} \approx q_y$ .

The theoretical treatment of GISAXS is, of course, related to the fundamentals of SAXS.<sup>[73]</sup> However, it requires substantial extension due to multiple scattering, reflection, and refraction events that are significant due to the grazing incidence reflection geometry. To an extent, analogies can be drawn between GISAXS and X-ray crystallography as described in Section 2.2: The effective average particle form factor  $W(\vec{q})$  in GISAXS

\* GISAXS is also referred to as the combination of SAXS and grazing-incidence diffraction.<sup>[159,190]</sup>

corresponds to the atomic form factor  $f_a$ , Eq. (2.16). The GISAXS structure factor\*  $S(\vec{q})$  resembles the lattice structure factor, Eq. (2.26).

### Isolated nanoparticles on a substrate

For isolated nanoparticles on a substrate,<sup>[132,159,194]</sup> the differential scattering cross-section is proportional to a scattering function  $F$ ,

$$\frac{d\sigma}{d\Omega} \propto \left| F(\vec{q}, \vec{k}_i, \vec{k}_f) \right|^2. \quad (2.42)$$

In kinematic approximation, the scattering function  $F$  is the Fourier transform of the nanoparticle shape function  $C(\vec{r})$  and is known as the particle form factor  $W(\vec{q})$ ,

$$F(\vec{q}) \equiv W(\vec{q}) \int_{C(\vec{r})} \exp(i\vec{q} \cdot \vec{r}) d\vec{r}, \quad (2.43)$$

analogous to Eq. (2.16). Kinematic scattering theory, frequently called Born approximation as described in the previous section, accounts for a single scattering or refraction event and neglects refraction and multiple scattering, as discussed in the previous section. However, especially at grazing incidence angles close to the critical angle at  $\alpha_i \approx \alpha_c$ , multiple scattering and refraction prevails and must be taken into account for a theoretical treatment of the scattering process.

A widely applied extension of the Born approximation in GISAXS is the semi-dynamic distorted wave Born approximation (DWBA).<sup>[94,192,207,220,245]</sup> Alternative dynamic scattering theories are the dynamic multilayer theory,<sup>[259,260]</sup> or the full electromagnetic wave field solvers ('Maxwell solvers').<sup>[265]</sup> In DWBA, a first order perturbation potential is added to the solution of an unperturbed reference potential in the Born approximation. In the case of isolated particles on substrate, the reference potential solution is that of a semi-infinite layer, i.e. the substrate, and the perturbation is the spatial distribution  $\delta U(\vec{r})$  of the nanoparticles. A consequence of applying DWBA is that the form factor, Eq. (2.43), splits up in four terms instead of being simply the Fourier transform of the nanoparticle shape function. These four terms are schematically illustrated in Fig. 2.12 by the four different refraction and scattering events that can occur. The first term on the left of Fig. 2.12 of a single scattering event in the nanoparticle is the Born approximation term. The other terms involve reflection by the substrate prior and/or after scattering by the nanoparticle. Each of the four form factor terms in DWBA includes, again, the Fourier transform of the particle shape function  $C(\vec{r})$ , but with different  $\vec{q}$  vectors that result from the different  $\vec{k}_{i,f}$  vectors shown in Fig. 2.12.

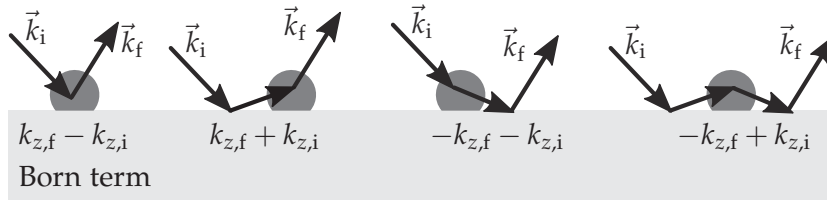


**Figure 2.12** | Illustration of the four scattering terms in the DWBA form factor (analog to [194]). The first scattering event (left side) corresponds to the Born approximation term. The other events account for additional reflection by the substrate.

\* The structure factor is also frequently named interference function in GISAXS.

Another consequence of the form factor terms in DWBA is the appearance of constructive interference of the four contributions when the incident angle  $\alpha_i$  and/or the scattering angle  $\alpha_f$  are equal to the critical angle  $\alpha_c$ . This results in an enhancement of the diffuse scattering intensity, known as the Yoneda or Vineyard peak,<sup>[266]</sup> which can be seen in a typical GISAXS image along the line of  $\alpha_f = \alpha_c$ . It is common to extract  $q_y$  or  $q_z$  cuts through the Yoneda peak to analyse scattering data as it yields better counting statistics of the weak diffuse scattering features. Particle form factors  $W(\vec{q})$  are in many cases tabulated analytical expressions for rather simple shapes such as spheres, spheroids, cylinders, boxes, or trapezoids.<sup>[133,194]</sup>

### Ensembles of particles

Most sample systems are not isolated particles, but consist of large ensembles of particles, often of different shapes and sizes. In many cases, the particles are correlated in their size and spatial distribution, which leads to a specific arrangement of the objects on or in the support material (e.g. on substrate, buried in a film, etc.) that influences the scattering pattern. The two extreme cases of inter-particle correlations are

- (i) a completely random ordering: no long-range ordering, the only correlation length present is the mean pair distance, i.e. the pair correlation function;
- (ii) a regular lattice or grating: well-defined positions which give rise to sharp, regularly spaced scattering intensity maxima, the so called grating truncation rods (GTRs).

Between these two extreme cases, virtually any type of size-spacing correlation between the same and different kinds of particles may exist, which is sometimes difficult to account for. In GISAXS, the arrangement of the scattering objects is expressed by the structure factor  $S(\vec{q})$ . Various models exist<sup>[137,185]</sup> to account for inter-particle correlations. The validity and suitability of the selected model is, however, frequently a source of controversy among the research community.

Staying with the extreme cases, it can be concluded<sup>[46]</sup> that the scattering cross section  $\frac{d\sigma}{d\Omega}$  and, thus, the scattering intensity distribution is dominated by the average particle form factor  $W(\vec{q})$  in the case of completely random ordering. The structure factor is very close to unity. In the case of a regular lattice,  $\frac{d\sigma}{d\Omega}$  is dominated by the structure factor, the form factor is strongly correlated with  $S(\vec{q})$ , and is only visible in the so called Guinier regime of low  $q$  values.<sup>[194,221]</sup>

Some simplifications<sup>[159,167]</sup> can be made to illustrate the connection between the measurable scattering intensity  $I(\vec{q}) \propto \frac{d\sigma}{d\Omega}$  in reciprocal space and the structural features of the ensemble of scatterers. This is the goal of any GISAXS measurement. The intensity distribution  $I(\vec{q})$  has the form

$$I(\vec{q}) \propto NW(\vec{q})S(\vec{q}) . \quad (2.44)$$

within the Born approximation ( $\alpha_i \gtrsim 3\alpha_c$ ) for line cuts along  $q_y$  or  $q_z$ , i.e. probing lateral or vertical features, and for  $N$  centrosymmetrical scatterers with an average particle form factor  $W(\vec{q})$  and a structure factor  $S(\vec{q})$ ,

In this picture, the form factor is the Fourier transform of the average particle shape function, Eq. (2.43), and the structure factor is the Fourier transform of the particle pair correlation function, as discussed above. Both quantities are strongly correlated in the Guinier regime and less correlated in the high  $q$  range, which is called the Porod regime.

The scattering intensity distribution is thus in general a correlated product of the form factor and the scattering factor that needs to be separated.

### Phase problem

The unambiguous separation of the product in Eq. (2.44) in conventional X-ray scattering is not possible because only the absolute square of the magnitude  $|\psi_f(\vec{k}_i, \vec{k}_f)|^2$  of any scattered wave  $\psi_f$  is measured by an X-ray detector. This is widely known as the phase problem or inverse problem since the early days of X-ray crystallography. Measuring only the absolute square of a wave function preserves the information of the wave amplitude, but results in the loss of the phase information. As a consequence, the form factor, Eq. (2.43), cannot be obtained directly by an inverse Fourier transform of the measured scattering pattern.

Instead, strategies in data acquisition and data analysis are required to solve the phase problem in order to obtain real-space structural information from a reciprocal space scattering pattern. Some common methods in small-angle scattering are:

- (i) Numerical modelling of  $W(\vec{q})$  and  $S(\vec{q})$  to find the closest resemblance of the calculated and measured scattering pattern (one-dimensional  $q_y$  or  $q_z$  cuts or full two-dimensional modelling). This approach requires the careful selection of suitable and physically meaningful models for the form factor and the structure factor and, ideally, a validation of the appropriateness of the chosen models. In GISAXS, a number of software packages is available for the calculation and fitting of scattering patterns in Born approximation and in DWBA.<sup>[7,39,52,133]</sup>
- (ii) Restricting the analysis to the Fourier transform of intensities. This is known as the Patterson function<sup>[183]</sup> and yields the PSD or autocorrelation function. The PSD is also not unambiguous, but yields information on lateral and vertical correlation lengths that give rise to the observed oscillatory part of the scattering pattern.
- (iii) Use of coherent radiation. A fundamentally different approach is the use of a fully coherent X-ray beam for scattering experiments. In lensless X-ray imaging,<sup>[55,56]</sup> the fully coherent soft X-ray beam of a dedicated beamline at a synchrotron radiation facility or at a free electron laser is split into an  $\mu\text{m}$ -sized object beam and a nm-sized reference beam that are separated by several  $\mu\text{m}$ . The object beam is scattered by the sample in transmission geometry and interferes with the reference beam, which generates a holographic SAXS pattern. In contrast to conventional X-ray scattering, where the scattering pattern is an incoherent superposition of coherent scattering, this X-ray Fourier holography<sup>[189]</sup> technique preserves the phase relations of the scattered waves by the interference with the reference beam. In this way, the phase problem is solved and the scattering pattern can be treated by direct Fourier inversion with numerical algorithms. The Fourier holography technique can be coupled with scattering contrast enhancement by anomalous magnetic scattering and by a variation of the X-ray polarisation. This scattering method, called soft X-ray spectro-holography, allows to determine the magnetic domain structure, e.g. of multilayer systems, with nm resolution.<sup>[56,57,68,89]</sup>

## 2.5 GISAXS on nanostructured films and surfaces

GISAXS now is a widely used X-ray technique,<sup>[135,158,166,222,247]</sup> that offers access to nanostructured surfaces, buried structures and depth-resolved measurements<sup>[45,97,176]</sup> in thin films and layer systems. Moreover, the tunable photon energy of a synchrotron radiation beamline provides access to GISAXS measurements of element-specific spatial distributions by anomalous scattering and to contrast variation techniques (Section 2.1.2). From the application point of view, GISAXS is a popular technique for monitoring the morphology of self-assembled block polymers for nanopatterning<sup>[10,24,35,47,79,80,95,156,171,180,218,233]</sup> or for chemical functionalisation, e.g. for the sensing of humidity.<sup>[9,72,181,255]</sup> Recent developments on the instrumental and methodological side are the use of micro- and nanofocus beams,<sup>[130,198,209]</sup> in-situ measurements with high repetition rate,<sup>[149,150,197]</sup> and in-situ deposition and annealing during GISAXS measurements.<sup>[71,78,91,156,268]</sup>

### GISAXS on grating structures

Periodically structured surfaces in the sub- $\mu\text{m}$  and nm regime are becoming increasingly important for many technological applications. Principal applications are masks for semiconductor photolithography or diffraction gratings for spectrometers and monochromators, e.g. at synchrotron radiation beamlines and free-electron lasers. Gratings are not only relevant for their technological application in itself, but also as very precisely fabricated model systems for methodological studies of tools in dimensional nanometrology (see Section 2.7). One- and two-dimensional gratings are, for example, currently under discussion<sup>[27]</sup> as possible future reference structures for a ‘golden standard’ that could be used to calibrate and cross-validate real-space and reciprocal space nanometrology methods on a common basis.

A typical surface reflection grating has a cross-section as schematically depicted in Fig. 2.13a. The grating period  $P$  is commonly referred to as the pitch and is the sum of the critical dimension, i.e. line width,  $CD$ , and the groove width  $G$ . Gratings are highly ordered systems of scatterers, which means that the structure factor prevails in the scattering intensity distribution, Eq. (2.44). The form factor characterises the mean shape of typical scatterers and is thus indicative of the cross-sectional line shape. The particular case of scattering from surfaces and multilayer gratings has been described in detail.<sup>[92,108,152,153,237,263,264]</sup> The observed scattering patterns can be well understood by reciprocal space construction.<sup>[153]</sup> The reciprocal space representation of a line grating, shown in Fig. 2.13b, is a series of so-called grating truncation planes that are perpendicular to the grating surface and parallel to the grating lines, i.e. parallel to  $q_z$  and  $q_x$  (orange planes in Fig. 2.13b). Adjacent planes are separated by  $\delta q_y = 2\pi/P$  in accordance with the pitch  $P$  of the grating.

All possible elastically scattered wave vectors  $\vec{k}_f$  can be represented by the Ewald sphere (Fig. 2.7) with the radius  $2\pi/\lambda$  at a fixed photon energy  $E_{ph} = hc/\lambda$ . Hence, the scattering pattern in the detector plane arises from the intersection of the Ewald sphere with the reciprocal space representation of the lattice. In terms of the azimuthal orientation angle  $\varphi$  between the projection of the incident beam on the sample plane and the lines of the grating, see the inset in Fig. 2.14, two special cases can be identified: Alignment of beam projection and grating lines parallel ( $\varphi = 0^\circ$ ) and perpendicular ( $\varphi = 90^\circ$ ) with respect to each other.

In parallel orientation, i.e.  $\varphi = 0^\circ$ , the Ewald sphere intersects the grating truncation

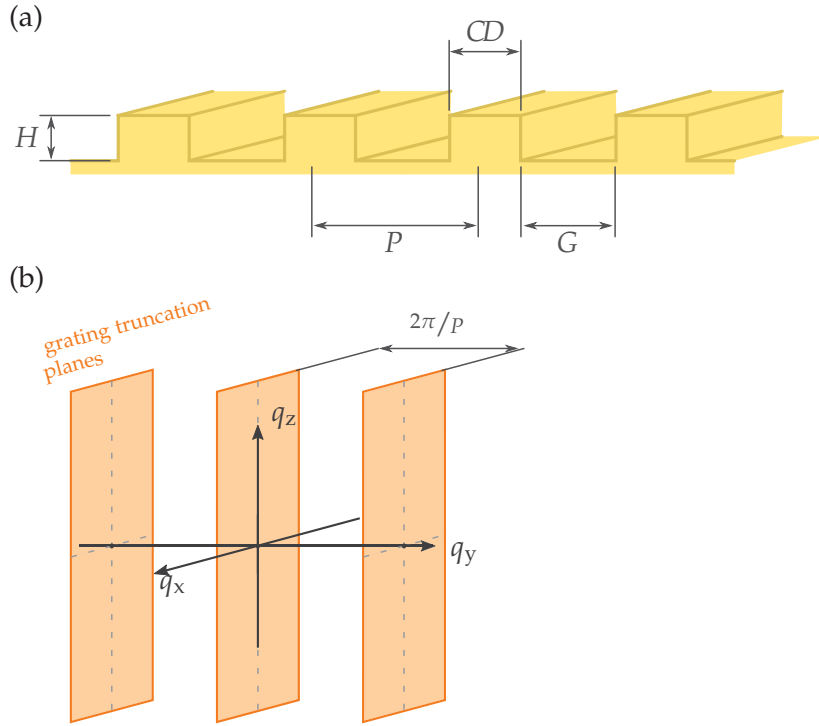


**Figure 2.13** | Schematic representation of a surface grating with pitch  $P$ , critical dimension  $CD$ , groove width  $G$ , and line height  $H$ . (a) Cross-sectional view in real space. (b) Reciprocal space representation with grating truncation planes (orange), parallel to the  $q_x$ - $q_z$  plane and separated by  $\Delta q_y = 2\pi/P$ .

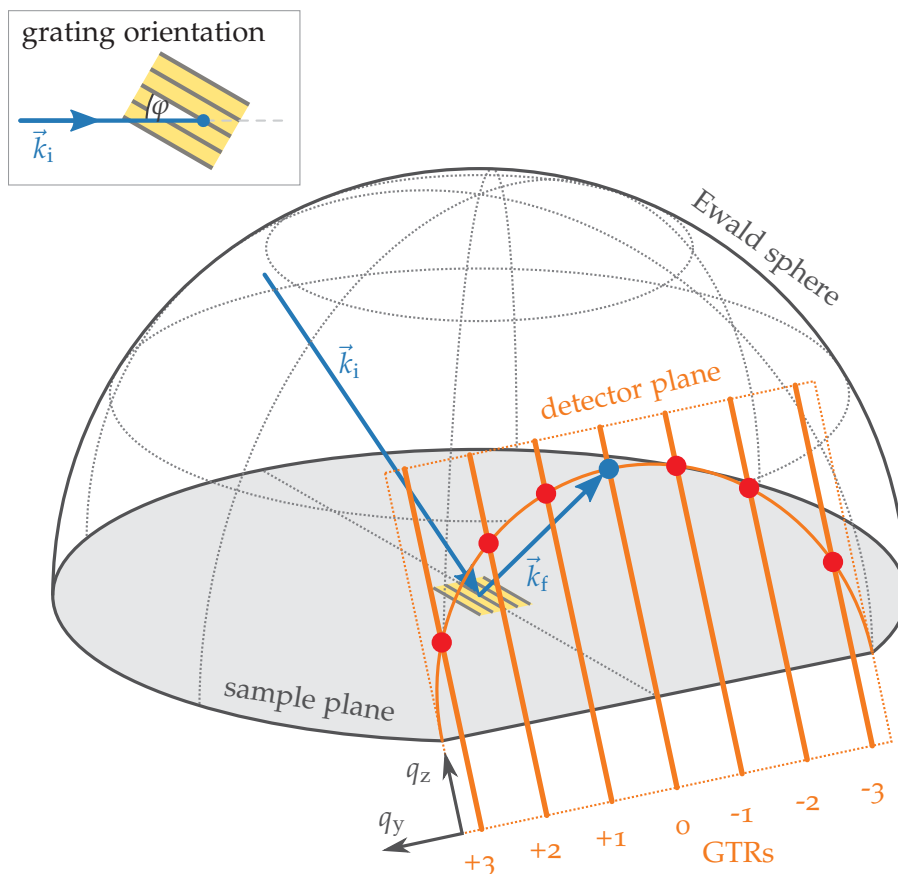
planes as depicted in Fig. 2.14. This gives rise to grating truncation rods (GTRs) in the detector plane along  $q_z$ , periodically repeated along  $q_y$ , represented by the orange lines in Fig. 2.14. The intersection of GTRs and Ewald sphere (grey wire frame hemisphere in Fig. 2.14) becomes visible on the detector as a series of sharp spots along a semi-circular intersection (red dots in Fig. 2.14, the blue dot indicates the specular reflection spot). It is known that the GISAXS pattern is very sensitive to smallest azimuthal rotations  $\varphi$  away from the parallel orientation. Deviations of  $0.002^\circ$  can already be observed by a visual distortion of the scattering image. Due to geometrical reasons,<sup>[263]</sup> the intersection of Ewald sphere and GTRs bends up in one direction and the GTR scattering spots move along  $\pm q_z$ .

In perpendicular alignment, i.e.  $\varphi = 90^\circ$ , the grating is aligned in the usual orientation of a diffractive optical element. The dominant features are the grating diffraction orders along  $q_z$  due to the constructive interference of waves reflected at the top and at the bottom of the grating lines. The expression of the optical path difference  $\Delta s = P (\cos(\alpha_f) - \cos(\alpha_i))$  leads to the well-known reflection grating formula for the distance of interference maxima of the orders  $m$  and  $m + \Delta m$  along  $q_z$

$$\Delta m \lambda = P \left( \cos(\alpha_{f,(m+\Delta m)}) - \cos(\alpha_{f,(m)}) \right) . \quad (2.45)$$

In terms of diffuse scattering, the grating truncation planes shown in Fig. 2.13b are parallel to the detector plane at  $\varphi = 90^\circ$ . Consequently, no GTRs are visible and the detector plane contains the specular axis.

**Figure 2.14** | Intersection of GTRs and the Ewald sphere in reciprocal space reconstruction. The inset shows the orientation angle  $\varphi$  between incident beam and grating lines. The intersection is shown for the case of parallel orientation, i.e.  $\varphi = 0^\circ$ .



## 2.6 Dealing with the phase problem: Direct data analysis and numerical simulation

It is helpful to take another look at the phase problem that was already discussed in Section 2.4, in particular with regard to metrology. As stated, conventional X-ray scattering is an incoherent superposition of coherent scattering, thus, there is no access to the phase. Instead, it is common to numerically simulate a measured GISAXS pattern by parameter optimisation of suitable models for the form factor and structure factor (Eq. (2.44)). This is a very successful approach to gain qualitative insights into the morphology and into the evolution of dimensional parameters in a wide range of nanostructured systems using all the benefits of a scattering technique, such as non-contact measurements, depth sensitivity, or element selectivity. However, when absolute values are of interest, e.g. the *CD* of a grating or the mean size of nanoparticles, modelling is challenging in terms of assessing the associated uncertainties. It is difficult to estimate the accuracy of an optimised model parameter and even more difficult to quantitatively evaluate the appropriateness of the chosen model itself. Moreover, different kinematic, semi-dynamic and dynamic frameworks exist to treat the scattering process, which require an in-depth evaluation of the consistency and validity of obtained values.

Hence, it is desirable to get structural parameters ‘directly’ from the scattering data, that is, without numerical modelling of structure and form factors.\* In this way, it is possible to determine the uncertainties of dimensional parameters obtained by a scattering measurement. This includes XRR and GISAXS in the context of this work,

\* Throughout this work, an analysis of this kind is named ‘direct analysis’.

solely by the contributions of the experimental parameters and the numerical data analysis. The complex modelling process is completely avoided and the traceability of the parameters becomes easier to obtain. A dimensional value determined in this way could then serve as a starting point or reference value for more complex data analysis such as modelling. Any model must reproduce such a value, which enables the systematic testing and validation of the model and the modelling process. Moreover, reference values and uncertainties obtained by direct analysis help to reduce the parameter space of a simulation and increase the accuracy of the optimised model parameters by providing robust variation ranges of the start parameters.

In this way, direct data analysis of GISAXS and XRR measurements contributes in two ways to the methodological benefits of structure parameter determination: (i) It can establish the traceability of the scattering measurements; (ii) and it yields a more general understanding of the modelling process and its uncertainties, not just for the particular sample system under investigation.

The direct analysis methods in this work are based on an analysis of the frequencies in measured GISAXS and XRR data, e.g. by Fourier transform of the intensity, or by determining separation distances directly on the scattering image or on the reflectance profile, respectively.

### Fourier transform

Details of the implemented direct analysis for the specific application can be found in the relevant Chapters 4 and 6 on GISAXS and XRR, respectively. The common basis of the analysis method is the Fourier transform of one-dimensional data profiles, i.e. reflectance curves in XRR and cuts along  $q_y$  or  $q_z$  in GISAXS. The Fourier transform of the integrable function  $f(x) : \mathbb{R} \rightarrow \mathbb{C}$  is here defined as

$$\mathcal{F}(\xi) = \int_{-\infty}^{\infty} f(x) \exp(-i2\pi\xi x) dx . \quad (2.46)$$

Discrete and equidistant sequences of possibly complex numbers  $f_0, f_1, \dots, f_{N-1}$ , e.g. data points of a recorded signal, are converted by their discrete Fourier transform (DFT)  $\mathcal{F}_{\text{DFT}}(k)$  according to the definition

$$\mathcal{F}_{\text{DFT}}(k) = \sum_{n=0}^{N-1} f_n \exp(-i 2\pi k n/N) . \quad (2.47)$$

The PSD of  $f(x)$  is obtained by taking the absolute square of the complex Fourier transform, i.e.

$$\text{PSD}(\xi) = |\mathcal{F}(\xi)|^2 . \quad (2.48)$$

The PSD contains no information on the Fourier phase any more, which makes a unambiguous back-transformation impossible. This is another illustration of the phase problem between reciprocal space and real space in X-ray scattering measurements, which are interlinked by Fourier transforms, e.g. see Eqs. (2.27) and (2.38).

## Window function

When applying Eq. (2.47) to a finite series of data points, there is frequently the problem of non-zero boundaries. As a consequence, the signal to be transformed is not periodic any more, which results in a smearing of the Fourier amplitudes. This is frequently called *leakage*. Leakage also leads to the appearance of unwanted side-maxima around peaks in the Fourier amplitude spectrum. Window functions are used to reduce the smearing and to preserve the true Fourier amplitude.<sup>[23,87,221]</sup> A window function is basically a function that varies between zero and one along a given interval, e.g. the number of data points, the boundary values are typically zero. Multiplication of the window function with the data to be transformed results in a weighing of the data within the interval and a damping of the start and end values to zero. In this way, the data is brought into a periodic shape within the window and leakage is reduced. In Fourier space, such multiplication results in a convolution of the Fourier transform of the data and the window. However, the convolution results in additional spectral components, i.e. the leakage of the window function, which may overlay spectral information of the data. Thus, the selection of a window function for a specific application is always a compromise between minimising the leakage, i.e. unwanted frequency components in the spectrum, and preserving spectral resolution, i.e. the ability to distinguish two different frequencies in a spectrum.<sup>[179]</sup>

A large variety of window functions exist,<sup>[87]</sup> the selection depends on the purpose and goals of the signal processing task. For the Fourier transform of GISAXS and XRR profiles, common and suitable window functions are the Hann window<sup>[21]</sup> (frequently also called Hanning window) and the Kaiser window (or Kaiser-Bessel window).<sup>[113]</sup> The Hann window of  $n \in N$  interval points as shown in Fig. 2.15 is defined by

$$w_H(n) = \frac{1}{2} \left[ 1 - \cos \left( \frac{2\pi n}{N} \right) \right]. \quad (2.49)$$

The Kaiser window is based on the modified Bessel function of zeroth order  $J_0$  and has an additional parameter  $\gamma$  that allows to vary the shape and width of the window within the interval (the window at different  $\gamma$  values is displayed in Fig. 2.15). The Kaiser window is defined by

$$w_K(n) = \frac{J_0 \left( \pi\gamma \sqrt{1 - \left( \frac{2n}{N-1} - 1 \right)^2} \right)}{J_0(\pi\gamma)} \quad (2.50)$$

inside the interval  $(1 \dots N)$  and zero otherwise. The parameter  $\gamma$  is a non-negative real-valued number that determines the trade-off between spectral leakage and spectral resolution. The lower  $\gamma$ , the higher is the spectral resolution, but also the spectral leakage of the window. The value  $\gamma = 0$  corresponds to a rectangular window, i.e. no window,  $\gamma = 6$  is very similar to the Hann window, see Fig. 2.15.

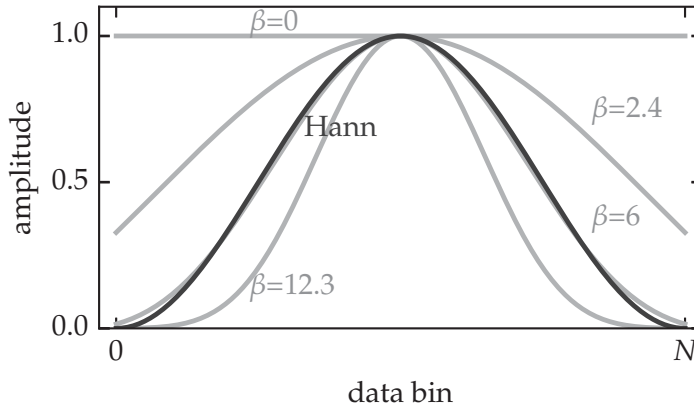


**Figure 2.15** | Two common windows in signal processing. The Kaiser window (grey lines) width is varied by  $\gamma$ .  $\gamma = 6$  closely resembles the Hann window (black line).

### Tikhonov regularisation

Another mathematical tool that will be needed later on, in Section 4.2.4, is the Tikhonov regularisation.<sup>[236]</sup> Regularisation in general is a method to solve an ill-posed problem, e.g. to find a good approximation of the vector  $\vec{z}$  to solve the linear equation

$$\hat{A}\vec{z} - \vec{y} \approx \vec{0} \quad (2.51)$$

with the given vector  $\vec{y}$ , e.g. data points, and the coefficient matrix  $\hat{A}$ .<sup>[168]</sup> Ill-posed means that the matrix  $\hat{A}$  is singular or changes drastically with small variations of the initial conditions and that the given vector  $\vec{y}$  is contaminated with noise. The result of solving such an ill-posed problem would be a solution  $\vec{z}$  that is completely dominated by contributions from noise and rounding errors.<sup>[85]</sup> Regularisation, in particular Tikhonov regularisation, is the process of introducing additional assumptions on the smoothness of the solution, which allows to adapt the problem to a meaningful numerical analysis.

The specific application in this work can be summarised as performing a Fourier amplitude fit. Again, the starting point is a one-dimensional data set such as an intensity profile extracted from a GISAXS image. However, the data set is not uniformly distributed in many cases, but has discontinuities or, in other words, gaps. This is in particular the case for GISAXS profiles extracted from scattering images recorded using the PIL-ATUS 1M detector (see Sections 3.5.2 and 4.2). Such discontinuities are problematic for Fourier transforms as described in the previous section because it induces unwanted additional spectral contributions due to the necessary ‘filling’ of the gaps with zeros, which is called *zero padding*.

Hence, a different approach is required in the case of non-uniformly spaced data: Instead of a direct Fourier transform, a best fit optimisation of the amplitudes of a finite basis of Fourier coefficients is carried out in conjunction with the Tikhonov regularisation.<sup>[236]</sup> In this way, discontinuities in the data are not relevant because the best fit optimisation (in this case by least-squares optimisation) does not require uniformly spaced mesh points.

In the following, the basic procedure of the implementation of the linear least-squares minimisation problem, Eq. (2.51),

$$\|\hat{A}\vec{z} - \vec{y}\|_2 \xrightarrow[\text{optimisation}]{\text{least-squares}} \text{minimum} \quad (2.52)$$

is described. For the specific application case described above,  $\hat{A}$  is the matrix to be regularised,  $\vec{z}$  is the solution vector. Thus,  $\vec{z}$  contains the amplitudes of the Fourier

coefficients, i.e., sine and cosine terms, of the best approximation of Eq. (2.51) to the vector of data points  $\vec{y}$ . The function  $\|\cdots\|_2$  denotes the 2-norm, or Euclidean norm, of a vector.

The matrix  $\hat{A} \in \mathbb{R}^{m \times (n+2)}$  contains a finite number  $n$  of Fourier coefficients ( $n \lesssim 1/2 \times N_{\text{data}}$ , where  $N_{\text{data}}$  is the number of data points of the intensity profile,  $m = N_{\text{data}}$ ), that is, cosine and sine base vectors matrices  $\hat{C} \in \mathbb{R}^{m \times n}$  and  $\hat{S} \in \mathbb{R}^{m \times n}$ , respectively. Additionally, a constant vector  $\vec{K}_{1/2} = (1/2, \dots, 1/2)^T \in \mathbb{R}^m$  and a linear vector  $\vec{x} = (0, 2\pi/m, \dots, 2\pi/m(m-1))^T \in \mathbb{R}^m$  are added to account for offset and linear trend of the data. Altogether, the matrix  $\hat{A}$  has the structure

$$\hat{A} = \left( \vec{K}_{1/2}, \vec{x}, \hat{C}(\vec{x}), \hat{S}(\vec{x}) \right) = \begin{pmatrix} 1/2 & 0 & \cos(0) & \dots & \cos(0) & \sin(0) & \dots & \sin(0) \\ 1/2 & \frac{2\pi}{m} & \cos(\frac{2\pi}{m}) & \dots & \cos(\frac{2\pi}{m} n) & \sin(\frac{2\pi}{m}) & \dots & \sin(\frac{2\pi}{m} n) \\ 1/2 & 2\frac{2\pi}{m} & \cos(2\frac{2\pi}{m}) & \dots & \cos(2\frac{2\pi}{m} n) & \sin(2\frac{2\pi}{m}) & \dots & \sin(2\frac{2\pi}{m} n) \\ \vdots & \vdots & \vdots & & \vdots & \vdots & & \vdots \\ 1/2 & g_m & \cos(g_m) & \dots & \cos(g_m n) & \sin(g_m) & \dots & \sin(g_m n) \end{pmatrix}, \quad (2.53)$$

with the factor  $g_m = (m-1)\frac{2\pi}{m}$ . So far,  $\hat{A}$  is just a coefficient matrix containing all Fourier amplitudes that should be optimised. Tikhonov regularisation is applied by extending  $\hat{A}$  by the matrix  $\hat{L} \in \mathbb{R}^{m \times m}$  that has the structure

$$\hat{L} = h_T \cdot \begin{pmatrix} 1 & 0 & \dots & 0 \\ 0 & 1 & \dots & 0 \\ \vdots & 0 & \ddots & \vdots \\ 0 & \dots & 0 & 1 \end{pmatrix} \equiv h_T \cdot \hat{1}. \quad (2.54)$$

with the regularisation parameter  $h_T \in \mathbb{R}$ . Thus, the extended matrix  $\hat{A}_{h_T}$  looks like

$$\hat{A}_{h_T} = \begin{pmatrix} \hat{A} \\ h_T \cdot \hat{1} \end{pmatrix}. \quad (2.55)$$

The optimal regularisation parameter  $h_T$  is determined by an L-curve,<sup>[84–86]</sup> which plots the norm of the solutions  $\|\vec{z}\|_2$  corresponding to an optimisation parameter  $h_T$  versus the norm of the residuum of the solution  $\|\hat{A}_{h_T}\vec{z} - \vec{y}\|_2$ . Each point in an L-curve, Fig. 2.16, is the pair of both norms for a specific value of  $h_T$ , which increases typically on a decade scale. Figure 2.16 illustrates that regularisation is always a trade-off between a too small smoothing (small  $h_T$ ), i.e. large solution norm, and an over-smoothing (large  $h_T$ ) that does not fit to the data any more, i.e. the residual norm gets large. Hence, the optimal Tikhonov parameter  $h_T$  is usually found at the beginning of the plateau in the L-curve, which would be between  $10^{-3}$  and  $10^{-2}$  in Fig. 2.16.

Once  $\hat{A}_{h_T}$  is determined, Eq. (2.52) can be solved by least-squares optimisation. The solution vector  $\vec{z}$  contains the Fourier amplitudes of the  $n$  Fourier base vector sine and cosine terms and the product  $\hat{A}_{h_T}\vec{z}$  yields the best fit of the vector  $\vec{y}$  by the finite Fourier series. A plot of the absolute squares of the sine and cosine amplitudes in  $\vec{z}$  as a function of the Fourier coefficient number  $(0, \dots, n)$  yields the PSD of the profile, just like the DFT of uniformly spaced data.

The direct frequency analysis techniques are applied to GISAXS and XRR data of laterally and/or vertically nanostructured films and layers. One of the primary goals

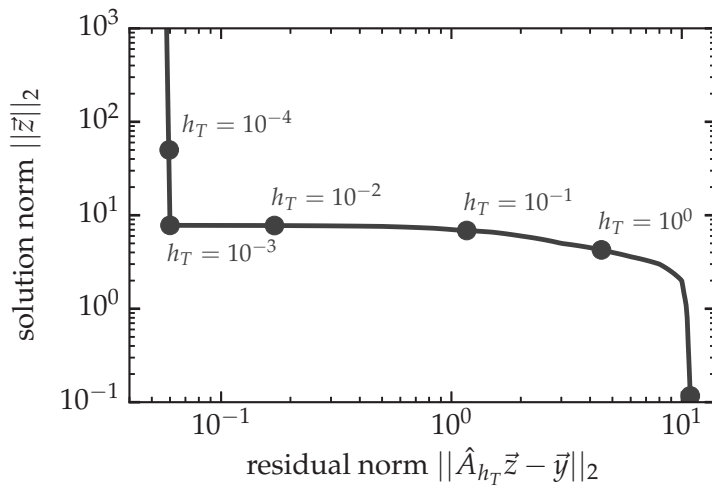


**Figure 2.16** | A typical L-curve of a Tikhonov regularisation. Each dot corresponds to a best fit optimisation using the stated regularisation parameter  $h_T$ .

of this approach is the traceability of obtained dimensional parameters, which is the field of dimensional nanometrology. In the next section, some of the goals and questions of nanometrology are presented along with some basic vocabulary and some typical nanometrology tools that are relevant for the context of this work, other than GISAXS and XRR.

## 2.7 Dimensional nanometrology

Modern nanotechnology<sup>[13]</sup> offers a wide range of prospective applications, e.g. in materials science, electronics, communication, or drug delivery. One of the strong driving forces is the microelectronics industry, together with the compliance with ‘Moore’s law’ of doubling the number of transistors on a chip every 18 months. New materials and ever decreasing structure sizes down to the atomic scale are needed for future devices because traditional silicon MOSFET technology is reaching its limits.<sup>[157,246]</sup> Next-generation photolithography tools in the extreme UV regime (EUV lithography) and directed self-assembly of block copolymer (BCP)<sup>[2,11,47,81,136]</sup> thin films are promising techniques for producing a wide variety of structures with great accuracy and dimensions down to several nanometres. Not only microelectronics, but also other emerging fields such as organic photovoltaics,<sup>[28,211]</sup> nanotemplating,<sup>[171,184]</sup> or surface functionalisation<sup>[102,196]</sup> make increasing use of structuring in the nanometre range by thin film deposition, processing, and self-assembly techniques.

What all these different applications have in common is the need for suitable metrology tools to measure surface and subsurface structural parameters with sufficient accuracy, which is the field of dimensional nanometrology.<sup>[27,134]</sup> There is a large variety of different analytical techniques: Direct methods, such as atomic force microscopy (AFM)<sup>[154,261]</sup> and critical-dimension electron microscopy (CD-SEM)<sup>[30,244]</sup> as well as indirect methods, such as GISAXS,<sup>[92,129,253]</sup> critical dimension SAXS (CD-SAXS),<sup>[98,111,231]</sup> extreme UV (EUV) scatterometry,<sup>[77,187]</sup> or ellipsometry.<sup>[5,169,239]</sup> All of them have very specific advantages and drawbacks. Moreover, only a few of the methods are traceable, that is, related to the International System of Units (SI system) by an unbroken chain of comparisons with known uncertainties, which is ultimately required in order to associate uncertainty values with any measured quantity.

## 2.7.1 Terminology

In principle, any value that is measured cannot stand in isolation. In order to represent a meaningful physical quantity, two additional components must be associated with the value: A physical unit and an uncertainty. The physical unit states the internationally agreed convention on the magnitude of a quantity under examination. The existence of a commonly agreed definition of basic physical quantities such as length, time or mass is of crucial importance for the exchange of goods, materials, and knowledge since the rise of civilizations. The current global standard of base unit definitions, the SI system,<sup>[15]</sup> is monitored and continually developed by the Comité International des Poids et Mesures (CIPM), an international organisation.

Metrology, the science of measurement, is coordinated by national metrology institutes (NMIs) such as the Physikalisch-Technische Bundesanstalt (PTB) in Germany, the National Physical Laboratory (NPL) in the United Kingdom, or the National Institute for Standards and Technology (NIST) in the United States. NMIs all over the world also provide national standards that are based on the SI. An important term in this context is the *traceability* of a measurement. To *trace* a measurement of an instrument, i.e. to make it *traceable*, means to establish an unbroken chain of comparisons that relate the instrumental output to a known standard, e.g. an SI unit and/or a national standard.<sup>[18]</sup> Each step contributes to the measurement uncertainty of the experiment. Thus, the traceability of a result establishes a measurement uncertainty budget of the quantity. The measurement uncertainty is an interval that contains the true, but unknown and non-retrievable value of a quantity with a certain probability. The uncertainty and the average value of an experiment, or measurement, are influenced by different types of errors (random and systematic errors) and are evaluated by a statistical model. The 'Guide to the Expression of Uncertainty in Measurement'<sup>[16]</sup> and its supplements<sup>[17,19]</sup> give detailed guidelines on how to evaluate measurement data. The following definitions of some basic terms in metrology have been taken from the guide of the *International Vocabulary of Metrology*.<sup>[18]</sup>

**Measurand** is the physical quantity that is intended to be measured.

**Accuracy** is the closeness of agreement between a measured quantity value and the true quantity value of a measurand. The accuracy of a measurement is determined by the systematic errors that are present in the experiment.

**Precision** is the closeness of agreement between indications or measured quantity values obtained by replicate measurements on the same or similar objects under specified conditions. The precision is in most cases expressed as the standard deviation or variance of the mean result of a series of repeated measurements under the same conditions.

**Measurement uncertainty** is the non-negative parameter characterising the dispersion of the quantity values being attributed to a measurand, based on the information used. The measurement uncertainty includes all contributions of systematic and random effects. The evaluation of the components is frequently divided into *Type A* and *Type B* uncertainty evaluation. *Type A* is characterised by standard deviations of statistical distributions of measurement series. *Type B* evaluation includes all other components and can also be characterised by standard deviations, e.g. derived from probability density functions or other information.

---

Passages of Section 2.7.1 have been implemented from [255].

## 2.7.2 Microscopy methods

Microscopy methods, such as scanning probe microscopy and electron microscopy, belong to the real space or direct methods of nanometrology. The images produced by these techniques show the real space microscopic representation of the sample on the field of measurement, which typically covers an area in the range of  $\mu\text{m}^2$ . Thus, real space methods do not require abstract models for the shape of the investigated nanostructures like indirect scattering methods. However, real space images can be subject to severe measurement artefacts and yield only local information on the structure with limited statistical representativeness.

### Atomic force microscopy

Atomic force microscopy (AFM) is a scanning probe microscopy technique that maps laterally the height of a sample surface with a resolution down to the atomic scale.<sup>[14,151]</sup> It is thus a surface sensitive technique that probes real-space lengths. The measurement principle is shown schematically in Fig. 2.17. The tip at the end of the cantilever with a radius in the order of nanometres is brought in very close proximity to the surface of a sample by piezoelectric tube scanners. Surface forces such as Van-der-Waals interaction, electrostatic, or magnetic forces result in a deflection of the cantilever. The cantilever deflection is measured by a feedback control system that uses a photodiode to determine the position of a laser beam reflected on the cantilever surface. Typical interaction forces between tip and sample range from  $10^{-11}$  N to  $10^{-6}$  N.<sup>[151]</sup>

Different operation modes exist that are distinguished by the tip motion and the feedback control system:

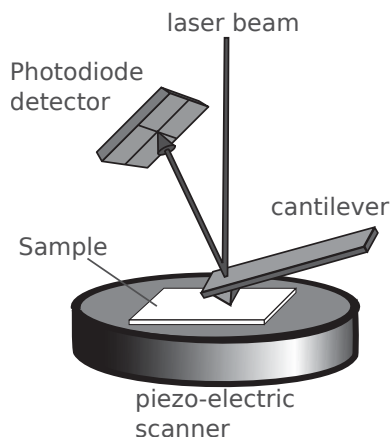
- (i) In *contact mode*, the tip is moved across the sample surface. The deflection of the cantilever is measured either directly from the laser spot position, or is kept constant through maintaining the same force by motion of the piezoelectric scanners. Contact mode scans provide high resolution and scanning speed, but may cause measurement distortions and damage to the sample and the tip as both are in constant contact.<sup>[53]</sup>
- (ii) In *tapping mode*, the cantilever oscillates close to its resonance frequency, which is typically in the range of kHz. When the tip approaches the sample, the oscillation changes due to the tip-surface interactions. The tip is not in physical contact with the surface, but is repulsed and attracted by interaction forces, which is why it is also called non-contact mode. The oscillation amplitude can range from hundreds of nm to only a few nm and the changes in amplitude, phase, or frequency can be detected depending on the sample system and the physical properties that are of interest.<sup>[53]</sup>

Measuring the phase shift of the cantilever oscillation in non-contact mode is frequently called *phase imaging*. Phase images yield information on the local stiffness and friction and, thus, on the spatial distribution of different materials.

A metrological AFM provides high dimensional measurement accuracy in conjunction with traceability to the SI unit of length in lateral and vertical direction.<sup>[261]</sup> The lateral and vertical traceability is realised in most cases by three laser interferometers that control the position of the piezoelectric scanner tubes of the  $x$ ,  $y$ , and  $z$  axis.<sup>[43]</sup> The

**Figure 2.17** | Schematic measuring principle of atomic force microscopy.<sup>a</sup>

<sup>a</sup> Image source: Charles Roduit, 2010, www.freesbi.ch, Creative Commons Attribution.



interferometers have to be carefully aligned and non-linearities have to be corrected for in real-time to achieve sub-nm resolution.<sup>[44]</sup>

AFM is a very widely used tool in surface science as it requires little sample preparation, can be applied to conductive, non-conductive, solid, and liquid surfaces and provides real-space images with atomic resolution. Drawbacks of AFM are the low counting statistics due to the small areas, i.e. field width in  $\mu\text{m}$  range, that are probed, and the appearance of imaging artefacts,<sup>[256]</sup> which makes traceability challenging.<sup>[154,261]</sup> Moreover, it is a method that is only sensitive to the surface, i.e. depth-resolution and access to buried features cannot be achieved. AFM and X-ray scattering techniques such as GISAXS are complementary techniques as the drawbacks of one method are compensated by the strengths of the other. Thus, numerous studies exist where both techniques have been used in combination for investigations of morphological features on and within thin films.<sup>[6,40,148,162,172,188,193,200,212,219,252]</sup>

## Electron microscopy

In electron microscopy<sup>[65,76]</sup> (EM), a conducting sample is illuminated with electrons accelerated by high voltages to obtain a real-space image of the sample. The electrons usually possess kinetic energies of 1 keV to 400 keV and are focussed by electrostatic and magnetic lenses on the sample. Basically, two types of EM exist: Transmission electron microscope (TEM), which generates a full-field image and scanning electron microscope (SEM), which is a raster scanning technique. In a TEM as shown exemplary in Fig. 2.18, the primary electrons accelerated by the high voltage are detected directly. The electron beam with kinetic energies of tens of keV is partially scattered during the passage through the sample, the spatial intensity distribution of the transmitted primary electrons is recorded by an analog or digital area detector. This is the same principle as in optical transmission microscopy using visible light, but the wavelength and, consequently, the diffraction limit of 40 keV electrons according to  $\lambda = hc/eE_e = 0.03 \text{ nm}$  is much smaller than for visible light. It is thus possible to reach a resolution of 50 pm and below,<sup>[60]</sup> which is unattained by any other imaging technique. In an SEM as shown in Fig. 2.19, the primary electrons are not detected, but focussed and raster scanned over the sample. The electron energies are around an order of magnitude smaller than in TEM, sometimes below 1 keV. The electrons interact with the atoms close to the sample surface and emit different signals, such as secondary electrons, backscattered electrons, and photons (visible light up to X-ray fluorescence). The emitted interaction products carry the topographical information and are detected, the secondary electrons are used in most

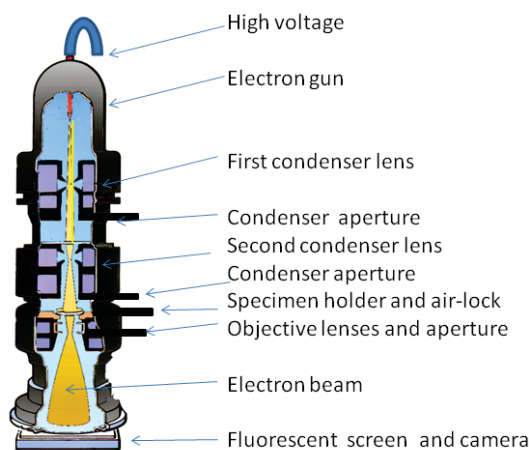


**Figure 2.18** | Schematic representation of a transmission electron microscope (TEM).<sup>a</sup>

<sup>a</sup> Image source: Graham Colm, 2014, Wikimedia Commons, Public domain.

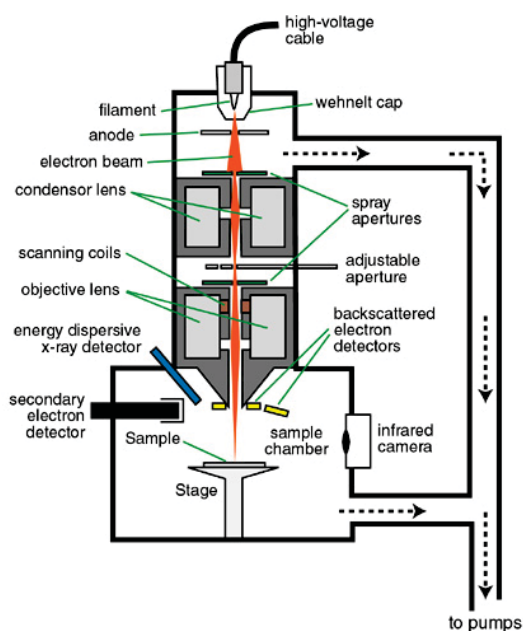


**Figure 2.19** | Schematic representation of a scanning electron microscope (SEM).<sup>a</sup>

<sup>a</sup> Image source: <http://www4.nau.edu/microanalysis/microprobe-sem/instrumentation.html>

cases. The magnification of SEM is poorer than that of TEM, but since the interactions are restricted to the surface region in SEM, it is possible to measure on large and bulky samples. An advantage of SEM, especially in comparison to AFM, is the ability to vary the depth of field of the electron beam, e.g. by changing the energy or the focal point. Information on the three-dimensional shape of an object topography can be obtained by shifting the focal plane. Another variant is the transmission SEM (TSEM).<sup>[119]</sup> There, a detector is placed behind a sufficiently thin sample in transmission geometry. Bright field and dark field images can be recorded at lower voltages than with TEM, which increases the contrast in biological sample systems.

In most cases, EM requires an extensive preparation to produce a suitable sample. Biological and organic materials need to be fixed and stabilised to be compatible with the vacuum environment of the microscope. Furthermore, the sample needs to be conductive enough to prevent a significant charge accumulation of the illuminated area. This might require the coating of the sample surface with a thin metal layer, which may induce artefacts and structure distortions. All these processing steps may induce significant changes in the structure and properties of the sample to be investigated. Another source of possible severe structural distortions is the slicing of the sample for TEM, which is

frequently necessary to obtain samples that are thin enough for the electron beam to pass through, since the sample thickness usually is in the  $\mu\text{m}$  range down to tens of nm). Slicing can be done by mechanical cutting or focused ion beam milling, both methods induce a great amount of thermal energy load and mechanical stress on the sample.

Nonetheless, electron microscopy is also frequently used in conjunction with X-ray scattering as a complementary technique, mostly for studies of hard condensed matter nanostructures.<sup>[1,49,108,206]</sup>

### 2.7.3 Other indirect methods

#### CD-SAXS

Critical dimension SAXS (CD-SAXS)<sup>[111,112,248,249]</sup> is the application of SAXS for dimensional measurements of grating structures. Photolithographically patterned structures, such as gratings (Fig. 2.13a) with typical feature sizes of 500 nm and below, are produced sufficiently thin to allow the transmission of X-rays. In the case of a silicon sample, the attenuation length, i.e. the intensity reduction to  $\exp(-1)$ , is around  $130\ \mu\text{m}$  at 10 keV and around  $1\ \text{mm}$  at 20 keV, which sets the demands on photon energy and sample thickness. For a typical CD-SAXS measurement, the sample is mounted perpendicular to the incident beam ( $\alpha_i = 90^\circ$ ) and the transmitted intensity distribution is collected by an area detector as shown in Fig. 2.20. The scattering image consists of equidistant GTRs (Section 2.5) that are aligned with the transmitted direct beam. A  $q$ -cut through this line is used to fit a form factor to the data, which yields the pitch  $P$  and the  $CD$  for a rectangular form factor and additionally the sidewall angle in the case of a trapezoid form factor model. The sample can also be rotated around the  $\vec{\omega}$  axis, which is perpendicular to the direct beam and parallel to the sample surface, to obtain information on the line shape, line edge roughness, and line width roughness.<sup>[248,249]</sup>

Like GISAXS, CD-SAXS yields statistically significant average feature sizes, which is in many cases more relevant than the very localised size information of real-space techniques such as AFM or EM. For example, this is a central requirement in industrial photolithography pattern inspection and homogeneity assessment. A strength of CD-SAXS in comparison to GISAXS is the smaller beam footprint due to the normal incidence, which is particularly relevant in semiconductor photolithography industry, and the easier theoretical treatment in the framework of kinematic scattering. However, the low thickness of the sample might be problematic, especially for large structures and in industrial applications. Another challenge is the unfavourable ratio of structured and unstructured material along the transmission path of the beam. A wafer with a total thickness of  $0.5\ \text{mm}$  and a feature height of  $50\ \text{nm}$  has only a fraction of  $10^{-4}$  of structured volume, the rest is substrate. The sample can be mounted with the nanostructured substrate facing the incident beam or the detector, but in both cases there is additional scattering by the substrate, either of the incident beam or of the scattered waves. This is especially critical for inhomogeneous substrates with depth structures, e.g. an underlying multilayer. In that case, GISAXS might be the better choice as it provides surface sensitivity and a variation of the probed scattering depth (Eq. (2.18)).

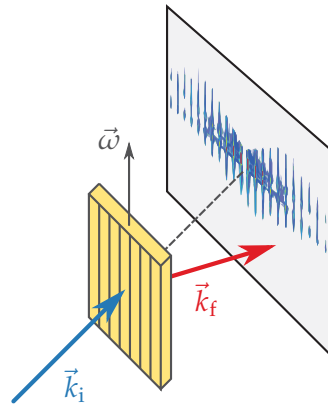


**Figure 2.20** | Scattering geometry in CD-SAXS.

### EUV scatterometry

Scatterometry is a generic term for light scattering techniques in reflection geometry used on lateral and/or vertical periodic structures to determine structural informations, such as grating line sidewall angles, critical dimension, and pitch in the sub- $\mu\text{m}$  and nm range.<sup>[77,99,115,214]</sup> Consequently, GISAXS measurements on grating structures, as described in Section 2.5 and Chapter 4 also belong to the scatterometry techniques. The particular case of EUV scatterometry refers to the usage of wavelengths around 13 nm, which is the wavelength of the upcoming EUV lithography technology of the semiconductor industry.<sup>[30]</sup> EUV scatterometry is a metrology tool for the inspection of EUV masks and structured wafers, for example at the EUV reflectometer in the PTB laboratory at BESSY II.<sup>[131]</sup> As an indirect measurement method, it is necessary to solve the phase problem of the measured scattering intensity patterns by numerical simulation using appropriate models, as discussed in Section 2.6.

### Ellipsometry

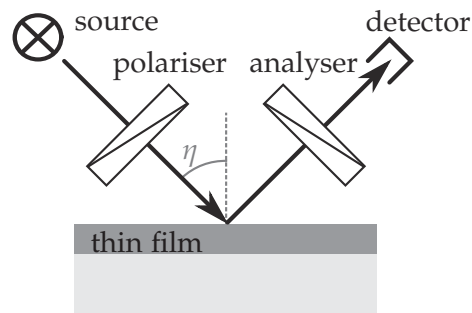
Ellipsometry is an optical measurement technique that determines the change in polarisation between incident and reflected light in order to probe the dielectric parameters, i.e. the complex refractive index  $\hat{n}$  of a layered sample.<sup>[5,169,239]</sup> The change in polarisation due to surface reflection by a sample yields information on the material composition, interface roughness, layer thickness, and other material properties that influence the optical parameters of the sample. Ellipsometry yields information along the vertical direction only, it is not sensitive to lateral variations like the other methods mentioned in this section. Just as XRR, ellipsometry can only be used for layer thickness and composition measurements, but not for dimensional measurements of laterally nanostructured surfaces. The basic measurement setup is displayed in Fig. 2.21. A source generates monochromatic light (typically in the visible range up to UV), which is linearly polarised by the polariser. The incident light interacts with the sample surface by reflection, Eq. (2.34), absorption, diffuse scattering, and transmission, which cause a change of the initial polarisation. The specularly reflected beam passes through a second polariser, the analyser, and its intensity is measured by a detector. The final state of polarisation is determined by rotating the analyser and measuring the rotation angle dependent intensity distribution. The polarisation is subdivided in an  $s$  component and  $p$  component that are perpendicular and parallel to the plane of incidence, respectively. The incidence angle  $\eta$  is usually set to the Brewster angle of the sample material to obtain a large contrast

between the reflection coefficients  $r_s$  and  $r_p$  of  $s$  and  $p$ , respectively. The complex ratio  $\Gamma$  of the elliptically polarised reflected beam components

$$\Gamma = \frac{r_s}{r_p} = \tan(\Psi)e^{i\Delta} \quad (2.56)$$

is the measured quantity in ellipsometry. It is decomposed in an amplitude term  $\Psi$  and a phase shift term  $\Delta$ . Generally, it is not possible to directly obtain the optical constants of the sample by inversion.<sup>[239]</sup> Instead, a model is established that includes the structural properties (thickness, roughness, crystallinity) and optical parameters (refractive index) of each homogeneous layer or horizontal slice of an inhomogeneous layer. The Fresnel reflectance equations for  $R_s$  and  $R_p$  are solved for different values of  $\Psi$  and  $\Delta$  in an iterative procedure, e.g. least-squares minimisation, to find the best match with the experimental data. Hence, ellipsometry is an indirect, model-based method such as XRR.

**Figure 2.21** | Schematic setup of an ellipsometry measurement.



Ellipsometry is a widely used technique for surface and thickness analysis in thin film characterisation, biology or industrial microelectronics quality management, to name but a few applications. The method is robust as it measures intensity ratios instead of absolute intensities, just as XRR. The precision of thickness measurements is very high, in the sub-nm range,<sup>[199]</sup> which makes ellipsometry also an appealing and widely used tool for dimensional nanometrology of layers and films.<sup>[3,32,33,51,146]</sup> It is known<sup>[32,33]</sup> that ellipsometry possesses a high precision, but a low accuracy in itself. Thus, the absolute value offset needs to be determined by an absolute method such as XRR. Ellipsometry is frequently combined with X-ray scattering techniques (XRR, GISAXS) to provide depth-sensitivity, absolute length scaling, and 3D-morphology at the same time.<sup>[3,122]</sup>

After the description of the theoretical and methodological framework, the next chapter is dedicated to the experimental details of this work. This includes the basics of synchrotron radiation and a description of the beamline setup for small-angle scattering that was used for the experiments presented. A particular focus is also on the development and characterisation of an in-vacuum detector that is able to cover the previously inaccessible tender X-ray regime below 5 keV for scattering measurements.

# 3

## Experimental setup and new instrumentation

X-rays enable a broad variety of different elastic and inelastic techniques to study dimensional, compositional, electric, magnetic, and many other properties of materials. In order to perform dimensional measurements on nanostructured surfaces and layers using elastically scattered X-rays, basically three components are needed: An X-ray source, an instrument to align the sample, and a suitable X-ray detector.

The use of synchrotron radiation as a source of X-rays has some appealing properties, such as<sup>[120,258]</sup>

- tunable photon energy from the infrared to the hard X-ray region;
- high intensities and fluxes;
- high brilliance;
- possibility to achieve any polarisation (using dedicated insertion devices); and
- calculability as a primary calibration standard for electromagnetic radiation,<sup>[234]</sup>

to name but the most important characteristics. All experiments reported in this work were carried out in the laboratory of PTB<sup>[12]</sup> at the electron storage ring for synchrotron radiation (BESSY II) of the Helmholtz-Zentrum Berlin (HZB). After a brief overview of the most relevant parameters of a third generation synchrotron radiation facility such as BESSY II, the small-angle scattering setup at the four-crystal monochromator (FCM) beamline of PTB is reviewed. Then, the development and characterisation of a new vacuum compatible PILATUS 1M hybrid pixel detector that took place during this work is described. The extended capabilities of the in-vacuum PILATUS 1M, especially in terms of access to photon energies below 4 keV, are demonstrated by several applications in Chapters 4 and 5.

## 3.1 Synchrotron radiation

Synchrotron radiation is electromagnetic radiation of a broad spectral range that is emitted by relativistic charged particles (electrons in most cases) that are radially accelerated by a magnetic field. The theory has been developed in the middle of the last century mainly by Schwinger [217], Ivanenko and Pomeranchuk [105], detailed descriptions can be found in Refs. [106, 120, 223].

In summary, Liénard-Wiechert fields of the electric and the magnetic field are used to calculate the radiant power of a single relativistic electron moving along a circle with a radius  $R$  in a homogeneous magnetic field. This yields the equation of the total emitted power  $P_{\text{tot}}$ ,

$$P_{\text{tot}} = \iint I(\lambda, \zeta) d\lambda d\zeta = \frac{2}{3} \frac{e^2 c}{6\pi\epsilon_0 R^2} \left( \frac{E_e}{m_e c^2} \right)^4. \quad (3.1)$$

The function  $I(\lambda, \zeta)$  is the Schwinger equation that denotes the emitted power of an electron per unit of wavelength  $\lambda$  and per unit of azimuthal emission angle  $\zeta$ .  $P_{\text{tot}}$  depends on the fourth power of the particle rest mass  $m_e$ , which is why there is virtually no synchrotron radiation detectable from heavier charged particles such as protons, except at the Large Hadron Collider.<sup>[243]</sup>

In an electron storage ring, the deflection radius  $R$  of the electron trajectory is given by the magnetic field  $B_0$  of the bending magnets (dipole magnets) that is oriented vertical to the electron orbit plane and by the electron energy  $E_e$ . The deflection radius is related to both parameters according to<sup>[61]</sup>

$$\frac{1}{R/\text{m}} = \frac{0.2908 B_0/\text{T}}{E_e/\text{GeV}}. \quad (3.2)$$

The radiant power spectrum of a bending magnet at BESSY II in comparison to a black body radiator is displayed in Fig. 3.1. Two common parameters for the comparison of different synchrotron radiation sources are the brilliance of the source and the critical wavelength or, equivalently, the critical photon energy. The spectral brilliance as a function of wavelength is the photon flux (photons per second) divided by the angular divergence in both directions perpendicular to the beam ( $\text{mrad}^2$ ) and by the beam cross-section (source size of the synchrotron radiation, in  $\text{mm}^2$ ) within a bandwidth of 0.1% of the given wavelength. The unit is of the spectral brilliance is thus  $[\text{s mrad}^2 \text{mm}^2 (0.1\% \text{ bandwidth})]^{-1}$ . The critical wavelength  $\lambda_c \propto RE_e^{-3}$ , or photon energy  $E_c \propto B_0 E_e^2$ , separates the radiated total power: Half the power is radiated below  $E_c$  and half is emitted above.<sup>[258]</sup> Displayed in Fig. 3.2 are the average brilliance and the critical photon energy of different synchrotron radiation facilities. Table 3.1 shows some basic parameters of BESSY II where the experiments presented in this work have been carried out. The brilliance at a given photon energy or, alternatively, the photon flux at photon energies above  $E_c$  can be significantly increased by the use of dedicated insertion devices.

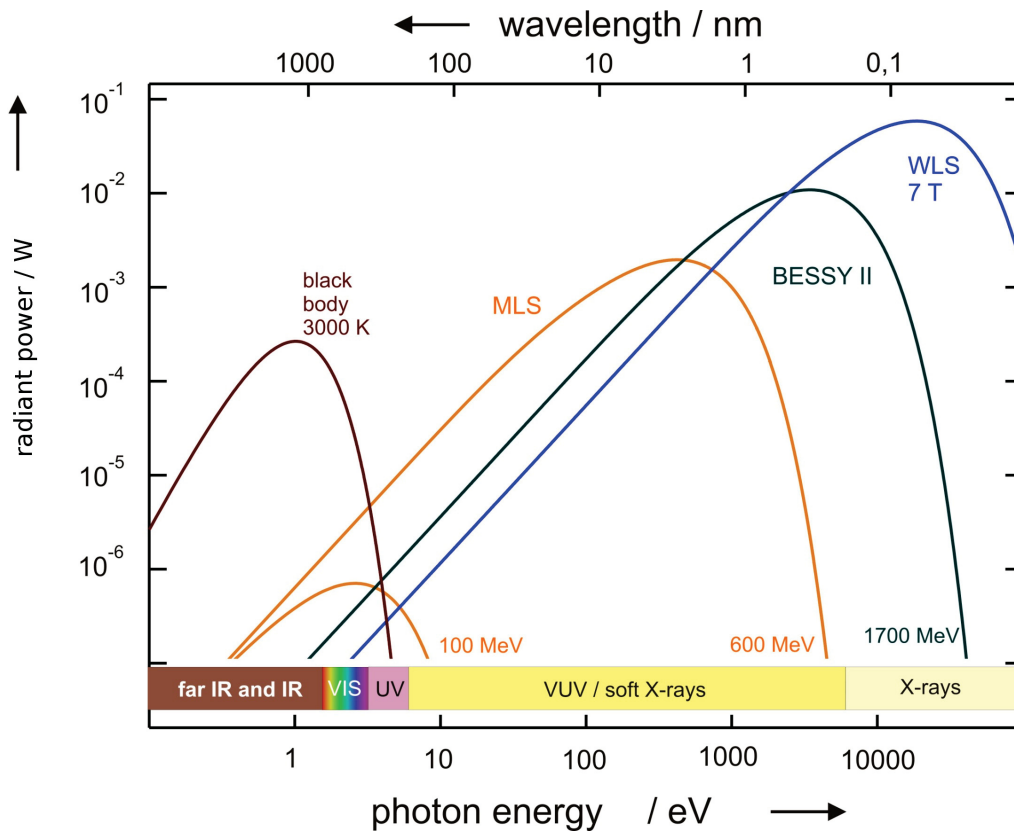


**Figure 3.1** | Calculated radiant power of radiation sources into a spectral bandwidth of 1 % of the photon energy through an aperture with a 10 mm radius. Brown line: Black body radiator with a of temperature 3000 K and an emitting area of  $78.5 \text{ mm}^2$  in a source distance of 1 m. Orange lines: Metrology Light Source (MLS) with an electron energy of 100 MeV and 600 MeV with a bending magnet field of 0.2 T and 1.3 T, respectively (ring current 200 mA, source distance 5 m). Green line: BESSY II with an electron energy of 1.7 GeV, a bending magnet field of 1.3 T, a ring current of 200 mA, and a source distance of 20 m. Blue line: Same as for the green line, but for a wavelength shifter (WLS) with a magnetic field of 7 T. <sup>b</sup>

<sup>b</sup> Image source: Beckhoff et al. [12].

## Insertion devices

Third generation synchrotron radiation facilities make use of insertion devices along the straight sections of the storage ring to generate brighter, more brilliant, or differently polarised light than bending magnets. One main characteristic of any insertion device is that it is transparent for the electron beam, i.e. the orbit of electrons behind the device is not disturbed by it. Otherwise, a stable operation of the storage ring would not be possible. It is usually distinguished between three types insertion devices: wavelength shifters, wigglers and undulators, which have different objectives, but are similar in their construction.<sup>[61,120,258]</sup>

A wavelength shifter consists of periodically alternating magnets, frequently only one period, that deflect the electron beam. The field strength of the magnets is much higher than that of bending magnets,\* which results in a reduced deflection radius  $R$ , Eq. (3.2), and consequently in an increase of the critical energy of the emitted spectrum. There is no coherent overlap of the emitted radiation due to the large deflection angle. Consequently,

\* BESSY II: 7 T in the wavelength shifter, compared to 1.3 T in the bending magnets.

**Figure 3.2** | Average spectral brilliance versus photon energy of different light sources.<sup>a</sup>

<sup>a</sup> image source: <http://www.embl-hamburg.de/xfel/annex.html>

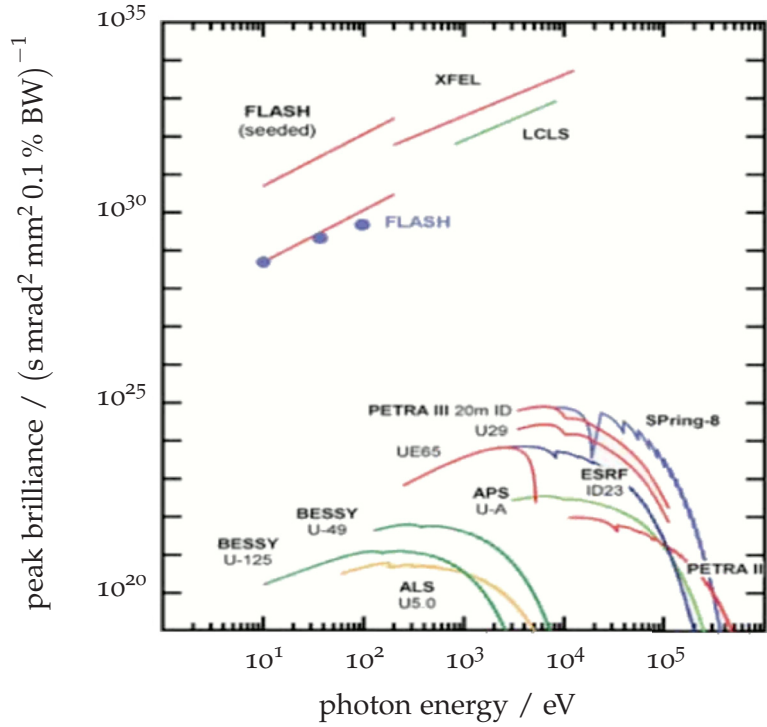


**Table 3.1** | Basic properties of BESSY II.

parameter	value
ring circumference /m	240
electron energy /GeV	1.70
electron beam current /mA	300
electron bunch length /ps	20
bending magnet radius /m	4.2
bending magnet mag. field /T	1.3
critical photon energy /keV	2.5

the emitted spectrum is that of a bending magnet, but shifted to higher photon energies as shown in Fig. 3.1.

Wigglers and undulators have the same structure, in fact, most devices can be used in both operation modes. The device consists of two arrays of periodically alternating magnets above and below the electron pathway with typical period lengths in the range of cm and array lengths in the range of metres. The Lorentz force of the magnet structure causes a sinusoidal oscillatory motion of the electrons in the horizontal plane. Consequently, the emission of synchrotron radiation is stimulated. In the case of undulators, the radiation is quasi-monochromatic with high intensities and narrow bandwidth at a characteristic wavelength  $\lambda_{und}$  and its odd-numbered higher harmonics, which is called undulator radiation. Wigglers emit an intensified quasi-continuous radiation with a broad spectral distribution. Both types of insertion devices can be distinguished by the *deflection parameter*  $K$ , defined as

$$K = \frac{e B_0 \lambda_u}{2\pi m_e c} \tag{3.3}$$

with the magnetic field  $B_0$  in the electron pathway and the period length of the magnet cascade  $\lambda_u$ . The deflection parameter is a measure for the maximal deflection angle of an electron during the oscillatory motion with  $K \gg 1$  for wigglers and  $K \leq 1$  for undulators.

The magnetic field  $B_0$  is usually varied by changing the distance from the magnet arrays to the electron beam, called the *gap* of the insertion device. Thus, by choosing a small gap, the magnetic field and, thus, the deflection parameter is large (wiggler mode), while a large gap results in a small deflection (undulator mode).

In wigglers, the large deflection angle results in a broad emission cone. Thus, the radiation emitted at each bend of the electron trajectory in the wiggler adds up incoherently, while the emitted spectrum is similar to a bending magnet due to the comparable magnetic field strength. Consequently, wigglers increase the photon flux due to the numerous undulations of the electron beam, while the spectrum resembles that of a bending magnet.

The magnetic field strength of an undulator is weaker, which results in a smaller deflection of the emitted radiation from the forward direction. In this way, the emitted radiation from the bends of the electron trajectory overlap and interfere with one another. The result is the emission of quasi-monochromatic, highly brilliant undulator radiation that can be tuned by a variation of the gap distance between the magnet array, i.e. by the magnetic field strength. Advanced undulators such as the APPLE II type<sup>[8,210]</sup> provide variable polarisation (linear, circular, elliptical) by using a total of four lines of magnet cascades, two next to each other above and below the straight storage ring segment.

Storage rings are used for decades as tunable high brightness sources for synchrotron radiation and have undergone a tremendous development during that time. One major advantage of storage rings is the parallel supply of broadband synchrotron radiation to many experimental end stations at the same time.<sup>†</sup> Recent further developments of third-generation light sources such as, for example, top-up operation,<sup>[173]</sup> variable pulse time structure,<sup>[93]</sup> or coherent micro- and nano-beams<sup>[215]</sup> offer a very wide range of parameters for many different applications and make sure that storage rings continue to remain among the world-leading light sources.

Another recent light source is the FEL, frequently called *accelerator-based light source*. A pre-accelerated bunched electron beam is accelerated to GeV energy in longitudinal direction and passes at the same time through an undulator, which causes a periodic transverse deflection.<sup>[100,143]</sup> This causes the emission of undulator radiation, which interacts with the emitting electrons. In this way, microbunches are shaped that emit radiation in phase with full coherency. The resulting radiation with wavelengths down to X-rays<sup>[58,104,235]</sup> has a very high flux and brilliance (orders of magnitude above third-generation light sources, see Fig. 3.2), full coherence, and pulse lengths in the femto-second range. Yet, the large scale FEL facilities can only provide radiation for a small number of end stations because each accelerated electron is only used once to generate radiation before it is dumped at the end of the linear accelerator pathway. Thus, storage rings and FELs complement one another, the suitability of one or the other light source strongly depends on the scientific question, the sample system as well as the physical parameter and domain to be investigated.

For the X-ray scattering experiments described in this work, the typical experimental setup is as follows: (i) The ‘white’ bending magnet radiation enters the FCM beamline where the beam is shaped and monochromatised. (ii) The monochromatic beam impinges on the sample in the measurement chamber. (iii) The scattering pattern is measured by a 2D-detector in a distance of tens of centimetres up to several metres. Each component of the setup is described in the following sections.

<sup>†</sup> For example, BESSY and ESRF each have more than 40 beamlines for experiments.

## 3.2 Four-crystal monochromator beamline

The FCM beamline<sup>[125,128]</sup> at BESSY II is a bending magnet beamline in the PTB laboratory, denoted '2a' in Fig. 3.3. A schematic representation of the beamline is shown in Fig. 3.4 and some of the beamline parameters are listed in Table 3.2. The monochromator consists of sets of four single crystals of the same material and orientation. The crystals are mounted on two main wheels, each carrying a fixed crystal in the centre of rotation and another crystal on a smaller cradle. The incoming bending magnet radiation is monochromatised by four consecutive Bragg reflections according to Eq. (2.25) and the photon energy is selected by the rotation angle of the main wheels. The angle of the first wheel defines the angular position of the second wheel. Two types of crystals, Si(111) and InSb(111), are available and can be interchanged under vacuum to cover a total energy range of 1.75 keV to 10 keV. The four-crystal configuration offers advantages such as fixed exit without crystal translations, a high reproducibility of the photon flux at any given photon energy, and a high energy resolution due to the narrow convolution of the Bragg peaks of the monochromator crystals. Movable diodes between the crystals allow the alignment of both pairs of monochromator crystals to maximise the photon flux of the monochromatic beam. The complete beamline is windowless, i.e. the monochromator is operated under ultra high vacuum conditions (UHV, low  $10^{-6}$  Pa range).

**Figure 3.3** | The beamlines of the PTB laboratory at BESSY II.<sup>[12]</sup> Highlighted in red (2a) is the FCM beamline.

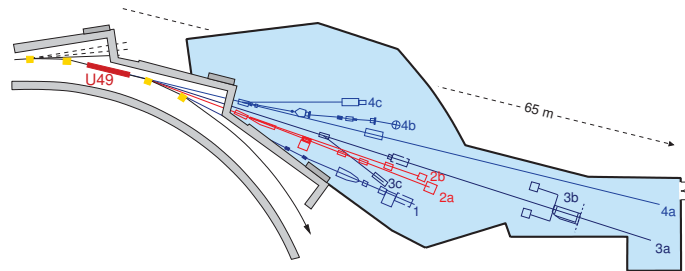
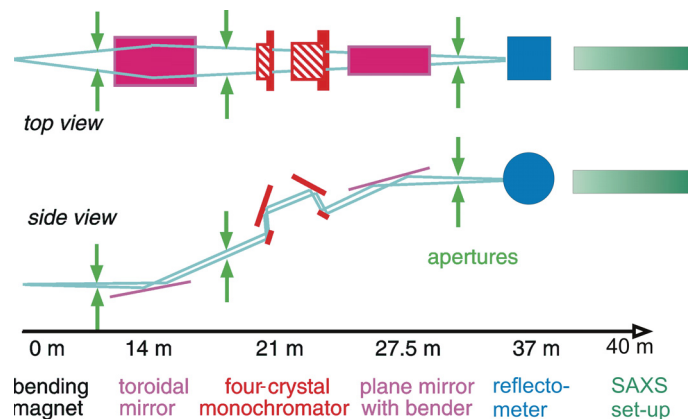


**Figure 3.4** | Scheme of the optical elements of the FCM beamline.



The beamline is equipped with a toroidal mirror (Pt coated Si, radii of curvature 131 mm and 4.3 km, respectively) behind the first slit to focus the beam in the horizontal direction and to collimate in the vertical direction. Further downstream behind the monochromator, a bendable coated Zerodur ceramic mirror focusses the beam. The plane mirror has two different coating stripes that can be moved into the beam, a Pt coating and a  $\text{MgF}_2$  coating. The  $\text{MgF}_2$  coated area has to be used for photon energies below 4 keV to suppress higher orders, the Pt coated area for energies above 4 keV for

parameter	value/range
photon energy	1.75 keV to 3.6 keV (InSb) 2.1 keV to 10 keV (Si)
resolving power	$4.0 \times 10^3$ (1978 eV) to $12.7 \times 10^3$ (6457 eV)
sum of higher order contributions	$< 1 \times 10^{-3}$ ( $< 2.5$ keV) $< 1 \times 10^{-4}$ ( $> 2.5$ keV)
focal beam spot size	$(0.3 \times 0.3)$ mm <sup>2</sup>
flux monitor range	$\geq 3$ keV

**Table 3.2** | Parameters and specifications of the FCM beamline for the InSb(111) and the Si(111) monochromator crystal types.

maximised reflectivity and, thus, photon flux. Five different filters (25  $\mu\text{m}$ /125  $\mu\text{m}$  Be, 12.5  $\mu\text{m}$ /200  $\mu\text{m}$  Al, 10  $\mu\text{m}$  Cu) can be brought into the beam path at two positions to eliminate stray light and to reduce the heat load on the first crystal.

Three horizontal and four vertical slits can be moved independently to shape the beam. The first slit pair is positioned directly behind the junction of storage ring and beamline and is used to restrict the acceptance angle of the white bending magnet radiation. The other slits are placed further downstream and are usually used as guard slits to remove parasitic scattering and halos. A motorised linear feedthrough directly behind the last slit pair can be used to place a transmission diode, different absorption diodes, or a Ge pinhole ( $\text{\O} 520 \mu\text{m}$ , Incoatec<sup>‡</sup>) in the beam pathway. The approximately 8  $\mu\text{m}$  thick calibrated Si transmission diode serves as a flux monitor during measurements at  $E_{\text{ph}} \geq 3$  keV.

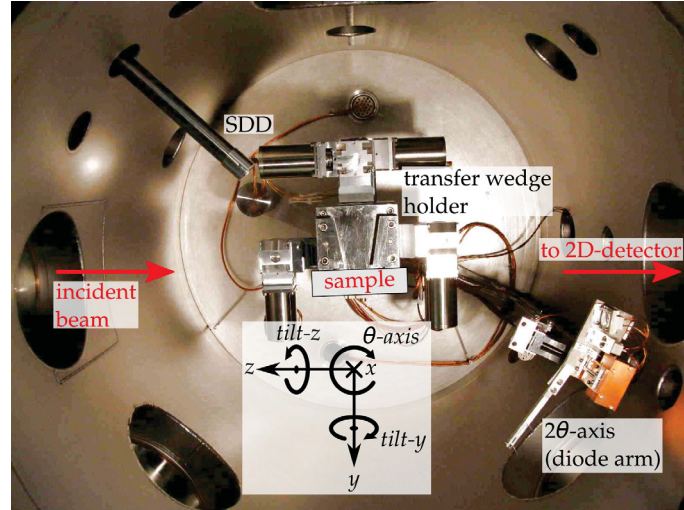
Traceability of the energy scale has been established by relating the photon energy  $E_{\text{ph}}$  to the fundamental lattice constant of silicon via back-reflection from a silicon single crystal.<sup>[128]</sup> For this purpose, the lattice axes of a single-crystalline silicon photodiode were aligned parallel to the incident beam. During scans of the photon energy, the Bragg condition of reflection is fulfilled at certain energies according to Eq. (2.25) for the well known silicon lattice constant,<sup>§</sup> which results in dips of the measured photocurrent. The energy scale is calibrated by the positions of these dips. The monochromator wheel accuracy of  $0.001^\circ$  results in a relative uncertainty of the photon energy below  $2.5 \times 10^{-4}$  using the InSb monochromator crystals and below  $1 \times 10^{-4}$  using the Si crystals.<sup>¶</sup> For the daily energy calibration, the K-absorption edge of the 10  $\mu\text{m}$  Cu filter at 8980.5 eV is observed by measuring the transmitted intensity during a photon energy scan using a photodiode with an accuracy of better than 0.5 eV.

<sup>‡</sup> Incoatec GmbH, <http://www.incoatec.de> <sup>§</sup> Current CODATA value in [155]. <sup>¶</sup> See Table 1 in Krumrey and Ulm [128].

### 3.3 UHV measurement chamber

Attached to the beamline, right behind the flux monitor diode, is the sample chamber.<sup>[67]</sup> The chamber ( $\varnothing$  600 mm, length 700 mm), Fig. 3.5, has no windows along the beam path and is fully evacuated. A smaller load-lock chamber facilitates the quick exchange of samples without ventilating the full measurement chamber, which reduces the evacuation time after a change of samples to about 10 minutes.

**Figure 3.5** | Detectors and axes in the UHV measurement chamber attached to the FCM beamline.



The chamber is equipped with a rotation axis perpendicular to the direct beam in the horizontal plane (which typically sets the incidence angle  $\alpha_i$  in the notation used in this work), named the  $\theta$ -axis, which provides a resolution of  $0.001^\circ$ . Mounted on top of the  $\theta$ -axis are two axis for rotations around the other two directions (named *tilt-y* and *tilt-z* in Fig. 3.5) as well as three linear axes  $x$ ,  $y$ ,  $z$  for sample positioning. The movements of each axis are calibrated and checked with an autocollimator on a regular basis, a summary of the axes ranges and motor resolutions is shown in Table 3.3.

**Table 3.3** | Technical specifications of axes and diodes in the sample chamber. See Fig. 3.5 for the orientation of the coordinate system.

parameter	range	resolution
<u>axes on <math>\theta</math>-axis</u>		
$\theta$	$-175^\circ$ to $175^\circ$	$0.001^\circ$
<i>tilt-y</i>	$-12^\circ$ to $12^\circ$	$0.000\ 25^\circ$
<i>tilt-z</i>	$-12^\circ$ to $12^\circ$	$0.000\ 25^\circ$
$x$	0 mm to 162 mm	0.0005 mm
$y$	$-12.5$ mm to $12.5$ mm	$0.000\ 25$ mm
$z$	$-12.5$ mm to $12.5$ mm	$0.000\ 25$ mm
<u>detectors on <math>2\theta</math>-axis</u>		
Si slit diode ( $0.3 \times 2.5$ ) mm <sup>2</sup>	1.75 keV to 10 keV	
GaP diode ( $4.7 \times 4.7$ ) mm <sup>2</sup>	1.75 keV to 10 keV	
Can500C Si diode ( $10 \times 10$ ) mm <sup>2</sup>	1.75 keV to 10 keV	
SDD ( $0.3 \times 3$ ) mm <sup>2</sup>	5 keV to 10 keV	

A detector arm, the  $2\theta$ -axis, is installed concentrically around the  $\theta$ -axis and can be

rotated in a full circle and independently from the  $\theta$ -axis around the same rotation axis. The detector arm is equipped with three highly linear photodiodes, which can be brought into the path of the direct, transmitted, reflected, or scattered beam. One diode is vertically confined by a slit to a height of 300  $\mu\text{m}$ , resulting in an angular resolution of only  $0.07^\circ$ , which can be used for precise alignment of a sample or of the measurement chamber with respect to the direct beam. Reflectometry measurements ( $\theta/2\theta$ -scans) are usually carried out using one of the other two diodes, which offer a larger area (edge lengths of 4.7 mm and 10 mm, respectively) and, thus, ensure that the reflected beam spot is fully covered by the sensitive area. All diodes were calibrated against a cryogenic electric substitution radiometer<sup>||</sup> within a relative uncertainty of 1%.<sup>[70]</sup> This enables traceable radiometric measurements of photon fluxes, for example for detector calibrations. The detector arm is also equipped with an uncooled silicon drift detector (SDD) for measurements of weak reflection intensities above 5 keV.

A large variety of sample holders can be used, depending on the sample dimension and on the intended measurement method. The holder is attached to a transfer wedge that slides with high positional accuracy into the corresponding socket on the  $\theta$ -axis during the sample transfer procedure.

The chamber is also equipped with a motorised linear feedthrough with different pinholes in front of the sample holder, which can be used to confine the beam or to remove parasitic scattering directly before the beam impinges on the sample. Currently, a piezoelectric slit system using Ge blades from Xenocs\*\* is installed, which allows to adjust the width and height of the pinhole during the measurements without breaking the vacuum in the chamber.

It is also possible to install one of the available Ketek and Bruker SDDs at an angle of  $-45^\circ$  above the direct beam path (see Fig. 3.5), which allows to measure the spectral X-ray fluorescence radiation from samples.

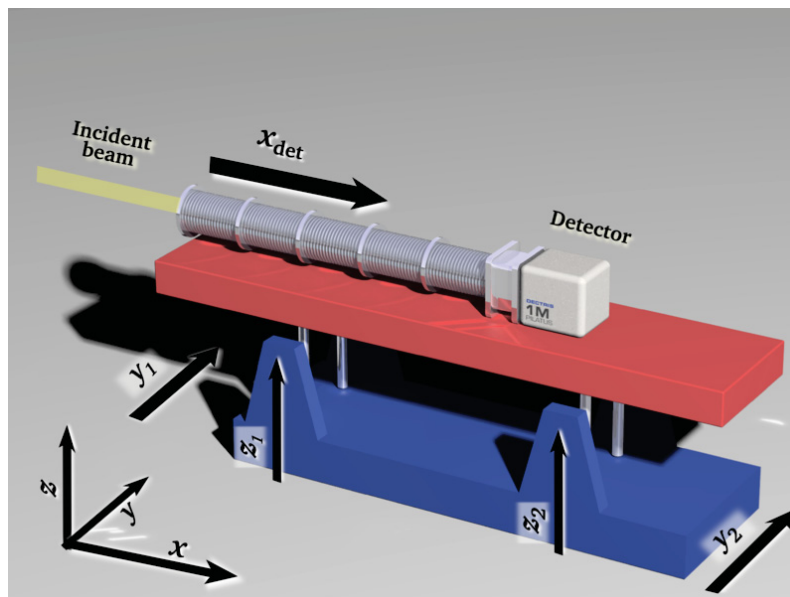
### 3.4 HZB SAXS instrument

For small-angle X-ray scattering experiments in transmission (SAXS) and under grazing incidence reflection (GISAXS), a two-dimensional X-ray detector is needed to record the intensity distribution of the diffuse scattering behind the sample.

At the FCM beamline, such a detector can be mounted on the SAXS instrument of HZB<sup>††</sup> as illustrated in Fig. 3.6. The detector is directly connected to the sample chamber via a  $\varnothing$  100 mm flange. It is installed on a stage that moves along  $x_{\text{det}}$  as shown in Fig. 3.6. The edge-welded bellow allows any sample-to-detector distance between 1.75 m and 4.5 m, and a vertical tilt angle up to  $3^\circ$  without breaking the vacuum. Both vertical axes  $z_1$ ,  $z_2$  as well as the horizontal distance variation axis  $x_{\text{det}}$  are equipped with optical encoders (calibrated Heidenhain LC 182 and two LC 483) which measure the displacement with an accuracy of 0.003 mm and 0.005 mm for LC 483 and LC 182, respectively. These encoders establish the traceability of the detector displacement along these axes. The entire setup can also be moved in horizontal direction perpendicular to the direct beam by the motorised axes  $y_1$  and  $y_2$  that can be used for the correction of any horizontal tilt of the SAXS instrument as well as for a horizontal displacement of the detector with respect to the incoming beam. The detector side of the bellow holds a interchangeable,  $xy$ -moveable beamstop to block the intense transmitted or specularly reflected fraction

<sup>||</sup> Which is a primary radiometric standard.    <sup>\*\*</sup> Xenocs, <http://www.xenocs.com>    <sup>††</sup> patent DE102006029449 B3.

**Figure 3.6** | Motor axes of the SAXS instrument. The axes for longitudinal detector movement  $x_{\text{det}}$  and for vertical movement of the stage  $z_1$  and  $z_2$  are equipped with optical encoders for absolute length measurements with micrometer resolution.



of the beam. As a 2D-detector, a CCD-based pixel detector (MarCCD, 4 Mpx, binned in blocks of  $2 \times 2$ , 165 mm diameter of active surface) or, since August 2012, the in-vacuum PILATUS 1M hybrid pixel detector (presented in Section 3.5) can be installed on the detector stage.

Since December 2013, there is also a ‘short-distance’ setup available, which is independent from the SAXS instrument. In this configuration, the in-vacuum PILATUS 1M is directly attached to the measurement chamber via an adaptor segment that contains the beamstop. The sample-detector distance can be set in a range of around 55 cm to 80 cm. This facilitates larger scattering angles up to around  $\pm 8^\circ$  in horizontal and vertical direction, which is needed for the large scattering angles of very small scattering objects down to around 3 nm.

Presented in the next section is the development and characterisation of the in-vacuum PILATUS 1M detector that took place during the course of this work. Section 3.5.3 on the radiometric and geometric characterisation of the in-vacuum PILATUS 1M is published in J. Wernecke, C. Gollwitzer, P. Müller and M. Krumrey: ‘Characterization of an in-vacuum PILATUS 1M detector’, *J. Synchrotron Rad.* **21.3** (2014), pp. 529–536.

### 3.5 The new in-vacuum PILATUS 1M detector

The advances of integrated circuits in the last few decades have significantly boosted the development of X-ray detectors.<sup>[262]</sup> So-called hybrid pixel X-ray detectors have been developed, which consist of a readout chip bump bonded on a silicon sensor that acts as a radiation absorber.<sup>[88]</sup> State-of-the-art detectors such as the XPAD,<sup>[48]</sup> detectors based on the Medipix readout chip,<sup>[186,191]</sup> and the PILATUS<sup>[29,123]</sup> combine a semiconductor pixel matrix with a readout chip providing an amplifier, comparator, and digital counter for every single pixel. This is appealing especially for scattering and diffraction experiments, where the photon flux on individual pixels may vary over many orders of magnitude. As opposed to dose-proportional detectors, photon counting can provide very low darkcount rates, and consequently huge dynamic ranges, signal-to-noise ratios close to the quantum limit, and negligible crosstalk between neighbouring pixels resulting in a nearly perfect

point spread function.<sup>[38]</sup>

The commercially available large-area hybrid pixel detectors of 1 Mpx and above are operated in air and the radiation enters through a thin window. This window limits the detectable photon energy range to energies above approximately 5 keV due to absorption of the window material. Yet, the absorption edges of technologically and biologically relevant elements such as silicon, phosphorus, sulphur, chlorine, or calcium are situated below 5 keV. To overcome this limitation, windowless operation in vacuum with a direct connection to the sample chamber is necessary. The suitability and performance of a PILATUS 100k detector under such conditions has been shown previously.<sup>[144,145]</sup> Moreover, extensive testing and characterisation of detector modules in vacuum<sup>[50]</sup> has been carried out in collaboration with Dectris Ltd.<sup>‡‡</sup> at the FCM beamline. The setups were preliminary experiments using a single module as a proof of concept at that time, a fully operational multi-module large-area in-vacuum PILATUS 1M has not been realised up to then. From August 2011 to June 2012, a standard PILATUS 1M detector was modified together with Dectris Ltd. to operate under vacuum. This widened the experimentally accessible energy range downwards to a photon energy  $E_{\text{ph}}$  of 1.75 keV. The in-vacuum PILATUS 1M detector, Fig. 3.7, was delivered in June 2012 and is in regular operation at the FCM beamline since then.

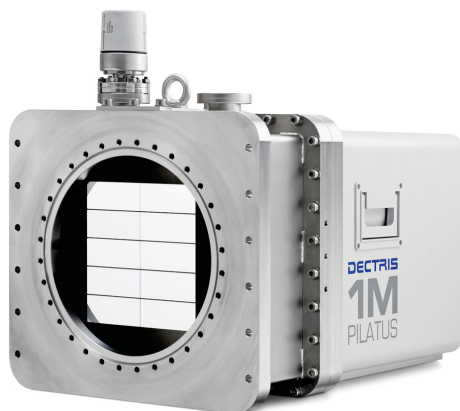


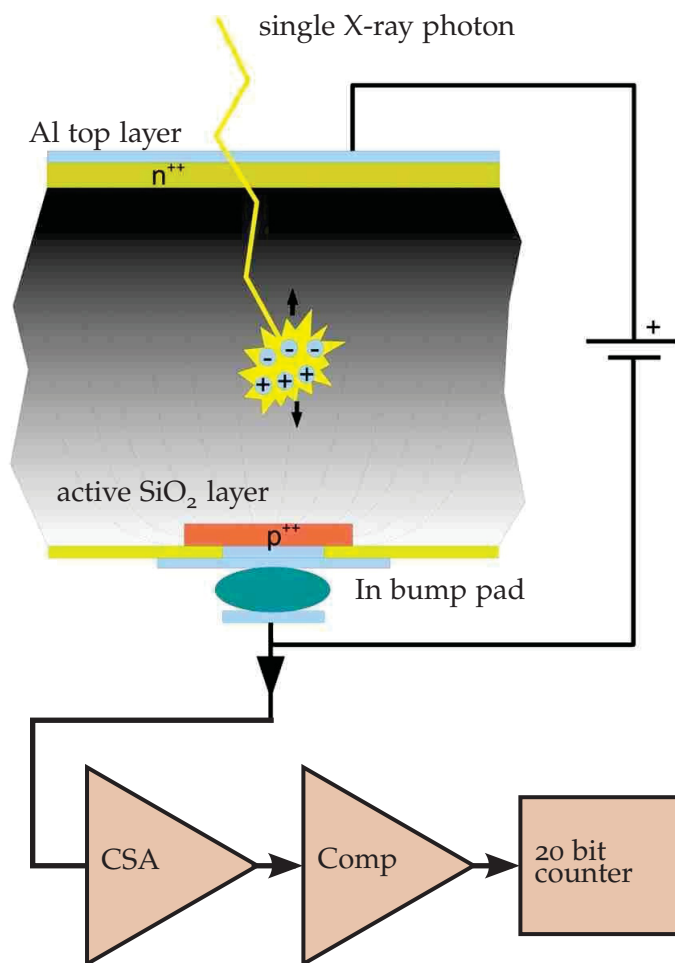
**Figure 3.7** | The in-vacuum PILATUS 1M detector.

### 3.5.1 Operation principle of PILATUS detectors

Before the necessary adoptions of the detector setup are described, the operation principle of the PILATUS pixel readout chain, shown schematically in Fig. 3.8, needs to be briefly reviewed. Many more details can be found in Refs. [29, 123, 124]. The detection principle in each pixel is based on the generation of electron-hole pairs in a silicon pn-junction induced by an absorbed X-ray photon as shown in the upper part of Fig. 3.8. The readout of the generated current pulse in the pixel is facilitated through the indium bump pad, which is connected to the readout chain of the pixel (amplifier-comparator-counter) as illustrated in the lower part of Fig. 3.8. The electric charge is amplified by a charge-sensitive preamplifier (CSA), the amplification of which can be set in discrete steps, which are called the gain modes.<sup>[124]</sup> For the standard air-operated PILATUS detector, there are three different gain modes: High gain for photon energies down to around 7 keV, medium gain from around 9 keV to 28 keV and low gain for photon energies of 13 keV and above. The amplified pulse is then compared to an adjustable threshold voltage  $V_{\text{thresh}}$  by a comparator (Comp). The pulse is registered and counted in the 20 bit

<sup>‡‡</sup> DECTRIS Ltd., Neuenhoferstrasse 111, 5400 Baden, Switzerland, [www.dectris.com](http://www.dectris.com)

**Figure 3.8** | Schematic representation of the PILATUS hybrid pixel principle. An X-ray photon generates charges in the active pixel volume (grey shaded area), which is a silicon pn-junction. The pn-junction of each pixel is connected to an indium bump pad with a diameter of  $\approx 20 \mu\text{m}$ . The bump pad is connected to the readout chip (bottom part) that consists of the charge-sensitive amplifier (CSA), the comparator (Comp) and the 20 bit counter. <sup>a</sup>



<sup>a</sup> Image adapted from Kraft et al. [124].

counter only if it exceeds the threshold, and discarded otherwise. The voltage threshold  $V_{\text{thresh}}$  corresponding to a photon energy threshold  $E_{\text{thresh}}$  is determined by the software depending on the amplifier gain. In normal operation mode, the energy threshold  $E_{\text{thresh}}$  is set to  $1/2 E_{\text{ph}}$  to avoid charge-sharing counts in neighbouring pixels.<sup>[38]</sup>

### 3.5.2 Development of a vacuum-compatible PILATUS 1M

#### Test measurements using single modules

Test and calibration measurements during several beamtimes were carried out with Dectris at the FCM beamline since September 2011. The results presented here and many more have been published in Donath et al. [50]. Dectris designed a flange plate ( $\varnothing 100 \text{ mm}$ ) with a tube loop for water cooling and connections from the vacuum to the air side to place a fully functional standard PILATUS 100k module directly in vacuum for the test measurements. Two different experimental configurations were set up as shown in Fig. 3.9: The fluorescence setup is displayed in Fig. 3.9a using indirect illumination and the direct beam setup is shown in Fig. 3.9b.

In the fluorescence setup, the direct beam excites fluorescence radiation in samples of different materials with a suitable photon energy, i.e. above an absorption edge. The samples are mounted under  $45^\circ$  with respect to the direct beam and to the 100k detector module. The distribution of the fluorescence radiation along the detector is monochromatic and fairly homogeneous in its intensity distribution. This so-called

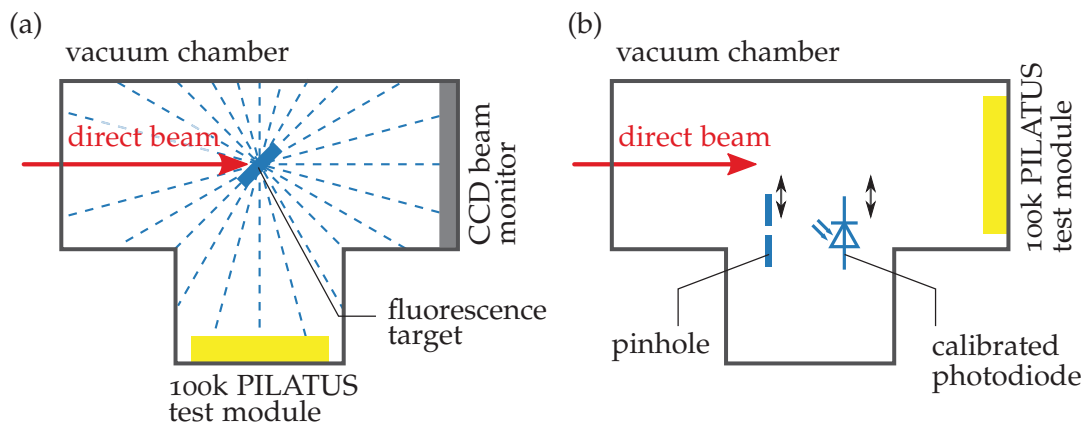


**Figure 3.9** | Experimental setups for measurements of the flatfield, the line spread function, the point spread function, and the quantum efficiency using a 100k PILATUS module (yellow). (a) In the fluorescence setup, the direct beam excites fluorescence from the target (blue) with a broad spatial distribution. (b) In the direct beam setup, the flux of the direct beam is measured using the PILATUS module and a calibrated photodiode with and without a 20  $\mu\text{m}$  pinhole.

flatfield image is used for adjusting the counting electronics of each pixel at different energies. Moreover, the measured flatfield images provide reference points for the extrapolation of the numeric flatfield correction that is carried out by the detector electronics at each image exposure. The fluorescence lines of silicon ( $K_{\alpha} = 1740 \text{ eV}$ ), phosphorous ( $K_{\alpha} = 2014 \text{ eV}$ ), chlorine ( $K_{\alpha} = 2622 \text{ eV}$ ), potassium ( $K_{\alpha} = 3314 \text{ eV}$ ), and titanium ( $K_{\alpha} = 4511 \text{ eV}$ ) were used for flatfield measurements to provide a range of energies below 5 keV.

In the direct beam setup, Fig. 3.9, the point spread function (PSF)<sup>§§</sup> and the quantum efficiency  $QE$  were measured using a 20  $\mu\text{m}$  pinhole and calibrated photodiodes, respectively. The detector is raster scanned with respect to the pinhole-restricted sub-pixel sized direct beam in steps of 10  $\mu\text{m}$  in both directions. The intensity of the pixel is measured at each position. Figure 3.10a shows the superimposed intensity map of a raster scan over a pixel. Horizontal line cuts through the central pixel, Fig. 3.10b and c, show a drop of detected counts at the pixel edges from about 8000 counts in the pixel centre to about 15 counts in the centre of the neighbouring pixel. This illustrates the sharp point spread of the detector. In another set of measurements, the direct beam is defocused and attenuated to provide an illuminated area of about 1  $\text{mm}^2$  on the detector with count rates below 20 000  $\text{s}^{-1}$  in any pixel. The absolute flux in photons per second is determined using calibrated photodiodes that were moved into the beam path before and after the total sum of counts is measured on the detector. The results of the complete and operational in-vacuum PILATUS 1M are presented in detail in the next section. The single module measurements were found to be in full agreement with the  $QE$  measurements of the in-vacuum PILATUS 1M.<sup>[50,250]</sup>

<sup>§§</sup> which is the response of a pixel to a sub-pixel sized beam

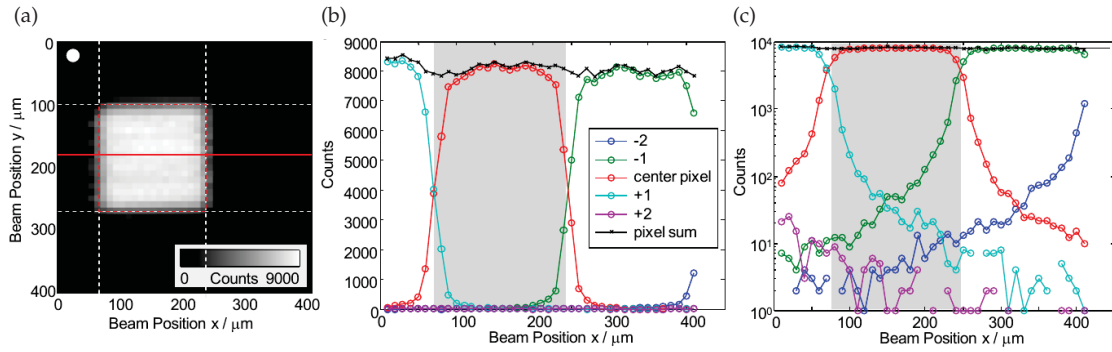


**Figure 3.10** | Point spread function measurement at 3.3 keV using a 20  $\mu\text{m}$  pinhole. (a) Intensity map of a single pixel. The horizontal solid line indicates the position of the line cuts. The white circle represents the size of the direct beam. (b) Intensity profiles along the horizontal line cuts for the centre pixel and neighbouring pixels ( $\pm 1$ ,  $\pm 2$ ). (c) As in (b), but on a logarithmic intensity scale. <sup>a</sup>

<sup>a</sup> Image from Donath et al. [50].

### Technical implementation of the in-vacuum version

One of the design goals for a vacuum-compatible version of the PILATUS 1M detector was to minimise the number of modifications from the standard detector. The final solution was a vacuum-proof separation of the detector modules from the electronic control units. To this end, a vacuum chamber for the modules and a feed-through flange plate were developed, see Fig. 3.11a and Fig. 3.11b, respectively. The ten detector modules are mounted on a size-reduced module carrier plate shown in Fig. 3.11c. The carrier plate is connected to the feed-through flange plate, which closes the vacuum chamber at the detector side. Figure 3.12 shows a schematic representation of the assembly of (a) the components and (b) a sketch of the connections of the feed-through flange plate. The vacuum chamber encloses the detector modules that provide a total sensitive area of  $(179 \times 169) \text{ mm}^2$  with a sensor thickness of 320  $\mu\text{m}$ . The entrance flange has a diameter of 250 mm to prevent any shadowing of the detector surface and is directly connected to the HZB SAXS instrument. A vacuum gauge is used for pressure monitoring and controls an interlock system, which shuts down the high voltage of the detector in the event of a vacuum loss. The feed-through flange plate, Fig. 3.12b, seals the vacuum chamber on the opposite side and facilitates the connection of the 575 electric lines and the channels for water cooling. On the air side, standard PILATUS 1M electronic units are used for data processing. The module carrier plate is cooled by circulating water and is kept at a constant temperature of typically 5  $^{\circ}\text{C}$ . Table 3.4 gives an overview of the technical specifications of the in-vacuum PILATUS 1M detector. Operation in air at higher photon energies is still possible with the modified PILATUS 1M setup. A Mylar window can be attached to the entrance flange of the vacuum chamber to blank out ambient light and to facilitate flushing of the modules using dry nitrogen or air.

For the in-vacuum PILATUS 1M detector, an additional ultra-high gain mode with higher amplification than the standard high-gain mode was added to the charge-sensitive amplifier to account for the reduced number of electron-hole pairs generated by each photon at low X-ray photon energy (Fig. 3.8). The lowest achievable  $E_{\text{thresh}}$  is ultimately limited by amplifier noise exceeding the comparator threshold  $V_{\text{thresh}}$  or by the onset of instable operation. The minimum threshold determined is  $E_{\text{thresh}} = 1.7 \text{ keV}$  for stable operation in ultra-high gain mode. For the preferred threshold setting of  $E_{\text{thresh}} = 1/2 E_{\text{ph}}$ , this would only allow a minimal photon energy of 3.4 keV. In order to reach lower

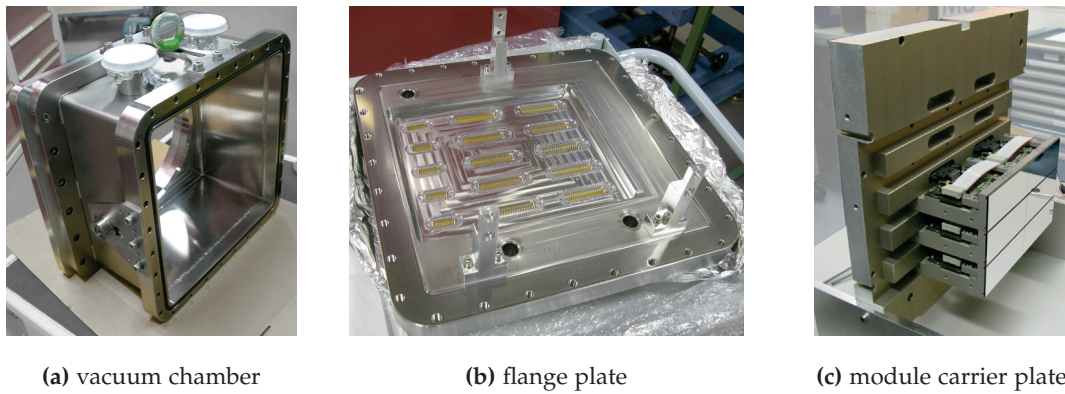


**Figure 3.11** | Components of the in-vacuum PILATUS 1M before assembly.

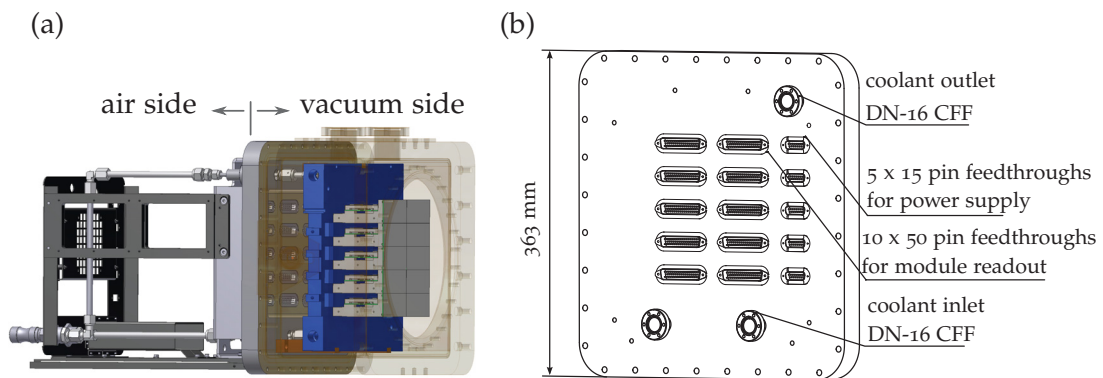


**Figure 3.12** | (a) Sketch of the vacuum-compatible version of the PILATUS 1M detector. The vacuum side (on the right) consists of the ten detector modules (grey) mounted on the downsized module carrier plate (blue). The latter is attached to the feed-through flange plate that contains the 575 electric connections and the water supply lines. The vacuum chamber (semi-transparent structure) is directly connected to the beamline. The air side (on the left) consists of the standard electronic units of the PILATUS 1M and the water cooling supply. (b) Sketch of the feed-through flange plate (Fig. 3.11b) that separates the vacuum and the air side and facilitates the electrical connection of the detector modules.

photon energies, for example, the silicon K-absorption edge at 1.84 keV,  $E_{\text{thresh}}$  can be set independently of the photon energy to a higher level. This results in a decreased count rate, but it also leads to a smaller effective pixel area because only photons that deposit at least a fraction of  $E_{\text{thresh}}/E_{\text{ph}}$  of their energy in the pixel contribute to the counts.<sup>[216]</sup> Such a smaller effective pixel size is even an advantageous effect in some experiments, as it produces sub-pixel resolution.<sup>[62]</sup> However, the usage of the ultra-high gain mode results in an increased detector dead-time of about 4  $\mu\text{s}$ , which leads to a loss of registered photons, as shown by Marchal and Wagner [144].

**Table 3.4** | Technical specifications of the in-vacuum PILATUS 1M detector.

parameter	value / setting
accessible photon energy	1.75 keV ... > 36 keV
sensitive detector area	(179 × 169) mm <sup>2</sup>
sensor thickness	320 μm
dimensions	approx. (60 × 37 × 37) cm <sup>3</sup>
mass	approx. 80 kg
entrance flange	DN 250 CF
typical cooler temperature	5 °C to 10 °C
typical operation pressure	below 10 <sup>-5</sup> mbar
pressure gauge	Pfeiffer PKR 251

### 3.5.3 Characterisation of the in-vacuum PILATUS 1M

#### Quantum efficiency

The quantum efficiency  $QE$  of the detector, which is the ratio of registered counts to incident photons, was determined as a basis for measurements of absolute scattering intensities.  $QE$  measurements were accomplished by taking sequences of images of the monochromatised synchrotron beam at different energies. Before and after each sequence, the incident photon flux at each energy was determined by a calibrated photodiode. The monochromatic photon flux of the beamline is in the order of  $10^9 \text{ s}^{-1}$  to  $10^{10} \text{ s}^{-1}$  in an area of about  $0.5 \text{ mm}^2$  at the usual top-up ring current of 300 mA of the storage ring. This photon flux is well beyond the linear unsaturated detector response range, in particular in ultra-high gain mode and at low threshold energies. Hence, BESSY II was operated in a special mode where the ring current was reduced stepwise to 832 μA, 409 μA, 95 μA, and finally 6 μA. This also allowed to evaluate the linearity of the registered count rate in relation to the rate of incoming photons. The  $QE$  was determined from the measurements at the lowest ring current of 6 μA, which resulted in photocurrents of the calibrated diodes from 14 pA to 1.2 nA (darkcurrent  $\ll 1$  pA). Additionally, the beam was defocused so that the most intense spot covered an area of approximately 100 px. In this way, the maximum flux of incoming photons per pixel was kept below  $20\,000 \text{ s}^{-1}$ , while the minimum photon flux in the evaluated region of  $10 \text{ s}^{-1}$  still exceeded the darkcount rate of  $10^{-5} \text{ s}^{-1}$  by several orders of magnitude.

Before the  $QE$  is accurately determined, the linear response of the detector must be tested and the uncertainty contributions have to be evaluated. Displayed in Fig. 3.13 are the registered counts per second and per pixel along the most intense line of the illuminated area (see the red dashed line in the inset) for the four different ring currents, recorded under otherwise identical conditions at  $E_{\text{ph}} = 2.5 \text{ keV}$ . The spiky shape of the profiles is not important, it merely shows the variation along the beam profile on the detector as seen in the inset. The profiles are scaled by the ratio of the ring current of 6 μA that is used for the  $QE$  measurements to the corresponding ring current of the measured profile. In this way, an increase of detector saturation due to a too high rate of incoming photons (which is equivalent to the ring current) can be observed by a deviation from the profile measured at 6 μA. It can be seen that the profiles of 832 μA and 409 μA deviate significantly from the 6 μA profile (red line), clearly indicating the occurrence of saturation. However, the profile of 95 μA (blue line) differs by less than 2.2 % from the 6 μA data, which should give an upper estimate for the increase of saturation from 6 μA

to  $95 \mu\text{A}$ . The  $QE$  measurements were carried out at a ring current of  $6 \mu\text{A}$ , where an even much lower deviation from the linear counting behaviour can be expected. Nonetheless, a relative uncertainty contribution of 2 % to the  $QE$  measurement is used as an upper estimate for the effect of nonlinear counting. The contribution of the uncertainty of the photon energy of  $u(E_{\text{ph}})/E_{\text{ph}} = 10^{-4}$ , see Table 3.2, is negligible. The comparison of photodiode measurements before and after each set of PILATUS measurements yields a mean deviation of 0.5 %. In conjunction with the uncertainty of the diode calibration, this yields a relative uncertainty of 1 % of the incoming photons flux. In total, the resulting relative uncertainty of  $QE$  in ultra-high gain mode is 3 % in particular at low photon energies below 4 keV. In high gain mode, the incoming photon flux is well within the linear regime. Therefore, the corresponding relative uncertainty in this setting is only determined by the variation of before-and-after measurements of the photodiodes, which is within 1 %.

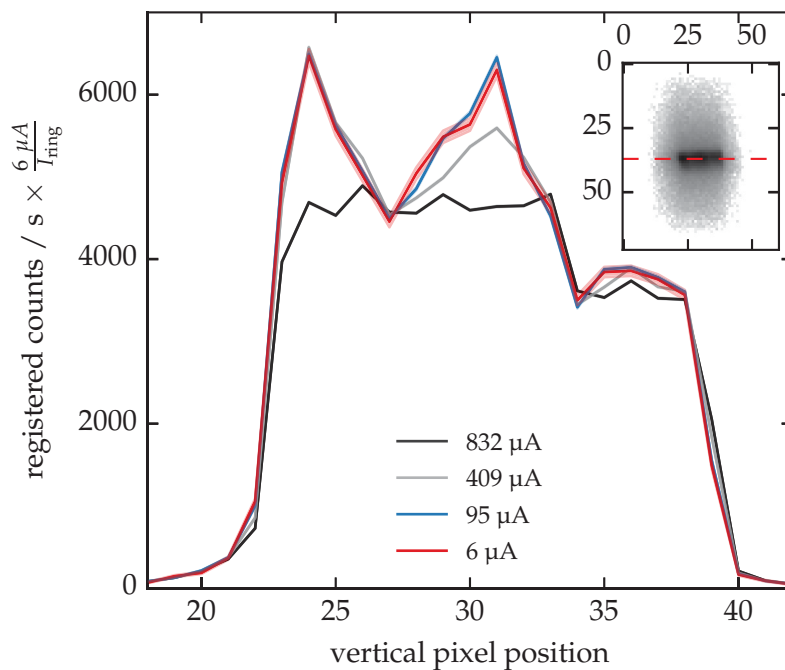


**Figure 3.13** | Registered counts per second along the most intense region of the direct beam. The inset shows a logarithmic scale beam image (rotated by  $90^\circ$ ), the red dashed line indicates the line cut of the plotted beam profiles. The detector images were recorded at four different storage ring currents at  $E_{\text{ph}} = 2.5 \text{ keV}$  as indicated in the legend. Each profile has been scaled by the ratio of minimal ring current ( $6 \mu\text{A}$ ) and the ring current of the profile.

The measured  $QE$  with the associated uncertainty (colour-shaded areas around the curves) is displayed in Fig. 3.14. As already discussed, the  $QE$  depends on the photon energy  $E_{\text{ph}}$  and also on the threshold level  $E_{\text{thresh}}$  setting of the detector. The threshold level was set to the preferred value  $E_{\text{thresh}} = 1/2 E_{\text{ph}}$  above  $E_{\text{ph}} = 3.4 \text{ keV}$ , which is shown in Fig. 3.14a by the red squares for the ultra-high gain mode and by the green triangles for the high-gain mode. The high-gain mode is limited to threshold settings  $E_{\text{thresh}}$  above  $3.75 \text{ keV}$ , or equivalently to  $E_{\text{ph}}$  above  $7.5 \text{ keV}$ . Below  $E_{\text{ph}} = 3.4 \text{ keV}$ , the threshold in ultra-high gain mode was fixed to  $E_{\text{thresh}} = 1.7 \text{ keV}$  (blue circles in Fig. 3.14a). In addition, the  $QE$  was measured in this range for larger settings of  $E_{\text{thresh}}$  up to  $2.0 \text{ keV}$  (Fig. 3.14b).

The  $QE$  exceeds 80 % over the range from  $3.4 \text{ keV}$  to  $10 \text{ keV}$  with a maximum of 96 % at  $8 \text{ keV}$ . Below  $3 \text{ keV}$ , the quantum efficiency is reduced due to the absorption of photons in the non-sensitive surface layers of the sensor, which are always present in semiconductor detectors.<sup>[127]</sup> Just above the Si K-edge, the  $QE$  drops to about 5 %. However, measurements are feasible down to  $1.75 \text{ keV}$ . The measured  $QE$ , in particular at low energy, is in full agreement with the previously reported  $QE$  of the single module test setup at the corresponding threshold setting.<sup>[50]</sup> The two different gain settings result in

a relative deviation of less than 1 %, which is within the uncertainty of the measurement. The threshold level settings have a noticeable influence, as displayed in Fig. 3.14b. The highest  $QE$  is achieved by the lowest possible threshold setting  $E_{\text{thresh}} = 1.7 \text{ keV}$ , as expected,<sup>[123]</sup> and is therefore chosen as the recommended setting for all measurements.

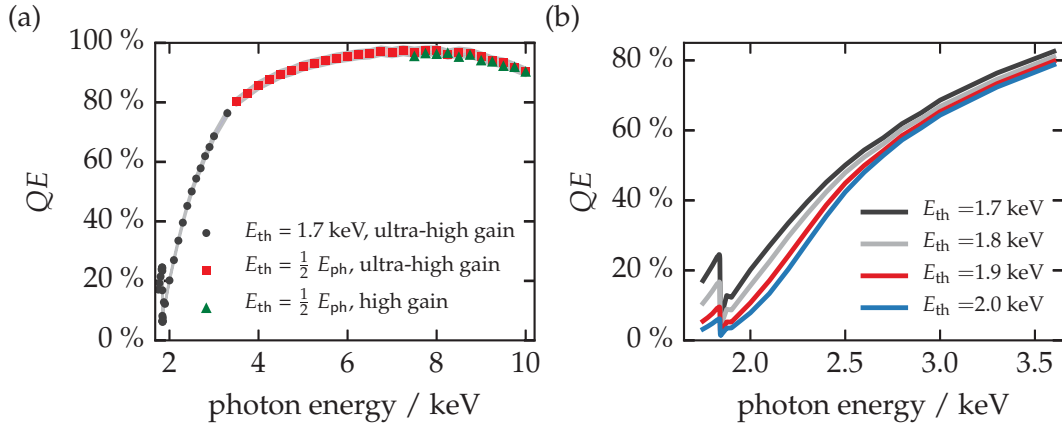


**Figure 3.14** | The quantum efficiency  $QE$  of the detector, measured over the full energy range of the beamline using (a) the recommended settings and (b) different threshold levels at the low end of the energy range. The green triangular symbols in (a) denote measurements using the high-gain mode, while all other data was measured using the ultra-high gain mode. The colour-shaded areas around the data points indicate the relative uncertainty of the values (3 % in ultra-high gain mode, 1 % in high gain mode). The ring current of the storage ring was reduced to 22  $\mu\text{A}$  (6  $\mu\text{A}$ ) for photon energies above (below) 3.5 keV, respectively.

In principle, the fill pattern of the electrons in the storage ring may also influence the registered count rate as described in Trueb et al. [242]. However, the circulation period of the electrons at BESSY II is 800 ns, which is much lower than the discussed detector dead-time of 4  $\mu\text{s}$ . Hence, the detector is completely insensitive to the electron fill pattern and the dead-time causes only a systematic loss in the registered count rate.<sup>[242]</sup>

### Detector homogeneity

SAXS images in the range from 4 keV to 10 keV were recorded using a sample of glassy carbon. The scattering pattern of glassy carbon exhibits a flat plateau in the range of the scattering vector  $q$  from  $0.1 \text{ nm}^{-1}$  to  $1 \text{ nm}^{-1}$  and is frequently used in SAXS for absolute intensity scaling.<sup>[267]</sup> By dividing the whole image by the azimuthally averaged scattering curve pixel by pixel, an image with the relative deviation of each pixel value from the mean is obtained. Displayed in Fig. 3.15 is the intensity deviation after averaging patches of  $(10 \times 10) \text{ px}^2$  in order to reduce the shot noise. At 10 keV (Fig. 3.15a), the intensity difference amounts to 0.5 % across the whole detector. At 5 keV (Fig. 3.15b), the intensity varies by 2.5 % although the manufacturer-supplied flat field correction was enabled. This discrepancy can be explained by the absorption of radiation in the upper insensitive layer of the detector.<sup>[127]</sup> At high energies, this layer is nearly transparent, while at lower energies, the absorption and, therefore, the variation increases. This may result in a limited accuracy of the extrapolation of calibration values for threshold fine-adjustment per pixel, which is based on flat field reference measurements at higher photon energies. The inhomogeneity might possibly be reduced by applying better flat field corrections by the manufacturer in the low photon energy range on the basis of these images.

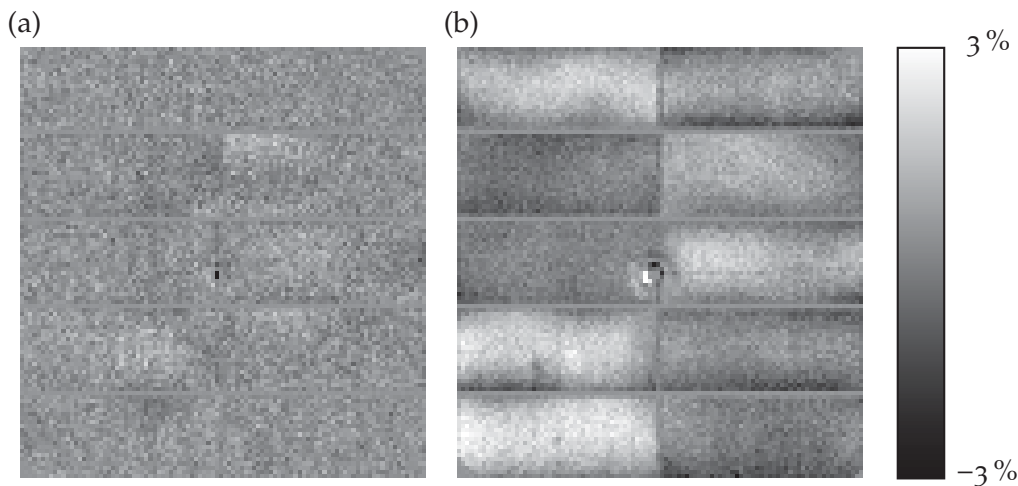


**Figure 3.15** | Homogeneity of the detector at a photon energy of (a) 10 keV and (b) 5 keV in ultra-high gain mode and with  $E_{\text{thresh}} = 1/2 E_{\text{ph}}$ . The raw data was preprocessed by binning  $(10 \times 10) \text{ px}^2$  into one in order to overcome the quantum noise in comparison to the inhomogeneous detector response. The ring in the centre is an artefact which arises from the positioning of the beamstop in the centre of the scattering pattern.

### Geometric characterisation

A possible geometric distortion introduced by the detector must be known to determine uncertainty bounds for metrological nanodimensional measurements. Two different measurement setups were used for the geometric characterisation: (i) SAXS images as displayed in Fig. 3.16 were recorded to determine the pixel pitch. (ii) GISAXS patterns with many sharp, well defined peaks as shown in Fig. 3.17 were generated to characterise the displacement of adjacent modules and their angular misalignment.

The measurements in SAXS geometry were taken at  $E_{\text{ph}} = 8 \text{ keV}$  using the standard sample silver behenate, which displays an intense ring at  $q = 1.076 \text{ nm}^{-1}$ .<sup>[22]</sup> The detector was positioned at a distance of  $L_s = 2754 \text{ mm}$  to the sample and 240 images were recorded. Between the exposures, the detector was vertically shifted in a stepwise fashion by moving both vertical translation axes  $z_1$  and  $z_2$  in parallel, see Fig. 3.6. The total distance by which the detector was moved amounts to 7 mm. The traceability of the  $z_1$  and  $z_2$  movement was established by the Heidenhain linear encoders (Section 3.4).

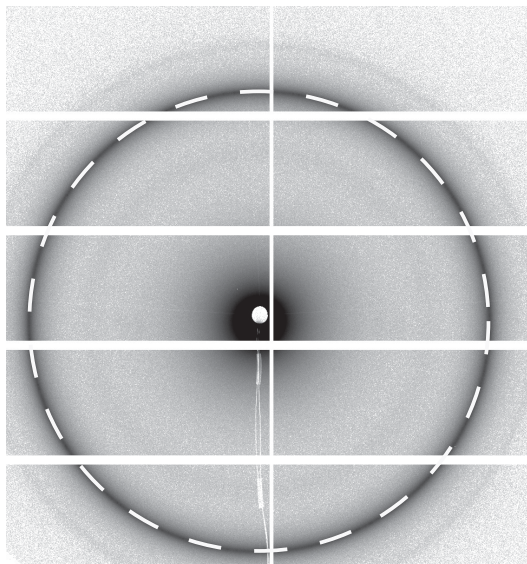
Next, a circle was fitted to every recorded image by maximising the average intensity along the ring, which was represented by a Gaussian line with a width of  $\sigma = 1.06 \text{ px}$ . An example image together with the fitted circle (dashed line) is shown in Fig. 3.16. The centre positions of the best fit circles were fitted linearly to the corresponding vertical detector displacement values  $z_1$  and  $z_2$ . The residuals of this fit did not exceed one tenth of the pixel pitch for any circle position. From this linear fit, the pixel pitch

$$L_{\text{px}} = (172.1 \pm 0.2) \mu\text{m} \quad (3.4)$$

can be derived. The uncertainty estimate of this value is derived from the comparison of both vertical shift axes and two independent measurements. The pure statistical error from the linear fit is smaller by an order of magnitude.

For the second sequence of measurements, the GISAXS pattern of a reflection grating in parallel alignment of grating lines and incident beam was used (see Chapter 4, Fig. 2.7, and Refs. [251, 253]). This setup produces a series of equidistantly spaced sharp peaks ordered on an extended semi-circle as shown in Fig. 3.17a, which was used

**Figure 3.16** | SAXS image of silver behenate at 8 keV together with the fit circle (dashed white line) for the determination of the pixel size.



to characterise the placement of the individual detector modules with respect to each other. The basic idea is to determine the peak positions during horizontal and vertical detector displacements that cross a detector module gap. Some of the peaks cross the module borders, some remain on a single module during the detector displacement. A comparison of the former with the latter together with the previously determined pixel pitch yields information on the module misalignment.

Displayed in Fig. 3.17b are the traces of the peaks (series of black dots) on the detector for one contiguous series of images. The inset shows a magnification of two peak traces for better visibility. The detector was moved vertically upwards in 20 steps and an image was taken at every position. The peak positions were extracted from each image with sub-pixel resolution by computing the intensity-weighted centre for every peak. The peaks can be divided into three categories: Peaks in the first category that are labelled as 1, 2, 14 and 15 in Fig. 3.17b stay on a single module. These were used as a reference trace. The peaks 4 to 12 cross the horizontal module borders between the upper and lower modules to the left and right of the central gap (grey shaded areas in Fig. 3.17b). The remaining unlabelled peaks are neither confined to a single module nor do they cross the module borders completely to reach the next module. Similar datasets were recorded for all module borders in the horizontal and vertical direction.

The relative displacement of the modules from the nominal position results in a discontinuity of the trace for the border-crossing peaks. However, on the subpixel scale it has to be considered that the movement of the detector is slightly irregular due to deviations of the mechanical positioning. By comparing the border-crossing traces, i.e. peaks 4-12, with the traces of the reference peaks 1, 2, 14 and 15, the displacement of the upper modules with regard to the modules below can be detected regardless of irregularities in mechanical positioning. The analysis was performed by least-squares fitting of the reference trace to the border-crossing traces at both sides of the gap. The maximum deviation from the nominal position amounts to 60  $\mu\text{m}$  over the whole detector, which is less than 0.4 px.

In principle, the same method could be used to determine the in-plane angular misalignment between two neighbouring modules. The angular deviation was found to be below  $0.1^\circ$ , but this is already beyond the limit of this method due to the limited resolution of finding the peak centre of approx. 20  $\mu\text{m}$ . An out-of-plane angular misalignment only

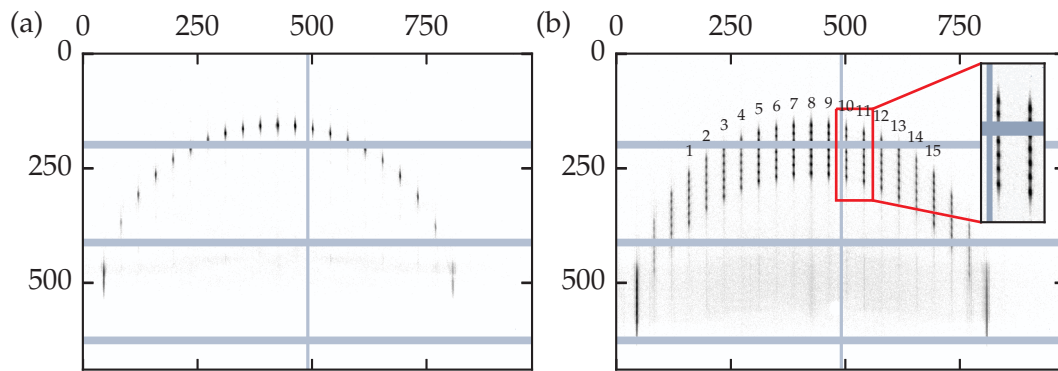


**Figure 3.17** | GISAXS measurements to determine the module alignment. Image series were recorded for vertical and horizontal displacements of the detector. (a) A single GISAXS image with sharp peaks on the upper detector modules, the module gaps are shaded in grey. (b) A series of images was recorded for a vertical displacement of the detector to cross the upper horizontal module gap. The inset shows the magnification of a region to illustrate the trace of the peaks. Only every other image of the measured displacement series was used in this plot to make the individual peaks visible. The numbered maxima indicate the peaks that were tracked to determine the detector movement. One group of peaks (4-12) crosses the module borders; the other group (1, 2, 14 and 15) stays on a module and is used for reference. The same procedure is applied to the other module gaps on the detector.

leads to smaller pixel length in the direction perpendicular to the axis of rotation. A deviation of at most  $0.4^\circ$  was measured for the same detector with great sensitivity by Bragg diffraction at the surface of the detector.<sup>[75]</sup> However, it cannot be distinguished whether the deviation originates from a possible miscut of the silicon wafers or from a mechanical misalignment of the modules. Since the cosine of this angle deviates by less than  $2.5 \times 10^{-5}$  from unity, this has no effect on the scattering images.

## 3.6 Summary

The energy range from 1.75 keV to 10 keV of the FCM beamline is well suited for the critical energy of BESSY II at 2.5 keV. The UHV sample chamber facilitates high precision alignment of a wide range of samples on six axes and the detectors allow a variety of different  $q$  space scans. Additional equipment such as a silicon drift detector extend the measurement capabilities to spectroscopic fluorescence measurement methods. The HZB SAXS instrument offers a variation in  $q$  range and  $q$  resolution by more than a factor of 2 just by geometric sample-detector distance variation, which provides flexibility in the probed size regime. Especially the ability to tilt the entire setup upward is beneficial for GISAXS measurements as it allows to use the full detector area for imaging even at larger incidence angles. With the development of the in-vacuum PILATUS 1M, a detector is available that is capable to cover the full energy range of the beamline, which brings important K-absorption edges (Si, P, S, Cl, Ca) into reach for resonant scattering imaging. The narrow point-spread function of the detector and the increase of  $q$  resolution at lower  $E_{\text{ph}}$  is beneficial for nanodimensional metrological GISAXS measurements on grating structures (Chapter 4). The access to the silicon K-absorption edge at 1.84 keV enables X-ray scattering contrast matching using the most commonly used substrate material, which is demonstrated in Chapter 5 by depth-resolved GISAXS measurements of nanostructured block copolymer thin films.



# 4

## Dimensional nanometrology of surface gratings using GISAXS

Extensive research has been conducted with regard to the scattering of X-rays by gratings and multilayer gratings. The features of the occurring scattering patterns have been explained by reciprocal space construction described by Mikulík et al. [153], see Section 2.5 and Fig. 2.14. The scattering process has been profoundly described within the framework of kinematic and dynamical theories<sup>[108,152,237,259,260]</sup> that take refraction, multiple scattering events and roughness into account. Hofmann et al. [92] used the framework of DWBA for the analysis and demonstrated that GISAXS is a suitable tool for the dimensional characterisation of nanopatterns.

This chapter is dedicated to the field of dimensional nanometrology on grating structures using GISAXS and aims to establish the traceability of GISAXS measurements as well as to offer new insights into the technique itself. Each sub-chapter presents the results from one out of three different grating pitch size regimes, measured with two different area detectors. Each size regime requires a different method of analysis, which offers new insights into different aspects of the determination of structural parameters from GISAXS data. What these analysis methods have in common is that they are kept as simple as possible to extract structural parameters such as critical dimension  $CD$ , i.e. line width, groove width  $G$ , line height  $H$ , and the grating pitch  $P$  (see Fig. 2.13) directly from the data, in contrast to numerical modelling. As discussed in Section 2.6, it is important to realise that any of such direct analysis methods limits the evaluation of the measured scattering intensity pattern, which is the product of the line form factor and the grating structure factor, Eq. (2.44), to the analysis of the structure factor only. This is a severe limitation as well as a great advantage, compared to solving the inverse problem by full modelling of the GISAXS pattern. Neglecting the form factor limits the obtainable parameters to the above mentioned structure factor-specific parameters, which excludes other interesting parameters such as sidewall angle, roughness, corner rounding, etc. Yet, by doing so, there is no need to find a suitable form factor for the cross-sectional line shape. This would be very problematic for traceability, because it is impossible to evaluate the ‘correctness’ of the model selection itself by an uncertainty

analysis *within* the model. Even though the intensity of the grating diffraction orders depends on the form factor,<sup>[178,225]</sup> their positions are solely governed by the grating structure factor. The limitation to a direct analysis of the structure factor opens up the possibility of traceability of the structural parameters by avoiding the introduction of non-traceable assumptions about the form factor of the grating lines.

The sub-chapters are ordered by decreasing pitch size, which also represents the chronological order of the work carried out. Consequently, the methods of determining common parameters such as the sample-detector distance are improved, adapted, and refined from section to section. Large parts of every sub-chapter are published in peer-reviewed journals.<sup>[224,225,251,253]</sup> For this reason, the state of analysis at that time was kept for consistency in some cases where later measurements for a refined analysis were not possible because the samples were not available any more.

## 4.1 Large pitches close to 1 $\mu\text{m}$ : Discrete Fourier transform

The first direct structure parameter determination method is the discrete Fourier transform (DFT) of extracted and pre-processed GISAXS intensity profiles of different grating structures on a common ( $152 \times 152$ )  $\text{mm}^2$  quartz substrate. In the regime of total reflection at incidence angles  $\alpha_i$  below the critical angle  $\alpha_c$ , Eq. (2.9), there is a well-defined relationship between the scattered intensity distribution and the PSD function, Eq. (2.48), of the sample surface<sup>[229]</sup> because only an evanescent wave propagates through the material. Measurements have also been carried out at  $\alpha_i > \alpha_c$  to increase the spacing between adjacent intensity maxima on the detector. Thus, transmission through the surface and scattering from within the material may occur.

One of the goals of the work presented in this section is to explore whether the simple picture of surface scattering and interference is still applicable for  $\alpha_i$  being slightly larger than  $\alpha_c$  and can, therefore, be used to determine the structural parameters. Other new aspects of this work are the successful application of Fourier analysis by DFT to GISAXS data of line gratings in parallel orientation ( $\varphi = 0^\circ$ , see Fig. 2.14) to directly extract fundamental structural parameters such as critical dimension  $CD$  and groove width  $G$ . The analysis method is validated by a simulation of the full two-dimensional  $q_y$ - $q_z$  map of the GISAXS pattern of surface gratings within the framework of DWBA, which has not been reported previously. It is found that the semicircular pattern due to the intersection of the Ewald sphere and the GTRs, see Section 2.5, is not influenced by refraction, because the pattern appears also in the regime of total refraction at  $\alpha_i < \alpha_c$ . Extensive parts of this section have been published in J. Wernecke, F. Scholze and M. Krumrey: 'Direct structural characterisation of line gratings with grazing incidence small-angle x-ray scattering', *Rev. Sci. Instrum.* **83**.10 (2012), p. 103906.

### 4.1.1 Materials and methods

The sample is a  $(152.4 \times 152.4 \times 6.35)$  mm<sup>3</sup> quartz (SiO<sub>2</sub>) substrate with 12 different grating structures with a size of  $(30 \times 15)$  mm<sup>2</sup> per field.\* A schematic cross section with relevant grating parameters is shown in Fig. 2.13. The nominal pitch of  $P = 833$  nm is the same for every field. Differences between the fields exist in nominal groove width  $G = (0.65, 0.70, 0.75) \times P$  and nominal line height  $H = 26.6$  nm, 30.6 nm, 35.6 nm and 41.0 nm. The structure was produced by electron lithography. It was then coated with a thin layer of ruthenium with a nominal thickness of 10 nm to improve smoothness and, hence, specular reflectivity.

The GISAXS measurements were performed at the FCM beamline using the MarCCD X-ray area detector mounted on the HZB SAXS instrument as described in Section 3.2. XRR measurements were carried out at  $E_{\text{ph}} = 8$  keV using highly linear photodiodes. GISAXS patterns have been recorded at 6 keV, 8 keV or 10 keV photon energy and with an incident angle  $\alpha_i$  ranging from  $0.4^\circ$  to  $1.4^\circ$ .

For the traceability of the grating parameters obtained using GISAXS, every experimental parameter has to be measured in a traceable manner. The relative uncertainty of the photon energy is  $u(E_{\text{ph}})/E_{\text{ph}} < 10^{-4}$  in the used photon energy range, see Section 3.2. The size of MarCCD pixels  $L_{\text{px}}$  has been measured by observing the direct beam position while incrementally moving the detector perpendicular to the beam with an absolute length measurement, yielding a relative uncertainty of  $u(L_{\text{px}})/L_{\text{px}} = 10^{-3}$ .<sup>[74]</sup> Tracing of incidence and scattering angles as well as of the sample-detector distance  $L_s$  has been carried out by observing the direct and the specularly reflected beam positions at different incidence angles  $\alpha_i$  and sample-detector distances. These measurements resulted in a comparatively large uncertainty of  $u(L_s)/L_s = 2.6 \times 10^{-3}$  due to the grazing incidence geometry. In later measurements, see Sections 4.2 and 4.3 and Chapter 5, the data recording of the specular beam positions was refined and the extrapolation algorithm was improved. This resulted in a decrease of  $u(L_s)/L_s$  by more than a factor of 10. However, this approach is not applicable to the data shown in this section, nor was it possible to repeat the measurements because the grating structure was not available any more.

The instrumental resolution is governed by the energy resolution  $\Delta E_{\text{ph}}/E_{\text{ph}} = 10^{-4}$  and the divergence of the incident beam. The angular resolution of the detector of  $\Delta\alpha_f \approx \Delta\theta_f = 0.02$  mrad is not a limiting factor due to the experimental set-up of  $L_s = 3920$  mm and  $L_{\text{px}} = 0.079$  mm. The beamline slits were chosen to provide a vertical and horizontal divergence of  $\Delta\alpha_i = 0.4$  mrad and  $\Delta\theta_i = 0.2$  mrad, respectively. This corresponds to the resolution of a maximum lateral structure size of  $d_{\parallel} \approx \lambda/\Delta\theta_i = 1$   $\mu\text{m}$  (at 6 keV). To sum up, feature sizes of 833 nm and larger can be resolved with this set-up in the specified energy range.

\* The gratings were kindly provided by the CMN-Optics group of Dr. Uwe Zeitner from IOF Jena.

### 4.1.2 Determining the capping layer thickness using XRR

For the characterisation of the sample layer structure, XRR was carried out to determine the ruthenium layer thickness  $d_{\text{Ru}}$  and the rms roughness of the ruthenium surface  $\sigma_{\text{vac/Ru}}$  as well as of the ruthenium/quartz interface  $\sigma_{\text{Ru/SiO}_2}$ . Figure 4.1 shows the reflectance curve at a photon energy of  $E_{\text{ph}} = 8 \text{ keV}$  at a position on the sample without any grating structure. Thus, a single layer of ruthenium on  $\text{SiO}_2$  substrate can be assumed as a vertical structure model. Also depicted in Fig. 4.1 is the best fit result of the utilised monolayer system model (solid line) obtained by the IMD software<sup>[257]</sup> according to Eq. (2.37). A ruthenium layer thickness of  $d_{\text{Ru}} = 9.4 \text{ nm}$  is determined, the other fit parameters are shown in Table 4.1.

**Figure 4.1** | X-ray reflectivity data (grey symbols) of the sample measured at a position without any grating structure. Also shown is the best fit (solid line) of the reflectance of a ruthenium layer on  $\text{SiO}_2$  in dynamic scattering theory (Eq. (2.37)) using IMD.<sup>[257]</sup> Parameters of the fit are displayed in Table 4.1.

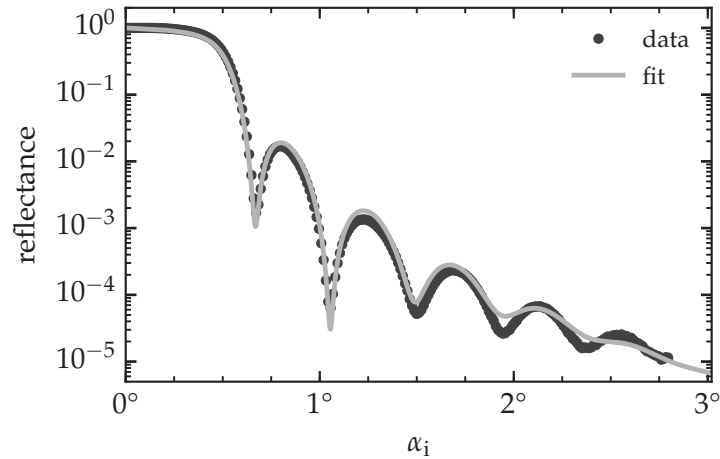


**Table 4.1** | Parameters of XRR fitting.

	parameter	best fit
Ru layer thickness	$d_{\text{Ru}} / \text{nm}$	9.4
rms roughness vacuum/Ru	$\sigma_{\text{vac/Ru}} / \text{nm}$	0.26
rms roughness Ru/ $\text{SiO}_2$	$\sigma_{\text{Ru/SiO}_2} / \text{nm}$	0.75
Ru mass density	$\rho_{\text{Ru}} / \text{g cm}^{-3}$	11.9

### 4.1.3 GISAXS in perpendicular orientation

First, GISAXS measurements in perpendicular orientation ( $\varphi = 90^\circ$ ), i.e. in the dispersive direction of the grating, are discussed (see Section 2.5, the coordinates are defined as shown in Fig. 2.4). Displayed in Fig. 4.2a is a corresponding GISAXS pattern recorded at  $E_{\text{ph}} = 8 \text{ keV}$ ,  $\alpha_i = 0.8^\circ$ . A beamstop to block the specular spot is faintly visible in the central part of the image. Intense maxima are visible along the specular axis, i.e. at  $q_y = 0 \text{ nm}^{-1}$ . These are the grating diffraction orders, as discussed in Section 2.5. The expression of the optical path difference from interfering rays reflected at the top and bottom of the grating lines yields the grating equation, see Eq. (2.45).

The peak positions of the GISAXS pattern recorded at 8 keV are found at  $\alpha_f = 1.34^\circ$  and  $1.73^\circ$  as shown in Fig. 4.2b. Equation (2.45) yields  $P = 847 \text{ nm}$  and is the same for the various fields of different line heights. The deviation from the nominal value of 833 nm

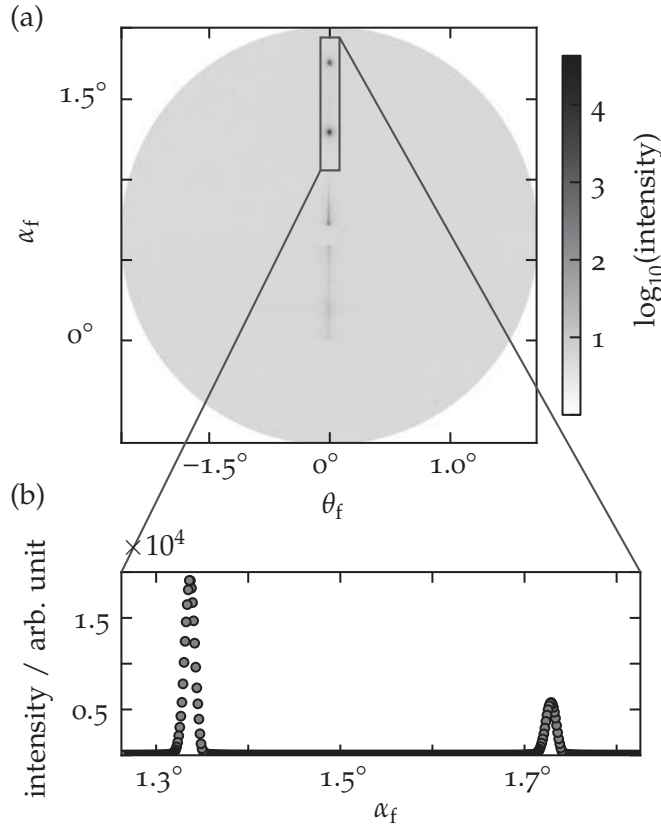


**Figure 4.2** | (a) GISAXS scattering image in perpendicular orientation of incident beam plane and grating lines ( $E_{\text{ph}} = 8 \text{ keV}$ ,  $\alpha_i = 0.8^\circ$ ). (b) Intensity profile along the vertical specular axis ( $\theta_f = 0^\circ$ ) as a function of  $\alpha_f$ . The diffraction peak positions at  $1.34^\circ$  and  $1.73^\circ$ , respectively, are used to determine  $P$ .

can be explained by an analysis of the uncertainty,

$$\begin{aligned} \left(\frac{u(P)}{P}\right)^2 &= \left(\frac{u(\lambda)}{\lambda}\right)^2 + \left(\frac{P}{\lambda} \sin(\alpha_{f,(m+\Delta m)}) u(\alpha_{f,(m+\Delta m)})\right)^2 \\ &+ \left(\frac{P}{\lambda} \sin(\alpha_{f,(m)}) u(\alpha_{f,(m)})\right)^2. \end{aligned} \quad (4.1)$$

The first term,  $u(\lambda)/\lambda = 10^{-4}$ , can be neglected here because it is an order of magnitude smaller than the other contributions, see Table 3.2. The second and third term for the uncertainty of diffraction peak angles are governed by the uncertainty of the pixel size  $L_{\text{px}}$ , the sample-detector distance  $L_s$ , and of the peak position on the detector,  $u(x_{\text{px}})/x_{\text{px}} = 10^{-3}$ , according to

$$\left(\frac{u(\alpha_f)}{\alpha_f}\right)^2 = \left(\frac{u(x_{\text{px}})}{x_{\text{px}}}\right)^2 + \left(\frac{u(L_{\text{px}})}{L_{\text{px}}}\right)^2 + \left(\frac{u(L_s)}{L_s}\right)^2 = 4.6 \times 10^{-3}. \quad (4.2)$$

This results in a relative uncertainty of  $u(P)/P = 3.6 \times 10^{-2}$ , in particular due to the comparably large uncertainty of the sample-detector distance  $L_s$  at the time of the measurements. During later measurements for other projects, the determination of  $L_s$  was significantly improved by a refinement of the peak fitting algorithm, see Section 4.3.3.

#### 4.1.4 Discrete Fourier analysis of GISAXS in parallel orientation

The scattering pattern in parallel alignment ( $\varphi = 0^\circ$ , inset of Fig. 2.14) has a very different appearance. The GISAXS pattern, Fig. 4.3a ( $E_{\text{ph}} = 6 \text{ keV}$ ,  $\alpha_i = 0.8^\circ$ ,  $L_s = 3920 \text{ mm}$ ), is a complex superposition of different features. As discussed in Section 2.5, the most prominent feature is the intersection of the Ewald sphere and GTRs along  $q_z$  with a periodicity of  $\delta q_y = 2\pi/p$ , see Fig. 2.14. The resulting semi-circular pattern is centred around the intersection of the specular axis and the horizon of the sample surface, contains the specular beam (covered by the beamstop in the centre of the image), and has a radius of  $L_s \times \tan \alpha_i$ . It should be noted that the semi-circular shape is known to be very sensitive to the perfect parallel alignment of the beam and the grating,<sup>[153,264]</sup> which was also the case in the measurements presented here.

The semi-circular pattern is also visible at incidence angles well below the critical angle, e.g.  $\alpha_i = 0.2^\circ$  at 6 keV. Moreover, the specular spot is located directly on the semi-circle at higher incidence angles, e.g.  $\alpha_i = 1.4^\circ$  which allows the image recording without a beamstop. Both findings clearly indicate that the scattering features are surface scattering effects rather than scattering from within the material.

Other features can be identified in the scattering pattern, such as satellite rings and diffuse Bragg sheet-like structures, which are affected by many structural features such as the line sidewall angle, line roughness, stitching pattern of the electron beam lithography machine,<sup>[115,214,224,225]</sup> and others, and are investigated in more detail in Section 4.2. In this context it is sufficient to say that these additional features have no significant influence on the determined correlation lengths of  $CD$  and  $G$ .

The detector coordinates are converted to the  $q_z$ - $q_y$  coordinate system by the corresponding geometric and experimental parameters. The relevant component for lateral structure information is  $q_y$  (Section 2.4). For the averaging of the  $I(q_y)$  profile, Fig. 4.3b, a ring-shaped mask with a radial width of 12 px around the Ewald sphere intersection is applied to the GISAXS pattern. For each pixel position along  $\theta_f$ , the average value of counts inside the masked area in the corresponding column is calculated. The  $I(q_y)$  profile is convoluted with a Hann window function, Eq. (2.49), to mask the beamstop and the margins of the profile. A Fourier transform, see Section 2.6 is applied to the resulting  $I(q_y)$  profile (solid line in Fig. 4.3b) to determine the PSD from the absolute square of the Fourier amplitude. This has been implemented according to Eq. (2.47) by a DFT of the  $N$  data points of the extracted  $I(q_y)$  profile for each equidistant position  $q_y(n) = n q_{y0}$  on the detector as

$$\mathcal{F}_{\text{DFT}}(\xi) = \sum_{n=0}^N I_n(n q_{y0}) e^{-i 2\pi \xi n q_{y0}} \quad (4.3)$$

$$\text{PSD}(\xi) = |\mathcal{F}_{\text{DFT}}(\xi)|^2 . \quad (4.4)$$

The resulting PSD profile is expressed in terms of the signal frequency  $\xi$ , which is directly proportional to the real-space correlation lengths  $d_{\text{corr}} = 2\pi\xi$  that contributes to the scattering pattern.

The PSD as a function of the correlation length is displayed in Fig. 4.3c. Three distinct peaks are visible in the spectrum and are each fitted by a Gaussian function  $f(d_{\text{corr}}) = A_0 \exp\left(-[d_{\text{corr}} - d_{\text{corr},i}]^2 / \sigma_i^2\right)$  to determine the centre position  $d_{\text{corr},i}$  and the width  $\sigma_i$ . The first peak in Fig. 4.3c is located at a centre position of  $d_{\text{corr},1} = 256 \text{ nm}$  with a width of  $\sigma_1 = 12 \text{ nm}$ , the second and third peak are at  $d_{\text{corr},2} = 576 \text{ nm}$  and  $d_{\text{corr},3} = 833 \text{ nm}$

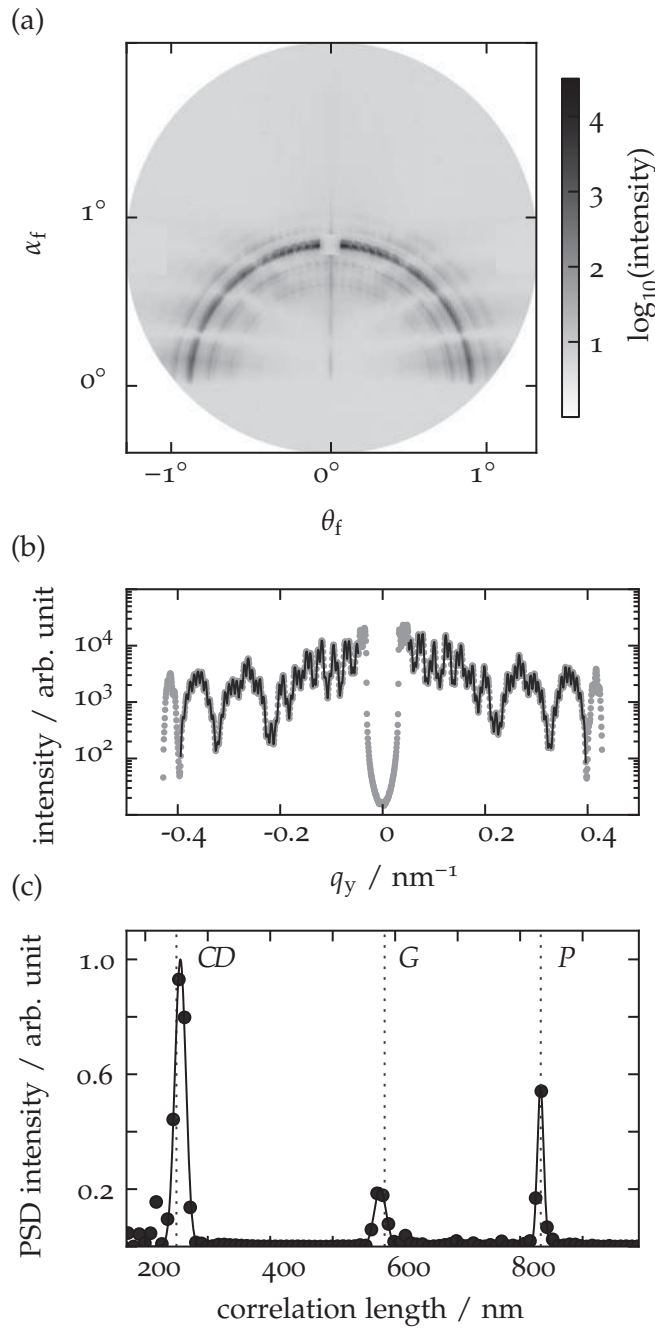


**Figure 4.3** | GISAXS analysis method. (a) GISAXS pattern of beam orientation parallel to grating lines;  $\alpha_i = 0.8^\circ$ ,  $E_{\text{ph}} = 6 \text{ keV}$ . (b) Extracted  $I(q_y)$  profile along the intersection of the Ewald sphere and GTRs in (a) as a function of  $q_y$ . For averaging, each column within a ring of 12 px width around the semi-circle is averaged column-wise for each corresponding  $q_y$ . (c) PSD of the  $I(q_y)$  profile. Black solid lines represent peak fits using Gaussian functions. Dotted vertical lines indicate the nominal lengths of grating pitch  $P$ , critical dimension  $CD$  and groove width  $G$ .

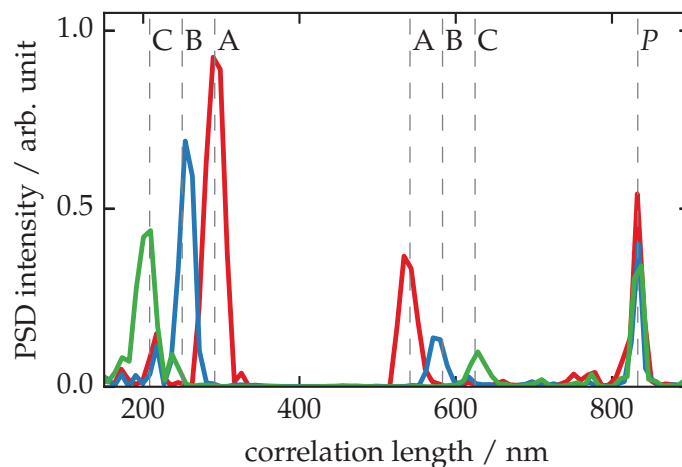
with peak widths of  $\sigma_2 = 13$  nm and  $\sigma_3 = 7$  nm, respectively. Comparison with nominal grating parameters of critical dimension and groove width, indicated by dashed vertical lines in Fig. 4.3c, show close agreement of peak positions and nominal parameters within the widths of the peaks. It has to be noted that the abscissa of each PSD shown here has been scaled by a factor very close to 1 (deviation below  $\pm 0.01$ ) to facilitate the coincidence of the third peak centre and the grating pitch  $P = 833$  nm. This was necessary because of the still relatively large uncertainty of  $L_s$  in the range of 50 nm during these measurements, as explained in the previous section. Consequently, the independent information on the pitch of the grating is lost, but the reference value of  $P = 833$  nm has been verified in independent measurements by EUV scatterometry.\*

This analysis procedure is applied to GISAXS scattering patterns of various grating fields on the sample, which differ in their  $CD$  to groove width ratio  $CD/G$  at constant grating pitch  $P$  and constant line height  $H$ . Depicted in Fig. 4.4 are PSDs of  $I(q_y)$  profiles from three different gratings, named A, B, and C. Vertical dotted lines indicate nominal positions of  $CD$  and  $G$ . All spectra show a peak at around 833 nm, which is the grating period. The peaks of  $CD$  and  $G$  are self-consistent in terms of  $CD + G = P$  and are in agreement with the nominal grating parameters within their peak widths. Summarised in Table 4.2 are nominal grating parameters and mean peak positions from PSDs of different fields, measured at different photon energies of  $E_{ph} = 6$  keV, 8 keV and 10 keV. The range values in Table 4.2 indicate the standard deviations of the corresponding mean peak position. The nominal grating parameters are well within the standard deviations of the peak positions.

**Table 4.2** | Mean grating parameters obtained from PSD of various GISAXS images with corresponding standard deviation.

field	critical dimension $CD$ / nm		groove width $G$ / nm	
	nominal	experimental	nominal	experimental
1-4 A	292	$292 \pm 6$	541	$542 \pm 9$
1-4 B	250	$249 \pm 16$	583	$583 \pm 16$
1-4 C	208	$214 \pm 12$	625	$615 \pm 10$

**Figure 4.4** | PSD versus correlation length of various grating fields (A, B, C) with different ratios  $CD/G$  at constant grating pitch  $P$  and constant line height  $H$ . Dashed vertical lines indicate the positions of nominal values for  $CD$ ,  $G$  and  $P$  for the respective field as specified by the manufacturer.



\* Dr. Frank Scholze, PTB workgroup 7.12, private communication.

### 4.1.5 Validation by simulation using IsGISAXS

For the validation of the analysis process, scattering patterns of grating structures similar to those under investigation are numerically simulated and analysed using the same procedure as described for the experimental data in the previous section. The software IsGISAXS<sup>[133]</sup> is a well-established tool for simulating GISAXS patterns, interference functions, and form factors of structure models to solve Eq. (2.44). The program is most useful for many sorts of correlated and uncorrelated particles on a substrate or buried in a matrix. The construction of a reflection line grating structure has been implemented here by box-shaped ruthenium particles on a ruthenium substrate (6 keV, refractive index components  $\delta = 6.236 \times 10^{-5}$ ,  $\beta = 7.612 \times 10^{-6}$ , values from the X-ray database<sup>[90]</sup>) using a box width of  $2R = 250$  nm (Gaussian probability distribution  $\sigma^{(R)}/R = 0.01$ ), a height of  $H = 26$  nm (Gaussian probability distribution  $\sigma^{(H/R)}/(H/R) = 0.01$ ), and a very extended length of  $4000 \times 2R$ . The peak position of the interference function is chosen at  $D = 833$  nm and a Gaussian probability distribution of 2 nm width. A certain degree of disorder is introduced by a one-dimensional paracrystal particle distribution. The calculations are carried out in the framework of DWBA with size-space coupling approximation at  $\lambda = 0.207$  nm and  $\alpha_i = 0.8^\circ$ .

Depicted in Fig. 4.5a is the calculated GISAXS pattern of non-specular scattering. GTRs as well as the Ewald sphere intersection can be observed. Small radial-symmetric oscillations are faintly visible throughout the image on the logarithmic scale. These are only numerical artefacts of the structure factor calculation due to the finite number of discrete scattering angles in the simulation. Again, an  $I(q_y)$  profile is averaged and extracted along the semi-circle in the same way as before and the Fourier transform is carried out. Figure 4.5b shows the resulting PSD of the simulated profile Fourier transform. The three distinct peaks are fitted using Gaussian functions, the peak centre positions are found at correlation lengths of 245 nm, 587 nm and 832 nm (peak width  $\sigma = 9$  nm in all cases). Comparison with simulation parameters for box width, groove width, and pitch length of 250 nm, 583 nm and 833 nm (dashed lines), respectively, shows close agreement of peaks and simulation parameters well within the peak widths. As expected, the third peak appears very close to 833 nm without any scaling.

### 4.1.6 Energy series from 4.5 keV to 9 keV

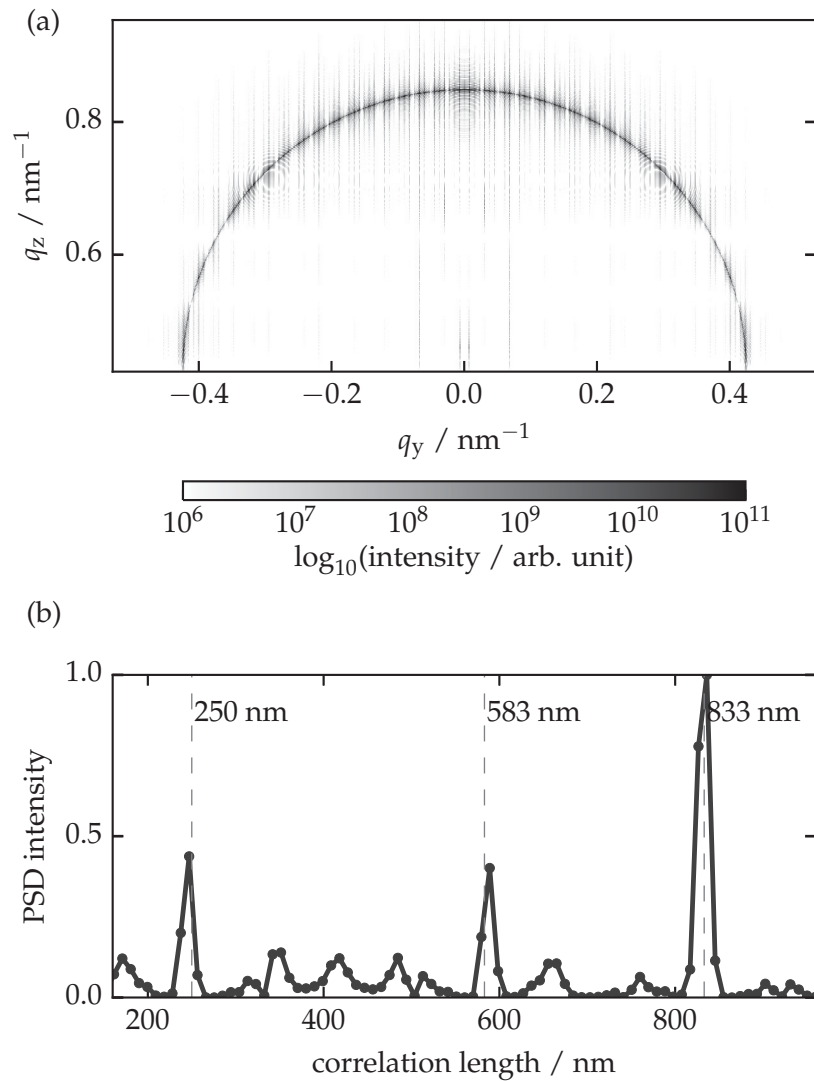
The question for some general recommendations in regard to the selection of a photon energy for the measurements remains. For that purpose, the DFT analysis algorithm described in Section 4.1.4 is applied to test data of ideal  $I(q_y)$  profiles in order to evaluate the photon energy dependent characteristics.

The test data are sums of three cosine functions of the form

$$f_{\cos}(N_x, E_{\text{ph}}) = \cos\left(\frac{2\pi}{CD}E_{\text{ph}}N_x\right) + \cos\left(\frac{2\pi}{G}E_{\text{ph}}N_x\right) + \cos\left(\frac{2\pi}{P}E_{\text{ph}}N_x\right) \quad (4.5)$$

as shown in Fig. 4.6a to emulate an idealised  $I(q_y)$  profile analogous to Fig. 4.3b that contains only the frequency contributions of the critical dimension, the groove width, and the pitch of an ideal grating. The cosine periods in Eq. (4.5) correspond to  $CD=292$  nm and  $G=542$  nm of grating field 'A' as listed in Table 4.2, respectively, and to the pitch of 833 nm. The index of the independent variable  $N_x \in (1, 2, \dots, 800)$  represents the equidistant data point index with the length of a typical  $I(q_y)$  profile, e.g. Fig. 4.3b. The arguments of the cosines also depend on the photon energy  $E_{\text{ph}}$  to vary the  $q$  resolution

**Figure 4.5** | Simulation of scattering by a grating structure using IsGISAXS with a 1D-paracrystal model. (a) Calculated two-dimensional GISAXS pattern. (b) PSD of the  $I(q_y)$  profile that has been obtained by averaging and extraction along the Ewald sphere intersection. Vertical dashed lines indicate the model parameters for the box width  $2R = 250$  nm, the interference function peak position  $D = 833$  nm and the groove width  $G = D - 2R = 583$  nm.



and  $q$  range while keeping the same number of data points in the same way as it is the case for measured data profiles at fixed geometry as in Fig. 4.3. Consequently, the  $q$  range probed increases and the  $q$  resolution per pixel decreases with increasing photon energy, the former is obvious from the increasing profile length in Fig. 4.6a. Displayed in Fig. 4.6b are PSDs of test data profiles at photon energies from 4.5 keV to 9 keV, obtained by the same analysis algorithm that was used in the previous sections. Each PSD has been normalised to the peak amplitude of the highest peak for better comparability. As expected, the PSD peak positions are fully congruent with the corresponding cosine function period  $CD$ ,  $G$ , and  $P$ , respectively. The important point here is that the PSD peak widths get narrower with increasing photon energy, which is clearly visible for all peaks in Fig. 4.6a. This is due to the increased  $q$  range probed at higher  $E_{\text{ph}}$ , which results in a smaller bin size in DFT and thus in narrower peaks. However, the peak centre position does not change throughout the photon energy variation, which is another validation of the presented DFT-PSD analysis algorithm. Thus, the photon energy should be selected as high as possible to obtain the narrowest PSD peaks possible due to the large  $q$  range probed. At the same time,  $E_{\text{ph}}$  must be low enough to allow for the clear separation of adjacent GTR peaks on the detector. Otherwise, the  $q$  resolution per pixel is too low to resolve the oscillation due to the pitch in the intensity profile and, thus, results in the absence of a pitch peak in the PSD.

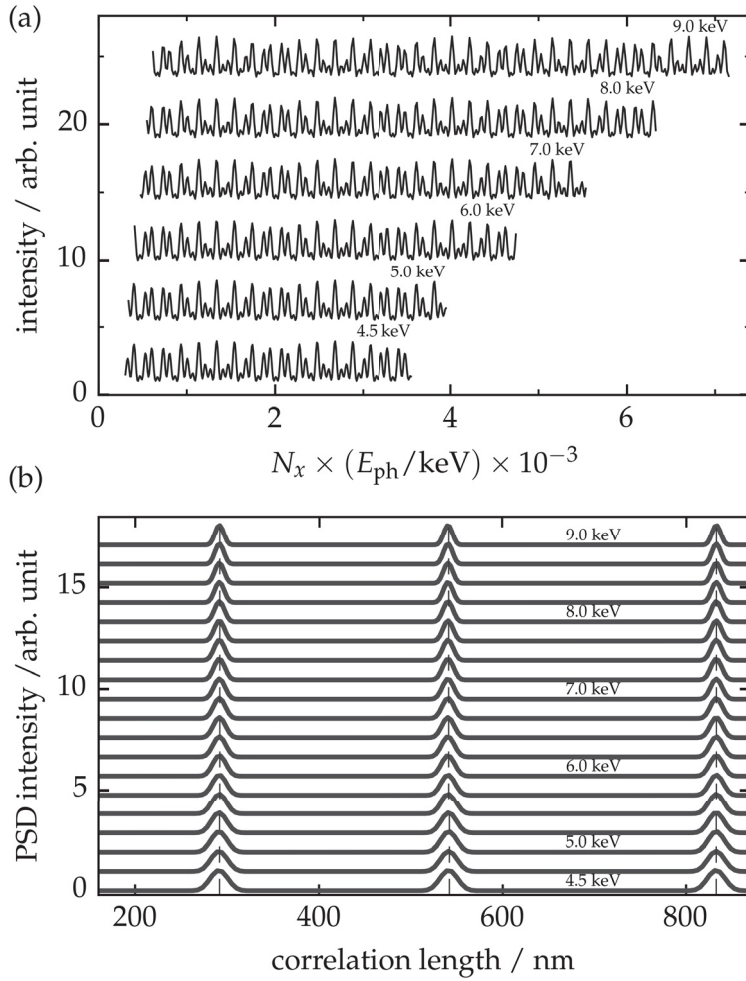


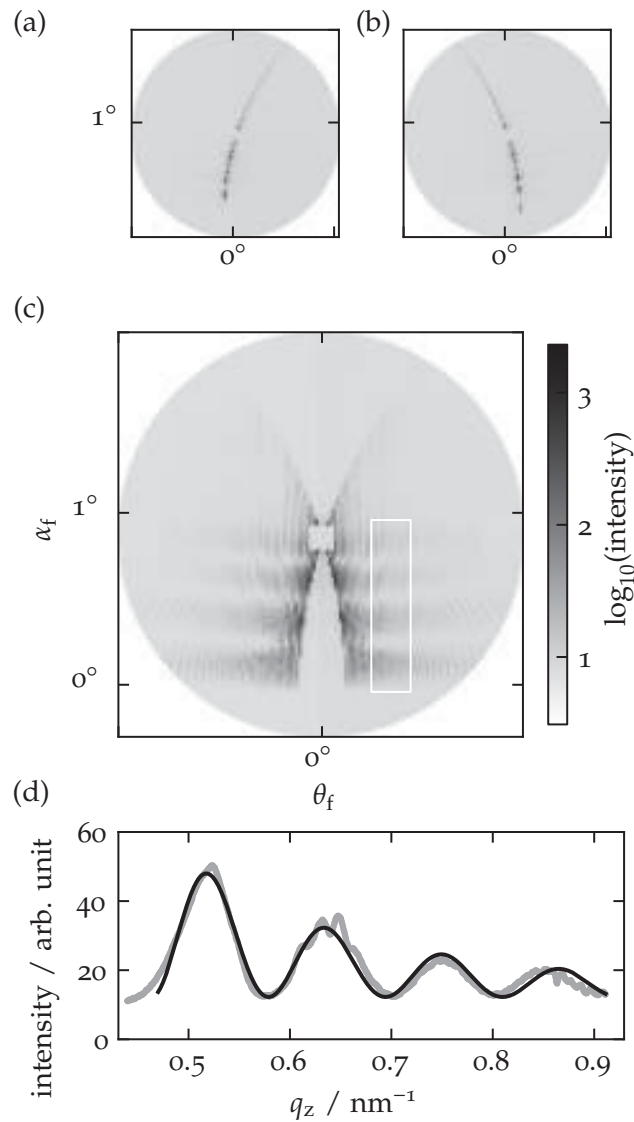
**Figure 4.6** | Test data and corresponding PSDs for different photon energies  $E_{ph}$  from 4.5 keV to 9 keV to evaluate the influence of  $E_{ph}$  on the PSD peaks (data profiles and PSD were shifted vertically for clarity). (a) Test data consisting of sums of three cosine functions, Eq. (4.5), representing the oscillation frequencies of  $CD=292$  nm,  $G=542$  nm, and  $P=833$  nm (sample A, Table 4.2) of the  $I(q_y)$  profile of an ideal line grating, analogous to Fig. 4.3b. The abscissa  $N_x \times E_{ph}$  of the data point index  $N_x \in (0, 1, \dots, 800)$  multiplied with  $E_{ph}$  is proportional to  $q_y$  in Fig. 4.3b. (b) PSDs of the test data. Dashed lines indicate the input parameters  $CD$ ,  $G$ , and  $P$ .

#### 4.1.7 Rotation around the surface normal vector

Another set of GISAXS measurements has been performed by the rotation of the gratings around the surface normal vector close to the parallel orientation of grating lines from  $\varphi = -2.50^\circ$  to  $2.50^\circ$ , which is similar to powder-diffraction averaging. Depicted in Fig. 4.7 are measured GISAXS patterns of different azimuthal orientations, more specifically at the maximum distortion angles of  $\varphi = 2.50^\circ$ , Fig. 4.7a, and  $\varphi = -2.50^\circ$ , Fig. 4.7b. GTRs are aligned along a hyperbola due to the geometric distortion, their positions can be calculated in the same framework as for perfect parallel alignment.<sup>[264]</sup> Figure 4.7c shows the superposition of all 101 individual GISAXS images for each angle in the rotation range  $\varphi$  using a step width of  $\Delta\varphi = 0.05^\circ$  at  $E_{ph} = 6$  keV and  $\alpha_i = 0.8^\circ$ . As a result of the superposition, horizontal Bragg sheets parallel to  $q_y$  and periodically repeated along  $q_z$  become visible. This is again a surface scattering effect, which can be seen by the intensity distribution of the sheets well below the critical angle of  $\alpha_c = 0.66^\circ$  down to the sample horizon. Each individual image represents the scattering pattern of a well-ordered system with the same shape. Hence, the periodicity of Bragg sheets represents the form factor and is primarily a measure of the morphological parameter of line height  $H$ .\* It may be noted that the superimposed image in Fig. 4.7c can equivalently be described by scattering from an effective surface layer of width  $H$  without the presence of refraction

\* The  $q_z$  modulation of the Bragg sheets is also influenced by other structural features such as side wall angle, roughness, etc., but these contributions are usually minor and can be disregarded here.

**Figure 4.7** | GISAXS of the azimuthally rotated grating close to parallel orientation ( $\varphi = 0^\circ$ ), recorded at  $E_{\text{ph}} = 6$  keV,  $\alpha_i = 0.8^\circ$ . GISAXS patterns at (a)  $\varphi = 2.50^\circ$  azimuthal angle and (b)  $\varphi = -2.50^\circ$ . (c) Superposition of 101 individual GISAXS images, each rotated by  $\Delta\varphi = 0.05^\circ$  with respect to its predecessor in the range of  $\varphi = -2.50^\circ$  to  $2.50^\circ$ . The white box indicates the averaging range of the extracted vertical intensity profile  $I(q_z)$  shown in (d). The profile has been fitted by a Bessel function of first order (black solid line) to determine a grating line height of  $H = 27.3$  nm.



for the same reason as described above. The box in Fig. 4.7c indicates the range of the averaged and extracted  $I(q_z)$  profile, which is displayed in Fig. 4.7d. The intensity of the profile along  $q_z$  is averaged horizontally inside the box. The  $I(q_z)$  profile has been fitted by a Bessel function of first order of the form  $J_1(x)/x$  (black solid line in Fig. 4.7d) to account for the form factor of the set of scattering images. A Bessel function of first order is the Fraunhofer diffraction pattern of a circular aperture (Airy disk) and is used as a form factor model. A height of  $H = 27.3$  nm has been determined from the period of the functions, which is close to the nominal etching depth of 26.6 nm as stated by the manufacturer.

## 4.2 Intermediate pitches from 100 to 300 nm: Fourier amplitude fitting using Tikhonov regularisation

After the rather large structure sizes of the previous section, which are challenging especially in terms of  $q$  resolution, the focus is now on ‘real’ nanostructures around and below 100 nm. Such structures possess a high relevance in science as well as in industrial applications. Consequently, the reliable and accurate dimensional characterisation is crucial for any field of interest. One of the main driving forces in industrial applications is the semiconductor industry, in particular the extreme ultraviolet (EUV) photolithography for next-generation wafer patterning at a wavelength of around 13 nm ( $E_{\text{ph}} \approx 90$  eV). The International Technology Roadmap for Semiconductors (ITRS),\* the common research strategy paper of the world-leading semiconductor industry associations, identifies the development and advancement of suitable dimensional metrology beyond the current 22 nm device fabrication process step as one of the key challenges in future technology development. Such nanometrology tools must offer non-destructive measurements within a short time that can be used *in-situ* along the fabrication line and with single-digit nm accuracy,<sup>[117,134]</sup> for example for mask inspection. Surface scattering techniques such as GISAXS and (E)UV scatterometry offer fast and non-invasive measurements of structural parameters in the nm range, which fulfils some of the core requirements of industrial EUV lithography tools. Thus, on the one hand, it is important to study the techniques themselves as tools for dimensional nanometrology of the critical dimension (CD) of structures, e.g. in terms of accessible parameters and uncertainties. On the other hand, GISAXS and scatterometry can be applied to analyse and improve the fabrication process of nanostructures, e.g. in electron beam lithography.

The work presented in this section continues to deal with the determination of structural grating parameters such as  $CD$ ,  $G$ ,  $H$ , and  $P$  by direct GISAXS data analysis, thus circumventing the postulation of a specific form factor for the line shape, as before. With decreasing structure size, the number of GTRs intersecting the Ewald sphere also decreases. Moreover, the measurements presented here have been recorded using the in-vacuum PILATUS 1M detector, which exhibits discontinuities in the intensity profiles extracted along the intersection due to gaps between detector modules. Both conditions necessitate a different Fourier analysis method, in particular because DFT fails in the case of a non-uniform data distribution, as discussed in Section 2.6. Instead, the direct GISAXS data analysis method of Fourier amplitude fitting using Tikhonov regularisation is developed and implemented in this section.

Parts of this work were published in V. Soltwisch, J. Wernecke, A. Haase, J. Probst, M. Schoengen, M. Krumrey and F. Scholze: ‘Nanometrology on gratings with GISAXS: FEM reconstruction and Fourier analysis’, *Proc. SPIE* vol. 9050. (2014), p. 905012.

---

\* <http://www.itrs.net>

### 4.2.1 Project framework and samples

The GISAXS measurements and analysis were embedded in the framework of the European Metrology Research Programme (EMRP) IND17 Scatterometry project ‘Metrology of small structures for the manufacturing of electronic and optical devices’. The main goals of this Joint Research Project are

- the development of advanced scatterometry from deep ultraviolet (DUV) to X-ray wavelengths with the goal of traceability in dimensional measurements of sub- $\mu\text{m}$  and nm-sized surface structures;
- the further development of high resolution SEM and AFM by establishing traceability and pitch measurements over long ranges with sub-nm accuracy;
- the comparison of dimensional parameters obtained using AFM, SEM and scattering techniques (DUV, EUV, GISAXS);
- the improvement and development of algorithms for the data evaluation and numerical modelling of the inverse problem in scattering; and
- the development of scatterometry reference standards, in particular with the perspective of a common ‘golden reference standard’ for scatterometry, AFM, and SEM.

The samples were prepared at the Institute for Nanometre Optics and Technology\* of the HZB. The sample layout, see Fig. 4.8, was optimised to support the different measurement systems and their individual requirements. For the GISAXS experiments, a grating field of  $(15 \times 1) \text{ mm}^2$  was prepared via electron beam lithography, the grating lines are aligned in the direction of the longer axis. This allows to fit the full beam footprint onto the grating structure to prevent the occurrence of scattering from the blank substrate. The silicon substrate was spin coated with ZEP520A,<sup>†</sup> a positive electron beam resist. Electron beam lithography was performed using a Vistec EBPG5000+, which operates at an electron acceleration voltage of 100 kV. After resist development, the grating was etched into the silicon substrate using reactive ion etching, using the etching gases  $\text{SF}_6$  and  $\text{C}_4\text{F}_8$ . This etching process was thoroughly optimised beforehand with regard to an optimal sidewall angle, surface and line edge roughness as well as a high selectivity between silicon substrate and resist. Finally, the remaining organic polymer resist was removed by an oxygen plasma treatment. Different samples with pitches ranging from 50 nm to 250 nm and critical dimensions from 25 nm to 150 nm were fabricated. The notation of the samples follows the scheme ‘ $Px/CDy$ ’, where  $x$  denotes the grating pitch  $P$  in nm and  $y$  the  $CD$  in nm.

GISAXS measurements were carried out at the FCM beamline in conjunction with the HZB SAXS instrument and the in-vacuum PILATUS 1M detector as described in Chapter 3. In addition, XRR measurements were performed at the SX700 beamline in the PTB laboratory at BESSY II.<sup>[213,214]</sup> The SX700 beamline is a bending magnet beamline using a plane grating monochromator that covers a photon energy range from 35 eV to 1850 eV. The beamline is primarily used for EUV reflectometry and scatterometry.

\* contact: max.schoengen@helmholtz-berlin.de, juergen.probst@helmholtz-berlin.de. <sup>†</sup> commercial product of ZEON Corporation, Japan

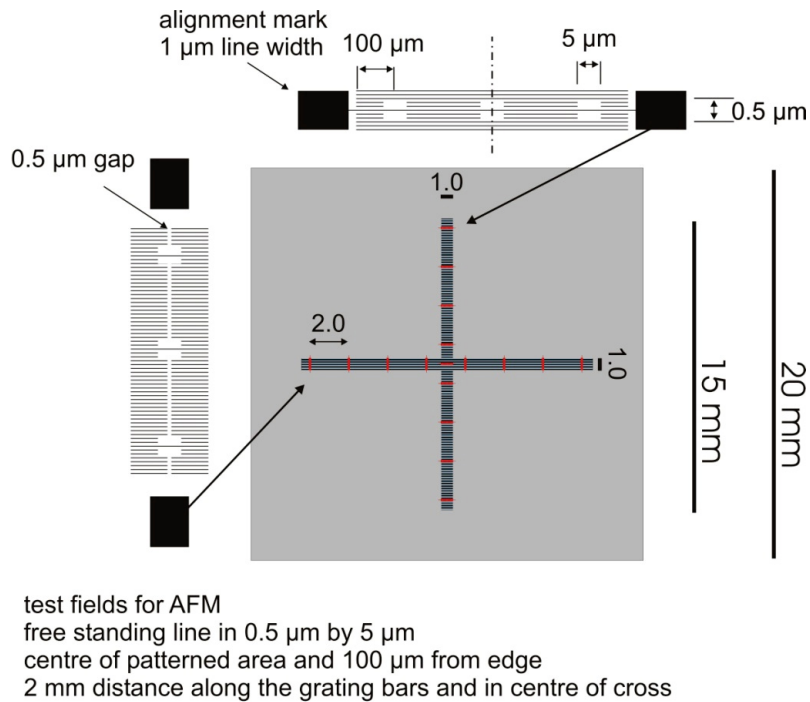


**Figure 4.8** | Scheme of the sample layout. The grating lines inside the horizontal bar with a length of 15 mm is used for GISAXS measurements. The sample contains a large number of position markers for other measurement methods, such as AFM.

## 4.2.2 GISAXS data analysis

The previously shown approach of DFT analysis of the  $I(q_y)$  profile along the semi-circular intersection of Ewald sphere and reciprocal grating representation becomes unstable here for several reasons: (i) As the structure sizes decrease, the spacing between the diffraction order increases. Consequently, the signal extracted from the detector image contains fewer periods, which results in less pronounced peaks in the DFT-PSD. (ii) The GISAXS images were recorded using the in-vacuum PILATUS 1M detector, which consists of 10 individual detector modules, as described in Section 3.5. The gaps between the detector modules cause discontinuities in the extracted  $I(q_y)$  profiles. In other words, the signal to be analysed is non-uniformly distributed. DFT, however, requires uniformly binned data for a correct transformation (Section 2.6).

The impact of the first issue can only be minimised by an increase in photon energy and/or incidence angle. Upper limits are imposed by the loss in  $q$  resolution at photon energy increase, i.e. largest correlation length to be resolved, and by the total  $q_y$  range that is possible to cover with the detector area. The detector gaps could be bridged by recording images in the same scattering configuration, but at different vertical and horizontal positions of the detector. The two images are brought in congruence and the resulting 'stitched' image is free of horizontal gaps, provided the vertical displacement distance exceeds the gap height. While this approach is useful and easy in many cases, it is error-prone or not applicable when the scattering pattern changes due to beam fluctuations, sample degradation or when a large number of images has to be recorded. For this reason, a different frequency analysis method is implemented here that can handle non-uniformly spaced data. This is realised by a best fit optimisation of the amplitudes of a finite basis of Fourier coefficients with the help of Tikhonov regularisation.<sup>[236]</sup> The implementation of the method is described in detail in Section 2.6.

### 4.2.3 XRR results of line height and capping layer thickness

XRR measurements on the grating lines and on a structureless region of the samples were carried out to determine the height of the grating lines and the thickness and composition of the capping layer. The measurements were performed at the SX700 beamline, which gives access to photon energies around the oxygen K-absorption edge at 543.1 eV and also to the target wavelength of 13.4 nm (92.5 eV) of EUV lithography. Measuring the reflectance in resonance around the oxygen K-edge enables the separation of the silicon substrate and a silicon oxide layer as well as to identify small carbonaceous contaminations due to the significant change in the optical constants of the SiO<sub>2</sub> at the absorption edge.<sup>[129]</sup>

For the characterisation of the capping layer, several XRR scans at five different photon energies from 530.0 eV to 551.6 eV were carried out on a featureless substrate region of the sample P250/CD100, the curves are displayed in Fig. 4.9a. All reflectance curves (solid lines) were simultaneously fitted using common parameters for thickness and roughness by the Parrat formalism analogous to Eq. (2.36) with Névot-Croce roughness<sup>[170,190,203]</sup> and a two-layer model (contamination layer – silicon oxide layer – silicon substrate). As best fit values, a carbonaceous contamination layer thickness of 0.3 nm and a silicon oxide layer thickness of 5.4 nm was obtained. The oxide layer thickness (also confirmed by scatterometry<sup>[59]</sup>) is considerable, given that a natural oxidation layer on top of a silicon substrate usually has a thickness of around 1 nm. XRR measurements on substrates from different stages of lithographic treatment clearly showed that a thick oxide layer occurs after the final step of residual resist removal by oxygen plasma etching. The oxygen plasma also causes an increased oxidation of the silicon, especially because of the large surface area of the lines.

XRR measurements on the lines of the P250/CD100 grating, Fig. 4.9b, show the typical oscillations due to constructive and destructive interference of reflections from the top and the bottom of the grating lines. The period length of  $\Delta q_r = 0.055 \text{ nm}^{-1}$  corresponds to a real-space correlation length  $2\pi/\Delta q_r$  of 114 nm, which can be identified as the line height.

### 4.2.4 GISAXS grating parameter determination

GISAXS measurements at photon energies ranging from 3 keV to 10 keV were performed at the FCM beamline. Scattering images were recorded using the in-vacuum PILATUS 1M detector mounted on the HZB SAXS instrument. The sample-detector distance  $L_s$  was determined by observing the specular spot positions at different incidence angles and at a large number of detector positions, monitored by Heidenhain optical encoders with  $\mu\text{m}$ -precision as described previously. In this way, a sample-detector distance of  $L_s = (3221 \pm 10) \text{ mm}$  was determined. In conjunction with the pixel size  $L_{\text{px}}$  of  $(172.1 \pm 0.2) \mu\text{m}$ , see Section 3.5.3, the conversion from units of horizontal detector pixel pitch to the change in  $q_y$  per pixel can be determined to

$$\Delta q_y|_{\text{px}} = \frac{2\pi e}{hc} E_{\text{ph}} \frac{L_{\text{px}}}{L_s} . \quad (4.6)$$

With the relative uncertainties of the sample-detector distance  $u(L_s)/L_s = 3 \times 10^{-3}$ , the pixel pitch  $u(L_{\text{px}})/L_{\text{px}} = 1 \times 10^{-3}$  (Eq. (3.4)), and the photon energy  $u(E_{\text{ph}})/E_{\text{ph}} = 0.08 \times 10^{-3}$

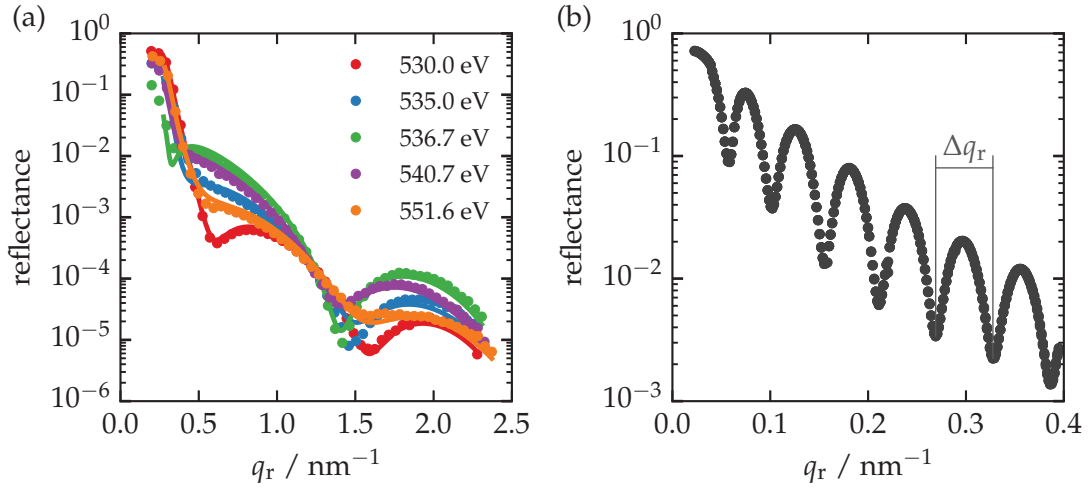


**Figure 4.9** | XRR measurements on a sample, carried out at the SX700 beamline. (a) Reflectance data (dots) and fits (lines) using common parameters for layer thickness for photon energies close to the oxygen K-absorption edge. The high scattering contrast at the absorption edge enables a separate thickness determination of a  $\text{SiO}_2$  capping layer (5.4 nm) and a carbonaceous contamination layer (0.3 nm). (b) Reflectance curve measured at  $E_{\text{ph}} = 92.5$  eV on the lines of the P250/CD100 grating. The oscillation period  $\Delta q_r$  results from the top and bottom surface interference and corresponds to a line height  $l_T = 2\pi/\Delta q_z$  of 114 nm.

(Table 3.2), the relative uncertainty of  $\Delta q_y|_{\text{px}}$  yields

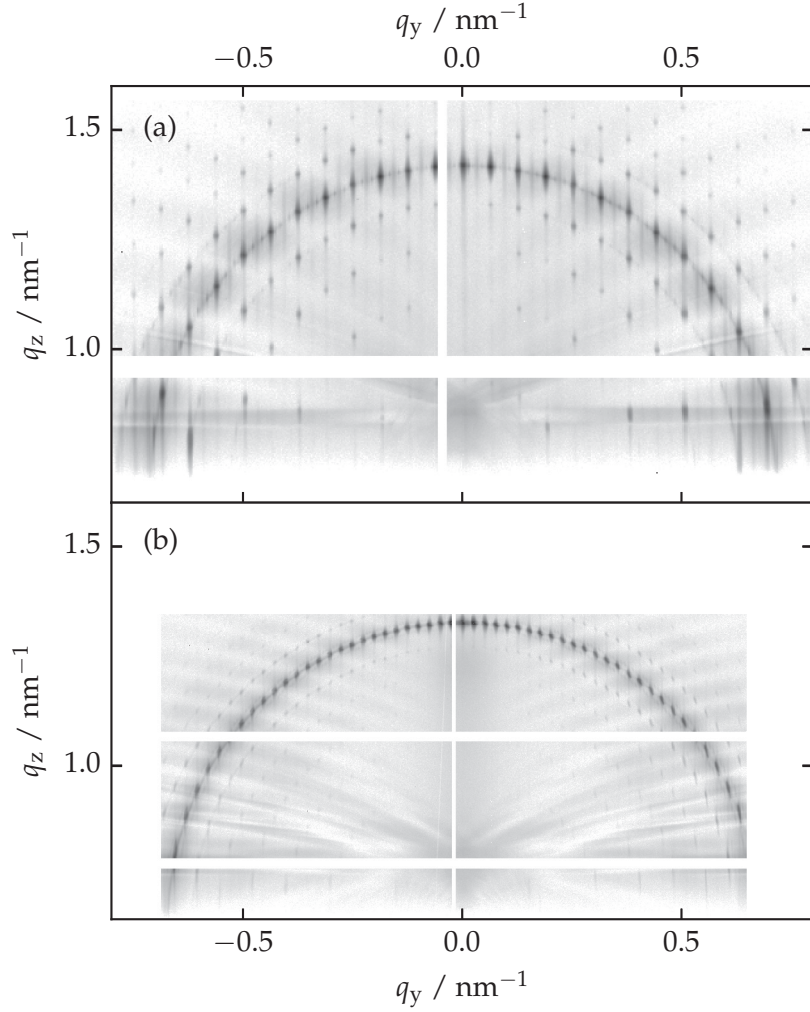
$$\frac{u(\Delta q_y|_{\text{px}})}{\Delta q_y|_{\text{px}}} = \sqrt{\sum_i \left( \frac{u(p_i)}{p_i} \right)^2} = 3.3 \times 10^{-3}. \quad (4.7)$$

Displayed in Fig. 4.10 are two typical GISAXS images (a) of the P100/CD50 grating and (b) of the P250/CD100 grating in parallel orientation of incident beam and grating lines. In addition to the semi-circular Ewald sphere intersection with the GTR orders as the main feature of the detector images, many other diffuse scattering features are visible. These features are highly complex and are strongly correlated with the specific morphology of the grating, i.e. top/bottom corner rounding, sidewall angle, capping layer, CD, etc. This cannot be assessed by simple Fourier analysis or geometric considerations, but must be systematically analysed by full two-dimensional modelling using arbitrary form factors for the line cross section, as described briefly in the outlook.

Coming back to a direct analysis of the GISAXS patterns, the intensity profile along the semi-circular intersection of Ewald sphere and GTR in the scattering patterns is extracted and converted from pixel coordinates to  $q_y$  coordinates according to Eq. (4.6). As before, the goal of the analysis is to determine the frequencies that are present in the oscillating intensity profile as shown in Fig. 4.11a and Fig. 4.12a. These frequencies correspond to characteristic scattering lengths, i.e. pitch  $P$  and critical dimension  $CD$ . Again, this is done by Fourier analysis of the extracted intensity profile. But, as initially discussed, a standard DFT is not possible here due to the discontinuities in the signal originating from the gaps between neighbouring detector modules.

The implemented method of Fourier amplitude fitting using Tikhonov regularisation is described in detail in Section 2.6. As explained there, the basis forms a coefficient matrix  $\hat{A}$  containing the Fourier coefficient amplitudes, the vector  $\vec{y}$  of the GISAXS  $I(q_y)$  data, and the coordinates of the Fourier transform space, termed  $\vec{x}$  in Eq. (2.53). The equation

**Figure 4.10** | GISAXS images of (a) P100/CD50 and (b) P250/CD100 gratings in parallel orientation of incident beam and grating lines. Both images are displayed using the same scaling of  $q_y$  and  $q_z$  for better comparability.



(cf. Eq. (2.51))

$$\hat{A}\vec{z} - \vec{y} \approx \vec{0} \quad (4.8)$$

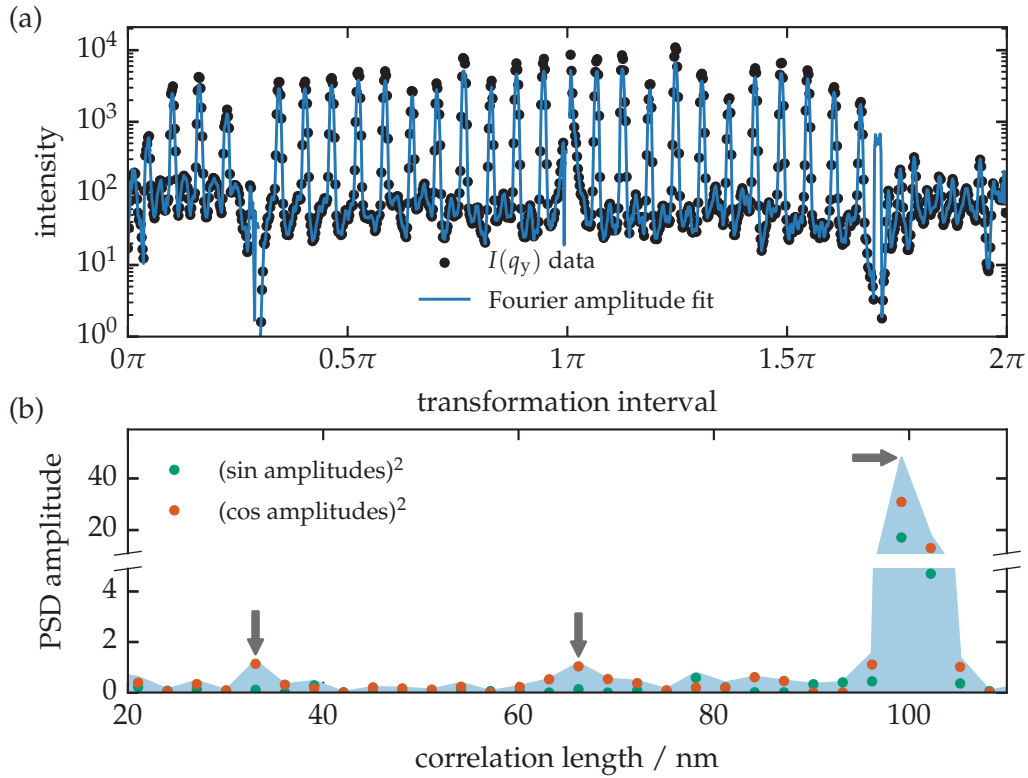
is solved, i.e. best-fit optimised, by Tikhonov regularisation and least-squares optimisation to obtain the solution vector of the Fourier amplitudes  $\vec{z}$ . The optimal regularisation parameter  $h_T$  of all examined profiles is determined by the L-curve (cf. Fig. 2.16) to  $h_T = 0.11$ .  $\hat{A}_{h_T}$  and  $\vec{z}$  represent the best fit of the intensity profile by the finite Fourier series. Displayed in Fig. 4.11a is the measured intensity profile (black dots) of the P100/CD35 grating along with the reconstruction from the optimised Fourier coefficients (blue line). The Fourier reconstruction is in close resemblance with the data.

Figure 4.11b shows the squares of the amplitudes of the Fourier coefficients, i.e. the elements of  $\vec{z}$ , which are equivalent to the PSD of the intensity profile. Green dots indicate the amplitudes of the sine coefficients, orange dots that of the cosine coefficients and the colour-shaded area is the sum of the two parameters. It can be seen that PSD peaks appear mainly due to the cosine amplitudes. The abscissa of the PSD has been converted from Fourier space frequencies  $f_F$  to real-space correlation lengths  $\Lambda$  by

$$\Lambda = f_F \times \frac{1}{N_{\text{data}} \Delta q_y |_{\text{px}}} \quad (4.9)$$

A characteristic peak is found at  $\Lambda = 99$  nm, which corresponds to the nominal pitch of the grating. Two smaller peaks, indicated by arrows, appear at 32 nm and 68 nm, which

can be identified as  $CD$  and  $G$ , respectively. The influence of the regularisation parameter  $h_T$  on the pitch peak position has been controlled. A variation of  $h_T$  within a numerically meaningful range of  $1 \times 10^{-5}$  to 2 resulted in no detectable shift of the peak position, which means that the corresponding uncertainty is well below 1 nm. This example of a grating with incommensurable  $CD$  and  $G$  illustrates that the GISAXS Fourier analysis is capable of a simultaneous and consistent determination of pitch, critical dimension, and groove width from a single image. The same procedure is applied to the GISAXS data of other gratings.



**Figure 4.11** | Fourier analysis of the P100/CD35 grating. (a) Extracted intensity profile along the Ewald sphere intersection (black dots) and reconstruction of the signal using the best fit Fourier coefficients (blue line). (b) PSD of the reconstructed profile as a function of correlation length. The colour-shaded area indicates the sum of the squares of sine coefficient amplitudes (green dots) and cosine coefficient amplitudes (orange dots). Arrows indicate positions of characteristic correlation lengths that can be attributed to  $CD$ ,  $G$ , and  $P$ .

In principle, the relative uncertainty of the PSD peak positions is determined by the uncertainty of the conversion from pixel to  $\text{nm}^{-1}$  and should thus be  $3.3 \times 10^{-3}$  in accordance with Eq. (4.7). However, the relative variations of the PSD peak positions for different data sets on the same grating structure were within a range of  $\pm 2 \times 10^{-2}$ . This value can be seen as an upper limit estimate of the uncertainty of the determined PSD peak positions.

Displayed in Fig. 4.12 are the same plots as in Fig. 4.11 of the  $I(q_y)$  data and optimised Fourier coefficients as well as the corresponding PSD of the P250/CD100 grating. The pronounced peak at 250 nm can be identified as the grating pitch. A broad peak is visible at a centre position of 119 nm. From the nominal values, two peaks at around 100 nm and 150 nm corresponding to  $CD$  and  $G$  would be expected. It remains unclear whether the broad peak is a superposition of both correlation lengths or the result of an erroneous

lithographic writing process. The position and width of the peak could be reproduced in a range of different GISAXS images recorded at different incidence angles and photon energies. Results from other measurement methods are not available to date.

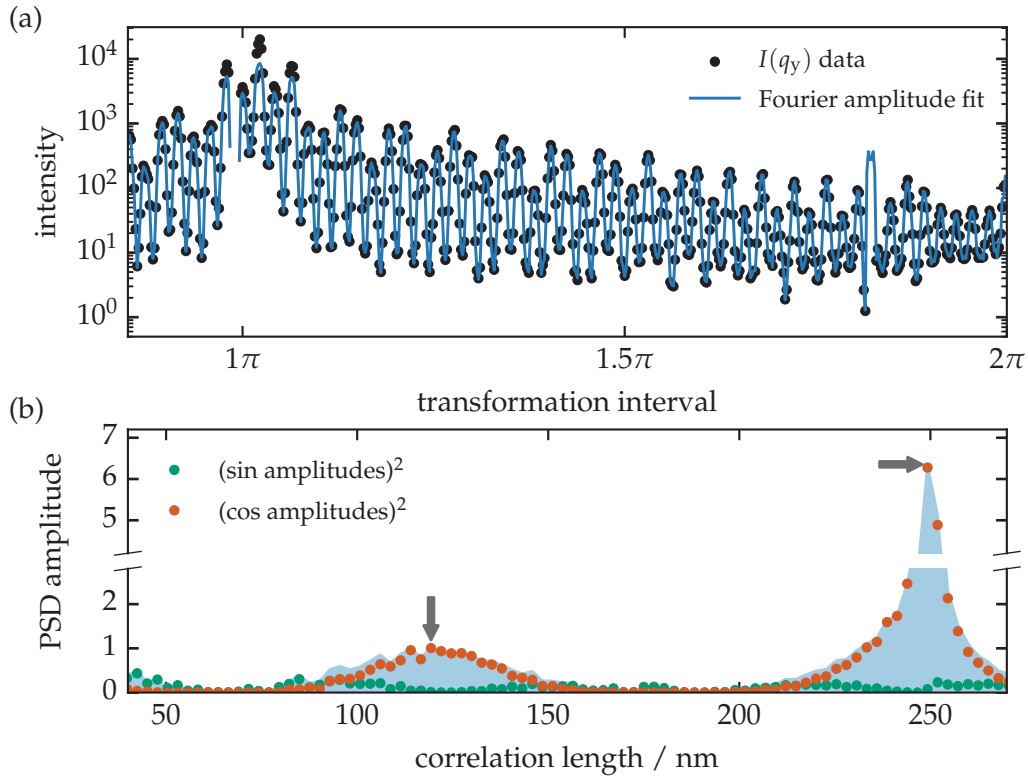


**Figure 4.12** | Analogous to Fig. 4.11 for the P250/CD100 grating. (a) Intensity data profile (black dots) and reconstruction (blue line). Only a part of the profile is shown to improve the visibility. (b) PSD of the reconstruction, i.e. squares of sine-coefficient amplitudes (green dots), cosine-coefficient amplitudes (orange dots) as well as their sum (colour-shaded area). The arrows indicate the PSD peaks that can be associated with CD and P.

### 4.2.5 Stitching period of electron beam lithography

Close examination of the GISAXS patterns, e.g. in Fig. 4.10, shows a large number of faint ‘satellite orders’ around the semi-circular main structure, which are located around the same origin, but with different radii. The radius of the Ewald sphere in  $q_y$  on the detector is only determined by  $L_s \tan \alpha_i$ , i.e. only by two geometric parameters. The satellite rings are by far too wide-spread on the detector to originate from a possible divergence in the incidence angle or from the difference in  $L_s$  at both ends of the extended beam footprint on the sample. Both has been excluded by measurements: The former by observation of a sharp specular reflection spot, the latter by shifting the sample or the detector along the axis of the incident beam. Moreover, the occurrence of such effects would not result in sharp satellite rings with well-defined radius variations, but rather as a smearing of the main semi-circle.

GISAXS detector images map not only the  $q_z$ - $q_y$  plane, but cover also a small range in  $q_x$ , as illustrated by Eq. (2.15). In the typical GISAXS configuration of several metres of distance between sample and detector and in the keV range, this change in  $q_x$  can usually be neglected as there are no distinct features present in the corresponding correlation

length range. However, if a GISAXS detector image recorded in parallel orientation such as the one shown in Fig. 4.10a is plotted as a  $q_x$ - $q_y$  intensity map as shown in Fig. 4.13 (note the scale of  $q_x$  in comparison to  $q_y$ ), it becomes apparent that the satellite orders are caused by a  $q_x$  modulation. The semi-circles are transformed to horizontal lines that are equidistantly spaced along  $q_x$ .<sup>\*</sup> The vertical spacing  $\Delta q_x$  of the lines corresponds to a real-space length of  $4.52 \mu\text{m}$ . A review of the writing process of the electron beam lithography machine revealed that the sample structure (Fig. 4.8) is generated by nanostructuring within areas of nominal  $(4.5 \times 4.5) \mu\text{m}^2$  that are joined line by line. Hence, the subtle changes from tile to tile cause a periodic modulation of the structure on the  $\mu\text{m}$  range. This is an instructive illustration of the different  $q$  ranges that are mapped with GISAXS at the same time. The periodicity in  $q_y$  of such a large structure is well beyond the resolution limit of the experimental setup, but the much smaller change in  $q_x$  in the order of  $10^{-3} \text{ nm}^{-1}$  along the detector gives direct access to the size regime without additional image recording or geometric changes. Moreover, the writing area size is a parameter that is not so easily obtained by other methods and it is new and valuable to know that it has a noticeable influence on the scattering, which is important for the design of optical devices, for example.

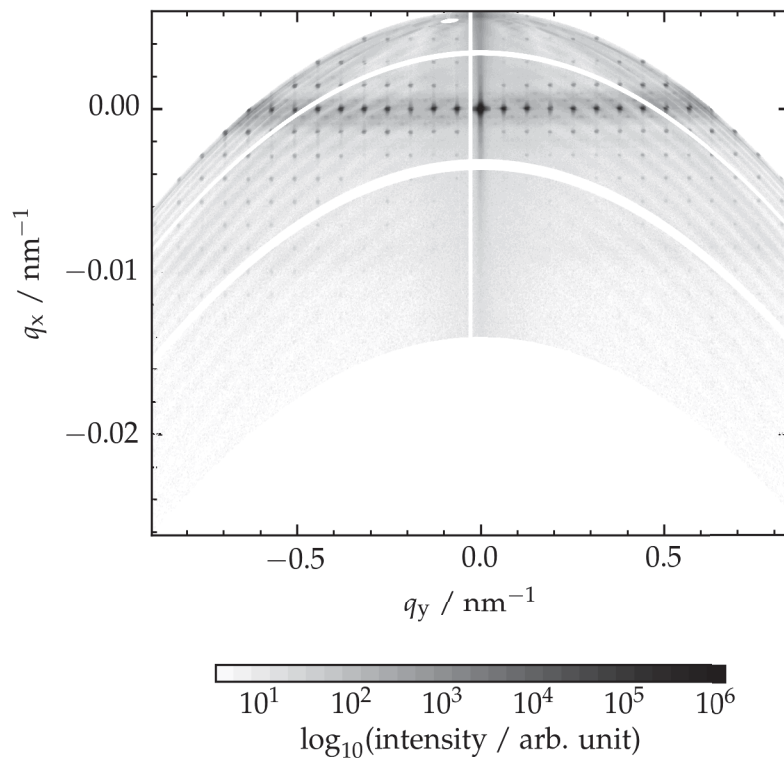


**Figure 4.13** |  $q_x$ - $q_y$  plot of a 'typical' GISAXS  $q_z$ - $q_y$  map such as the one shown in Fig. 4.10a. Please note the different scales of  $q_x$  and  $q_y$ .

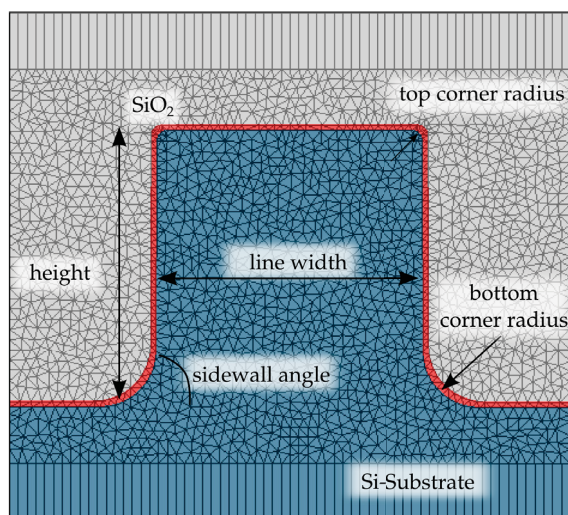
<sup>\*</sup> The horizontal spacing  $\Delta q_y$  of the maxima still corresponds to the pitch of 100 nm, of course.

## 4.2.6 Outlook: FEM reconstruction

Fourier analysis of the data has the advantage of yielding directly information on the structure factor, such as  $P$  and  $CD$ , without the need to introduce a complex and in detail not easily obtainable form factor of the grating lines. However, this limits the analysis to a small set of grating parameters. For a fundamental understanding of the rich set of features of the GISAXS patterns of gratings, e.g. visible in Fig. 4.10, as well as for the perspective of GISAXS as an advanced nanometrology tool in the next-generation microelectronics technology, it is of high interest to include a larger set of structural parameters. Consequently, the inverse problem needs to be solved by modelling of the full 2D scattering pattern (Section 2.4). The most common approach in GISAXS modelling is the semi-kinematic DWBA<sup>[94,192,208,220]</sup> which takes multiple scattering effects into account. A drawback of this approach is the limitation to analytically describable form factors, such as spheres, cylinders, trapezoids, boxes, etc. In the case of arbitrary shapes, an elaborate density slab model has to be implemented. For this reason, a different technique can be applied, which is the rigorous simulation of the electric field distribution of radiation scattered by an arbitrarily structured surface by solving Maxwell's equations. This is implemented by using the finite element method (FEM) Maxwell solver JCMsuite,<sup>[31]</sup> which incorporates a highly customisable cross-section shape, automatic computation of first- and second-order parameter derivatives, and fast algorithms for solving time-harmonic Maxwell equations.

The solver allows arbitrary form factors, which are constructed in a mesh grid. Figure 4.14 shows a typical mesh grid scheme for a line cross section. The form factor and, thus, the FEM reconstruction accounts for six structural parameters: Critical dimension, line height, sidewall angle, top corner radius, bottom corner radius, and thickness of an oxide capping layer.

**Figure 4.14** | A typical mesh layout used for FEM simulation of GISAXS pattern of a line grating.



First reconstructions in GISAXS geometry showed good agreement with the nominal values as well as with the Fourier analysis results.<sup>[25,224,225]</sup> The extensive study of the influence of changes to the model in terms of different parameter variations, e.g. corner rounding, line space/width roughness, and over-etching, is currently in progress to ultimately explain the entirety of different scattering features as well as to promote GISAXS as a high-throughput single-shot nanometrology tool, for example for EUV lithography wafer inspection.

## 4.3 Small pitches below 50 nm: Grating Truncation Rod distances

The gratings presented so far have been created by electron beam lithography and subsequent selective etching into the material. Another method of creating grating structures in the nanometre size regime is self-assembly of block copolymers (BCPs).<sup>[2,47,81]</sup> The emerging field of block copolymer lithography<sup>[10,47,79,80,82,180,226]</sup> strives to provide a broad tunability of shapes and compositions on length scales from a few to hundreds of nanometres at lower cost compared to conventional top-down techniques.

In this section, the first traceable GISAXS measurements are presented, demonstrated on a self-assembled BCP thin film grating with a nominal pitch of 25 nm. Only a few GTRs are intersecting the Ewald sphere at this pitch size, which makes a Fourier analysis by DFT or Tikhonov regularisation impossible and unnecessary. Instead, the ‘manual’ determination of GTR distances is carried out as a third variant of direct parameter determination of grating structures.

Parts of the work presented in this section were published in J. Wernecke, M. Krumrey, A. Hoell, R. J. Kline, H.-k. Liu and W.-l. Wu: ‘Traceable GISAXS measurements for pitch determination of a 25 nm self-assembled polymer grating’, *J. Appl. Cryst.* **47**. (2014), pp. 1912–1920.

### 4.3.1 Analysis method and validity

The grating pitch  $P$  can be extracted directly from GISAXS data without any semi-kinematic or dynamic modelling. Thus, for small angles, the grating pitch  $P$  can be determined in this simple picture by the grating equation, which is equivalent to the structure factor of a grating in reciprocal space<sup>[120,264]</sup>

$$P = \frac{n\lambda}{2 \cos \varphi \sin(\theta_f)_n}. \quad (4.10)$$

The wavelength  $\lambda$  and the azimuthal scattering angle  $(\theta_f)_n$  of the  $n$ -th order GTR can be expressed by the actual experimental input parameters photon energy  $E_{\text{ph}}$ , sample-detector distance  $L_s$ , detector pixel size  $L_{\text{px}}$ , and GTR distance  $d_{\text{GTR}}$ . Equation (4.10) can then be written as

$$P = \frac{m_e h c}{E_{\text{ph}}} \frac{1}{2 \cos \varphi \frac{d_{\text{GTR}} L_{\text{px}}}{L_s}}, \quad (4.11)$$

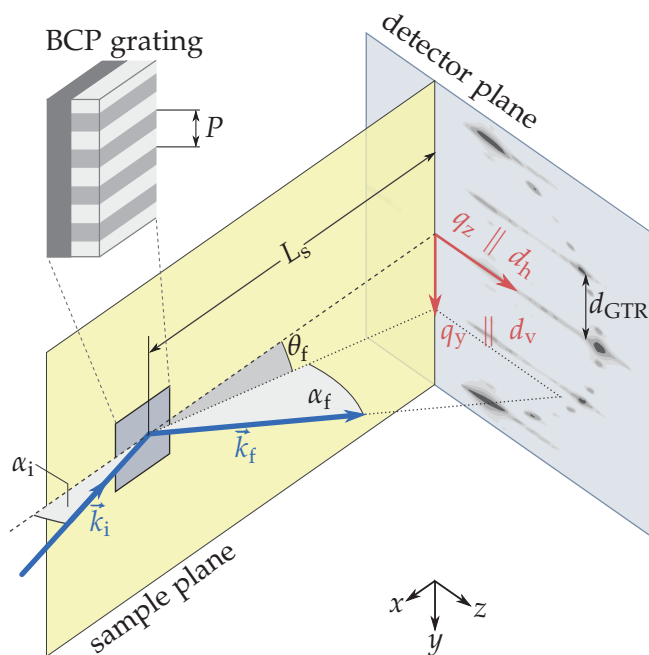
which is suitable for establishing traceability.

### 4.3.2 Materials and methods

Directed self assembly of a lamellar phase of polystyrene-poly(methyl methacrylate) block copolymer (PS-*b*-PMMA) on a (25 × 25) mm<sup>2</sup> silicon wafer was carried out via a frequency quadrupling process by the following procedure.\* A line grating template with a nominal pitch of 100 nm was prepared using 193 nm water immersion lithography, followed by the deposition of a neutralisation layer and a lift-off process. The PMMA blocks were etched off and the resultant PS line gratings possess a nominal pitch of 25 nm. Details of the sample preparation can be found in the literature.<sup>[37]</sup>

The GISAXS measurements were performed at the FCM beamline using the MarCCD X-ray area detector mounted on the HZB SAXS instrument as described in Section 3.2. Traceability of the energy scale has been established as described in Section 3.2 with the uncertainties listed in Table 3.2. Figure 4.15 shows the modified orientation and notation of the laboratory, the reciprocal space, and the detector coordinate systems. Note that the sample was mounted in an upright position to determine the GTR distances and pixel size along the traceable vertical direction. As a consequence, the  $q_z$  axis is parallel to the horizontal detector coordinate  $d_h$  to comply with the common orientation convention of the  $(q_x, q_y, q_z)$  coordinates.

**Figure 4.15** | Modified vertical GISAXS scattering geometry. The coordinates  $(x, y, z)$  denote the laboratory coordinate system,  $(q_x, q_y, q_z)$  the reciprocal space coordinates, and  $(d_h, d_v)$  the horizontal and vertical detector coordinates. The enlargement shows an illustration of the self-assembled block copolymer grating with a nominal pitch  $P$  of 25 nm.



Traceability of the pitch determination using GISAXS is established by tracing all input quantities of Eq. (4.11). Hence, the uncertainties of the sample-detector distance, the azimuthal angular misalignment from parallel orientation, the pixel size, and the GTR positions are discussed and evaluated in the next section. With these input parameters and corresponding uncertainty contributions, the grating pitch can be determined in a traceable way according to the *Guide to the Expression of Uncertainty in Measurement* (GUM).<sup>[16]</sup>

\* sample courtesy of J. Y. Cheng, IBM Almaden Research Center, CA.

### 4.3.3 Establishing traceability of the input parameters

#### Sample-detector distance

The HZB SAXS instrument is equipped with a Heidenhain encoder to measure the relative position of the detector along the  $x_{\text{det}}$  axis with  $\mu\text{m}$  precision, see Section 3.4 and Fig. 3.6. However, since the entire setup can be moved with respect to the beamline, it is necessary to determine the offset distance  $L_{\text{off}}$  between the sample and the position of the instrument to obtain the sample-detector distance  $L_s$  by  $L_s = L_{\text{off}} - x_{\text{det}}$  ( $x_{\text{det}}$  value decreases with increasing sample-detector distance). This is achieved by triangulation with the incoming X-ray beam. The incident beam is specularly reflected from the sample surface and impinges on the detector at a designated position  $(d_{\text{h,spec}}, d_{\text{v,spec}})$ . The vertical spot position  $d_{\text{v,spec}}$  is determined for different incidence angles  $\alpha_i = 0.15^\circ$  to  $0.65^\circ$  and at different relative detector positions to cover an  $x_{\text{det}}$  range of 1.6 m. Displayed in Fig. 4.16 are the measured spot positions (dots) for different incidence angles and detector positions. Then, the data are grouped by incidence angle and simultaneously fitted by linear functions that have individual parameters for the slope and a common intersection point  $(L_{\text{off}}, d_{\text{v,isp}})$ . The solid lines in Fig. 4.16 show the fit results. The intersection point position  $L_{\text{off}}$  indicates the offset distance under the assumption that the position of reflection on the sample surface is independent from  $\alpha_i$  and  $x_{\text{det}}$ , which was verified by visual observation. From the resulting values  $L_{\text{off}} = (4621 \pm 3)$  mm and  $x_{\text{det}} = (1797.704 \pm 0.005)$  mm, a sample-detector distance  $L_s$  of

$$L_s = (2823 \pm 3) \text{ mm} \quad (4.12)$$

is obtained.

It has to be noted that the geometric footprint of the beam along the incidence direction of  $V/\tan \alpha_i$  with a vertical beam size of  $V = 0.3$  mm is larger than the sample length of 25 mm. Hence,  $L_s$  is more precisely the distance between the sample rotation axis of  $\alpha_i$  and the detector surface. Yet, the term ‘sample-detector distance’ is still used here as it is the term that is the most familiar to most X-ray scattering users, but it should be understood according to the above definition.

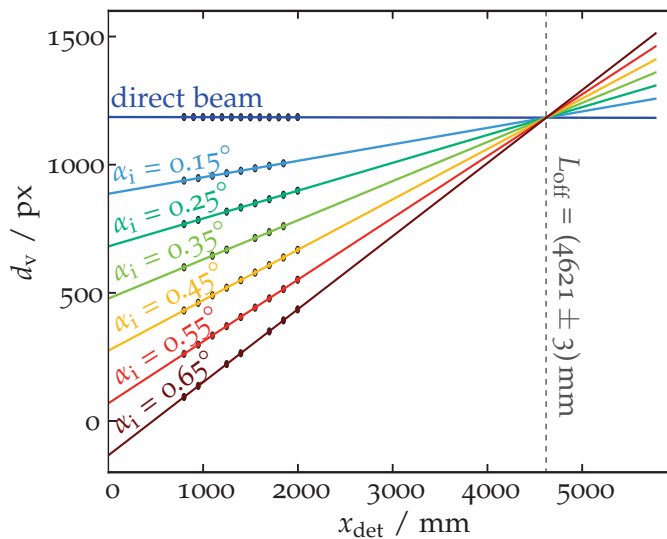


**Figure 4.16** | The vertical reflection spot positions (coloured dots) at different relative detector positions and different incidence angles  $\alpha_i$  were simultaneously fitted by linear functions with a common intersection point (solid lines).



the boxes remain fixed in size and position for every rotation angle. Within each box, a filter is applied to cut off the lowest 10% of counts inside the box to remove the detector background, cosmic radiation, and other weak irrelevant scattering features. A preliminary test showed that the GTR position varied within 0.5 px for a filter threshold between 5% and 95%. The effect of the filter on the GTR position is thus negligible. The intensity-weighted centre position  $(d_{h,cp}, d_{v,cp})$  of the GTR is determined for each evaluated box to find the diffraction peak position.

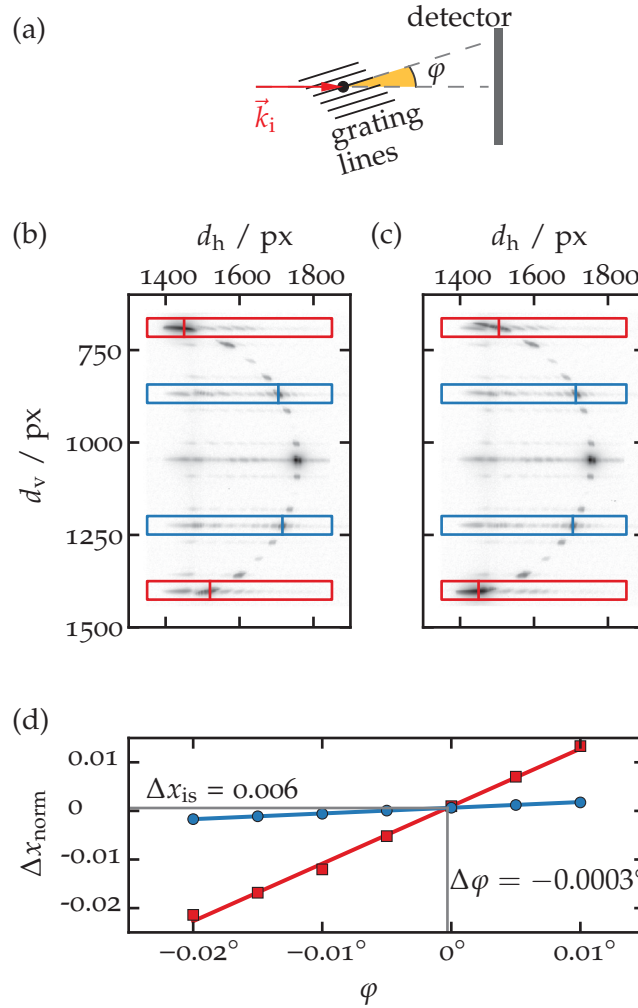


**Figure 4.18** | Evaluating the misalignment from parallel orientation of incident beam and grating lines. (a) Definition of the azimuthal tilt angle  $\phi$ . (b,c) GISAXS pattern of smallest and largest tilt angle  $-0.020^\circ$  and  $0.010^\circ$ , respectively. The boxes of GTRs  $\pm 2$  (red) and GTRs  $\pm 1$  (blue), as defined in Fig. 4.17, indicate the regions used to determine the intensity-weighted centre positions of the GTRs, which is indicated by the vertical line inside each box. (d) Plots of the horizontal top/bottom spot pair distances,  $\Delta x_{\text{norm}} = \frac{d_{h(\text{top})} - d_{h(\text{bottom})}}{d_{h(\text{top})} + d_{h(\text{bottom})}}$ , of GTRs  $\pm 2$  (red) and GTRs  $\pm 1$  (blue) as a function of  $\phi$ . The intersection  $\Delta \phi$  represents the misalignment from parallel orientation of beam and lines.

The misalignment was analysed via the diffraction peak positions  $d_{h,cp}$  of the GTR pairs  $\pm 2$  (red boxes in Figs. 4.17 and 4.18b,c) and  $\pm 1$  (blue boxes) and was determined throughout the rotation series. Parallel alignment of grating lines and incident beam is reached if  $d_{h,cp}$  of both spots of a GTR pair ( $\pm 2$ , and  $\pm 1$ , respectively) is equal, which means  $d_{h,cp \text{ top}} - d_{h,cp \text{ bottom}} = 0$ . In order to compare both GTR pairs, the difference is normalised by the sum of both positions,  $\Delta x_{\text{norm}} = \frac{d_{h,cp \text{ top}} - d_{h,cp \text{ bottom}}}{d_{h,cp \text{ top}} + d_{h,cp \text{ bottom}}}$ . The intersection of

$\Delta x_{\text{norm}}$  as a function of  $\varphi$  of GTR pair  $\pm 2$  and  $\pm 1$  yields the misalignment  $\Delta\varphi$  as well as the deviation from the perpendicular orientation of the sample surface and the detector  $\Delta x_{\text{is}}$  (Fig. 4.18d). The obtained values of  $\Delta\varphi = -0.0003^\circ$  and  $\Delta x_{\text{is}} = 0.0006$  illustrate that the detector is well aligned in terms of incident beam and grating lines as well as  $q_z$  being parallel to  $d_h$  at  $\varphi = 0^\circ$ . Since  $\cos(-0.0003^\circ)$  deviates by less than  $10^{-10}$  from unity, the term can be neglected for the calculation of the pitch  $P$  and its uncertainty.

### Pixel size

For the pixel size determination, the relation between the absolute length scale measurement and the corresponding number of pixels on the detector needs to be established.<sup>[250]</sup> For that purpose, the detector was shifted vertically along  $z_1$  and  $z_2$  (Fig. 3.6) in steps of 2 mm up to a total displacement of 8 mm (nominal values). GISAXS images, similar to Fig. 4.17, using  $E_{\text{ph}} = 10$  keV and  $\alpha_i = 0.57^\circ$  were recorded at each position and the real displacement was measured using the Heidenhain encoders attached to both lifting axes, the results are listed in Table 4.3.

**Table 4.3** | Vertical detector displacement positions, nominal values and values measured using the Heidenhain encoders attached to both lifting axes.

nominal value / mm	measured value / mm
0.0	0.000
2.0	2.002
4.0	4.009
6.0	6.010
8.0	8.007

The beam footprint at this incidence angle is around 30 mm, which is longer than the sample length. The uniformity of the GISAXS patterns and the GTR positions within 1 px has been verified by comparing images recorded at different sample stage positions along both directions parallel to the sample surface. Moreover, a change of the horizontal beam width from 0.3 mm to 1.0 mm did not cause any detectable changes of the GTR positions on the detector. The measured displacement values are the mean of both encoder readings, which had a relative standard deviation of  $\leq 0.2\%$  in all measurements. From each image, the relevant section containing the scattering pattern is extracted, i.e. the full range for  $d_v$  and from 1530 px to 1820 px for  $d_h$ . The row-wise sum, i.e. along  $d_h$ , of every subimage is calculated, which results in five profiles  $S_k(d_h)$ , one for each vertical detector position  $k = (1, \dots, 5)$  (Fig. 4.19a). For each pair  $[S_k(d_v), S_l(d_v)]$ , i.e. 10 combinations, one of the two profiles is shifted with respect to the other along the  $d_v$  axis by  $\Delta s$ . The absolute difference between both profiles is calculated and summed over  $d_v$ , i.e.  $\Delta S_{k,l}(\Delta s) = \sum_{d_v} |S_k(d_v + \Delta s) - S_l(d_v)|$ . For a more convenient analysis, the reciprocal of  $\Delta S_{k,l}(\Delta s)$  was calculated to yield maxima  $\Delta s_{\text{min},k,l}$  instead of minima at the offsets between the two vertical positions  $k$  and  $l$ , see Fig. 4.19b. The peak positions can be determined with sub-pixel accuracy by fitting of Lorentzian functions of the form  $f(x) = \frac{A_0/\pi}{1 + (\frac{x-x_0}{\sigma})^2} + A_1$ . The fitted position of a peak at  $x_0$  represents the position of the least squares minimum, the amplitude  $A_0$  is used as a weighting factor. The offset positions  $\Delta s_{\text{min},k,l}$  of each pair are associated with the absolute length measurement of the corresponding vertical displacement  $v_{k,l}$ . The data points are fitted by a linear function where each point is weighed by the peak amplitude  $A_0$ . The slope of the fit function

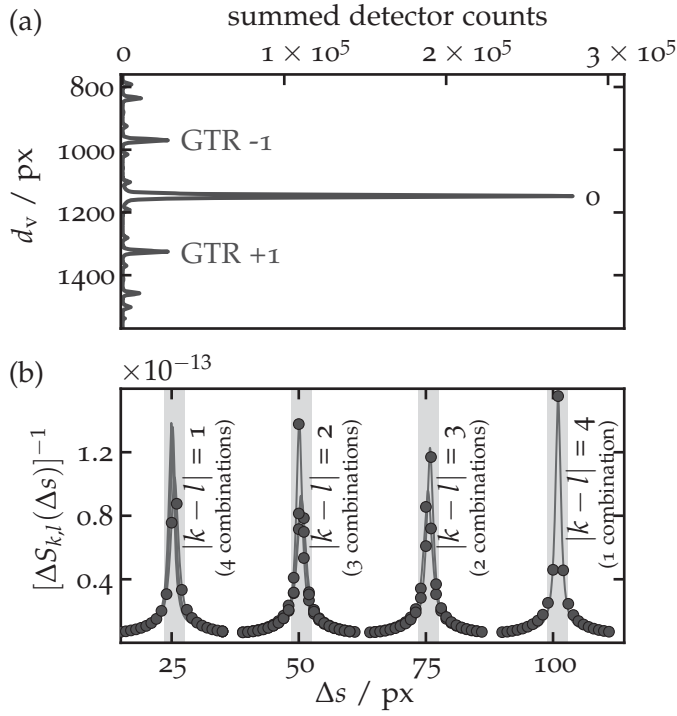


**Figure 4.19** | Pixel size determination. (a) Exemplary vertical profile  $S_k(d_v)$  of the vertical displacement series. Each point of the profile represents the sum of counts within the  $d_h$  range from 1530 px to 1820 px. (b) Reciprocal  $[\Delta S_{k,l}(\Delta s)]^{-1}$  of the difference between the profile  $S_k(d_v)$  and the shifted profile  $S_l(d_v + \Delta s)$  for all combinations of vertical positions  $k$  and  $l$  (dots). The reciprocal values of the  $\Delta S_{k,l}$  profiles are used in order to fit Lorentzian functions (solid lines) to the peaks for sub-pixel resolution of the offset peak positions.

yields the pixel size

$$L_{\text{px}} = (79.2 \pm 0.2) \mu\text{m} \quad (4.13)$$

and the uncertainty is defined by the square root of the fit variance  $\sigma^2$ . There might be still some potential for a further reduction of the uncertainty by a larger dataset with a wider vertical displacement range, however, this was not possible at the time of the measurements due to technical constraints.

### GTR asymmetry

Before the positions of the GTRs are determined, a detail needs to be discussed. A close examination of the diffraction lines, especially the ones further away from the central line as shown in Fig. 4.20, reveals their lack of symmetry. The intensity distribution and symmetry of the intersection of GTRs with the Ewald sphere in grazing incidence geometry is also governed by the form factor of the cross-sectional line profile, as discussed in Section 2.5. Only the structure factor is evaluated by determining the GTR positions in order to maintain traceability. Hence, the asymmetry, even though not qualitatively evaluated by a form factor model, is accounted for. The additional scattering features that can be seen in Fig. 4.17 and Fig. 4.18b are caused by superstructures within the polymer film and can be disregarded for the pitch determination. It should be also noted that the observed asymmetry of the diffraction intensity is not caused by an asymmetric incident beam. The incident beam shape was found to be symmetric in a short exposure time image of the attenuated direct beam.

The asymmetry of the GTRs causes a slight variation of the distance of a GTR from the specular axis, depending on the GTR order. This can be assessed by calculating the

itches  $P_i$  from the individual GTR distances by

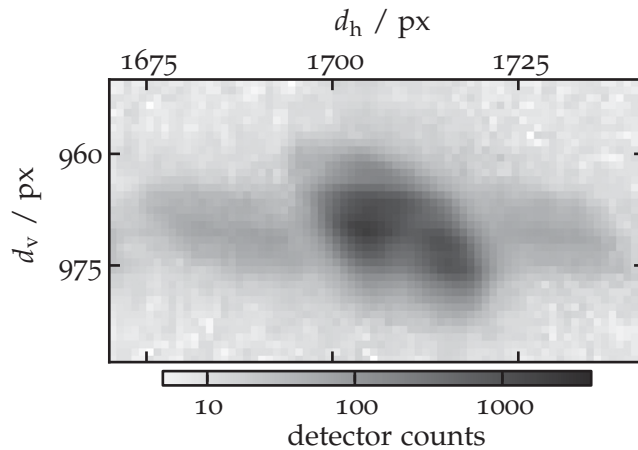
$$P_i = \frac{hc}{eE_{ph}} \left[ 2 \cos \Delta\varphi \left( \frac{L_{px} d_{GTR,i}}{L_s |i|} \right) \right]^{-1},$$

with  $i \in \{-3, -2, -1, +1, +2, +3\}$ ,

$$\text{and } P = \frac{1}{N_i} \sum_i P_i,$$
(4.14)

instead of averaging the intensity-weighted centre positions of the GTRs and using Eq. (4.11). A possibility to quantitatively evaluate the spot asymmetry is to record scattering images at different azimuthal angles  $\varphi$  around the parallel alignment in small steps, e.g.  $0.002^\circ$ . In this way, the GTR intersects the Ewald sphere at various distances from the GTR centre with the most pronounced asymmetry close to the sample horizon. Consequently, the peak intensity of the spot on the detector varies as a function of  $\varphi$ . The position of maximum intensity yields the centre position of the GTR. While this highlights the importance and the arising complexity of defining the ‘correct’ centre position of the diffraction maxima, it should be noted that the asymmetry corrections are usually minor. In the present case, as well as in most other cases of gratings with well-defined line structures, the asymmetry correction was insignificant, that is, well within the pitch uncertainty. When calculating  $P$  using either Eq. (4.14) or Eq. (4.11), a relative deviation of only  $2 \times 10^{-5}$  is found, which is two orders of magnitude below the final relative uncertainty of the pitch uncertainty.

**Figure 4.20** | Asymmetric shape of a GISAXS GTR maximum.



### GTR distances

The goal is to calculate the pitch  $P$  from the distances of GTRs from the corresponding specular axis, i.e. (o) in Fig. 4.17. The distance is determined by approximating the GTR and the specular axis each by a linear function and calculation of the average distance of these two lines along the scattering pattern. The GTR distances were evaluated in each of the five images of the vertical displacement series (the same series that was used for the pixel size determination, p. 88), the index  $k$  denotes the GISAXS image,  $k = (1, \dots, 5)$ . As before, the index  $i$  denotes the GTR order,  $i \in \{-3, -2, -1, +1, +2, +3\}$ .

The boxes around the GTRs and the specular axis were defined on each image as illustrated in Fig. 4.17 and described in the paragraph on misalignment from parallel orientation (p. 86). As before, a 10%-threshold filter was applied to remove irrelevant weak scattering features and background counts. Within each box, a sub-box with full

height and a width of 5 px was moved horizontally along  $d_h$  of the GTR box in steps of 5 px. At every position  $j$  of the sub-box, the vertical intensity-weighted centre position inside the sub-box  $d_{v,cp}(j)$  is determined. In this way, a trace of the GTR or specular axis is created that follows the highest intensity along the rod. The trace is then approximated by a linear function  $d_v(j) = mj + n$  with  $j = (1, 2, \dots, N_j)$ . The distance  $(d_{GTR,i})_k$  of the  $i$ -th GTR to the specular axis  $(m_{spec}, n_{spec})$  of GISAXS image  $k$  is determined by the arithmetic mean

$$(d_{GTR,i})_k = \frac{1}{N_j} \left( \sum_{j=1}^{N_j} (m_i - m_{spec})j + (n_i - n_{spec}) \right) \quad (4.15)$$

and the corresponding square root of the variance  $(\sigma_i^2)_k$  is taken as the uncertainty of  $(d_{GTR,i})_k$ . The resulting five values  $(d_{GTR,i})_k$  and  $(\sigma_i^2)_k$  for each GTR  $i$  are then used to calculate the weighted arithmetic mean  $d_{GTR,i}$  and the weighted variance  $\sigma_i^2$  by

$$d_{GTR,i} = \frac{\sum_{k=1}^5 (\sigma_i^{-2})_k (d_{GTR,i})_k}{\sum_{k=1}^5 (\sigma_i^{-2})_k} \quad , \quad (4.16)$$

$$\sigma_i^2 = \frac{1}{\sum_{k=1}^5 (\sigma_i^{-2})_k} \quad .$$

The resulting values are listed in Table 4.4.

GTR $i$	$d_{GTR,i}$ / px	$\sigma_{GTR,i}$ / px	$P$ / nm
-3	534.7	0.9	24.79
-2	355.8	0.1	24.83
-1	178.0	0.1	24.82
+1	178.2	0.1	24.79
+2	354.5	0.1	24.93
+3	533.5	0.3	24.84

**Table 4.4** | Weighted mean distance  $d_{GTR,i}$  and weighted standard deviation  $\sigma_{GTR,i}$  of the  $i$ -th GTR from the specular axis.

### 4.3.4 Traceable pitch determination

With the values and uncertainties for the photon energy  $E_{ph}$  (Section 3.2), the sample-detector distance  $L_s$ , Eq. (4.12), the pixel size  $L_{px}$ , Eq. (4.13), and the GTR distances (Table 4.4), the grating pitch  $P$  can be calculated according to Eq. (4.14). Note that the misalignment term  $\cos \Delta\varphi$  has been completely neglected as it deviates only by  $10^{-10}$  from unity. The pitch  $P$  is the average of the six pitches  $P_i$  of the six GTR distances  $(d_{GTR})_i$ . The combined standard uncertainty  $u(P)$  is calculated according to the *Guide to the Expression of Uncertainty in Measurement* (GUM)<sup>[16]</sup> from the sum of absolute squares of the uncertainty contributions of all constituting input parameters as shown in Table 4.5. In this way, the pitch of the self-assembled block copolymer grating is determined in a traceable way as

$$P = (24.83 \pm 0.09) \text{ nm.} \quad (4.17)$$

**Table 4.5** | GISAXS pitch uncertainty contributions of the input quantities  $x_i$  (normal distributions), contribution uncertainty type (A or B) according to GUM, uncertainty components  $u_i(x_i)$ , relative uncertainty components  $\frac{u_i(x_i)}{x_i}$  and estimated combined standard uncertainty  $u_c(P)$  of the grating pitch  $P = 24.83$  nm.

input quantity $x_c$	type	$u(x_i)$	$\frac{u_i(x_i)}{x_i}$	$u_c(P) / \text{nm}$
photon energy $E_{\text{ph}}$	B	1 eV	$0.1 \times 10^{-3}$	0.002
sample-detector-distance $L_s$	B	3 mm	$1.0 \times 10^{-3}$	0.025
pixel size $L_{\text{px}}$	B	0.2 $\mu\text{m}$	$2.9 \times 10^{-3}$	0.071
GTR distances $d_{\text{GTR}}$	A	$\leq 0.87$ px	$1.6 \times 10^{-3}$	0.040
<i>Combined standard uncertainty <math>u(P)</math></i>				0.09

## 4.4 Summary

In this chapter, GISAXS and XRR have been applied for dimensional investigations of grating structures in three different size regimes, ranging from large pitches close to 1  $\mu\text{m}$  down to pitches of only 25 nm. The main goal was to assess the general uncertainties in GISAXS measurements and, thus, to establish traceability. This is an essential prerequisite in the evaluation of structural parameter values obtained by GISAXS in general and can serve as a starting point to validate model-based data analysis. The investigated structures are of immediate relevance for the next-generation lithography industry, for the characterisation of diffraction elements (Sections 4.1 and 4.2) as well as new materials for nanopatterning itself (Section 4.3). The investigations help to further develop GISAXS as an nanometrology tool suitable for such industrial applications.

While the presented PSD analysis methods are different for each size regime, the fundamental principle is the same: The analysis of the GTR positional periodicities directly from the GISAXS data, without reverse modelling of a form factor and a structure factor. This circumvents the need to evaluate the ‘correctness’ of the chosen form factor model and, thus, makes traceability possible. However, this comes at the cost of restricting the analysis to structure factor related dimensional parameters.

Standard discrete Fourier transform of GISAXS  $I(q_y)$  profiles from gratings with large pitch close to 1  $\mu\text{m}$  proved to be a suitable method to determine the critical dimension, groove width and pitch. The results were also validated by analysing modelled GISAXS data where nominal and determined structure sizes show close agreement well within the peak widths. The photon energy series test data and measurements recorded using the in-vacuum PILATUS 1M detector from 4.5 keV to 9 keV illustrated the interplay of  $q$  resolution,  $q$  range, wavelength, and largest structure size that should be resolved. Even though the  $q$  resolution increases with decreasing photon energy, the general advice is to rather select the highest possible photon energy that still allows to resolve the largest scattering features of interest, i.e. the lowest separation distance in  $q$ . In this way, the  $q$  range is maximised, which is inversely proportional to the DFT bin size and, consequently, generates sharper peaks in the PSD.

At intermediate pitches, the number of GTRs that intersect the Ewald sphere reduces. Moreover, considerable discontinuities appeared in the extracted data due to the module gaps of the PILATUS 1M detector. Both issues require a PSD calculation that is able to cope with non-uniformly spaced data. The developed method of Fourier amplitude fitting using Tikhonov regularisation fulfils these demands and is a straight-forward

technique to determine  $CD$ ,  $G$ , and  $P$  from a single exposure image. This is important for high-throughput measurements, for example in lithography wafer inspection.

It was possible to establish the traceability of the GISAXS measurements with an uncertainty below 0.1 nm for the sample system with the smallest nominal pitch of 25 nm. Traceability was achieved by the uncertainty analysis of the contributing parameters: sample-detector distance, detector pixel size, photon energy, and distance between the grating diffraction orders. The predominant uncertainty contributions arose from the geometric parameters sample-detector distance and pixel size. Once the grating was aligned by observing the symmetry of the scattering pattern, the remaining very small angular deviation  $\Delta\varphi$  from parallel orientation could be completely neglected in the uncertainty analysis as its magnitude is several orders below that of the other uncertainty contributions. The analysis showed that the scattering spots of the GTRs have to be carefully examined for possible asymmetries, which were also found in the GISAXS images of the investigated sample. However, the imposed corrections were minor and two orders of magnitude below the combined standard uncertainty of the pitch in the present case. The presented basic experimental GISAXS uncertainty may be used as an input parameter for more complex, but common GISAXS data analysis, e.g. within the framework of DWBA modelling or for FEM Maxwell solvers. In this way, it might become possible to establish the traceability of the larger set of structural parameters obtained from the numerical modelling of GISAXS data.

Self-organised nanostructured BCP thin films, the material of the smallest grating structures presented here, are not only interesting in lithography and for nanometrology. With the foundation of a profoundly characterised GISAXS measurement setup together with the currently unique capabilities of the in-vacuum PILATUS 1M detector of digital image recording down to photon energies of 1.75 keV at the FCM beamline, advanced measurement techniques for polymer thin film studies have become available. In the next chapter, these extended capabilities and techniques are used to gain new insights in the depth-dependent re-structuring of diblock copolymer films.



# 5

## Depth-resolved GISAXS using contrast-matching at the Si K-edge

### 5.1 Introduction

BCP thin films forming self-organised nanostructures have been very attractive materials in both science and cutting-edge applications for decades.<sup>[2,11,47,81,136]</sup> Such structures offer a wide range of attractive applications, for example, in organic photovoltaics,<sup>[142]</sup> for medical applications,<sup>[114]</sup> as nanostructuring templates of other materials,<sup>[148,149,171,180,233]</sup> or even as sensors.<sup>[24]</sup> Polystyrene-*block*-poly(2-vinylpyridine) (PS-*b*-P2VP) is a commonly used material<sup>[139–141]</sup> that is a typical example of the class of block copolymers possessing a large surface energy difference between the components.<sup>[110]</sup> It has been reported in many studies that it forms well-developed self-organised nanostructures<sup>[82,202,233]</sup> which can be controlled and changed by varying the environment such as addition of solvent, concentration change, annealing, electric fields, vapour annealing, etc.<sup>[109,110,156,201,240,241]</sup> However, despite the large number of reports on the variation of chemical and physical process parameters, detailed studies of the structure along the thin film depth using non-destructive techniques are scarce so far, due to the very limited number of suitable measurement methods.

Understanding the characteristics of the self-organisation, for example after annealing, is the key to control the shape of the nanostructures and tailor it to specific needs. This requires tools to assess the film morphology in lateral and vertical directions in a non-destructive way. GISAXS is a widely used and sometimes the only applicable technique for such studies in polymer films.<sup>[34,135,158,163,228]</sup> Depth resolution can be achieved by variation of the X-ray incidence angle around the critical angle of total reflection,<sup>[238]</sup> see Eq. (2.18). Yet major difficulties arise from the strong scattering contribution of the film interfaces.<sup>[175]</sup> Consequently, scattering induced by roughness, reflection from the film substrate as well as multiple scattering occur and overlay the weak film scattering on the GISAXS image.<sup>[135]</sup> The X-ray scattering contrast can be adjusted by varying the photon energy around an absorption edge of a specific element,<sup>[174,230,247]</sup> see Section 2.1.2. In this

way, it is possible to minimise the interface scattering effects by matching the scattering contrast between the polymer film and the silicon substrate.<sup>[103,175,176]</sup> A major challenge of this approach is that it requires GISAXS measurements to be performed around the K-absorption edge of silicon at 1839 eV, which is impossible to reach for most digital large-area X-ray detectors. Therefore, non-destructive X-ray investigations on the depth structure of BCP thin films are so far restricted to the use of image plates,<sup>[175,176]</sup> which have excellent imaging properties, but are time-consuming in handling and, consequently, limit the amount of data that can be acquired. In principle, the same could be achieved using hard X-rays and, for example, a gold substrate. But the critical angles at high photon energy are much smaller (Eq. (2.9) and Fig. 2.1), which results in less precise depth control, a much larger beam footprint, and possibly shadowing by surface undulations or artefacts due to a curved surface within the large illuminated area. However, combining GISAXS with advanced micro- and nanobeam instrumentation<sup>[130,197,198,209]</sup> greatly reduces the problems of over-illumination and surface curvature due to a large beam footprint. Invasive techniques, e.g. cross-section electron microscopy and plasma etching, or techniques sensitive only to the surface, e.g. AFM, carry the risk of inducing morphological changes during preparation or of missing relevant depth information. An alternative for non-invasive polymer thin film investigations is grazing incidence small-angle neutron scattering (GISANS). A number of depth resolved GISANS studies on triblock<sup>[162,164,165]</sup> and diblock<sup>[150]</sup> copolymer thin films profit from the widely tunable scattering contrast by deuteration of hydrogen bonds, but this requires a considerable alteration of the sample preparation process. As drawbacks, the limited availability of GISANS, long exposure times, low counting statistics, and low  $\vec{q}$  resolution have to be mentioned. In this chapter, the contrast-matching X-ray pendant to the depth-resolved GISANS studies is presented. While GISAXS does not offer the specific advantages of neutrons such as deuteration and probing from the substrate side, it principally can be performed more widely and circumvents most of the mentioned drawbacks.

Here, the structural changes in as spun and annealed PS-*b*-P2VP thin films on silicon substrates were studied by depth-resolved GISAXS using contrast matching around the silicon K-absorption edge at 1839 eV. The scattering images were recorded using the in-vacuum PILATUS 1M detector at photon energies down to 1770 eV. Prior to GISAXS, XRR was performed to determine the thickness and density of the film as well as to observe the contrast matching. AFM on both samples was applied to obtain complementary information on the surface structure before and after annealing.

The work presented in this section has been published in J. Wernecke, H. Okuda, H. Ogawa, F. Siewert and M. Krumrey: 'Depth-Dependent Structural Changes in PS-*b*-P2VP Thin Films Induced by Annealing', *Macromolecules* 47.16 (2014), pp. 5719–5727.

## 5.2 Materials and methods

The asymmetric block copolymer polystyrene-*block*-poly(2-vinylpyridine) (PS-*b*-P2VP) purchased from Polymer Source\* has a polydispersity index of  $M_w/M_n = 1.07$ , a PS volume fraction of 0.5 and molar masses of  $M_w = 40\,500\text{ g mol}^{-1}$  (PS block) and  $41\,000\text{ g mol}^{-1}$  (P2VP block), respectively. The polydispersity index  $M_w/M_n$  characterises the uniformity of the distribution of chain lengths of a polymer,  $M_w$  denotes the mass average molecular mass of a polymer and  $M_n$  is the number average molecular mass. The polydispersity

\* <http://www.polymer-source.com>

index of a polymer is unity when all molecules have the same chain length, i.e. molecular mass. PS-*b*-P2VP was dissolved in a toluene solution of 2 % mass fraction and spin-coated at 2000 rpm for 30 s on cleaned commercial Si(100) wafers. The films were then annealed at 60 °C for 24 h under vacuum to remove the residual solvent. The annealed sample was kept at a temperature of 105.0 °C for 2 h, which is just above the glass transition temperature of the PS-*b*-P2VP at 102.7 °C. The as-cleaned silicon substrate has a native SiO<sub>x</sub> oxide with a thickness around 1 nm. No chemical modification of the substrate other than cleaning in an ultrasonic bath, followed by a hot acid bath and thorough rinsing was applied to the sample substrates. It has been reported<sup>[164]</sup> that the substrate surface treatment influences the morphology of block copolymer thin films. In the present case, the Si/SiO<sub>x</sub> interface represents a hydrophilic neutral wall<sup>[164]</sup> for the PS-*b*-P2VP film, which means that the interface interactions of both blocks with the substrate are similar and result in an expected perpendicular orientation of the microphase separation structure.

GISAXS measurements were carried out using the PTB small-angle setup in conjunction with the in-vacuum PILATUS 1M detector and the HZB SAXS instrument as described in Chapter 3. A typical sample-detector distance of the presented GISAXS measurements is 3200 mm, which was determined by triangulation of the specularly reflected beam on the sample as demonstrated in Section 4.3.3. Typical total exposure times of the GISAXS data presented here are in the range of 30 s to 1200 s, depending on the photon energy and the incidence angle.

AFM, see Section 2.7, provides height resolution on the atomic scale.<sup>[14,151]</sup> It is thus a surface sensitive technique that probes real-space lengths, which is complementary to the X-ray scattering methods. The AFM measurements presented in this work were carried out by Frank Siewert\* from the Institute for Nanometre Optics and Technology at HZB.<sup>[252]</sup> The instrument used is a Bruker SIS-ULTRAObjective AFM with a (40 × 40) μm<sup>2</sup> scanner on a PICOStation system using active vibration damping. The tips applied for the measurements are silicon SPM sensor tips for the non-contact mode with a resonance frequency of 190 kHz and a force constant of 48 J m<sup>-2</sup>. The tip is shaped like a polygon-based pyramid with a height of 10 μm to 15 μm and the tip radius is less than 8 nm. Therefore, the achievable lateral resolution is in the range of about 20 nm. After every four scans, the tip was exchanged to avoid having the measurement be influenced by tip wear. In addition to tapping-mode amplitude images of the topography, phase images of the tip frequency phase shift were recorded. Phase images yield information on the local stiffness and friction and, thus, on the spatial distribution of different materials.

## 5.3 Results

### 5.3.1 XRR measurements

In order to perform depth-resolved GISAXS under the scattering contrast-matching condition, it is helpful to determine the optical constants, the film thickness, the surface roughness, and the substrate interface roughness of the film. These values are then used to calculate the intersection of the refractive indices of the polymer thin film and the Si substrate, which is the contrast matching energy  $E_{\text{match}}$ . The optical constants are also needed for GISAXS intensity modelling, for example within the framework of DWBA, to obtain the amplitude reconstruction of reflected X-rays. XRR measurements were

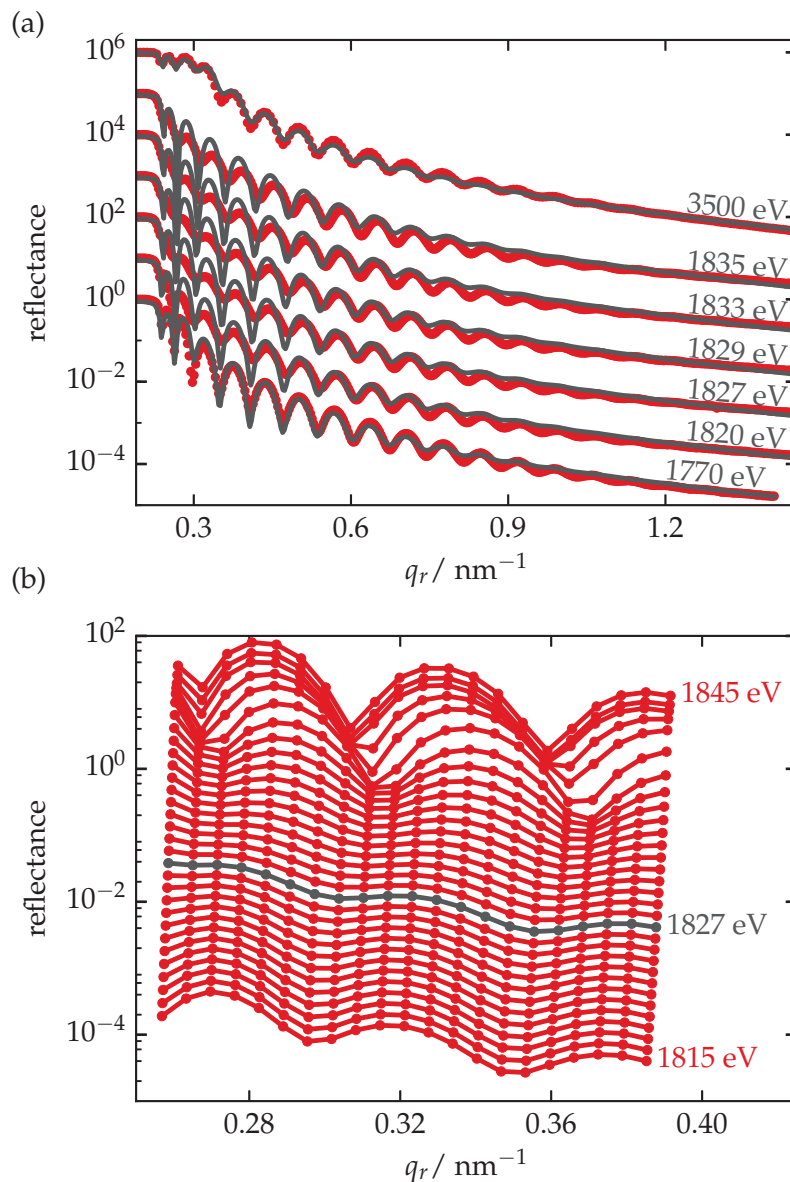
\* contact: frank.siewert@helmholtz-berlin.de

carried out on the as spun sample at different photon energies from 1770 eV to 3500 eV, that is, close to the silicon K-edge as well as far away from it as shown in Fig. 5.1a. Since the X-ray scattering contrast between both blocks of  $\delta^{(PS)}/\delta^{(P2VP)} = 1.1$  is low, the inner structure of the film is not visible. Consequently, the film is regarded as a homogeneous film with an average density, which is also supported by the observation of one critical angle only. A possible intermediate layer of  $\text{SiO}_x$  between the polymer film and the substrate is neglected in the model because the index of refraction is very similar to that of silicon.<sup>[34]</sup> All reflectance curves were simultaneously fitted with common parameters for film thickness, surface roughness and substrate interface roughness in accordance with Eq. (2.37). The best fit values of the parameters resulted in a film thickness of  $(85 \pm 3)$  nm and a film density of  $(1.16 \pm 0.03)$  g cm<sup>-3</sup>. The determined surface roughness of around 3 nm is about one order of magnitude higher than that of the substrate interface. The noticeable deviations in the oscillation amplitude close to the contrast matching energy, see the reflectance curves from 1820 eV to 1835 eV in Fig. 5.1a, are due to the pronounced change of  $\delta$  and  $\beta$  of the substrate close to the silicon K-absorption edge and the limited accuracy of the tabulated values of the optical constants. No Bragg peaks of any possible horizontal layering become visible in any of the reflectance curves for the as spun and the annealed sample.

The uncertainties of the fit shown in Fig. 5.1a are not simply the residual errors of each parameter as this completely neglects the cross-correlations of the parameters. Since the real cross-correlations of the coupled system cannot be determined, a method is used that assumes full correlation of all parameters, which yields an upper limit of the uncertainty intervals. This is done by evaluating the goodness-of-fit parameter  $\chi^2$  of different fits, which is the sum of the absolute squares of the residuals divided by the number of data points minus degree of freedom.<sup>[101]</sup> Each parameter is set to fixed values within a reasonable interval and the same fitting algorithm of all XRR profiles is applied for each value. This results in a  $\chi^2$  value for each parameter value as shown in Fig. 5.2 for the roughness of the surface, Fig. 5.2a, substrate interface roughness, Fig. 5.2b, and the film thickness, Fig. 5.2c. In order to determine the uncertainty interval of each parameter, the  $\chi^2$ -curves are normalised to the minimum value (position indicated by the black dots in Fig. 5.2), the parameter values at  $\chi^2 = 2$  enclose the  $1\sigma$  uncertainty interval of the parameter (vertical lines in Fig. 5.2a-c).<sup>[101]</sup> Note that the minimum positions do not correspond to the best fit values stated in the text. These are obtained by simultaneously fitting all parameters to the XRR data.

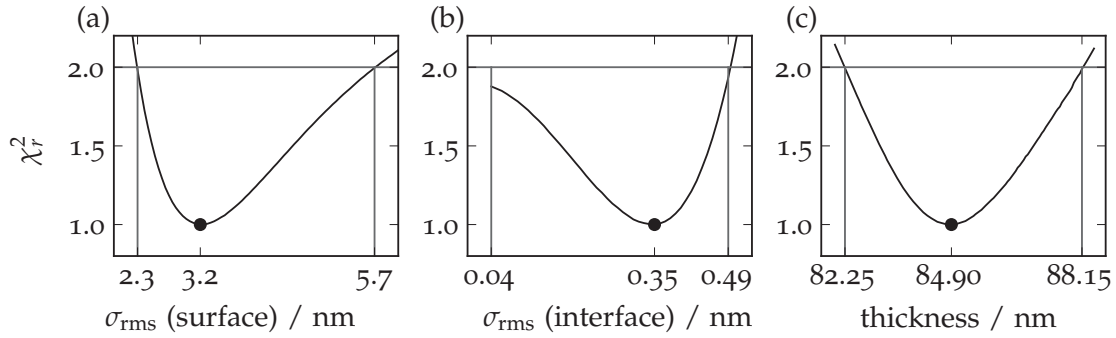
Displayed in Fig. 5.1b is a magnification of the low  $q_x$ -region of XRR measurements around the silicon K-edge. A strong damping of the oscillation amplitude is observed around a photon energy of  $E_{\text{match}} = 1827$  eV as shown by the black curve in Fig. 5.1b. This is due to the minimised scattering contrast at the film-substrate interface.

The film density can be used to calculate the real part component  $\delta$  and the imaginary part  $\beta$  of the refractive index of the film around the energy of contrast matching  $E_{\text{match}}$ , see Eqs. (2.5) and (2.6). Figure 5.3 shows the energy dependence of  $\delta$  and  $\beta$  of the PS-*b*-P2VP thin film and bulk Si substrate as calculated with reference data for Si<sup>[96]</sup> and the Henke data<sup>[90]</sup> for P2VP (the applied molecular formula is  $\text{C}_{21}\text{H}_{21}\text{N}_3$ ). An intersection of the  $\delta$  curves of P2VP and Si is found in the region around 1815 eV. The deviation from the experimentally observed  $E_{\text{match}}$  is due to the steep slope around the absorption edge and the uncertainty of the film density. The uncertainty of the density, i.e. of the critical angle, contributes to the uncertainty of  $\delta$  multiplied by a factor of 2 due to  $\alpha_c = \sqrt{2\delta}$ , see Eq. (2.9), which explains the discrepancy between theoretical and experimental values.



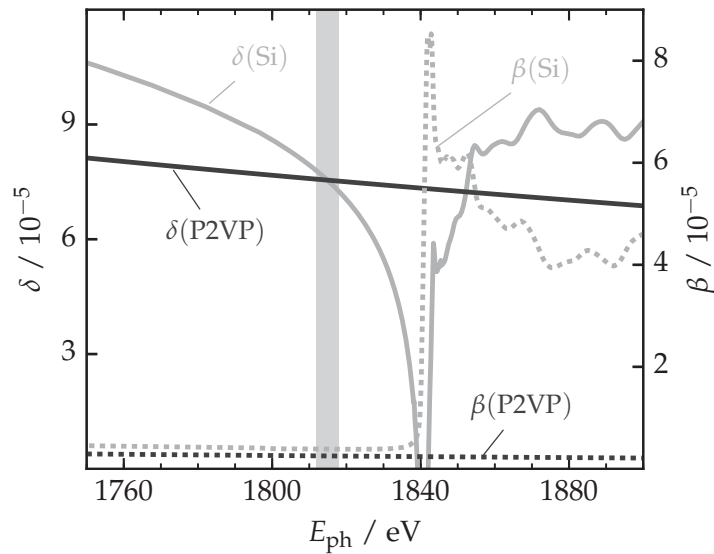
**Figure 5.1** | (a) XRR data measured at different energies close to the contrast matching energy (1820 eV to 1845 eV) and far away from it (1770 eV and 3500 eV). The reflectance curves were simultaneously fitted (solid lines) using a single layer model to obtain the common parameters of film thickness, density, surface roughness, and substrate interface roughness, see Section 2.3. The curves have been vertically offset for clarity. (b) Magnification of the XRR data in the low  $q_r$  range (vertically offset for clarity). The black line indicates the strongest damping of wiggles due to contrast matching at  $E_{\text{match}} = 1827$  eV.

Figure 5.3 also shows that there is no intersection of the  $\beta$ -curves of both materials, which is why the full matching of the complex refractive indices is not possible. A consequence of the unmatched  $\beta$  in XRR as well as in GISAXS is that the oscillations are attenuated, but still present at low  $q$  and less suppressed at higher  $q$  values. For a more detailed discussion of the topic, see the work of Ishiji et al. [103], especially Fig. 6 therein, and Okuda et al. [175].



**Figure 5.2** | Normalised  $\chi^2$  goodness-of-fit values as a function of the parameter that was kept fixed within the intervals of the abscissa axes for each fit. The black dots indicate the minimal  $\chi^2$  value, the line at  $\chi^2 = 2$  encloses the  $1\sigma$  uncertainty interval. (a) rms surface roughness, (b) rms substrate interface roughness, (c) film thickness.

**Figure 5.3** | The component of the real part  $\delta$  (solid lines) and the imaginary part  $\beta$  (dashed lines) of the complex refractive indices of silicon and PS-*b*-P2VP. The calculations were made using reference data for Si<sup>[96]</sup> ( $\rho = 2.3 \text{ g cm}^{-3}$ ) and the Henke data<sup>[90]</sup> for P2VP ( $\text{C}_{21}\text{H}_{21}\text{N}_3$ ) with  $\rho = 1.16 \text{ g cm}^{-3}$ , as obtained by XRR fitting (Fig. 5.1a).



### 5.3.2 GISAXS contrast matching

Based on the information on the contrast matching energy obtained by XRR, GISAXS images were recorded using the in-vacuum PILATUS 1M detector. Displayed in Fig. 5.4a is a GISAXS pattern measured at  $\alpha_i = 0.65^\circ$  with a photon energy of 2500 eV, which is far away from the silicon K-edge (shown is the as spun sample, the annealed sample exhibits the same pattern). Two symmetric diffuse scattering rods are visible at around  $q_y = \pm 0.11 \text{ nm}^{-1}$ . These are more intense at the Yoneda peak (cf. Section 2.4) at  $q_z = 0.21 \text{ nm}^{-1}$ , which appears at  $\alpha_f = \alpha_c$  due to the constructive interference of the dynamic scattering contributions (Fig. 2.12). The presence of scattering rods, i.e. first order Bragg peaks, extended along  $q_y$  in GISAXS is indicative of an in-plane ordering of structures with a characteristic separation distance  $D$  in the PS-*b*-P2VP film. It is well known from the literature<sup>[2,35,201]</sup> that PS-*b*-P2VP forms microdomains of vertically extended lamellae under the present preparation conditions, which possess a characteristic microphase separation distance due to self-ordering of both blocks. Thus, the Bragg peak  $q_y$  position corresponds to a period length of  $D = 2\pi/0.11 \text{ nm}^{-1} = 58 \text{ nm}$ , which is in full agreement with values from the literature.<sup>[109]</sup> Also visible in Fig. 5.4a are Kiessig-like fringes along  $q_z$  that are superimposed with the scattering rods of the film nanostructures.

Figure 5.4b was measured at the contrast matching energy  $E_{\text{match}} = 1827 \text{ eV}$  at

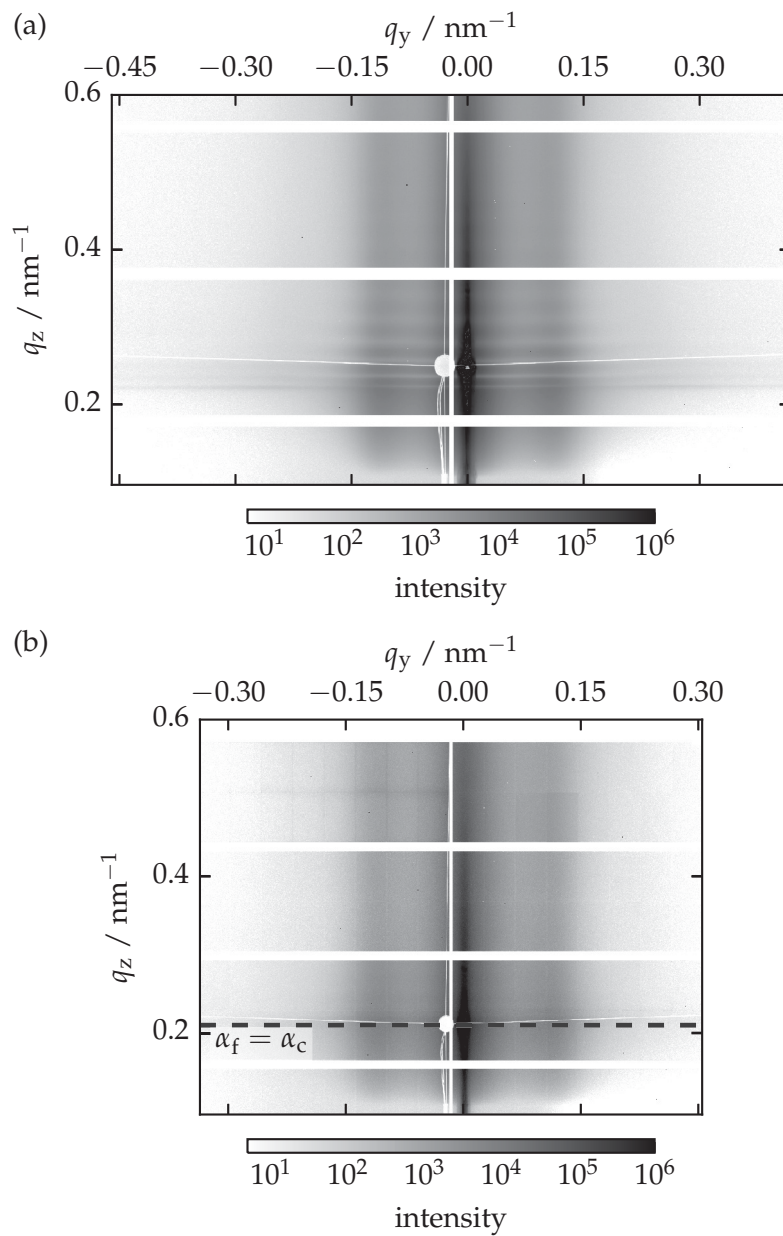


**Figure 5.4** | GISAXS pattern of the as spun sample measured at (a)  $\alpha_i = 0.65^\circ$ ,  $E_{\text{ph}} = 2500 \text{ eV}$  (300 s exposure time) and (b)  $0.65^\circ$ ,  $1827 \text{ eV}$  (1200 s exposure time). The dashed black line indicates the Yoneda line, i.e. the condition of  $\alpha_f = \alpha_c$  (see Section 2.4).

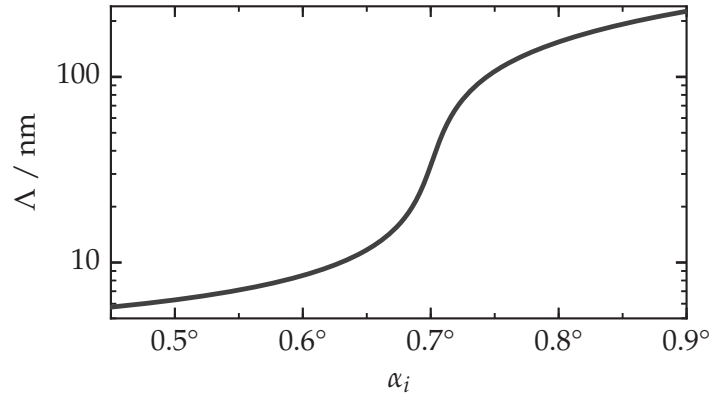
$\alpha_i = 0.65^\circ$  and shows no indication of any fringes. Consequently and as expected, the oscillations at 2500 eV originate from the interference of the incident beam and reflections from the film-substrate interface and reflect the film thickness and resonant diffuse scattering (RDS) due to correlated roughness.<sup>[94]</sup> Thus, RDS is strongly attenuated at 1827 eV because of the minimised scattering contrast at the interface, while the scattering rods of the film are preserved in the GISAXS pattern.

RDS can be used to study the degree of correlation of film surface and substrate interface.<sup>[158,160,161]</sup> The observed period length in  $q_z$  corresponds to a correlation length of  $d_{\text{corr}} = 85$  nm, i.e. there is full correlation of the surface and the substrate interface. This is no contradiction to the different rms roughness values that were determined by XRR fitting because the correlation does not extend over the full in-plane length scale spectrum.<sup>[160]</sup> The damping of the oscillations with increasing  $q_y$  indicates a loss of correlation and a cut-off at a minimal in-plane length. The polymer film acts as a band-pass filter for the interface height fluctuations.<sup>[161]</sup> Consequently, the short-wavelength roughness spectrum is more than an order of magnitude below the cut-off length and is thus statistically independent from the surface-interface correlation.<sup>[158]</sup>

### 5.3.3 Depth-resolved GISAXS using contrast matching

Depth-resolved GISAXS measurements at 1827 eV were performed on the as spun and on the annealed thin films by changing the incidence angle and, thus, the scattering depth  $\Lambda$ , see Fig. 5.5 and Eq. (2.18). Figure 5.6a and Fig. 5.6b show line cuts along  $q_y$  through the Yoneda peak at  $\alpha_f = \alpha_c$  (dashed line in Fig. 5.4b) for all incident angles of the as spun and the annealed film. In order to quantitatively characterise the depth-dependent film structure of both films, a similar analysis is carried out as shown in a depth-resolved GISANS study by Metwalli et al. [150] and in an in-situ GISAXS study of BCP solvent vapour annealing shown by Gu et al. [78].

**Figure 5.5** | Scattering depth  $\Lambda$  in PS-*b*-P2VP at 1827 eV as calculated with Eq. (2.18).



The  $q_y$  profiles were fitted by the function

$$I(q_y) = B_1 + B_2 q_y + q_y^{-B_3} + 2\sqrt{\frac{\ln 2}{\pi}} G_1 \exp \left[ -4 \ln 2 \left( \frac{q_y - q_{y0}}{w_{\text{fwhm}}} \right)^2 \right] \quad (5.1)$$

that accounts for the background  $B_{1,2}$ , the exponential decay along  $q_y$  ( $-B_3$ ) and a Gaussian-shaped function for the Bragg peak at around  $0.11 \text{ nm}^{-1}$  (amplitude  $G_1$ , centre position  $q_{y0}$  and peak width  $w_{\text{fwhm}}$ ). It should be noted that DWBA modelling<sup>[133]</sup> using various form factors, interference functions, and using a perturbation potential  $\delta U$  for

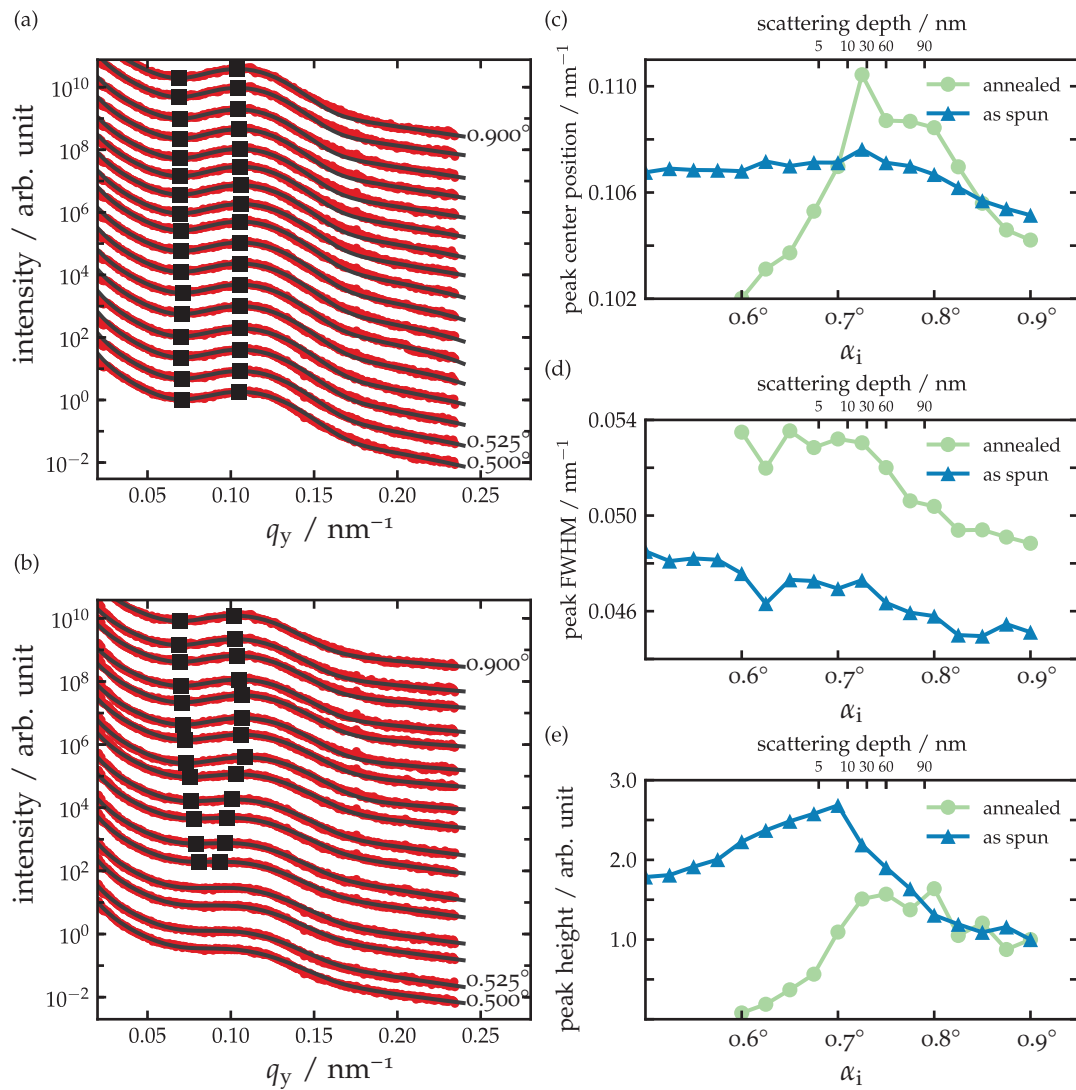


**Figure 5.6** | GISAXS  $q_y$  profiles through the Yoneda peak of the as spun (a) and annealed (b) sample for different incidence angles around the critical angle  $\alpha_c = 0.70^\circ$  (300 s exposure time). The profiles are vertically offset for clarity. The profiles are fitted by a function (Eq. (5.1)) to characterise the Bragg peak shape (solid lines in (a) and (b)). Black squares indicate the local minimum and maximum positions of the peak. Extracted (c) Bragg peak positions, (d) peak width and (e) peak heights of the as spun and annealed films as a function of incidence angle and with an indication of the scattering depth.

perpendicular lamellae<sup>[34]</sup> did not result in meaningful fits, which is probably due to the absence of well defined structure shapes. AFM data (see Section 5.3.4) also confirmed that the sample surface just consists of fingerprint-like lamellae, which can be characterised by the size and shape of the Bragg peak that corresponds to the average separation distance.

Thus, the profiles are adequately characterised by the Bragg peak position  $q_{yo}$ , the peak width  $w_{fwhm}$  and the peak height (Fig. 5.6c-e). The Bragg peak position of the as spun film (blue triangles) remains constant in a range of  $q_{yo} = 0.105 \text{ nm}^{-1}$  to  $0.107 \text{ nm}^{-1}$ , i.e. corresponding to 59 nm, throughout the entire film thickness. The peak width decreases slightly with increasing scattering depth, which is due to the fact that it resembles the degree of ordering within the film.<sup>[164]</sup> With increasing scattering depth, the scattering signal is averaged over a larger volume, i.e. from the surface down to the scattering depth, which implies that the ordering slightly decreases with increasing film depth as discussed in Section 2.1.2. The peak height, which is the difference of the minimum of the approximated peak function and the peak maximum (black squares in Fig. 5.6a) increases slightly up to the critical angle and decreases with increasing scattering depth. The former is the same dynamic effect that causes the intensity increase at  $\alpha_f = \alpha_c$ , the Yoneda peak. The latter can be mainly attributed to the reduction of reflectance and increase of absorption at higher incidence angles above the critical angle.

On the annealed sample (green dots in Fig. 5.6c-e), a significantly different depth-dependent behaviour is observed. The Figs. 5.6b and Fig. 5.6e clearly show that there is no Bragg peak at incidence angles below around  $0.65^\circ$ , only a flat plateau is present, while the peak re-appears around the critical angle and above. The increase of the peak centre position shown in Fig. 5.6c suggest that there is a slight increase of the separation distance towards a higher scattering depth. The peak width of the annealed film generally follows the slope of the curve of the as spun sample, which indicates that the sub-surface order has not changed after annealing. The peak height is zero in the surface-sensitive region of  $\alpha_i < \alpha_f$ , increases in the first 30 nm of the film and follows the same trend as that of the as spun film at greater depth. For better comparison, the Bragg peak heights of both samples in Fig. 5.6e were normalised to the corresponding peak height at full film penetration, i.e. at the largest incidence angle. In absolute numbers, the peak height in the annealed film is lower by a factor of about 5 compared to the as spun film.

### 5.3.4 AFM results

Different fields with sizes of  $(1 \times 1) \mu\text{m}^2$ ,  $(10 \times 10) \mu\text{m}^2$  as shown in Fig. 5.7, as well as  $(35 \times 35) \mu\text{m}^2$  were scanned on both samples and recorded as amplitude images (Fig. 5.7a-b) and phase images (Fig. 5.7c-d). Especially the phase images show a fingerprint-like surface distribution of the PS and P2VP blocks as vertical lamellae on the as spun and on the annealed film. The structures appear less pronounced on the annealed sample (Fig. 5.7(b,d)), which is also confirmed by a comparison of the average height roughness  $\sigma_{rms}$ . AFM  $\sigma_{rms}$  values of 2.1 nm and 1.45 nm are representative for the as spun and the annealed film, respectively. The radial PSD of the  $(10 \times 10) \mu\text{m}^2$  amplitude images, Fig. 5.7e, exhibit a maximum at a spacial frequency of around  $0.107 \text{ nm}^{-1}$  corresponding to a correlation length of 59 nm, which is again due to the spacing of the lamellae. No formation of islands was found on any of the AFM images up to the maximal scanning length of  $35 \mu\text{m}$ .

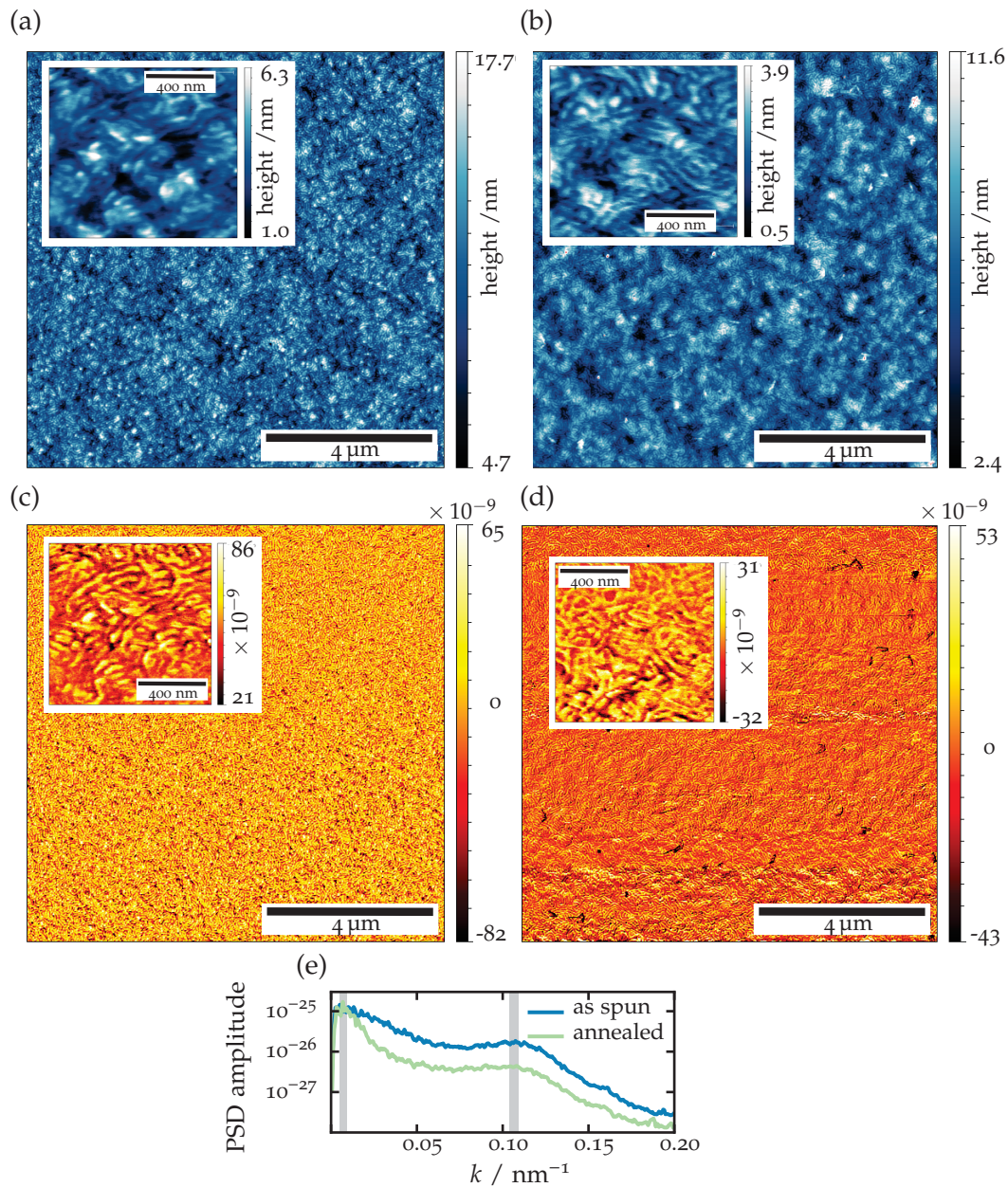
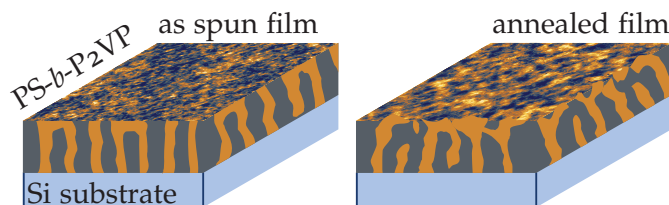


**Figure 5.7** | Representative AFM amplitude images (a,b) and phase images (c,d) of the as spun film (a,c) and the annealed film (b,d) on measurement fields of  $(10 \times 10) \mu\text{m}^2$  and  $(1 \times 1) \mu\text{m}^2$  (insets in (a-d)). (e) Radial power spectral densities as a function of spatial frequency  $k$  of the as spun film and the annealed film of the  $(10 \times 10) \mu\text{m}^2$  amplitude images shown in (a) and (b).

## 5.4 Proposed depth structure

Depth-resolved GISAXS and AFM measurements of the PS-*b*-P2VP thin films under the condition of matched contrast reveal structural changes on the surface and along the film thickness after annealing. From the combined results of XRR, AFM, and GISAXS data, a depth structure of the annealed film is proposed as sketched in Fig. 5.8.

**Figure 5.8** | Schematic representation of the depth structure of the as spun and annealed PS-*b*-P2VP thin films.



At the surface, the same fingerprint-like lamellar structure is observed by AFM on the as spun and on the annealed film surface. The maxima of the radial PSD of the AFM amplitude images fully agree with the  $q_y$  positions of the GISAXS Bragg peaks and correspond to the lamellar spacing of 59 nm. However, the in-plane lamellar ordering at the surface of the annealed sample is significantly reduced. This can be concluded from the absence of a Bragg peak in depth-resolved GISAXS measurements at incidence angles below  $\alpha_c$ , from the reduced rms roughness (lower by a factor of 1.4 compared to the as spun sample), and from the lower AFM PSD intensity at higher spacial frequencies, i.e. at shorter correlation lengths. The presence of RDS in non-contrast-matched GISAXS measurements on both films reveals a pronounced morphology correlation of film surface and interface at higher in-plane lengths. Consequently, there is no indication of any additional surface structuring after annealing in GISAXS.

With increasing X-ray scattering depth, i.e.  $\alpha_i > \alpha_c$ , the GISAXS Bragg peak height significantly increases in the  $q_y$  profiles of the annealed sample and follows the same trend as that of the as spun film when probing further down through the film. Hence, the in-plane ordering of the vertical lamellae is preserved after about 30 nm of film depth after annealing. The Bragg peak width and the absolute peak heights of the annealed film follow the slope of the as spun sample peak shapes, but are systematically lower. A reduced in-plane order at the surface and a preserved in-depth order causes a reduced total degree of order in the probed scattering volume from the film surface to the scattering depth, which results in a constant negative offset of the Bragg peak heights and widths in the annealed film compared to the as spun film. The Bragg peak centre position seems to decrease slightly with increasing scattering depth. This suggests that the lamellar separation distance increases, which might be due to strain induced by the transition close to the film surface. A very similar observation was made<sup>[241]</sup> after exposing PS-*b*-P2VP thin films to a temperature leap of 200 °C and subsequent cooling. Due to the complete suppression of RDS in GISAXS under the contrast-matching condition, the absence of Bragg peaks along the  $q_z$ -axis in GISAXS and XRR as well as due to the presence of only one critical angle in the XRR measurements, there is no indication of the formation of parallel lamellae towards the substrate interface as, for example, during solvent vapour annealing.<sup>[78,201]</sup> However, this is difficult to conclude from X-ray scattering measurements because of the low scattering contrast between both monomer units and due to the restriction to probing the film from the free surface side only. Depth-resolved GISANS investigation with the neutrons impinging from the substrate side<sup>[150,164]</sup> would add valuable insights in the film structures close to

the substrate interface. The discussed results are summed up in a sketch of the depth structure of the annealed PS-*b*-P2VP thin film in Fig. 5.8.

In terms of re-orientation processes of the monomer units after thermal treatment, it seems that the coalescence of microdomains to form horizontal lamellar structures has not been taken place after 2 h of annealing and mainly resembles a disordered state close to the film surface. It is suggested that the annealed sample is being frozen within the transition process from vertical to horizontal lamellar ordering, which takes much longer than the applied annealing time. The glass transition temperature is above 100 °C, which would mean that the transition process practically comes to rest at room temperature. The depth profiles imply that the transition starts at the surface within the topmost layer down to about half of the inter-lamellar separation distance. This could be explained by a higher mobility of the PS-*b*-P2VP microdomains at the surface in comparison to a greater film depth.

It has to be noted that AFM measurements alone would not have been sufficient to observe the full range of structural changes. Depth-resolved GISAXS is needed to observe the preservation of vertical order in greater depths of the film.

## 5.5 Summary

The presented contrast matching technique is not restricted to PS-*b*-P2VP, but can also be generally applied to studies of nanostructured layers of light materials, such as polymers on silicon, the most commonly used substrate material. A benefit of contrast matching is the minimisation of interface scattering effects, which overlay the weak scattering features of the film structure. GISAXS contrast matching can be seen, to some extent, as the X-ray pendant of depth-sensitive GISANS studies with contrast variation by deuteration.

Depth-sensitive GISAXS measurements at the contrast matching energy of 1827 eV on PS-*b*-P2VP thin films showed structural changes along the film depth after the annealing process. The as spun film exhibited fingerprint-like vertical lamellae with a separation distance of 59 nm throughout the entire film thickness of 85 nm. The annealed film showed a significantly reduced ordering towards the surface, within a depth of about 30 nm, while the order is preserved towards the bottom of the film.

Contrast-matched GISAXS and AFM measurements were used to clarify the state of in-plane ordering in the annealed film. Neither technique showed an indication of a significant formation of horizontal lamellae throughout the film thickness. It is suggested that the transition from vertical to horizontal ordering is not completed after 2 h of annealing and the transition process is frozen at room temperature. It was found that the transition starts in the topmost film layer, which suggests a higher mobility of the coalescing microdomains at the film surface.



# 6

## Dimensional nanometrology of organic thin film layers using XRR

XRR is a well established and widely used technique for measurements of the absolute thickness of thin film layers and layer systems on the nanometre scale. It also provides the interface roughness and the vertical electron density profile. However, organic layers with thicknesses above 10 nm have rarely been investigated using XRR. Within the framework of the EMRP IND15 ‘SurfChem’ project,\* reference materials are being developed for quantitative layer thickness determination of organic nanolayers. To establish the reference value for the layer thickness, a traceable measurement technique such as XRR is required. In contrast to the previous chapter, where an X-ray energy close to the silicon K-absorption edge was selected to minimise the contrast between substrate and polymer film, the goal here is to enhance the otherwise weak scattering contrast to reduce the uncertainties in XRR analysis.<sup>[126]</sup> This concept has also been applied previously to determine the individual layer thicknesses of an SiO<sub>2</sub> layer covered by a carbonaceous contamination layer, even on strongly curved surfaces.<sup>[129]</sup>

X-ray reflectometry data, regardless of the X-ray source used for the measurements, are most frequently analysed by modelling of the experimental data, for example, by using the Parrat formalism<sup>[182]</sup> (see Section 2.3 and Eq. (2.36)). While this approach is very successful for well defined sample systems with known optical constants, it becomes problematic in the case of samples with poorly known layer densities or limited confidence in the appropriateness of the model. This is particularly true for organic thin films, as the material density depends to a large extent on the preparation process and environment. A method to overcome the lack of an appropriate model is to analyse the frequency of the X-ray reflectance data,<sup>[41,204,205]</sup> analogous to the GISAXS analysis presented in Section 4.1. As expressed in Eq. (2.38), the measured reflectance  $R$  can be associated with the Fourier transform of the derivative of the electron density  $d\rho_e/dz$ , multiplied by the Fresnel reflectance  $R_F$ , as described in Section 2.3. Thus,  $R/R_F$  is by definition the PSD of  $d\rho_e/dz$ . By calculating the PSD spectrum of a measured XRR profile divided by its Fresnel reflectance, the thicknesses of the layers in the sample system

\* <http://www.emrp-surfchem.bam.de/en/home/index.htm>

can be deduced from the appearance of peaks at characteristic correlation lengths. The validity of such approach is limited to kinematic scattering (absence of anomalous, anisotropic, and multiple scattering; cf. Section 2.3) and to multilayer systems with a limited number of different layers that still allow to relate the PSD peaks to individual layers or groups of layers. Within this framework, frequency analysis is a robust and straightforward way to determine layer thicknesses in multilayer systems without the need of the density profile. Here, XRR and Fourier frequency analysis are developed and used to determine the individual thicknesses of organic layers and bilayers on top of an SiO<sub>2</sub> layer on Si substrates. Parts of this chapter have been published in J. Wernecke, A. G. Shard and M. Krumrey: 'Traceable thickness determination of organic nanolayers by X-ray reflectometry', *Surf. Interface Anal.* **46.10-11** (2014), pp. 911–914.

## 6.1 Materials and methods

The organic layer systems investigated are Irganox 1010 (C<sub>73</sub>H<sub>108</sub>O<sub>12</sub>) and Fmoc-pentafluoro-L-phenylalanine (C<sub>24</sub>H<sub>16</sub>F<sub>5</sub>NO<sub>4</sub>) layers, named Fmoc in the following, with nominal thicknesses from 20 nm to 100 nm. The samples were prepared by the National Physical Laboratory (NPL).<sup>\*</sup> The material was deposited by thermal evaporation using an Edwards AUTO306 vacuum coater on silicon wafer substrates. The wafers possessed a SiO<sub>2</sub> layer of a nominal thickness of 20 nm. Four different systems with the same total organic layer thickness were examined (all thicknesses are nominal values): A single Irganox layer of 100 nm (sample A), 50 nm Irganox on top of 50 nm Fmoc (sample B), 75 nm Irganox on 25 nm Fmoc (sample C), and 25 nm Irganox on 75 nm Fmoc (sample D). Ellipsometry measurements (see Section 2.7.3) were carried out at the NPL using a Woollam M2000DI spectroscopic ellipsometer to verify the homogeneity along the about 10 cm long and 1 cm wide samples. The variation in thickness of the organic coatings, caused by the evaporation geometry, was typically 1 % across the central 2 cm of the sample.<sup>†</sup>

The XRR measurements were performed at the FCM beamline of the PTB at BESSY II. The samples were mounted in the measurement chamber, the reflected and direct beam intensity was measured using a highly linear photodiode on the 2θ-axis, see Section 3.2. In principle, different photon energies near absorption edges of elements contained in the film layers could be used in order to maximise the contrast between the layers (Section 2.1.2): Measurements at the carbon K-edge are generally problematic due to the carbonaceous contamination of the optical elements in all synchrotron radiation beamlines. XRR tests were performed around the K-absorption edges of oxygen (present in all layers), fluorine (present in Fmoc), and at 1841 eV (between the absorption edges of silicon and silicon dioxide). As the observed oscillations of all layer systems were most pronounced at 1841 eV, this energy was chosen for all measurements. The reflected intensity was measured as a function of grazing incidence angle  $\alpha_i$  and normalised by the intensity of the incident X-ray beam.

For the analysis, the critical angle of total reflection  $\alpha_c$ , Eq. (2.8), is determined from the position of the first relevant maximum of the measured reflectance multiplied by  $q_i^4$ . The Fresnel reflectance  $R_F$  is then calculated according to Eq. (2.33).

Displayed in Fig. 6.1 are the measured reflectance curves and the deduced Fresnel reflectances of samples A and B, respectively. In order to prepare the XRR profiles for

<sup>\*</sup> contact: Alex G. Shard (alex.shard@npl.co.uk) <sup>†</sup> A. Shard, private communication.

Fourier transformation (Section 2.6), the Fresnel reflectance, Eq. (2.33), is fitted to the data (red line in Fig. 6.1) by least-squares optimisation of the critical angle  $\alpha_c$ . Fitting of the critical angle of all reflectance curves shown in Section 6.2 results in a mean value of  $0.694^\circ$  with a standard deviation of  $0.014^\circ$ . The measured reflectance profile is then divided by the Fresnel reflectance to obtain only the oscillatory part of the signal. This profile is multiplied by a Hann window function,<sup>[87]</sup> Eq. (2.49), to minimise the aliasing of the Fourier transform due to the finite signal length. The resulting profile is then transformed by a standard Fast Fourier transform algorithm, Eq. (2.47). The absolute square of the complex Fourier amplitude yields the PSD of the signal in accordance with Eq. (2.48). As before, the peaks in the PSD spectra correspond to characteristic vertical correlation lengths present in the XRR data, which is, in the present case, indicative of the thicknesses of individual layers and groups of layers.

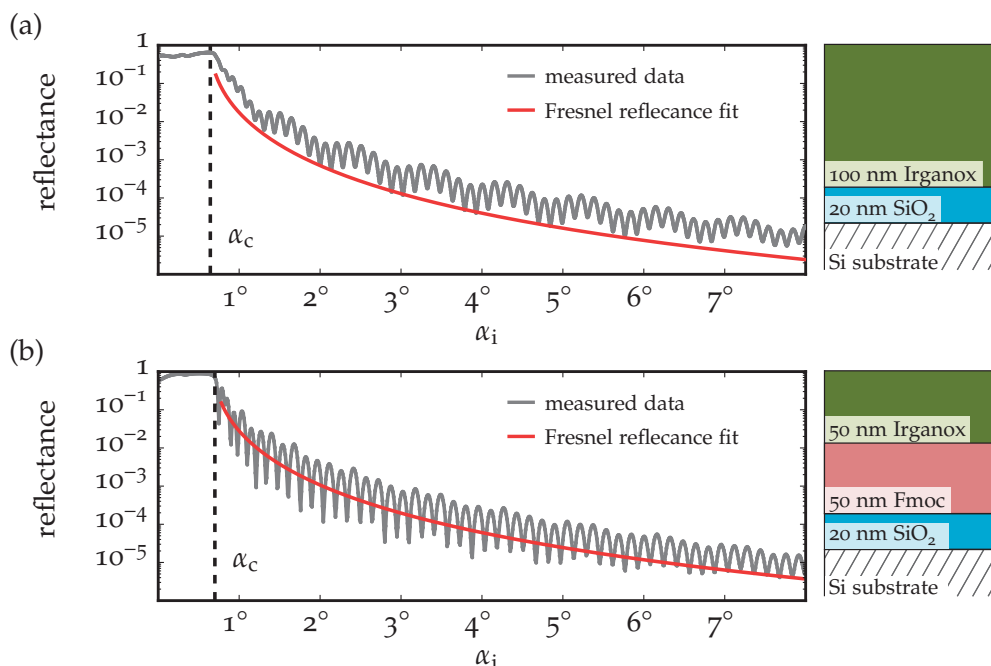


**Figure 6.1** | XRR profiles of (a) sample A and (b) B measured at a photon energy of 1841 eV. Also displayed are the schemes of the layer systems and the Fresnel reflectances (red lines), calculated from the critical angle  $\alpha_c$  as determined from the reflectance curves.

## 6.2 Results of the PSD peak analysis

Displayed in Fig. 6.2a–d are the PSD spectra of the samples A–D. The spectra of different layer systems are clearly distinct from one another. With some knowledge about the stacking order of the organic layers, the individual layer thicknesses can be obtained from the appearance of peaks corresponding to individual layers and groups of layers.

All PSD spectra exhibit a peak around 20.5 nm, which corresponds to the thickness of the  $\text{SiO}_2$  layer beneath the organic layer system, on top of the silicon substrate. The PSD spectrum of sample A as shown in Fig. 6.2a exhibits a peak at 107.0 nm, which corresponds to the Irganox layer thickness. The peak at 127.5 nm can be associated to the combined layer of Irganox and  $\text{SiO}_2$  and is in agreement with the sum of the thicknesses of the individual layers within 0.1 nm.

The organic layer system of sample B, Fig. 6.2b, has the same total thickness of

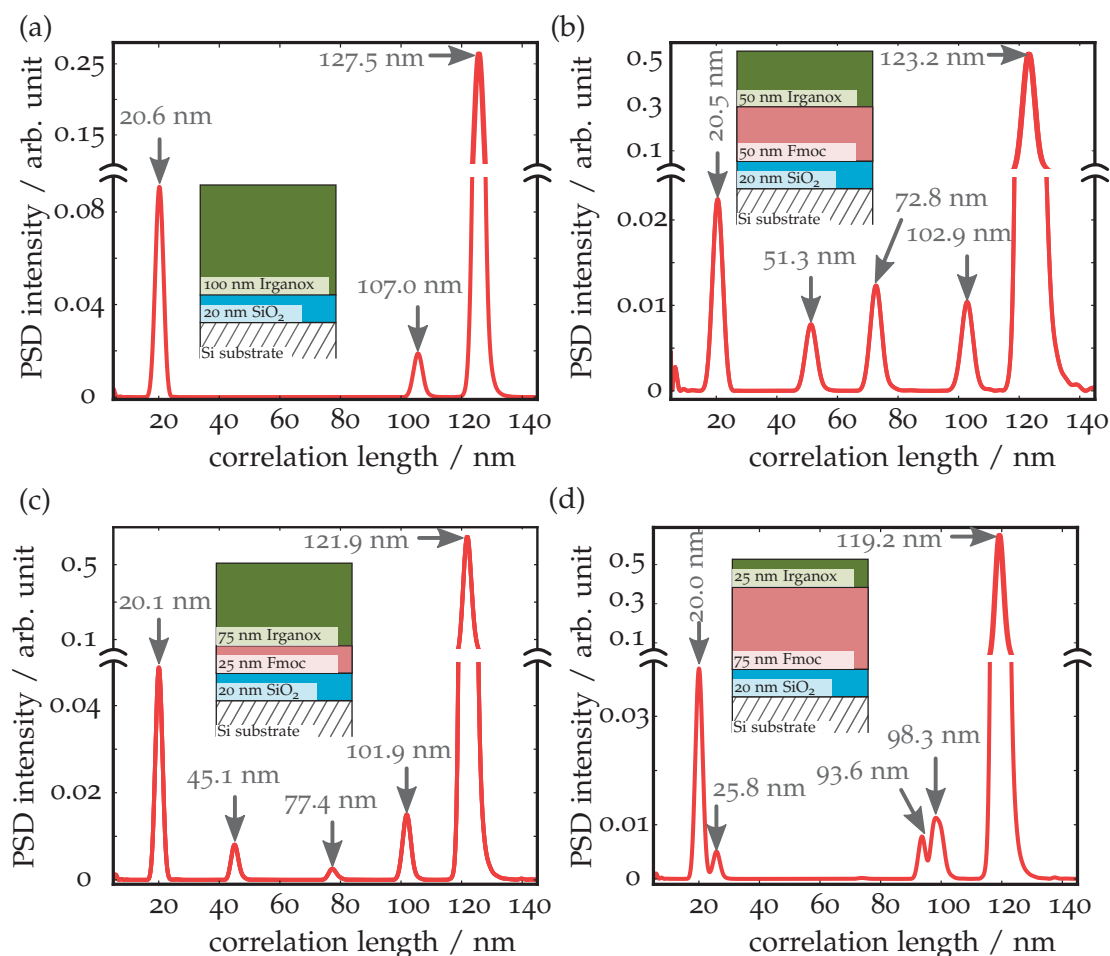


**Figure 6.2** | PSDs of the organic layer systems A-D (a-d) with a total layer thickness of 100 nm nominal value on SiO<sub>2</sub> (see insets for individual layer structure of the samples). Peaks in the PSD indicate characteristic correlation lengths, which correspond to single and compound layer thicknesses.

approximately 100 nm, but consists of two separate layers of Irganox and Fmoc, each with a nominal thickness of about 50 nm. Consequently, additional peaks at 51.3 nm and 72.8 nm appear in the PSD. These peaks originate from the individual organic layers and a grouped layer of Fmoc and SiO<sub>2</sub>. Table 6.1 summarises the individual layer thicknesses determined. The peak at 51.3 nm is a superposition of the Fmoc and the Irganox layer peaks as both have the same nominal thickness. Thus, this peak cannot be attributed unambiguously to one of the two layers, but both values must be close to 51.3 nm. By subtracting the SiO<sub>2</sub> layer peak at 20.5 nm from the peak at 72.8 nm, the thickness of Fmoc is determined as 52.3 nm. The thickness of the Irganox layer can be obtained from the peak at 102.9 nm by subtracting the Fmoc thickness of 52.3 nm or, alternatively, from the sum peak at 123.2 nm by subtracting the thickness of both other layers (nm). This results in values of the Irganox thickness of 50.6 nm and 50.4 nm, respectively. These values are in agreement within 0.2 nm, which is well within the PSD peak position uncertainty. The different thickness values stated in Table 6.1 for Fmoc and Irganox, respectively, are averaged and taken as the mean layer thicknesses as listed in Table 6.2

Sample C consists of a thick Irganox layer on top of a thin Fmoc layer, as illustrated by the inset of Fig. 6.2c. The Irganox layer thickness of 77.4 nm is obtained directly from the corresponding PSD peak. The Fmoc layer thickness of 25.0 nm is determined from the peak at 45.1 nm in the same way as described for sample B by subtracting the SiO<sub>2</sub> layer

PSD peak / nm	corresponding single layer thickness / nm		
	SiO <sub>2</sub>	Fmoc	Irganox
20.5	20.5	–	–
51.3	–	≈51.3	≈51.3
72.8	20.5	52.3	–
102.9	–	52.3	50.6
123.2	20.5	52.3	50.4

**Table 6.1** | PSD peak positions of reflectance data of sample B and the subsequently derived individual layer thickness of SiO<sub>2</sub>, Fmoc and Irganox. Values written in italics are obtained by combining other peaks of the same PSD.

thickness (20.1 nm).

In the case of sample D, Fig. 6.2d, the layer thicknesses of the topmost Irganox layer and the Fmoc layer beneath are reversed in comparison to sample C. Consequently, the PSD peak at 25.8 nm can be attributed to the Irganox layer, while the peaks at 93.6 nm and 98.3 nm correspond to a combination of Fmoc and SiO<sub>2</sub> as well as Irganox and Fmoc layer thicknesses, respectively. The resulting average Fmoc layer thickness of 73.6 nm in combination with the layer thicknesses of SiO<sub>2</sub> (20.0 nm) and Irganox (25.8 nm) is, again, in agreement within 0.2 nm with the sum peak at 119.2 nm corresponding to the combined thickness of all three layers.

The XRR results for all samples are summarised in Table 6.2 along with the results of the ellipsometry measurements, which were measured before and after each evaporation step. The data from ellipsometry are very close to the traceable XRR results. It is interesting to note that ellipsometry consistently under-estimates the XRR results by about 2 % for the organic materials. However, it is known<sup>[32,33]</sup> that ellipsometry possesses a high precision, but a low accuracy in itself and needs to be offset by an absolute method such as XRR, as mentioned in Section 2.7.3.

Sample	Layer (top → bottom)	measured thickness / nm	
		XRR	ellipsometry
A	Irganox	107.0	104.5
	SiO <sub>2</sub>	20.6	20.9
B	Irganox	50.5	49.2
	Fmoc	52.3	51.2
	SiO <sub>2</sub>	20.5	21.2
C	Irganox	77.4	75.7
	Fmoc	25.0	24.9
	SiO <sub>2</sub>	20.1	20.9
D	Irganox	25.8	25.2
	Fmoc	73.6	72.8
	SiO <sub>2</sub>	20.0	21.0

**Table 6.2** | Layer thicknesses determined by PSD analysis of the XRR data and from ellipsometric measurements performed before and after each evaporation step.

### 6.3 Traceability and Uncertainties

The correlation length scale is directly obtained from the vertical component of the scattering vector  $q_r = \frac{4\pi E_{ph}}{hc} \sin \alpha_i$ , Eq. (2.28), and depends only on the photon energy  $E_{ph}$  and on the grazing incidence angle  $\alpha_i$ . The photon energy scale uncertainty is listed in Table 3.2, while the angular scale of the goniometer is controlled by using a calibrated 12-sided polygon and an electronic autocollimator.<sup>[67]</sup> Both quantities have relative uncertainties below  $10^{-3}$ , see Section 3.2. To quantify the main uncertainty contribution due the Fourier analysis itself, the results for the layer thicknesses can be compared. The thickness of the SiO<sub>2</sub> layer should be identical for all samples, but values between 20.0 nm and 20.6 nm were obtained, corresponding to variations of  $\pm 1.5\%$ . Additionally, reflectance curves have been calculated in the framework of dynamic scattering theory using IMD<sup>[257]</sup> and then treated by Fourier analysis. The resulting layer thickness differed also by up to 1.5%, so that this value is a realistic estimate for the relative uncertainty. An example for the individual uncertainty contributions and the estimated combined standard uncertainty for the determined Irganox layer thickness of  $d = (107.0 \pm 1.5)$  nm in sample A is displayed in Table 6.3.

**Table 6.3** | Uncertainty budget of the Irganox layer thickness  $d = 107.0$  nm on sample A. Listed are the uncertainty contributions  $u(x_i)$  (normal-distributed) of each input quantity  $x_i$ , the uncertainty contribution type A or type B according to GUM,<sup>[16]</sup> the uncertainty components  $u_i(x_i)$ , and the estimated combined standard uncertainty  $u_c(d)$ .

input quantity $x_i$	type	$u_i(x_i)$	$u_i(d) / \text{nm}$
photon energy $E_{ph}$	B	0.4 eV	0.02
incidence angle $\alpha_i$	B	$< 0.005^\circ$	0.07
PSD peak position	A	1.4 nm	1.4
combined standard uncertainty $u_c(d)$ :			1.5

While the layer thicknesses can be obtained by pure Fourier analysis without modelling, surface and interface roughness are not accessible directly. However, the layer thicknesses from the Fourier analysis can serve as a starting point for modelling to obtain roughnesses and optical constants.

### 6.4 Comparison and validation of PSD peak positions with model data

#### 6.4.1 Refraction correction

The PSD analysis is now applied to model data calculated with IMD<sup>[257]</sup> according to Eq. (2.37) to compare and validate the PSD peak positions with the nominal model input parameters. The structure used for modelling is a single layer of palladium with the thickness  $d_{Pd}$ , the surface rms roughness  $\sigma_{Pd}$ , the mass density  $\rho_{Pd}$ , and the components

of the refractive index  $\delta_{\text{Pd}}$  as well as  $\beta_{\text{Pd}}$  on silicon substrate. Silicon has an interface rms roughness  $\sigma_{\text{Si}}$  and a mass density  $\rho_{\text{Si}}$ . The structure is restricted to a single layer on a substrate (as in Fig. 2.11) because otherwise, the number of different parameters and cross-correlations would be too large for a meaningful analysis. Each of the structural parameters of Si and Pd mentioned above is varied within a certain range as listed in Table 6.4, an XRR curve is calculated for every set of parameters. During a variation series of one of the input parameters, the others are kept fixed at the default value as stated in Table 6.4, unless stated otherwise. The other parameters in Table 6.4, which are the photon energy  $E_{\text{ph}}$ , the number of data points  $N$  of an XRR profile, the step size of the incidence angle  $\alpha_i$  between neighbouring reflectance values, the addition of zeros to the reflectance data array (zero padding), and for the width of the Fourier window  $\gamma$ , Eq. (2.50), are also evaluated in their influence on  $d_{\text{PSD}}$ , which is presented in Section 6.4.2.

Every calculated reflectance curve is processed by the same PSD analysis method as in Section 6.2 to generate the corresponding PSD with the characteristic correlation length peak at  $d_{\text{PSD}}$ . The relative deviation  $(\frac{d_{\text{PSD}}}{d_{\text{Pd}}} - 1) \times 100\%$  of the nominal model thickness  $d_{\text{Pd}}$  and the PSD peak position of the layer thickness  $d_{\text{PSD}}$  is a measure for the accuracy of the PSD analysis method. Figure 6.3 shows a typical XRR curve of a 100.4 nm Pd layer on silicon substrate, calculated using IMD, and the corresponding PSD. The spacing between the points in the PSD indicates the bin size of the Fourier spectrum of 2.4 nm due to the finite number of data points  $N$  of the reflectance curve.

**Table 6.4** | Variation ranges and default values for input parameters of reflectance model curves calculated with IMD. The model is a layer of palladium with a thickness  $d_{\text{Pd}}$ , an rms roughness  $\sigma_{\text{Pd}}$ , a mass density  $\rho_{\text{Pd}}$ , and refractive index components  $\delta_{\text{Pd}}$  and  $\beta_{\text{Pd}}$  on silicon substrate. Silicon has an rms roughness  $\sigma_{\text{Si}}$  and a mass density  $\rho_{\text{Si}}$ . Also listed are the variation ranges of the number of data points of the reflectance curve  $N$ , the number of zeros added to the end of the reflectance data array (zero padding, see Section 6.4.2), the photon energy  $E_{\text{ph}}$ , and the step size of the incidence angle  $\alpha_i$  of the calculated XRR curve.  $\gamma$  indicates the width of the Kaiser window, Eq. (2.50), of the PSD analysis (see Section 6.4.2).

input parameter	default value	variation range	
		min	max
$d_{\text{Pd}}$ / nm	–	3.2	173.9
$\rho_{\text{Pd}}$ / g cm <sup>-3</sup>	12.0	1.5	14.5
$\sigma_{\text{Pd}}$ / nm	0.3	0.01	1.2
$\delta_{\text{Pd}}$ at 5875 eV	$6.31 \times 10^{-5}$	$2 \times 10^{-5}$	$2 \times 10^{-4}$
$\beta_{\text{Pd}}$ at 5875 eV	$9.41 \times 10^{-6}$	$2.8 \times 10^{-6}$	$2.8 \times 10^{-5}$
$\rho_{\text{Si}}$ / g cm <sup>-3</sup>	2.3	–	–
$\sigma_{\text{Si}}$ / nm	0.3	0.01	0.7
$E_{\text{ph}}$ / eV	5875	1841	5875
number of data points $N$	1000	250	2500
$\alpha_i$ step size	0.01	0.005	0.05
zero padding	$20 \times N$	0	$40 \times N$
window width $\gamma$	8	0	30

First, a series of XRR curves for different layer thickness  $d_{\text{Pd}}$  from 3.2 nm to 173.9 nm is generated and analysed by PSD analysis. The relative thickness deviation of PSD-determined thickness  $d_{\text{PSD}}$  and nominal thickness  $d_{\text{Pd}}$  shown by black dots in Fig. 6.4a

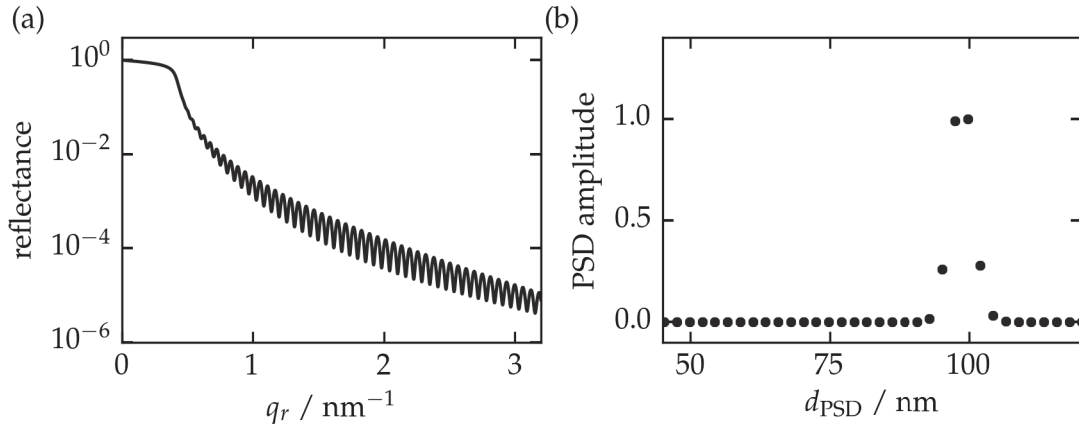


**Figure 6.3** | (a) XRR profile calculated by dynamic theory, Eq. (2.37), with IMD<sup>[257]</sup> for a layer of palladium (Pd) with a thickness of  $d_{\text{Pd}} = 100.4 \text{ nm}$  on a silicon substrate. (b) PSD of the XRR profile. The spacing between the points in the PSD corresponds to the bin size of 2.4 nm of the Fourier transform.

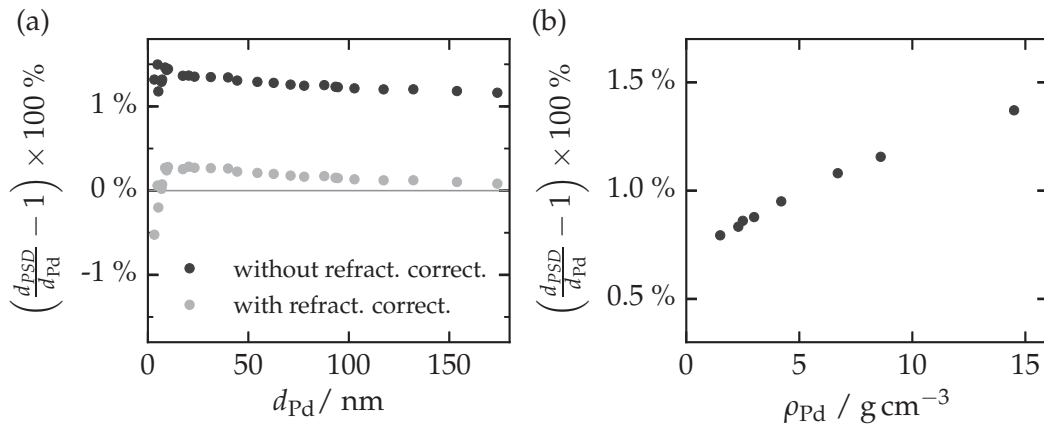


**Figure 6.4** | Relative deviation of thickness determined by PSD analysis  $d_{\text{PSD}}$  from nominal model thickness  $d_{\text{Pd}}$  ( $E_{\text{ph}} = 5875 \text{ eV}$ ). (a) Variation of  $d_{\text{Pd}}$ , relative deviation without (black dots) and with (grey dots) refraction correction (see text). (b) Variation of the nominal density of Pd at a given thickness of 153.8 nm.

exhibits a systematic, approximately constant relative deviation of  $d_{\text{PSD}}$  of 1.3% for all but the smallest thickness values.

A variation of the density of the layer  $\rho_{\text{Pd}}$ , shown exemplary in Fig. 6.4b for  $d_{\text{Pd}} = 153.8 \text{ nm}$ , reveals an increase in the relative thickness deviation with increasing layer density, i.e. with a increasing density contrast between layer and substrate. This indicates that the observed deviation between  $d_{\text{PSD}}$  and the nominal model value  $d_{\text{Pd}}$  is due to refraction in the layer as illustrated in Fig. 2.8. Thus, the influence of a variation of both refractive index components, Eq. (2.4), of the Pd layer,  $\delta_{\text{Pd}}$  and  $\beta_{\text{Pd}}$ , respectively, on the thickness deviation is examined. Figure 6.5 shows the relative thickness deviation of  $d_{\text{PSD}}$  as a function of  $\delta_{\text{Pd}}$  (black dots) and  $\beta_{\text{Pd}}$  (grey dots). The default value of the IMD database (black and grey square in Figure 6.5) for  $\delta_{\text{Pd}}$  and  $\beta_{\text{Pd}}$ , respectively, is used during the variation of the other parameter. The variation in  $\beta_{\text{Pd}}$  has only a minor influence, while the relative thickness deviation increases nearly linearly with increasing  $\delta_{\text{Pd}}$ . Consequently, a refraction correction in analogy to Eq. (2.31) should be applied to

the  $\alpha_i$  scale of the calculated reflectance curves by the replacement

$$R(\alpha_i) \longrightarrow R\left(\sqrt{\alpha_i^2 - \alpha_c^2}\right). \quad (6.1)$$

The square of the critical angle  $\alpha_c$  is proportional to  $\delta$ , see Eq. (2.9), hence Eq. (6.1) fully accounts for the linear dependence of the thickness deviation and  $\delta_{\text{Pd}}$  observed in Fig. 6.5. The critical  $\alpha_c$  is determined directly from the reflectance data by fitting the Fresnel reflectance, Eq. (2.33), to the data as described in Section 6.2. Applying the refraction correction Eq. (6.1) to the calculated XRR profiles of the  $d_{\text{Pd}}$  variation series shown in Fig. 6.4a results in a reduction of the relative deviation of the thickness determined with PSD analysis  $d_{\text{PSD}}$  from about 1.3 % (black dots in Fig. 6.4a) to about 0.2 % (grey dots).

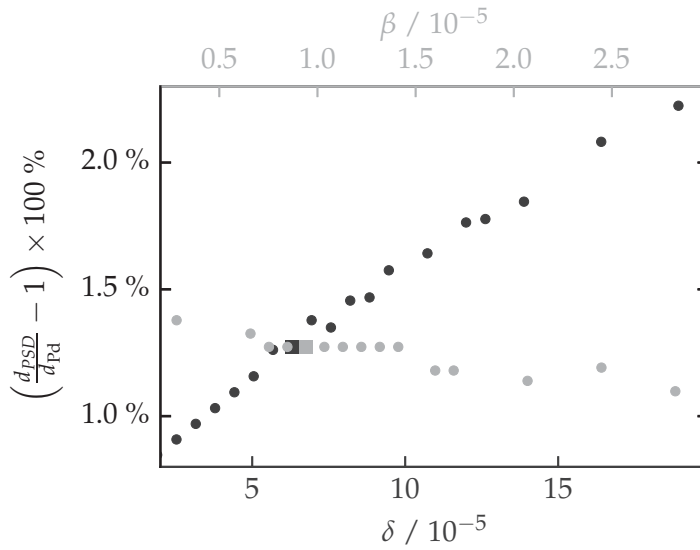


**Figure 6.5** | Relative deviation of thickness determined by PSD analysis from nominal thickness upon variation of  $\delta$  and  $\beta$  at  $E_{\text{ph}} = 5875 \text{ eV}$ . The black and grey square indicate the IMD database value of  $\delta_{\text{Pd}}$  and  $\beta_{\text{Pd}}$ , respectively.

The question remains if the results on the organic multilayer thicknesses determined in Section 6.2 are still correct in the light of the presented model comparison. Palladium with a bulk density of  $12 \text{ g cm}^{-3}$  has a high critical angle, which results in a comparably large effect of the refraction correction. The organic multilayers are, however, mainly carbon layers with a low density around  $1 \text{ g cm}^{-3}$ . It has been demonstrated in Fig. 6.4b that the thickness deviation decreases with decreasing layer density. In order to evaluate the effect of refraction on a sample system that is similar to the investigated organic layer systems, additional reflectance curves are calculated with IMD.

The model used is a carbon layer with a thickness  $d_C$  of  $47.8 \text{ nm}$  and mass density of  $\rho_C = 1.2 \text{ g cm}^{-3}$  on top of a  $\text{SiO}_2$  layer ( $d_{\text{SiO}_2} = 20.5 \text{ nm}$ ) on a silicon substrate, analogous to sample A in the inset of Fig. 6.2a. The XRR curves calculated at  $E_{\text{ph}} = 1841 \text{ eV}$  are analysed in the same way as before. Without refraction correction, the obtained PSD peak positions are  $21.0 \text{ nm}$  for  $\text{SiO}_2$  and  $48.6 \text{ nm}$  for carbon, respectively. Accounting for refraction yields PSD peaks at  $20.1 \text{ nm}$  and  $46.8 \text{ nm}$  for the oxide layer and the carbon layer, respectively. Both carbon layer thickness values differ by around  $1.0 \text{ nm}$  from the nominal thickness of  $47.8 \text{ nm}$ , which is well within the uncertainty contribution of the peak position of  $1.4 \text{ nm}$  as stated in Table 6.3. It seems that the under-estimation of the layer thickness by the refraction correction and the over-estimation without it have a similar magnitude under the investigated conditions of a low layer density. The analysis of the simulated reflectance curves illustrates that it is not straight forward to implement a refraction correction for a multilayer system and doing so does not necessarily yield

more accurate results. Consequently, the implementation of a refraction correction is not purposeful for the investigated organic multilayer systems. The determined uncertainty value of the PSD peak position also covers possible deviations induced by refraction, hence, the thickness values displayed in Table 6.2 remain accurate within the uncertainty range.

## 6.4.2 Recommended settings

The influence on the relative thickness deviation has been studied in the same way for the other parameters listed in Table 6.4, specifically for the interface rms roughness of silicon  $\sigma_{\text{Si}}$  and of palladium  $\sigma_{\text{Pd}}$ , for the number and of data points, for the  $\alpha_i$  step size, for the zero padding of the transformed data profile (see below), and the width of the Fourier window function. The latter is studied by using a Kaiser window, Eq. (2.50), with a variable width  $\gamma$  instead of a Hann window, Eq. (2.49), used in Sections 6.2 and 6.4.1. At  $\gamma = 6$ , the Kaiser window closely resembles the Hann window as illustrated in Fig. 2.15. Below is a summary of the main findings and some recommendations for settings that resulted in a minimisation of the relative thickness deviation  $(\frac{d_{\text{PSD}}}{d_{\text{Pd}}} - 1) \times 100\%$  of the nominal model thickness  $d_{\text{Pd}}$  and the PSD peak position of the layer thickness  $d_{\text{PSD}}$  as described in Section 6.4.1.

### Substrate and layer interface roughness

The deviation  $\frac{d_{\text{PSD}}}{d_{\text{Pd}}}$  increases with increasing interface roughness due to damping and smearing of the oscillations in the reflectance curve. A meaningful PSD analysis is not possible when less than  $\lesssim 4$  full oscillations are present in a reflectance curve such as Fig. 6.3 due to high interface roughness.

### Number and range of data points

The  $\alpha_i$  range measured should at least cover 4 to 5 full oscillations of the reflectance curve for a meaningful PSD analysis.  $\frac{d_{\text{PSD}}}{d_{\text{Pd}}}$  decreases with increasing number of oscillations in the profile and it remains constant from about 20 period lengths covered by the XRR range. The data point step size in  $\alpha_i$ , i.e. the  $\alpha_i$  resolution, should at least facilitate 4 to 5 points for the smallest oscillation period length, i.e. the largest correlation length. Much lower step sizes have no significant influence.

### Zero padding

Zero padding means to add a number of zeros to the beginning or to the end of the reflectance data points, i.e. to make the reflectance data array longer without adding any information. Padding of the data profile with zeros makes the shape of the resulting PSD peaks smoother, but does not improve the resolution, which is determined solely by the probed  $\alpha_i$  range. Increasing the amount of zero padding seems to shift the peaks systematically to slightly higher peak positions in comparison to unpadded PSD peaks, but stays well within the PSD bin size for the model system shown in Fig. 6.3. The observed peak shift with increasing zero padding ranges from 0.2 nm to a maximum of 1.0 nm, while the PSD bin size is 2.4 nm. Increasing the number of attached zeros beyond around 30 times the number of data points does not decrease the relative thickness deviation  $\frac{d_{\text{PSD}}}{d_{\text{Pd}}}$  any more. A recommended number of zero values attached to

the reflectance data is about 15 to 20 times the number of data points, which offers a reasonable compromise between computation time and thickness deviation.

### Kaiser window width $\gamma$

The thickness deviations at  $\gamma \lesssim 1$  are very diverse and highly depend on the first and last value of the profile to be transformed due to the periodic continuation in Fourier analysis. There is no significant influence on the relative deviation at larger values until the window gets too narrow for  $\gamma \gtrsim 20$ . A recommended  $\gamma$  range is roughly 5 to 10, i.e. a value of 6 that resembles very closely a Hann window would also be an adequate choice.

## 6.5 Summary

Synchrotron radiation XRR and Fourier analysis enable the measurement of the thickness of organic layer systems without prior knowledge of optical constants or densities of the individual thin film layers. By using the PSD analysis of reflectance curves measured at a photon energy of 1841 eV close to the Si K-absorption edge for maximal scattering contrast, it can be clearly distinguished between the Irganox 1010 layer and the Fmoc layer in spite of the low scattering contrast at the common interface. The PSD peaks of XRR curves of the different organic layer systems correspond to the thicknesses of individual layers or groups of layers with a common interface. Although the stacking order is not clear from the PSD spectrum, the electron density depth profile implies that individual layer peaks only appear for the topmost organic layer and for the SiO<sub>2</sub> layer, but not for buried organic layers with one or two interfaces to another organic layer due to the low scattering contrast. However, in combination with a general knowledge of the layer stacking order, it is also possible to determine the thickness of the buried organic layer and to clearly distinguish the different combinations of organic layers with a total thickness of about 100 nm. A comparison with model data of a single high-density layer on a silicon substrate shows that the relative deviation of PSD peak position and model thickness can be reduced by a factor of 3 to 5 for this system by introducing a refraction correction. A comparison of modelled XRR curves of a similar, yet simpler, system at 1841 eV analysed with and without refraction correction showed a similar absolute thickness deviation of around 1 nm in positive (without correction) and negative (with correction) direction. These deviations are, however, well within the uncertainty of the PSD peak position of 1.4 nm and are thus accounted for in the uncertainty budget in Table 6.3.

Hence, Fourier analysis of XRR data provides a robust method to determine thin film layer thicknesses and requires only very few model assumptions. The obtained thickness values can be used as traceable layer thickness data for reference materials, which are required to qualify other quantitative methods, e.g. for chemical surface analysis.



# 7

## Summary and Outlook

The purpose and goal of this work was to contribute to the fields in nanotechnology advancement as stated in the introduction:

- (i) How can the measurement of nano-dimensional size parameters, in the specific case of grazing incidence small-angle X-ray scattering (GISAXS) measurements, be evaluated in a metrologic manner by establishing traceability?
- (ii) How can the instrumentation for GISAXS measurements be extended to yield further insight into recent nanotechnological applications, i.e. nanostructured polymer thin films?

Regarding the first question on nanometrology, surface grating structures with structure sizes from almost  $1\ \mu\text{m}$  down to  $25\ \text{nm}$  were investigated using GISAXS and analysed by direct analysis methods. The term 'direct analysis' refers to the retrieval of structural parameters directly from the measurement data, that is, without the selection of suitable form factors and structure factors for numerical simulations. Such a direct analysis method restricts the analysis mainly to an evaluation of the structure factor and thus of the positions of scattering features. In this way, only a limited set of dimensional features, namely, the grating pitch, the critical dimension, the groove width, and the line height can be accessed. But it opens up the possibility of the traceability of GISAXS measurements, as it is independent from the selection of models for the form factor and the structure factor. Consequently, the 'correctness' of the model itself does not have to be evaluated in its influence on the uncertainty from *within* the model. The uncertainty is solely determined by the uncertainty contributions of the experimental input parameters. The different implementations of the direct analysis demonstrated are all based on the evaluation of the characteristic frequencies. These are present in GISAXS intensity patterns along the semi-circular intersection of the Ewald sphere and the grating truncation rods (GTRs) of the grating. For large pitches close to  $1\ \mu\text{m}$ , this is realised by computing the discrete Fourier transform (DFT) of the profile and evaluating the power spectral density (PSD). Scattering images of gratings with intermediate pitches between  $250\ \text{nm}$  and  $50\ \text{nm}$  were also evaluated by the PSD of the Fourier amplitudes. However, especially the non-uniformly spaced data and the reduced number of GTRs

along the intersection required a different approach to that of DFT. Instead, the Fourier amplitudes of a finite number of Fourier base vector coefficients were fitted to the data profile in conjunction with the Tikhonov regularisation. Small pitches below 50 nm were analysed by determining the distances between GTRs on the detector image because of the low number of GTRs along the Ewald sphere intersection. Traceability of a GISAXS measurement was established in determining the value and uncertainty of a self-assembled polymer grating pitch  $P = (24.83 \pm 0.09)$  nm, i.e. with a relative uncertainty below 0.4%, by tracing all contributing parameters: the sample-detector distance, the detector pixel size, the photon energy, and the separation distance between the GTRs. It was found that the predominant contributions to the uncertainty budget arise from the sample-detector distance and the pixel size, both in the range of  $10^{-3}$  in their relative uncertainty contributions. In any case, a traceable dimensional parameter determined by such direct GISAXS data analysis can serve as a reference value that must be reproduced by any other analysis method such as numerical modelling. In this way, traceable direct analysis provides a means to validate and compare other analysis methods in a general context, not just for grating structures. Moreover, it provides a value for the achievable measurement accuracy that can be expected in a GISAXS measurement, which is important for the interpretation of any GISAXS data analysis result.

As an outlook for future activities in the field of dimensional nanometrology, full modelling of the scattering intensities in semi-kinematic and dynamic theories, most notably by using distorted wave Born approximation (DWBA) and Maxwell solvers, could be investigated. Full modelling provides a larger set of dimensional parameters such as the sidewall angle, the corner rounding at top and bottom of the lines, as well as the line cross-section shape. Moreover, the parameters of the form factor and structure factor model can be varied in a well-defined way in order to evaluate the sensitivities of the different scattering features in the GISAXS image. This should yield additional information on the origin of these diffuse scattering features and especially on the question as to whether any of these features of a single-shot GISAXS image can be used to determine additional grating parameters. Another challenge and prospective field of activity is the realisation of traceability of one or several modelling-based analysis methods, e.g. Maxwell solver or DWBA. This would allow for the comparison of different methods of analysis and for the validation of the analysis results of the models against the reference values of direct analysis. The mid-term goal of such an analysis would be to realise a metrologic comparison and cross-validation of different direct and indirect tools of dimensional nanometrology (atomic force microscopy, electron microscopy, scatterometry, GISAXS) on common sample systems. A very desirable achievement would be a common 'golden' reference standard that can be used by all methods for calibration. From the instrumentation point of view, it could be beneficial to use a  $\mu\text{m}$ -sized X-ray beam. This would reduce the beam footprint drastically, which allows for smaller samples, i.e. of lithographic structures, and a reduced uncertainty of the sample-detector distance measurement.

Also related to the first point of contributing to dimensional nanometrology are the presented traceable X-ray reflectometry (XRR) thickness measurements of polymer layer systems. The samples were challenging because of the low scattering contrast between the different layers and the poorly known optical constants of the polymeric material. The investigation showed that it is possible to obtain traceable thickness values of different layer systems by maximising the scattering contrast at a photon energy of 1841 eV and by a direct analysis of the Fourier PSD of the reflectance curves. An analysis of calculated

XRR model curves using the PSD method to evaluate the influence of the direct analysis process showed that a refraction correction is useful in many cases. The correction can be implemented by determining the critical angle directly from the XRR data.

The other aspect of the stated goals of this work is the availability and application of extended instrumentation that allows GISAXS imaging in the tender X-ray regime below 5 keV. The in-vacuum PILATUS 1M detector developed is able to cover the full photon energy range from 1.75 keV to 10 keV of the four-crystal monochromator (FCM) beamline and has been in routine operation since July 2012. Geometric and radiometric characterisation of the detector showed an excellent quantum efficiency of  $> 80\%$  above 3.4 keV and a quantum efficiency sufficient for imaging down to 1.75 keV. The extension of the accessible photon energy range down to the lower limit of the beamline offers advantages in several ways: At a given sample-detector distance, the  $q$  resolution and the  $q$  range on the detector can be varied by a factor of more than 5 by a variation of the photon energy. The SAXS instrument allows a variation of the sample-detector distance by an additional factor of 2.5 without breaking the vacuum. In this way, it is possible to tune the accessible maximal correlation size, i.e. highest  $q$  resolution, and minimal size, i.e. highest  $q$  range, during the experiment by more than a factor of 12. This is, to a certain degree, a compact alternative to an ultra-small angle scattering setup, where the sample-detector distance is usually around 10 m and above. The second, probably more obvious, advantage of scattering measurements in the tender X-ray regime is access to the K-absorption edges of light elements such as silicon, sulphur, phosphorus, chlorine, and calcium. Such elements are present in many topical materials in semiconductor lithography, organic photovoltaics, functional polymer thin films, and bio-films, to mention but a few examples. This opens up the possibility for anomalous scattering techniques to enhance the element-specific scattering contrast or to selectively minimise the contrast between different constituents. Thus, structural information on the distribution, changes and morphology of the components of blend materials become available, which yields new insights into the fabrication, function, and manipulation of nanostructured materials.

An example of the extended GISAXS measurement capabilities in the tender X-ray regime was demonstrated and published on the topic of depth-resolved GISAXS measurements at the silicon K-edge on as spun and annealed block copolymer thin films (PS-*b*-P2VP). GISAXS measurements at 1827 eV enabled to match the scattering contrast between the polymer film and the underlying silicon substrate to minimise the contribution of substrate interface scattering. It was shown that such GISAXS contrast-matching allowed studies of nanostructures along the depth of the film without the superposition of unwanted substrate interface reflection and multiple scattering of reflected waves. Using this technique, it was possible to resolve the onset and progress of structural changes due to thermal annealing in PS-*b*-P2VP thin films along the depth of the film. As opposed to the untreated sample, the annealed film showed a significant decrease of ordering of the vertical fingerprint-like lamellae at the film surface. However, increasing the penetration depth of the incident X-ray beam revealed that the ordering is preserved below a depth of around 30 nm down to the substrate interface as in the untreated film. At the same time, no indication of a significant formation of horizontal lamellae was found at any depth, which is expected to occur at later stages of annealing. These depth-dependent structural properties would not be visible in a surface-sensitive technique such as atomic force microscopy (AFM) and are very difficult to obtain in any other way due to a lack of suitable non-destructive measurement methods. The only other technique capable of

## SUMMARY AND OUTLOOK

performing similar measurements is grazing incidence small-angle neutron scattering (GISANS). GISANS offers some appealing advantages, such as tunable scattering contrast of the different components of the blend polymer film, but is limited in the achievable  $q$  resolution, the exposure times are long (hours to days), and the counting statistics are low. Hence, the demonstrated method of depth-sensitive GISAXS using contrast matching is a useful addition and sometimes an alternative to very elaborate GISANS studies for a wide range of nanostructured polymer layers.

As an outlook, it would be interesting to continue the activities of scattering techniques in the tender X-ray regime on technologically and scientifically relevant sample systems. In terms of the PS-*b*-P2VP thin films investigated, an option could be to equip the sample chamber of the FCM beamline with a simple heating stage to perform *in-situ* GISAXS measurements with depth resolution and contrast matching during annealing. In this way, it might be possible to observe the different stages of ordering, for example, from vertical to horizontal lamellae, as a function of film depth and thermal annealing conditions. The demonstration of the possibilities of GISAXS experiments in the tender X-ray regime initiated a number of ongoing and prospective collaborations with groups from TU Munich, the Lawrence Berkeley National Laboratory, the University of Kyoto, and Stanford University in different areas of applications such as organic photovoltaics, thermoelectric polymer films, and fuel cell membranes. It seems attractive to take advantage of the currently quite exclusive measurement capabilities of the in-vacuum PILATUS 1M to contribute to these up-to-date fields of application-driven material research. Such collaborations also allow to contribute the expertise of the Physikalisch-Technische Bundesanstalt (PTB) in metrology in general and in dimensional nanometrology in particular to topical research activities as well as to provide a high visibility of the PTB in the field of expertise.

## References

- [1] D. Abou-Ras, R. Caballero, C.-H. Fischer, C. Kaufmann, I. Lauermann, R. Mainz, H. Mönig, A. Schöpke, C. Stephan, C. Streeck et al.: 'Comprehensive Comparison of Various Techniques for the Analysis of Elemental Distributions in Thin Films'. In: *Microsc. Microanal.* **17.05** (2011), pp. 728–751. DOI: 10.1017/S1431927611000523.
- [2] J. N. L. Albert and T. H. Epps III: 'Self-assembly of block copolymer thin films'. In: *Mater. Today* **13.6** (2010), pp. 24–33. DOI: 10.1016/S1369-7021(10)70106-1.
- [3] B. Andreas, Y. Azuma, G. Bartl, P. Becker, H. Bettin, M. Borys, I. Busch, M. Gray, P. Fuchs, K. Fujii et al.: 'Determination of the Avogadro Constant by Counting the Atoms in a Si<sub>28</sub> Crystal'. In: *Phys. Rev. Lett.* **106.3** (2011), p. 030801. DOI: 10.1103/PhysRevLett.106.030801.
- [4] P. Andreatza, H. Khelfane, O. Lyon, C. Andreatza-Vignolle, A. Y. Ramos and M. Samah: 'Trends in anomalous small-angle X-ray scattering in grazing incidence for supported nanoalloyed and core-shell metallic nanoparticles'. In: *Eur. Phys. J. Spec. Top.* **208.1** (2012), pp. 231–244. DOI: 10.1140/epjst/e2012-01621-4.
- [5] R. M. A. Azzam and N. M. Bashara: *Ellipsometry and polarized light*. North-Holland, Amsterdam, 1987.
- [6] D. Babonneau, S. Camelio, D. Lantiat, L. Simonot and A. Michel: 'Waveguiding and correlated roughness effects in layered nanocomposite thin films studied by grazing-incidence small-angle x-ray scattering'. In: *Phys. Rev. B* **80.15** (2009), p. 155446. DOI: 10.1103/PhysRevB.80.155446.
- [7] D. Babonneau: 'FitGISAXS: software package for modelling and analysis of GISAXS data using IGOR Pro'. In: *J. Appl. Cryst.* **43.4** (2010), pp. 929–936.
- [8] J. Bahrtdt, W. Frentrup, A. Gaupp, M. Scheer, W. Gudat, G. Ingold and S. Sasaki: 'Elliptically polarizing insertion devices at BESSY II'. In: *Nucl. Instrum. Meth. A.* 7th Int.Conf. on Synchrotron Radiation Instrumentation **467–468, Part 1** (2001), pp. 21–29. DOI: 10.1016/S0168-9002(01)00554-X.
- [9] J. Bang, B. J. Kim, G. E. Stein, T. P. Russell, X. Li, J. Wang, E. J. Kramer and C. J. Hawker: 'Effect of Humidity on the Ordering of PEO-Based Copolymer Thin Films'. In: *Macromolecules* **40.19** (2007), pp. 7019–7025. DOI: 10.1021/ma0710737.
- [10] C. M. Bates, M. J. Maher, D. W. Janes, C. J. Ellison and C. G. Willson: 'Block Copolymer Lithography'. In: *Macromolecules* **47.1** (2014), pp. 2–12. DOI: 10.1021/ma401762n.

## References

- [11] F. S. Bates and G. H. Fredrickson: 'Block Copolymer Thermodynamics: Theory and Experiment'. In: *Annu. Rev. Phys. Chem.* **41.1** (1990). PMID: 20462355, pp. 525–557. DOI: 10.1146/annurev.pc.41.100190.002521.
- [12] B. Beckhoff, A. Gottwald, R. Klein, M. Krumrey, R. Müller, M. Richter, F. Scholze, R. Thornagel and G. Ulm: 'A quarter-century of metrology using synchrotron radiation by PTB in Berlin'. In: *Phys. Status Solidi B* **246.7** (2009), pp. 1415–1434. DOI: 10.1002/pssb.200945162.
- [13] B. Bhushan, ed.: *Springer Handbook of Nanotechnology*. Springer, Berlin/Heidelberg, 2010. 1968 pp.
- [14] G. Binnig, C. F. Quate and C. Gerber: 'Atomic Force Microscope'. In: *Phys. Rev. Lett.* **56.9** (1986), pp. 930–933. DOI: 10.1103/PhysRevLett.56.930.
- [15] BIPM: *The International System of Units (SI)*. 8th ed. Sèvres, Paris: BIPM, 2006.
- [16] BIPM, IEC, IFCC, ILAC, IUPAC, IUPAP, ISO and OIML: *Evaluation of measurement data - Guide for the expression of uncertainty in measurement*. JCGM 100: 2008. BIPM, 2008.
- [17] BIPM, IEC, IFCC, ILAC, IUPAC, IUPAP, ISO and OIML: *Evaluation of measurement data - Supplement 1 to the 'Guide to the Expression of Uncertainty in Measurement' - Propagation of distributions using a Monte Carlo method*. Vol. JCGM 101. Joint Committee for Guides in Metrology, Bureau International des Poids et Mesures, 2008.
- [18] BIPM, IEC, IFCC, ILAC, IUPAC, IUPAP, ISO and OIML: *The international vocabulary of metrology - basic and general concepts and associated terms (VIM), 3rd edn*. JCGM 200: 2012. BIPM, 2008.
- [19] BIPM, IEC, IFCC, ILAC, IUPAC, IUPAP, ISO and OIML: *Evaluation of measurement data - Supplement 2 to the 'Guide to the expression of uncertainty in measurement' - Extension to any number of output quantities*. Vol. JCGM 102. Joint Committee for Guides in Metrology, Bureau International des Poids et Mesures, 2012.
- [20] M. Björck and G. Andersson: 'GenX : an extensible X-ray reflectivity refinement program utilizing differential evolution'. In: *J. Appl. Cryst.* **40.6** (2007), pp. 1174–1178. DOI: 10.1107/S0021889807045086.
- [21] R. B. Blackman and J. W. Tukey: *The measurement of power spectra: from the point of view of communications engineering*. Dover, New York, 1958. 190 pp.
- [22] T. N. Blanton, T. C. Huang, H. Toraya, C. R. Hubbard, S. B. Robie, D. Louër, H. E. Göbel, G. Will, R. Gilles and T. Raftery: 'JCPDS-International Centre for Diffraction Data round robin study of silver behenate. A possible low-angle X-ray diffraction calibration standard'. In: *Powder Diff.* **10.02** (1995), pp. 91–95. DOI: 10.1017/S0885715600014421.
- [23] P. Bloomfield: *Fourier Analysis of Time Series: An Introduction*. John Wiley & Sons, 2004. 285 pp.
- [24] M. R. Bockstaller, R. A. Mickiewicz and E. L. Thomas: 'Block Copolymer Nanocomposites: Perspectives for Tailored Functional Materials'. In: *Adv. Mater.* **17.11** (2005), pp. 1331–1349. DOI: 10.1002/adma.200500167.

- [25] B. Bodermann, B. Loechel, F. Scholze, G. Dai, J. Wernecke, J. Endres, J. Probst, M. Schoengen, M. Krumrey, P.-E. Hansen and V. Soltwisch: 'Development of a scatterometry reference standard'. In: *Proc. SPIE. Optical Micro- and Nanometrology V*. Ed. by C. Gorecki, A. K. Asundi and W. Osten. Vol. 9132. 2014, 91320A. DOI: 10.1117/12.2052278.
- [26] M. Born and E. Wolf: *Principals of optics*. Pergamon Press, New York, 1980.
- [27] H. Bosse, R. Boyd, U. Brand, T. Burke, A. Cuenat, H. U. Danzebrink, K. Dircherl, T. Dziomba, J. Flügge and G. Frase: *Nanometrology foresight review*. Co-nanomet project output, 2009.
- [28] C. Brabec, V. Dyakonov and U. Scherf: *Organic Photovoltaics: Materials, Device Physics, and Manufacturing Technologies*. Weinheim: Wiley-VCH, Weinheim, 2008.
- [29] C. Broennimann, E. F. Eikenberry, B. Henrich, R. Horisberger, G. Huelsen, E. Pohl, B. Schmitt, C. Schulze-Briese, M. Suzuki, T. Tomizaki, H. Toyokawa and A. Wagner: 'The PILATUS 1M detector'. In: *J. Synchrotron Rad.* **13.2** (2006), pp. 120–130. DOI: 10.1107/S0909049505038665.
- [30] B. D. Bunday, M. Bishop, J. S. Villarrubia and A. E. Vladar: 'CD-SEM measurement line-edge roughness test patterns for 193-nm lithography'. In: *Proc. SPIE. Metrology, Inspection, and Process Control for Microlithography XVII*. Vol. 5038. 2003, pp. 674–688. DOI: 10.1117/12.485007.
- [31] S. Burger, L. Zschiedrich, J. Pomplun and F. Schmidt: 'Rigorous simulations of 3D patterns on extreme ultraviolet lithography masks'. In: *Proc. SPIE. Modeling Aspects in Optical Metrology III*. Vol. 8083. 2011, DOI: 10.1117/12.889831.
- [32] I. Busch, Y. Azuma, H. Bettin, L. Cibik, P. Fuchs, K. Fujii, M. Krumrey, U. Kuetgens, N. Kuramoto and S. Mizushima: 'Surface layer determination for the Si spheres of the Avogadro project'. In: *Metrologia* **48.2** (2011), S62–S82.
- [33] I. Busch, H.-U. Danzebrink, M. Krumrey, M. Borys and H. Bettin: 'Oxide Layer Mass Determination at the Silicon Sphere of the Avogadro Project'. In: *IEEE T. Instrum. Meas.* **58.4** (2009), pp. 891–896. DOI: 10.1109/TIM.2008.2007037.
- [34] P. Busch, M. Rauscher, D.-M. Smilgies, D. Posselt and C. M. Papadakis: 'Grazing-incidence small-angle X-ray scattering from thin polymer films with lamellar structures – the scattering cross section in the distorted-wave Born approximation'. In: *J. Appl. Cryst.* **39.3** (2006), pp. 433–442. DOI: 10.1107/S0021889806012337.
- [35] J. Chai, D. Wang, X. Fan and J. M. Buriak: 'Assembly of aligned linear metallic patterns on silicon'. In: *Nat. Nano.* **2.8** (2007), pp. 500–506. DOI: 10.1038/nano.2007.227.
- [36] G. Che, B. B. Lakshmi, C. R. Martin and E. R. Fisher: 'Metal-Nanocluster-Filled Carbon Nanotubes: Catalytic Properties and Possible Applications in Electrochemical Energy Storage and Production'. In: *Langmuir* **15.3** (1999), pp. 750–758. DOI: 10.1021/la980663i.
- [37] J. Y. Cheng, D. P. Sanders, H. D. Truong, S. Harrer, A. Friz, S. Holmes, M. Colburn and W. D. Hinsberg: 'Simple and Versatile Methods To Integrate Directed Self-Assembly with Optical Lithography Using a Polarity-Switched Photoresist'. In: *ACS Nano* **4.8** (2010), pp. 4815–4823. DOI: 10.1021/nn100686v.

## References

- [38] M. Chmeissani, M. Maiorino, G. Blanchot, G. Pellegrini, J. Garcia, M. Lozano, R. Martinez, C. Puigdengoles and M. Ullan: 'Charge sharing measurements of pixilated CdTe using Medipix-II chip'. In: *Proc. of IMTC 04. 21st IEEE Instrumentation and Measurement Technology Conference*. Vol. 1. 2004, pp. 787–791. DOI: 10.1109/IMTC.2004.1351164.
- [39] S. T. Chourou, A. Sarje, X. S. Li, E. R. Chan and A. Hexemer: 'HipGISAXS : a high-performance computing code for simulating grazing-incidence X-ray scattering data'. In: *J. Appl. Cryst.* **46.6** (2013), pp. 1781–1795. DOI: 10.1107/S0021889813025843.
- [40] S. T. Christensen, B. Lee, Z. Feng, M. C. Hersam and M. J. Bedzyk: 'Hierarchical nanoparticle morphology for platinum supported on SrTiO<sub>3</sub> (0 0 1): A combined microscopy and X-ray scattering study'. In: *Appl. Surf. Sci.* **256.2** (2009), pp. 423–427. DOI: 10.1016/j.apsusc.2009.06.017.
- [41] P. Colombi, D. K. Agnihotri, V. E. Asadchikov, E. Bontempi, D. K. Bowen, C. H. Chang, L. E. Depero, M. Farnworth, T. Fujimoto, A. Gibaud, M. Jergel, M. Krumrey, T. A. Lafford, A. Lamperti, T. Ma, R. J. Matyi, M. Meduna, S. Milita, K. Sakurai, L. Shabel'nikov, A. Ulyanenkov, A. Van der Lee and C. Wiemer: 'Reproducibility in X-ray reflectometry: results from the first world-wide round-robin experiment'. In: *J. Appl. Cryst.* **41.1** (2008), pp. 143–152. DOI: 10.1107/S0021889807051904.
- [42] A. H. Compton: 'A Quantum Theory of the Scattering of X-rays by Light Elements'. In: *Phys. Rev.* **21.5** (1923), pp. 483–502. DOI: 10.1103/PhysRev.21.483.
- [43] G. Dai, L. Koenders, F. Pohlenz, T. Dziomba and H.-U. Danzebrink: 'Accurate and traceable calibration of one-dimensional gratings'. In: *Meas. Sci. Technol.* **16.6** (2005), p. 1241. DOI: 10.1088/0957-0233/16/6/001.
- [44] G. Dai, F. Pohlenz, H.-U. Danzebrink, K. Hasche and G. Wilkening: 'Improving the performance of interferometers in metrological scanning probe microscopes'. In: *Meas. Sci. Technol.* **15.2** (2004), p. 444. DOI: 10.1088/0957-0233/15/2/019.
- [45] J. Daillant: 'Recent developments and applications of grazing incidence scattering'. In: *Curr. Opin. Colloid In.* **14.6** (2009), pp. 396–401. DOI: doi:DOI:10.1016/j.cocis.2009.04.003.
- [46] J. Daillant and A. Gibaud, eds.: *X-ray and Neutron Reflectivity*. Vol. 770. Lecture Notes in Physics. Springer, Berlin/Heidelberg, 2009.
- [47] S. B. Darling: 'Directing the self-assembly of block copolymers'. In: *Progr. Polym. Sci.* **32.10** (2007), pp. 1152–1204. DOI: 10.1016/j.progpolymsci.2007.05.004.
- [48] P. Delpierre, S. Basolo, J. F. Berar, M. Bordesoule, N. Boudet, P. Breugnon, B. Caillot, B. Chantepie, J. C. Clemens, B. Dinkespiler, S. Hustache-Ottini, C. Meessen, M. Menouni, C. Morel, C. Mouget, P. Pangaud, R. Potheau and E. Vigeolas: 'XPAD: A photons counting pixel detector for material sciences and small-animal imaging'. In: *Nucl. Instrum. Meth. A* **572.1** (2007), pp. 250–253. DOI: 10.1016/j.nima.2006.10.315.
- [49] I. D. Desnica-Franković, P. Dubcek, U. V. Desnica, S. Bernstorff, M. C. Ridgway and C. J. Glover: 'GISAXS studies of structural modifications in ion-beam amorphized Ge'. In: *Nucl. Instrum. Meth. B* **249.1–2** (2006), pp. 114–117. DOI: 10.1016/j.nimb.2006.03.093.

- [50] T. Donath, S. Brandstetter, L. Cibik, S. Commichau, P. Hofer, M. Krumrey, B. Lüthi, S. Marggraf, P. Müller, M. Schneebeli, C. Schulze-Briese and J. Wernecke: 'Characterization of the PILATUS photon-counting pixel detector for X-ray energies from 1.75 keV to 60 keV'. In: *J. Phys.: Conf. Ser.* **425.6** (2013), p. 062001. DOI: 10.1088/1742-6596/425/6/062001.
- [51] P. Durgapal, J. R. Ehrstein and N. V. Nguyen: 'Thin film ellipsometry metrology'. In: *AIP Conf. Proc.* The 1998 International Conference on Characterization and Metrology for ULSI Technology. Vol. 449. AIP, 1998, pp. 121–131. DOI: 10.1063/1.56787.
- [52] C. Durniak, W. Van Herck, G. Pospelov and J. Wuttke: *BornAgain: simulating X-ray and neutron scattering at grazing incidence*. 2013.
- [53] P. J. Eaton and P. West: *Atomic force microscopy*. Vol. 10. Oxford University Press, 2010.
- [54] 'Einrichtung zur Kleinwinkelstreuung zur Analyse der Nanostruktur an Proben mittels Röntgenstrahlung'. DE102006029449 B3. H. Bieder, A. Hoell, L. Mokrani and I. Zizak. International Classification G01N23/201, G12B9/08; Co-operative Classification G01N23/201; European Classification G01N23/201. 2007.
- [55] S. Eisebitt, M. Lörger, W. Eberhardt, J. Lüning, J. Stöhr, C. Rettner, O. Hellwig, E. Fullerton and G. Denbeaux: 'Polarization effects in coherent scattering from magnetic specimen: Implications for x-ray holography, lensless imaging, and correlation spectroscopy'. In: *Phys. Rev. B* **68.10** (2003), p. 104419. DOI: 10.1103/PhysRevB.68.104419.
- [56] S. Eisebitt, J. Lüning, W. F. Schlotter, M. Lörger, O. Hellwig, W. Eberhardt and J. Stöhr: 'Lensless imaging of magnetic nanostructures by X-ray spectro-holography'. In: *Nature* **432.7019** (2004), pp. 885–888. DOI: 10.1038/nature03139.
- [57] S. Eisebitt: 'X-ray holography: The hole story'. In: *Nat. Photon.* **2.9** (2008), pp. 529–530. DOI: 10.1038/nphoton.2008.182.
- [58] P. Emma, R. Akre, J. Arthur, R. Bionta, C. Bostedt, J. Bozek, A. Brachmann, P. Bucksbaum, R. Coffee, F.-J. Decker et al.: 'First lasing and operation of an ångstrom-wavelength free-electron laser'. In: *Nat. Photon.* **4.9** (2010), pp. 641–647. DOI: 10.1038/nphoton.2010.176.
- [59] J. Endres, A. Diener, M. Wurm and B. Bodermann: 'Investigations of the influence of common approximations in scatterometry for dimensional nanometrology'. In: *Meas. Sci. Technol.* **25.4** (2014), p. 044004. DOI: 10.1088/0957-0233/25/4/044004.
- [60] R. Erni, M. Rossell, C. Kisielowski and U. Dahmen: 'Atomic-Resolution Imaging with a Sub-50-pm Electron Probe'. In: *Phys. Rev. Lett.* **102.9** (2009), p. 096101. DOI: 10.1103/PhysRevLett.102.096101.
- [61] J. Falta and T. Möller: *Forschung mit Synchrotronstrahlung: Eine Einführung in die Grundlagen und Anwendungen*. Springer, Berlin/Heidelberg, 2010. 492 pp.
- [62] S. Farsiou, D. Robinson, M. Elad and P. Milanfar: 'Advances and challenges in super-resolution'. In: *Int. J. Imaging Syst. Technol.* **14.2** (2004), pp. 47–57. DOI: 10.1002/ima.20007.
- [63] R. Feidenhans'l: 'Surface structure determination by X-ray diffraction'. In: *Surf. Sci. Rep.* **10.3** (1989), pp. 105–188. DOI: 10.1016/0167-5729(89)90002-2.

## References

- [64] L. A. Feigin, D. I. Svergun and G. W. Taylor: *Structure analysis by small-angle X-ray and neutron scattering*. 1st ed. Springer, Berlin/Heidelberg, 1987. 335 pp.
- [65] S. L. Flegler, J. W. Heckman and K. L. Klomparens: *Scanning and Transmission Electron Microscopy: An introduction*. Oxford University Press, 1993. 225 pp.
- [66] E. Frackowiak and F. Béguin: 'Carbon materials for the electrochemical storage of energy in capacitors'. In: *Carbon* **39.6** (2001), pp. 937–950. DOI: 10.1016/S0008-6223(00)00183-4.
- [67] D. Fuchs, M. Krumrey, P. Müller, F. Scholze and G. Ulm: 'High precision soft x-ray reflectometer'. In: *Rev. Sci. Instrum.* **66** (1995), pp. 2248–2250. DOI: 10.1063/1.1145720.
- [68] J. Geilhufe, B. Pfau, M. Schneider, F. Büttner, C. M. Günther, S. Werner, S. Schaffert, E. Guehrs, S. Frömmel, M. Kläui and S. Eisebitt: 'Monolithic focused reference beam X-ray holography'. In: *Nat. Commun.* **5** (2014). DOI: 10.1038/ncomms4008.
- [69] N. Gerken, S. Klumpp, A. A. Sorokin, K. Tiedtke, M. Richter, V. Bürk, K. Mertens, P. Juranić and M. Martins: 'Time-Dependent Multiphoton Ionization of Xenon in the Soft-X-Ray Regime'. In: *Phys. Rev. Lett.* **112.21** (2014), p. 213002. DOI: 10.1103/PhysRevLett.112.213002.
- [70] M. Gerlach, M. Krumrey, L. Cibik, P. Müller, H. Rabus and G. Ulm: 'Cryogenic radiometry in the hard x-ray range'. In: *Metrologia* **45.5** (2008), p. 577. DOI: 10.1088/0026-1394/45/5/012.
- [71] T. Ghoshal, R. Senthamaraiannan, M. T. Shaw, J. D. Holmes and M. A. Morris: 'An insitu hard mask block copolymer approach for the fabrication of ordered, large scale, horizontally aligned, Si nanowire arrays on Si substrate'. In: *Proc. SPIE. Advances in Patterning Materials and Processes XXXI*. Vol. 9051. 2014, 90510J. DOI: 10.1117/12.2045754.
- [72] A. Gibaud, S. Dourdain, O. Gang and B. Ocko: 'In situ grazing incidence small-angle x-ray scattering real-time monitoring of the role of humidity during the structural formation of templated silica thin films'. In: *Phys. Rev. B* **70.16** (2004), p. 161403. DOI: 10.1103/PhysRevB.70.161403.
- [73] O. Glatter and O. Kratky: *Small angle X-ray scattering*. Academic Press, 1982.
- [74] G. Gleber, L. Cibik, S. Haas, A. Hoell, P. Müller and M. Krumrey: 'Traceable size determination of PMMA nanoparticles based on Small Angle X-ray Scattering (SAXS)'. In: *J. Phys.: Conf. Ser.* **247** (2010), p. 012027. DOI: 10.1088/1742-6596/247/1/012027.
- [75] C. Gollwitzer and M. Krumrey: 'A diffraction effect in X-ray area detectors'. In: *J. Appl. Cryst.* **47.1** (2014), pp. 378–383. DOI: 10.1107/S1600576713031981.
- [76] M. D. Graef: *Introduction to Conventional Transmission Electron Microscopy*. Cambridge University Press, 2003. 741 pp.
- [77] H. Gross, A. Rathsfeld, F. Scholze and M. Bär: 'Profile reconstruction in extreme ultraviolet (EUV) scatterometry: modeling and uncertainty estimates'. In: *Meas. Sci. Technol.* **20.10** (2009), p. 105102. DOI: 10.1088/0957-0233/20/10/105102.
- [78] X. Gu, I. Gunkel, A. Hexemer, W. Gu and T. P. Russell: 'An In Situ Grazing Incidence X-Ray Scattering Study of Block Copolymer Thin Films During Solvent Vapor Annealing'. In: *Adv. Mater.* **26.2** (2014), pp. 273–281. DOI: 10.1002/adma.201302562.

- [79] X. Gu, I. Gunkel and T. P. Russell: 'Pattern transfer using block copolymers'. In: *Phil. Trans. R. Soc. A* **371.2000** (2013). PMID: 24000358, p. 20120306. DOI: 10.1098/rsta.2012.0306.
- [80] X. Gu, Z. Liu, I. Gunkel, S. T. Chourou, S. W. Hong, D. L. Olynick and T. P. Russell: 'High Aspect Ratio Sub-15 nm Silicon Trenches From Block Copolymer Templates'. In: *Adv. Mater.* **24.42** (2012), pp. 5688–5694. DOI: 10.1002/adma.201202361.
- [81] I. W. Hamley: 'Nanostructure fabrication using block copolymers'. In: *Nanotechnology* **14.10** (2003), R39. DOI: 10.1088/0957-4484/14/10/201.
- [82] I. W. Hamley: 'Ordering in thin films of block copolymers: Fundamentals to potential applications'. In: *Progr. Polym. Sci.* **34.11** (2009), pp. 1161–1210. DOI: 10.1016/j.progpolymsci.2009.06.003.
- [83] I. W. Hamley and J. S. Pedersen: 'Analysis of neutron and X-ray reflectivity data. I. Theory'. In: *J. Appl. Cryst.* **27.1** (1994), pp. 29–35. DOI: 10.1107/S0021889893006260.
- [84] P. Hansen: 'Analysis of Discrete Ill-Posed Problems by Means of the L-Curve'. In: *SIAM Rev.* **34.4** (1992), pp. 561–580. DOI: 10.1137/1034115.
- [85] P. C. Hansen: 'The L-Curve and its Use in the Numerical Treatment of Inverse Problems'. In: *Computational Inverse Problems in Electrocardiology*. Advances in Computational Bioengineering. WIT, 2001, pp. 119–142.
- [86] P. Hansen and D. O'Leary: 'The Use of the L-Curve in the Regularization of Discrete Ill-Posed Problems'. In: *SIAM J. Sci. Comput.* **14.6** (1993), pp. 1487–1503. DOI: 10.1137/0914086.
- [87] F. Harris: 'On the use of windows for harmonic analysis with the discrete Fourier transform'. In: *Proc. IEEE* **66.1** (1978), pp. 51–83. DOI: 10.1109/PROC.1978.10837.
- [88] E. H. M. Heijne and P. Jarron: 'Development of silicon pixel detectors: An introduction'. In: *Nucl. Instrum. Meth. A* **275.3** (1989), pp. 467–471. DOI: 10.1016/0168-9002(89)90730-4.
- [89] O. Hellwig, S. Eisebitt, W. Eberhardt, W. F. Schlotter, J. Lüning and J. Stöhr: 'Magnetic imaging with soft x-ray spectroholography'. In: *J. Appl. Phys.* **99.8** (2006), 08H307. DOI: 10.1063/1.2165925.
- [90] B. L. Henke, E. M. Gullikson and J. C. Davis: 'X-Ray Interactions: Photoabsorption, Scattering, Transmission, and Reflection at  $E = 50\text{--}30,000$  eV,  $Z = 1\text{--}92$ '. In: *Atomic Data and Nuclear Data Tables* **54.2** (1993), pp. 181–342. DOI: 10.1006/adnd.1993.1013.
- [91] G. Herzog, G. Benecke, A. Buffet, B. Heidmann, J. Perlich, J. F. H. Risch, G. Santoro, M. Schwartzkopf, S. Yu, W. Wurth and S. V. Roth: 'In Situ Grazing Incidence Small-Angle X-ray Scattering Investigation of Polystyrene Nanoparticle Spray Deposition onto Silicon'. In: *Langmuir* **29.36** (2013), pp. 11260–11266. DOI: 10.1021/la402254q.
- [92] T. Hofmann, E. Dobisz and B. M. Ocko: 'Grazing incident small angle x-ray scattering: A metrology to probe nanopatterned surfaces'. In: *J. Vac. Sci. Technol. B* **27.6** (2009), pp. 3238–3243. DOI: 10.1116/1.3253608.
- [93] K. Holldack, S. Khan, R. Mitzner and T. Quast: 'Femtosecond Terahertz Radiation from Femtoslicing at BESSY'. In: *Phys. Rev. Lett.* **96.5** (2006), p. 054801. DOI: 10.1103/PhysRevLett.96.054801.

## References

- [94] V. Holý and T. Baumbach: 'Nonspecular x-ray reflection from rough multilayers'. In: *Phys. Rev. B* **49.15** (1994), p. 10668. DOI: 10.1103/PhysRevB.49.10668.
- [95] S. W. Hong, W. Gu, J. Huh, B. R. Sveinbjornsson, G. Jeong, R. H. Grubbs and T. P. Russell: 'On the Self-Assembly of Brush Block Copolymers in Thin Films'. In: *ACS Nano* **7.11** (2013), pp. 9684–9692. DOI: 10.1021/nn402639g.
- [96] T. L. Hopman, C. M. Heirwegh, J. L. Campbell, M. Krumrey and F. Scholze: 'An accurate determination of the K-shell X-ray fluorescence yield of silicon'. In: *X-Ray Spectrom.* **41.3** (2012), pp. 164–171. DOI: 10.1002/xrs.2378.
- [97] K. Hoydalsvik, T. Barnardo, R. Winter, S. Haas, D. Tatchev and A. Hoell: 'Yttria-zirconia coatings studied by grazing-incidence small-angle X-ray scattering during in situ heating'. In: *Phys. Chem. Chem. Phys.* **12.43** (2010), p. 14492. DOI: 10.1039/c0cp00472c.
- [98] T. Hu, R. L. Jones, W.-l. Wu, E. K. Lin, Q. Lin, D. Keane, S. Weigand and J. Quintana: 'Small angle x-ray scattering metrology for sidewall angle and cross section of nanometer scale line gratings'. In: *J. Appl. Phys.* **96.4** (2004), pp. 1983–1987. DOI: 10.1063/1.1773376.
- [99] H.-T. Huang and F. L. Terry Jr: 'Spectroscopic ellipsometry and reflectometry from gratings (Scatterometry) for critical dimension measurement and in situ, real-time process monitoring'. In: *Thin Solid Films*. The 3rd International Conference on Spectroscopic Ellipsometry **455–456** (2004), pp. 828–836. DOI: 10.1016/j.tsf.2004.04.010.
- [100] Z. Huang and K.-J. Kim: 'Review of x-ray free-electron laser theory'. In: *Phys. Rev. ST Accel. Beams* **10.3** (2007), p. 034801. DOI: 10.1103/PhysRevSTAB.10.034801.
- [101] I. G. Hughes and T. Hase: *Measurements and their Uncertainties*. Oxford University Press, 2010.
- [102] M. Husemann, M. Morrison, D. Benoit, J. Frommer, C. M. Mate, W. D. Hinsberg, J. L. Hedrick and C. J. Hawker: 'Manipulation of Surface Properties by Patterning of Covalently Bound Polymer Brushes'. In: *J. Am. Chem. Soc.* **122.8** (2000), pp. 1844–1845. DOI: 10.1021/ja991450y.
- [103] K. Ishiji, H. Okuda, H. Hashizume, M. Almokhtar and N. Hosoi: 'Structures of submonatomic Sn layers in Fe/Cr(Sn)Cr magnetic multilayers determined by anomalous x-ray scattering measurements'. In: *Phys. Rev. B* **66.1** (2002), p. 014443. DOI: 10.1103/PhysRevB.66.014443.
- [104] T. Ishikawa, H. Aoyagi, T. Asaka, Y. Asano, N. Azumi, T. Bizen, H. Ego, K. Fukami, T. Fukui, Y. Furukawa et al.: 'A compact X-ray free-electron laser emitting in the sub-angstrom region'. In: *Nat. Photon.* **6.8** (2012), pp. 540–544. DOI: 10.1038/nphoton.2012.141.
- [105] D. Ivanenko and I. Pomeranchuk: 'Radiation losses in circular accelerating motions'. In: *Dokl. Akad. Nauk* **44** (1944), p. 315.
- [106] J. D. Jackson: *Classical electrodynamics*. Wiley, New York, 1975.
- [107] R. W. James: *The Optical Principles of the Diffraction of X-rays*. Vol. 2. G. Bell and Sons, 1948.

- [108] M. Jergel, P. Mikulík, E. Majková, S. Luby, R. Senderák, E. Pincík, M. Brunel, P. Hudek, I. Kostic and A. Konecniřková: 'Structural characterization of lamellar multilayer gratings by x-ray reflectivity and scanning electron microscopy'. In: *J. Phys. D: Appl. Phys.* **32.10A** (1999), A220–A223. DOI: 10.1088/0022-3727/32/10A/343.
- [109] S. Ji, C.-C. Liu, W. Liao, A. L. Fenske, G. S. W. Craig and P. F. Nealey: 'Domain Orientation and Grain Coarsening in Cylinder-Forming Poly(styrene-b-methyl methacrylate) Films'. In: *Macromolecules* **44.11** (2011), pp. 4291–4300. DOI: 10.1021/ma2005734.
- [110] S. Ji, C.-C. Liu, J. G. Son, K. Gotrik, G. S. W. Craig, P. Gopalan, F. J. Himpsel, K. Char and P. F. Nealey: 'Generalization of the Use of Random Copolymers To Control the Wetting Behavior of Block Copolymer Films'. In: *Macromolecules* **41.23** (2008), pp. 9098–9103. DOI: 10.1021/ma801861h.
- [111] R. L. Jones, T. Hu, E. K. Lin, W.-L. Wu, R. Kolb, D. M. Casa, P. J. Bolton and G. G. Barclay: 'Small angle x-ray scattering for sub-100 nm pattern characterization'. In: *Appl. Phys. Lett.* **83.19** (2003), pp. 4059–4061. DOI: 10.1063/1.1622793.
- [112] R. L. Jones, T. Hu, C. L. Soles, E. K. Lin, W.-l. Wu, D. M. Casa and A. Mahorowala: 'Preliminary evaluation of line-edge roughness metrology based on CD-SAXS'. In: *Proc. SPIE. Metrology, Inspection, and Process Control for Microlithography XVIII*. Vol. 5375. 2004, pp. 191–198. DOI: 10.1117/12.535693.
- [113] J. Kaiser and R. W. Schafer: 'On the use of the  $I_0 \text{-sinh}$  window for spectrum analysis'. In: *Acoust. Speech Signal Process. IEEE Trans. On* **28.1** (1980), pp. 105–107.
- [114] K. Kataoka, A. Harada and Y. Nagasaki: 'Block copolymer micelles for drug delivery: design, characterization and biological significance'. In: *Adv. Drug Deliver. Rev. Nanoparticulate Systems for Improved Drug Delivery* **47.1** (2001), pp. 113–131. DOI: 10.1016/S0169-409X(00)00124-1.
- [115] A. Kato and F. Scholze: 'Effect of line roughness on the diffraction intensities in angular resolved scatterometry'. In: *Appl. Opt.* **49.31** (2010), pp. 6102–6110. DOI: 10.1364/AO.49.006102.
- [116] E. Katz and I. Willner: 'Integrated Nanoparticle–Biomolecule Hybrid Systems: Synthesis, Properties, and Applications'. In: *Angew. Chem. Int. Edit.* **43.45** (2004), pp. 6042–6108. DOI: 10.1002/anie.200400651.
- [117] S. W. King, H. Simka, D. Herr, H. Akinaga and M. Garner: 'Research Updates: The three M's (materials, metrology, and modeling) together pave the path to future nanoelectronic technologies'. In: *APL Mater.* **1.4** (2013), p. 040701. DOI: 10.1063/1.4822437.
- [118] C. Kittel: *Introduction to solid state physics*. 5th ed. New York: Wiley, New York, 1976. 599 pp.
- [119] T. Klein, E. Buhr and C. Georg Frase: 'Chapter 6 - TSEM: A Review of Scanning Electron Microscopy in Transmission Mode and Its Applications'. In: *Advances in Imaging and Electron Physics*. Ed. by P. W. Hawkes. Vol. 171. Advances in Imaging and Electron Physics. Elsevier, 2012, pp. 297–356.
- [120] E.-E. Koch, G. S. Brown and D. E. Moncton, eds.: *Handbook on Synchrotron Radiation*. Vol. 1. North Holland Publishing, Amsterdam/New York, 1983.

## References

- [121] P. Kohn, Z. Rong, K. H. Scherer, A. Sepe, M. Sommer, P. Müller-Buschbaum, R. H. Friend, U. Steiner and S. Hüttner: 'Crystallization-Induced 10-nm Structure Formation in P<sub>3</sub>HT/PCBM Blends'. In: *Macromolecules* **46.10** (2013), pp. 4002–4013. DOI: 10.1021/ma400403c.
- [122] V. Körstgens, J. Wiedersich, R. Meier, J. Perlich, S. Roth, R. Gehrke and P. Müller-Buschbaum: 'Combining imaging ellipsometry and grazing incidence small angle X-ray scattering for in situ characterization of polymer nanostructures'. In: *Anal. Bioanal. Chem.* **396.1** (2010), pp. 139–149.
- [123] P. Kraft, A. Bergamaschi, C. Broennimann, R. Dinapoli, E. F. Eikenberry, B. Henrich, I. Johnson, A. Mozzanica, C. M. Schlepütz, P. R. Willmott and B. Schmitt: 'Performance of single-photon-counting PILATUS detector modules'. In: *J. Synchrotron Rad.* **16.3** (2009), pp. 368–375. DOI: 10.1107/S0909049509009911.
- [124] P. Kraft, A. Bergamaschi, C. Bronnimann, R. Dinapoli, E. Eikenberry, H. Graafsma, B. Henrich, I. Johnson, M. Kobas, A. Mozzanica, C. Schlepütz and B. Schmitt: 'Characterization and Calibration of PILATUS Detectors'. In: *IEEE T. Nucl. Sci.* **56.3** (2009), pp. 758–764. DOI: 10.1109/TNS.2008.2009448.
- [125] M. Krumrey: 'Design of a Four-Crystal Monochromator Beamline for Radiometry at BESSY II'. In: *J. Synchrotron Rad.* **5.1** (1998), pp. 6–9. DOI: 10.1107/S0909049597011825.
- [126] M. Krumrey, M. Hoffmann, G. Ulm, K. Hasche and P. Thomsen-Schmidt: 'Thickness determination for SiO<sub>2</sub> films on Si by X-ray reflectometry at the Si K edge'. In: *Thin Solid Films*. Proceedings of the 8th European Vacuum Congress Berlin 2003 **459.1–2** (2004), pp. 241–244. DOI: 10.1016/j.tsf.2003.12.100.
- [127] M. Krumrey and E. Tegeler: 'Self-calibration of semiconductor photodiodes in the soft x-ray region'. In: *Rev. Sci. Instrum.* **63.1** (1992), pp. 797–801. DOI: 10.1063/1.1143800.
- [128] M. Krumrey and G. Ulm: 'High-accuracy detector calibration at the PTB four-crystal monochromator beamline'. In: *Nucl. Instrum. Meth. A* **467-468** (2001), pp. 1175–1178. DOI: 10.1016/S0168-9002(01)00598-8.
- [129] M. Krumrey, G. Gleber, F. Scholze and J. Wernecke: 'Synchrotron radiation-based x-ray reflection and scattering techniques for dimensional nanometrology'. In: *Meas. Sci. Technol.* **22.9** (2011), p. 094032. DOI: 10.1088/0957-0233/22/9/094032.
- [130] M. Kuhlmann, J. M. Feldkamp, J. Patommel, S. V. Roth, A. Timmann, R. Gehrke, P. Müller-Buschbaum and C. G. Schroer: 'Grazing Incidence Small-Angle X-ray Scattering Microtomography Demonstrated on a Self-Ordered Dried Drop of Nanoparticles'. In: *Langmuir* **25.13** (2009), pp. 7241–7243. DOI: 10.1021/la901325y.
- [131] C. Laubis, C. Buchholz, A. Fischer, S. Plöger, F. Scholz, H. Wagner, F. Scholze, G. Ulm, H. Enkisch, S. Müllender, M. Wedowski, E. Louis and E. Zoethout: 'Characterization of large off-axis EUV mirrors with high accuracy reflectometry at PTB'. In: *Proc. SPIE*. Emerging Lithographic Technologies X. Vol. 6151. 2006, p. 61510I. DOI: 10.1117/12.656246.
- [132] R. Lazzari: 'Grazing Incidence Small-Angle X-Ray Scattering from Nanostructures'. In: *X-ray and Neutron Reflectivity*. Ed. by J. Daillant and A. Gibaud. Vol. 770. Lecture Notes in Physics. Springer Berlin/Heidelberg, 2009, pp. 283–342.

- [133] R. Lazzari: 'IsGISAXS: a program for grazing-incidence small-angle X-ray scattering analysis of supported islands'. In: *J. Appl. Cryst.* **35.4** (2002), pp. 406–421. DOI: 10.1107/S0021889802006088.
- [134] R. K. Leach, R. Boyd, T. Burke, H.-U. Danzebrink, K. Dirscherl, T. Dziomba, M. Gee, L. Koenders, V. Morazzani, A. Pidduck, D. Roy, W. E. S. Unger and A. Yacoot: 'The European nanometrology landscape'. In: *Nanotechnology* **22.6** (2011), p. 062001. DOI: 10.1088/0957-4484/22/6/062001.
- [135] B. Lee, I. Park, J. Yoon, S. Park, J. Kim, K.-W. Kim, T. Chang and M. Ree: 'Structural Analysis of Block Copolymer Thin Films with Grazing Incidence Small-Angle X-ray Scattering'. In: *Macromolecules* **38.10** (2005), pp. 4311–4323. DOI: 10.1021/ma047562d.
- [136] L. Leibler: 'Theory of Microphase Separation in Block Copolymers'. In: *Macromolecules* **13.6** (1980), pp. 1602–1617. DOI: 10.1021/ma60078a047.
- [137] F. Leroy, R. Lazzari and G. Renaud: 'Effects of near-neighbor correlations on the diffuse scattering from a one-dimensional paracrystal'. In: *Acta Crystallogr. A* **60.6** (2004), pp. 565–581. DOI: 10.1107/S0108767304018550.
- [138] J. R. Levine, J. B. Cohen, Y. W. Chung and P. Georgopoulos: 'Grazing-incidence small-angle X-ray scattering: new tool for studying thin film growth'. In: *J. Appl. Cryst.* **22.6** (1989), pp. 528–532. DOI: 10.1107/S002188988900717X.
- [139] X. Li, S. Tian, Y. Ping, D. H. Kim and W. Knoll: 'One-Step Route to the Fabrication of Highly Porous Polyaniline Nanofiber Films by Using PS-*b*-PVP Diblock Copolymers as Templates'. In: *Langmuir* **21.21** (2005), pp. 9393–9397. DOI: 10.1021/la0514009.
- [140] Y. Lin, A. Böker, J. He, K. Sill, H. Xiang, C. Abetz, X. Li, J. Wang, T. Emrick, S. Long, Q. Wang, A. Balazs and T. P. Russell: 'Self-directed self-assembly of nanoparticle/copolymer mixtures'. In: *Nature* **434.7029** (2005), pp. 55–59. DOI: 10.1038/nature03310.
- [141] J. Q. Lu and S. S. Yi: 'Uniformly Sized Gold Nanoparticles Derived from PS-*b*-P2VP Block Copolymer Templates for the Controllable Synthesis of Si Nanowires'. In: *Langmuir* **22.9** (2006), pp. 3951–3954. DOI: 10.1021/la053377x.
- [142] W. Ma, C. Yang, X. Gong, K. Lee and A. J. Heeger: 'Thermally Stable, Efficient Polymer Solar Cells with Nanoscale Control of the Interpenetrating Network Morphology'. In: *Adv. Funct. Mater.* **15.10** (2005), pp. 1617–1622. DOI: 10.1002/adfm.200500211.
- [143] J. M. J. Madey: 'Stimulated Emission of Bremsstrahlung in a Periodic Magnetic Field'. In: *J. Appl. Phys.* **42.5** (1971), pp. 1906–1913. DOI: 10.1063/1.1660466.
- [144] J. Marchal and A. Wagner: 'Performance of PILATUS detector technology for long-wavelength macromolecular crystallography'. In: *Nucl. Instrum. Meth. A*. **11th International Workshop on Radiation Imaging Detectors (IWORID) 633, Supplement 1** (2011), S121–S124. DOI: 10.1016/j.nima.2010.06.142.
- [145] J. Marchal, B. Luethi, C. Ursachi, V. Mykhaylyk and A. Wagner: 'Low-energy X-ray detection with an in-vacuum PILATUS detector'. In: *J. Inst.* **6.11** (2011), p. C11033. DOI: 10.1088/1748-0221/6/11/C11033.

## References

- [146] W. A. McGahan, B. R. Spady, J. A. Iacoponi and J. D. Williams: 'Combined spectroscopic ellipsometry and reflectometry for advanced semiconductor fabrication metrology'. In: *Proc. SPIE. Optical Characterization Techniques for High-Performance Microelectronic Device Manufacturing III*. Vol. 2877. 1996, pp. 132–141. DOI: 10.1117/12.250927.
- [147] A. McPherson, B. D. Thompson, A. B. Borisov, K. Boyer and C. K. Rhodes: 'Multiphoton-induced X-ray emission at 4–5 keV from Xe atoms with multiple core vacancies'. In: *Nature* **370**.6491 (1994), pp. 631–634. DOI: 10.1038/370631a0.
- [148] E. Metwalli, J.-F. Moulin, J. Perlich, W. Wang, A. Diethert, S. V. Roth and P. Müller-Buschbaum: 'Polymer-Template-Assisted Growth of Gold Nanowires Using a Novel Flow-Stream Technique'. In: *Langmuir* **25**.19 (2009), pp. 11815–11821. DOI: 10.1021/la901432j.
- [149] E. Metwalli, V. Körstgens, K. Schlage, R. Meier, G. Kaune, A. Buffet, S. Couet, S. V. Roth, R. Röhlberger and P. Müller-Buschbaum: 'Cobalt Nanoparticles Growth on a Block Copolymer Thin Film: A Time-Resolved GISAXS Study'. In: *Langmuir* **29**.21 (2013), pp. 6331–6340. DOI: 10.1021/la400741b.
- [150] E. Metwalli, J.-F. Moulin, M. Rauscher, G. Kaune, M. A. Ruderer, U. Van Bürck, M. Haese-Seiller, R. Kampmann and P. Müller-Buschbaum: 'Structural investigation of thin diblock copolymer films using time-of-flight grazing-incidence small-angle neutron scattering'. In: *J. Appl. Cryst.* **44**.1 (2011), pp. 84–92. DOI: 10.1107/S0021889810046194.
- [151] E. Meyer: 'Atomic force microscopy'. In: *Progr. Polym. Sci.* **41**.1 (1992), pp. 3–49. DOI: 10.1016/0079-6816(92)90009-7.
- [152] P. Mikulík and T. Baumbach: 'X-ray reflection by rough multilayer gratings: Dynamical and kinematical scattering'. In: *Phys. Rev. B* **59**.11 (1999), pp. 7632–7643. DOI: 10.1103/PhysRevB.59.7632.
- [153] P. Mikulík, M. Jergel, T. Baumbach, E. Majková, E. Pincík, S. Luby, L. Ortega, R. Tucoulou, P. Hudek and I. Kostic: 'Coplanar and non-coplanar x-ray reflectivity characterization of lateral W/Si multilayer gratings'. In: *J. Phys. D: Appl. Phys.* **34** (2001), A188–A192. DOI: 10.1088/0022-3727/34/10A/339.
- [154] I. Misumi, S. Gonda, T. Kurosawa and K. Takamasu: 'Uncertainty in pitch measurements of one-dimensional grating standards using a nanometrological atomic force microscope'. In: *Meas. Sci. Technol.* **14**.4 (2003), p. 463. DOI: 10.1088/0957-0233/14/4/309.
- [155] P. J. Mohr, B. N. Taylor and D. B. Newell: 'CODATA Recommended Values of the Fundamental Physical Constants: 2010a'. In: *J. Phys. Chem. Ref. Data* **41**.4 (2012), p. 043109. DOI: 10.1063/1.4724320.
- [156] T. L. Morkved, M. Lu, A. M. Urbas, E. E. Ehrichs, H. M. Jaeger, P. Mansky and T. P. Russell: 'Local Control of Microdomain Orientation in Diblock Copolymer Thin Films with Electric Fields'. In: *Science* **273**.5277 (1996). PMID: 8688070, pp. 931–933. DOI: 10.1126/science.273.5277.931.
- [157] D. A. Muller: 'A sound barrier for silicon?' In: *Nat. Mater.* **4**.9 (2005), pp. 645–647. DOI: 10.1038/nmat1466.

- [158] P. Müller-Buschbaum: 'Grazing incidence small-angle X-ray scattering: an advanced scattering technique for the investigation of nanostructured polymer films'. In: *Anal. Bioanal. Chem.* **376.1** (2003), pp. 3–10.
- [159] P. Müller-Buschbaum: 'A Basic Introduction to Grazing Incidence Small-Angle X-Ray Scattering'. In: *Applications of Synchrotron Light to Scattering and Diffraction in Materials and Life Sciences*. Vol. 776. Lecture Notes in Physics. Springer Berlin/Heidelberg, 2009, pp. 61–89.
- [160] P. Müller-Buschbaum, J. S. Gutmann, C. Lorenz, T. Schmitt and M. Stamm: 'Decay of Interface Correlation in Thin Polymer Films'. In: *Macromolecules* **31.26** (1998), pp. 9265–9272. DOI: 10.1021/ma9813111.
- [161] P. Müller-Buschbaum, J. S. Gutmann, C. Lorenz-Haas, B. Mahltig, M. Stamm and W. Petry: 'Early Stages of Film Creation in Thin Diblock Copolymer Films'. In: *Macromolecules* **34.21** (2001), pp. 7463–7470. DOI: 10.1021/ma002181v.
- [162] P. Müller-Buschbaum, E. Maurer, E. Bauer and R. Cubitt: 'Surface versus Confinement Induced Morphology Transition in Triblock Copolymer Films: A Grazing Incidence Small Angle Neutron Scattering Investigation'. In: *Langmuir* **22.22** (2006), pp. 9295–9303. DOI: 10.1021/la061455q.
- [163] P. Müller-Buschbaum, S. V. Roth, M. Burghammer, A. Diethert, P. Panagiotou and C. Riekkel: 'Multiple-scaled polymer surfaces investigated with micro-focus grazing-incidence small-angle X-ray scattering'. In: *Europhys. Lett.* **61.5** (2003), p. 639. DOI: 10.1209/epl/i2003-00119-4.
- [164] P. Müller-Buschbaum, L. Schulz, E. Metwalli, J.-F. Moulin and R. Cubitt: 'Lateral Structures of Buried Interfaces in ABA-Type Triblock Copolymer Films'. In: *Langmuir* **24.15** (2008), pp. 7639–7644. DOI: 10.1021/la801539r.
- [165] P. Müller-Buschbaum, L. Schulz, E. Metwalli, J.-F. Moulin and R. Cubitt: 'Interface-Induced Morphology Transition in Triblock Copolymer Films Swollen with Low-Molecular-Weight Homopolymer'. In: *Langmuir* **25.7** (2009), pp. 4235–4242. DOI: 10.1021/la802471p.
- [166] P. Müller-Buschbaum: 'Structure Determination in Thin Film Geometry Using Grazing Incidence Small-Angle Scattering'. In: *Polymer Surfaces and Interfaces*. Ed. by M. Stamm. Springer Berlin/Heidelberg, 2008, pp. 17–46.
- [167] A. Naudon, D. Babonneau, D. Thiaudière and S. Lequien: 'Grazing-incidence small-angle X-ray scattering applied to the characterization of aggregates in surface regions'. In: *Physica B Cond. Matter* **283.1-3** (2000), pp. 69–74. DOI: 10.1016/S0921-4526(99)01894-3.
- [168] A. Neumaier: 'Solving Ill-Conditioned and Singular Linear Systems: A Tutorial on Regularization'. In: *SIAM Rev.* **40.3** (1998), pp. 636–666. DOI: 10.1137/S0036144597321909.
- [169] M. D. Neumann, C. Cobet, H. Kaser, M. Kolbe, A. Gottwald, M. Richter and N. Esser: 'A synchrotron-radiation-based variable angle ellipsometer for the visible to vacuum ultraviolet spectral range'. In: *Rev. Sci. Instrum.* **85.5** (2014), p. 055117. DOI: 10.1063/1.4878919.
- [170] L. Névoit and P. Croce: 'Caractérisation des surfaces par réflexion rasante de rayons X. Application à l'étude du polissage de quelques verres silicates'. In: *Rev. Phys. Appl.* **15.3** (1980), pp. 761–779. DOI: 10.1051/rphysap:01980001503076100.

## References

- [171] Z. Nie and E. Kumacheva: 'Patterning surfaces with functional polymers'. In: *Nat. Mater.* **7.4** (2008), pp. 277–290. DOI: 10.1038/nmat2109.
- [172] M. A. Niedermeier, M. Rawolle, P. Lellig, V. Körstgens, E. M. Herzig, A. Buffet, S. V. Roth, J. S. Gutmann, T. Fröschl, N. Hüsing and P. Müller-Buschbaum: 'Low-Temperature Sol-Gel Synthesis of Nanostructured Polymer/Titania Hybrid Films based on Custom-Made Poly(3-Alkoxy Thiophene)'. In: *ChemPhysChem* **14.3** (2013), pp. 597–602. DOI: 10.1002/cphc.201200808.
- [173] H. Ohkuma: 'Top-up operation in light sources'. In: *Proc. EPACo8*. EPACo8. Genoa, 2008, pp. 36–40.
- [174] H. Okuda, M. Kato, S. Ochiai and Y. Kitajima: 'Anomalous Grazing Incidence Small-Angle Scattering of Capped Ge Nanodots at the Si K Absorption Edge'. In: *Appl. Phys. Express* **2.12** (2009), p. 126501. DOI: 10.1143/APEX.2.126501.
- [175] H. Okuda, K. Takeshita, S. Ochiai, Y. Kitajima, S. Sakurai and H. Ogawa: 'Contrast matching of an Si substrate with polymer films by anomalous dispersion at the Si K absorption edge'. In: *J. Appl. Cryst.* **45.1** (2012), pp. 119–121. DOI: 10.1107/S002188981105206X.
- [176] H. Okuda, K. Takeshita, S. Ochiai, S. Sakurai and Y. Kitajima: 'Near-surface relaxation structure of annealed block copolymer film on Si substrates examined by grazing-incidence small-angle scattering utilizing soft X-rays'. In: *J. Appl. Cryst.* **44.2** (2011), pp. 380–384. DOI: 10.1107/S0021889811003578.
- [177] H. Okuda, T. Yamamoto, K. Takeshita, M. Hirai, K. Senoo, H. Ogawa and Y. Kitajima: 'Normalization of grazing-incidence small angle scattering of phospholipid alloy systems at the K absorption edge of phosphorous: A standard sample approach'. In: *Jpn. J. Appl. Phys.* **53.5S1** (2014), 05FH02. DOI: 10.7567/JJAP.53.05FH02.
- [178] E. A. C. Panduro, H. Granlund, M. Sztucki, O. Konovalov, D. W. Breiby and A. Gibaud: 'Using Three-Dimensional 3D Grazing-Incidence Small-Angle X-ray Scattering (GISAXS) Analysis To Probe Pore Deformation in Mesoporous Silica Films'. In: *ACS Appl. Mater. Interfaces* **6.4** (2014), pp. 2686–2691. DOI: 10.1021/am404602t.
- [179] A. Papoulis: *Signal analysis*. McGraw, 1977. 456 pp.
- [180] M. Park, C. Harrison, P. M. Chaikin, R. A. Register and D. H. Adamson: 'Block Copolymer Lithography: Periodic Arrays of  $10^{11}$  Holes in 1 Square Centimeter'. In: *Science* **276.5317** (1997), pp. 1401–1404. DOI: 10.1126/science.276.5317.1401.
- [181] M. J. Park, S. Kim, A. M. Minor, A. Hexemer and N. P. Balsara: 'Control of Domain Orientation in Block Copolymer Electrolyte Membranes at the Interface with Humid Air'. In: *Adv. Mater.* **21.2** (2009), pp. 203–208. DOI: 10.1002/adma.200801613.
- [182] L. G. Parratt: 'Surface Studies of Solids by Total Reflection of X-Rays'. In: *Phys. Rev.* **95.2** (1954), pp. 359–369. DOI: 10.1103/PhysRev.95.359.
- [183] A. L. Patterson: 'A Direct Method for the Determination of the Components of Interatomic Distances in Crystals'. In: *Z. Für Krist. - Cryst. Mater.* **90.1** (1935), pp. 517–542. DOI: 10.1524/zkri.1935.90.1.517.

- [184] E. Pechkova, S. V. Roth, M. Burghammer, D. Fontani, C. Riekel and C. Nicolini: 'μGISAXS and protein nanotemplate crystallization: methods and instrumentation'. In: *J. Synchrotron Rad.* **12.6** (2005), pp. 713–716. DOI: 10.1107/S0909049505011684.
- [185] J. S. Pedersen: 'Determination of size distribution from small-angle scattering data for systems with effective hard-sphere interactions'. In: *J. Appl. Cryst.* **27.4** (1994), pp. 595–608. DOI: 10.1107/S0021889893013810.
- [186] D. Pennicard, J. Marchal, C. Fleta, G. Pellegrini, M. Lozano, C. Parkes, N. Tartoni, D. Barnett, I. Dolbnya, K. Sawhney, R. Bates, V. O'Shea and V. Wright: 'Synchrotron Tests of a 3D Medipix2 X-Ray Detector'. In: *IEEE T. Nucl. Sci.* **57.1** (2010), pp. 387–394. DOI: 10.1109/TNS.2009.2037746.
- [187] J. Perlich, F.-M. Kamm, J. Rau, F. Scholze and G. Ulm: 'Characterization of extreme ultraviolet masks by extreme ultraviolet scatterometry'. In: *J. Vac. Sci. Technol. B* **22.6** (2004), pp. 3059–3062. DOI: 10.1116/1.1809615.
- [188] J. Perlich, G. Kaune, M. Memesa, J. S. Gutmann and P. Müller-Buschbaum: 'Sponge-like structures for application in photovoltaics'. In: *Phil. Trans. R. Soc. A* **367**.1894 (2009), pp. 1783–1798. DOI: 10.1098/rsta.2009.0017.
- [189] B. Pfau, C. M. Günther, S. Schaffert, R. Mitzner, B. Siemer, S. Roling, H. Zacharias, O. Kutz, I. Rudolph, R. Treusch and S. Eisebitt: 'Femtosecond pulse x-ray imaging with a large field of view'. In: *New J. Phys.* **12.9** (2010), p. 095006. DOI: 10.1088/1367-2630/12/9/095006.
- [190] U. Pietsch, V. Holý and T. Baumbach: *High-resolution X-ray scattering from thin films to lateral nanostructures*. Springer, Berlin/Heidelberg, 2004. 428 pp.
- [191] C. Ponchut, J. L. Visschers, A. Fornaini, H. Graafsma, M. Maiorino, G. Mettievier and D. Calvet: 'Evaluation of a photon-counting hybrid pixel detector array with a synchrotron X-ray source'. In: *Nucl. Instrum. Meth. A* **484**.1–3 (2002), pp. 396–406. DOI: 10.1016/S0168-9002(01)02029-0.
- [192] M. Rauscher, T. Salditt and H. Spohn: 'Small-angle x-ray scattering under grazing incidence: The cross section in the distorted-wave Born approximation'. In: *Phys. Rev. B* **52.23** (1995), p. 16855. DOI: 10.1103/PhysRevB.52.16855.
- [193] E. Rebollar, S. Pérez, J. J. Hernández, I. Martín-Fabiani, D. R. Rueda, T. A. Ezquerra and M. Castillejo: 'Assessment and Formation Mechanism of Laser-Induced Periodic Surface Structures on Polymer Spin-Coated Films in Real and Reciprocal Space'. In: *Langmuir* **27.9** (2011), pp. 5596–5606. DOI: 10.1021/la200451c.
- [194] G. Renaud, R. Lazzari and F. Leroy: 'Probing surface and interface morphology with Grazing Incidence Small Angle X-Ray Scattering'. In: *Surf. Sci. Rep.* **64.8** (2009), pp. 255–380. DOI: 10.1016/j.surfrep.2009.07.002.
- [195] M. Richter, S. V. Bobashev, A. A. Sorokin and K. Tiedtke: 'Multiphoton ionization of atoms with soft x-ray pulses'. In: *J. Phys. B: At. Mol. Opt. Phys.* **43.19** (2010), p. 194005. DOI: 10.1088/0953-4075/43/19/194005.
- [196] A. Rösler, G. W. M. Vandermeulen and H.-A. Klok: 'Advanced drug delivery devices via self-assembly of amphiphilic block copolymers'. In: *Adv. Drug Deliver. Rev.* **53.1** (2001), pp. 95–108. DOI: 10.1016/S0169-409X(01)00222-8.

## References

- [197] S. V. Roth, T. Autenrieth, G. Grübel, C. Riekkel, M. Burghammer, R. Hengstler, L. Schulz and P. Müller-Buschbaum: 'In situ observation of nanoparticle ordering at the air-water-substrate boundary in colloidal solutions using x-ray nanobeams'. In: *Appl. Phys. Lett.* **91.9** (2007), p. 091915. DOI: 10.1063/1.2776850.
- [198] S. V. Roth, A. Rothkirch, T. Autenrieth, R. Gehrke, T. Wroblewski, M. C. Burghammer, C. Riekkel, L. Schulz, R. Hengstler and P. Müller-Buschbaum: 'Spatially Resolved Investigation of Solution Cast Nanoparticle Films by X-ray Scattering and Multidimensional Data Set Classification'. In: *Langmuir* **26.3** (2010), pp. 1496–1500. DOI: 10.1021/la9037414.
- [199] A. Rothen: 'The Ellipsometer, an Apparatus to Measure Thicknesses of Thin Surface Films'. In: *Rev. Sci. Instrum.* **16.2** (1945), pp. 26–30. DOI: 10.1063/1.1770315.
- [200] M. A. Ruderer, S. Guo, R. Meier, H.-Y. Chiang, V. Körstgens, J. Wiedersich, J. Perlich, S. V. Roth and P. Müller-Buschbaum: 'Solvent-Induced Morphology in Polymer-Based Systems for Organic Photovoltaics'. In: *Adv. Funct. Mater.* **21.17** (2011), pp. 3382–3391. DOI: 10.1002/adfm.201100945.
- [201] A. A. Rudov, E. S. Patyukova, I. V. Neratova, P. G. Khalatur, D. Posselt, C. M. Papadakis and I. I. Potemkin: 'Structural Changes in Lamellar Diblock Copolymer Thin Films upon Swelling in Nonselective Solvents'. In: *Macromolecules* **46.14** (2013), pp. 5786–5795. DOI: 10.1021/ma400810u.
- [202] J. Ruokolainen, M. Saariaho, O. Ikkala, G. ten Brinke, E. L. Thomas, M. Torkkeli and R. Serimaa: 'Supramolecular Routes to Hierarchical Structures: Comb-Coil Diblock Copolymers Organized with Two Length Scales'. In: *Macromolecules* **32.4** (1999), pp. 1152–1158. DOI: 10.1021/ma980189n.
- [203] T. P. Russell: 'X-ray and neutron reflectivity for the investigation of polymers'. In: *Mater. Sci. Rep.* **5.4** (1990), pp. 171–271. DOI: 10.1016/S0920-2307(05)80002-7.
- [204] K. Sakurai and A. Iida: 'Fourier Analysis of Interference Structure in X-Ray Specular Reflection from Thin Films'. In: *Jpn. J. Appl. Phys.* **31** (Part 2, No. 2A 1992), pp. L113–L115. DOI: 10.1143/JJAP.31.L113.
- [205] K. Sakurai, M. Mizusawa and M. Ishii: 'Significance of Frequency Analysis in X-ray Reflectivity: Towards analysis which does not depend too much on models'. In: *Trans. Mater. Res. Soc. Jpn.* **33.3** (2008), pp. 523–528.
- [206] T. Salditt, D. Lott, T. H. Metzger, J. Peisl, G. Vignaud, P. Ho/gho/j, O. Schärpf, P. Hinze and R. Lauer: 'Interfacial roughness and related growth mechanisms in sputtered W/Si multilayers'. In: *Phys. Rev. B* **54.8** (1996), pp. 5860–5872. DOI: 10.1103/PhysRevB.54.5860.
- [207] T. Salditt, T. H. Metzger, C. Brandt, U. Klemradt and J. Peisl: 'Determination of the static scaling exponent of self-affine interfaces by nonspecular x-ray scattering'. In: *Phys. Rev. B* **51.9** (1995), p. 5617. DOI: 10.1103/PhysRevB.51.5617.
- [208] T. Salditt, T. H. Metzger and J. Peisl: 'Kinetic Roughness of Amorphous Multilayers Studied by Diffuse X-Ray Scattering'. In: *Phys. Rev. Lett.* **73.16** (1994), p. 2228. DOI: 10.1103/PhysRevLett.73.2228.

- [209] G. Santoro, A. Buffet, R. Döhrmann, S. Yu, V. Körstgens, P. Müller-Buschbaum, U. Gedde, M. Hedenqvist and S. V. Roth: 'Use of intermediate focus for grazing incidence small and wide angle x-ray scattering experiments at the beamline P03 of PETRA III, DESY'. In: *Rev. Sci. Instrum.* **85.4** (2014), p. 043901. DOI: 10.1063/1.4869784.
- [210] S. Sasaki: 'Analyses for a planar variably-polarizing undulator'. In: *Nucl. Instrum. Meth. A* **347.1–3** (1994), pp. 83–86. DOI: 10.1016/0168-9002(94)91859-7.
- [211] C. J. Schaffer, C. M. Palumbiny, M. A. Niedermeier, C. Jendrzewski, G. Santoro, S. V. Roth and P. Müller-Buschbaum: 'A Direct Evidence of Morphological Degradation on a Nanometer Scale in Polymer Solar Cells'. In: *Adv. Mater.* **25.46** (2013), pp. 6760–6764. DOI: 10.1002/adma.201302854.
- [212] M. Schmidbauer, T. Wiebach, H. Raidt, M. Hanke, R. Köhler and H. Wawra: 'Ordering of self-assembled Si<sub>11</sub>-xGe<sub>x</sub> islands studied by grazing incidence small-angle x-ray scattering and atomic force microscopy'. In: *Phys. Rev. B* **58.16** (1998), pp. 10523–10531. DOI: 10.1103/PhysRevB.58.10523.
- [213] F. Scholze, M. Krumrey, P. Müller and D. Fuchs: 'Plane grating monochromator beamline for VUV radiometry'. In: *Rev. Sci. Instrum.* **65.10** (1994), pp. 3229–3232. DOI: 10.1063/1.1144555.
- [214] F. Scholze, A. Kato, J. Wernecke and M. Krumrey: 'EUV and x-ray scattering methods for CD and roughness measurement'. In: *Proc. SPIE. Photomask Technology 2011*. 2011, 81661P. DOI: 10.1117/12.896847.
- [215] C. G. Schroer, P. Boye, J. M. Feldkamp, J. Patommel, A. Schropp, A. Schwab, S. Stephan, M. Burghammer, S. Schöder and C. Riekkel: 'Coherent X-Ray Diffraction Imaging with Nanofocused Illumination'. In: *Phys. Rev. Lett.* **101.9** (2008), p. 090801. DOI: 10.1103/PhysRevLett.101.090801.
- [216] A. Schubert, G. J. O'Keefe, B. A. Sobott, N. M. Kirby and R. P. Rassool: 'Characterisation of individual pixel efficiency in the PILATUS II sensor'. In: *Radiat. Phys. Chem.* **79.11** (2010), pp. 1111–1114. DOI: 10.1016/j.radphyschem.2010.06.008.
- [217] J. Schwinger: 'On the Classical Radiation of Accelerated Electrons'. In: *Phys. Rev.* **75.12** (1949), pp. 1912–1925. DOI: 10.1103/PhysRev.75.1912.
- [218] R. A. Segalman: 'Patterning with block copolymer thin films'. In: *Mater. Sci. Eng. R* **48.6** (2005), pp. 191–226. DOI: 10.1016/j.mser.2004.12.003.
- [219] C. R. Singh, G. Gupta, R. Lohwasser, S. Engmann, J. Balko, M. Thelakkat, T. Thurn-Albrecht and H. Hoppe: 'Correlation of charge transport with structural order in highly ordered melt-crystallized poly(3-hexylthiophene) thin films'. In: *J. Polym. Sci. Pol. Phys.* **51.12** (2013), pp. 943–951. DOI: 10.1002/polb.23297.
- [220] S. K. Sinha, E. B. Sirota, S. Garoff and H. B. Stanley: 'X-ray and neutron scattering from rough surfaces'. In: *Phys. Rev. B* **38.4** (1988), p. 2297. DOI: 10.1103/PhysRevB.38.2297.
- [221] D. S. Sivia: *Elementary Scattering Theory: For X-ray and Neutron Users*. Oxford University Press, 2011. 215 pp.
- [222] D. Smilgies, P. Busch, C. M. Papadakis and D. Posselt: 'Characterization of polymer thin films with small-angle X-ray scattering under grazing incidence (GISAXS)'. In: *Synchrotron Radiat. News* **15.5** (2002), pp. 35–42. DOI: 10.1080/08940880208602975.

## References

- [223] A. A. Sokolov and I. M. Ternov: 'Synchrotron radiation'. In: *Soviet Physics Journal* **10.10** (1967), pp. 39–47. DOI: 10.1007/BF00820300.
- [224] V. Soltwisch, J. Wernecke, A. Haase, J. Probst, M. Schoengen, M. Krumrey and F. Scholze: 'Nanometrology on gratings with GISAXS: FEM reconstruction and Fourier analysis'. In: *Proc. SPIE. Metrology, Inspection, and Process Control for Microlithography XXVIII*. Vol. 9050. San Jose, 2014, p. 905012. DOI: 10.1117/12.2046212.
- [225] V. Soltwisch, J. Wernecke, A. Haase, J. Probst, M. Schoengen, F. Scholze, J. Pomplun and S. Burger: 'Determination of line profile on nanostructured surfaces using EUV and x-ray scattering'. In: *Proc. SPIE. Photomask Technology 2014*. Ed. by P. W. Ackmann and N. Hayashi. Vol. 9235. Monterey, 2014, p. 92351D. DOI: 10.1117/12.2066165.
- [226] J. G. Son, M. Son, K.-J. Moon, B. H. Lee, J.-M. Myoung, M. S. Strano, M.-H. Ham and C. A. Ross: 'Sub-10 nm Graphene Nanoribbon Array Field-Effect Transistors Fabricated by Block Copolymer Lithography'. In: *Adv. Mater.* **25.34** (2013), pp. 4723–4728. DOI: 10.1002/adma.201300813.
- [227] A. Sorokin, S. Bobashev, T. Feigl, K. Tiedtke, H. Wabnitz and M. Richter: 'Photoelectric Effect at Ultrahigh Intensities'. In: *Phys. Rev. Lett.* **99.21** (2007), p. 213002. DOI: 10.1103/PhysRevLett.99.213002.
- [228] M. Stamm, ed.: *Polymer Surfaces and Interfaces*. Springer, Berlin/Heidelberg, 2008.
- [229] J. C. Stover: *Optical scattering: measurement and analysis*. 3rd ed. Bellingham, Washington: SPIE, 2012. 330 pp.
- [230] H. B. Stuhmann: 'Resonance scattering in macromolecular structure research'. In: *Characterization of Polymers in the Solid State II: Synchrotron Radiation, X-ray Scattering and Electron Microscopy*. Ed. by H. H. Kausch and H. G. Zachmann. 67. Springer Berlin/Heidelberg, 1985, pp. 123–163.
- [231] D. F. Sunday, M. R. Hammond, C. Wang, W.-l. Wu, D. M. DeLongchamp, M. Tjio, J. Y. Cheng, J. W. Pitera and R. J. Kline: 'Determination of the Internal Morphology of Nanostructures Patterned by Directed Self Assembly'. In: *ACS Nano* **8.8** (2014), pp. 8426–8437. DOI: 10.1021/nn5029289.
- [232] S. Swaraj, C. Wang, T. Araki, G. Mitchell, L. Liu, S. Gaynor, B. Deshmukh, H. Yan, C. R. McNeill and H. Ade: 'The utility of resonant soft x-ray scattering and reflectivity for the nanoscale characterization of polymers'. In: *Eur. Phys. J. Spec. Top.* **167.1** (2009), pp. 121–126. DOI: 10.1140/epjst/e2009-00946-3.
- [233] C. Tang, E. M. Lennon, G. H. Fredrickson, E. J. Kramer and C. J. Hawker: 'Evolution of Block Copolymer Lithography to Highly Ordered Square Arrays'. In: *Science* **322.5900** (2008). PMID: 18818367, pp. 429–432. DOI: 10.1126/science.1162950.
- [234] R. Thornagel, R. Klein and G. Ulm: 'The electron storage ring BESSY II as a primary source standard from the visible to the the X-ray range'. In: *Metrologia* **38.5** (2001), p. 385. DOI: 10.1088/0026-1394/38/5/3.
- [235] K. Tiedtke, A. Azima, N. v. Bargaen, L. Bittner, S. Bonfigt, S. Düsterer, B. Faatz, U. Frühling, M. Gensch, C. Gerth et al.: 'The soft x-ray free-electron laser FLASH at DESY: beamlines, diagnostics and end-stations'. In: *New J. Phys.* **11.2** (2009), p. 023029. DOI: 10.1088/1367-2630/11/2/023029.

- [236] A. Tikhonov: 'Solution of Incorrectly Formulated Problems and the Regularization Method'. In: *Sov. Math Dokl* **5** (1963), pp. 1035–1038.
- [237] M. Tolan, W. Press, F. Brinkop and J. P. Kotthaus: 'X-ray diffraction from laterally structured surfaces: Total external reflection'. In: *Phys. Rev. B* **51.4** (1995), pp. 2239–2251. DOI: 10.1103/PhysRevB.51.2239.
- [238] M. Tolan: *X-ray scattering from soft-matter thin films: materials science and basic research*. Springer, Berlin/Heidelberg, 1999. 198 pp.
- [239] H. Tompkins and E. A. Irene: *Handbook of Ellipsometry*. William Andrew, Norwich, 2005. 888 pp.
- [240] N. Torikai, N. L. Yamada, D. Kawaguchi, A. Takano, Y. Matsushita, E. Watkins and J. P. Majewski: 'Depth distribution of different solvents in a phase-separated block copolymer thin film'. In: *J. Phys.: Conf. Ser.* **272.1** (2011), p. 012027. DOI: 10.1088/1742-6596/272/1/012027.
- [241] N. Torikai, N. L. Yamada, D. Kawaguchi, A. Takano, Y. Matsushita, E. Watkins, J. P. Majewski and H. Okuda: 'In-Situ Reflectometry Observation on Structural Changes of Thin Self-Assembled Block Copolymer Films'. In: *J. Phys.: Conf. Ser.* **83.1** (2007), p. 012028. DOI: 10.1088/1742-6596/83/1/012028.
- [242] P. Trueb, B. A. Sobott, R. Schnyder, T. Loeliger, M. Schneebeli, M. Kobas, R. P. Rassoool, D. J. Peake and C. Broennimann: 'Improved count rate corrections for highest data quality with PILATUS detectors'. In: *J. Synchrotron Rad.* **19.3** (2012), pp. 347–351. DOI: 10.1107/S0909049512003950.
- [243] K. Tuchin: 'Synchrotron radiation by fast fermions in heavy-ion collisions'. In: *Phys. Rev. C* **82.3** (2010), p. 034904. DOI: 10.1103/PhysRevC.82.034904.
- [244] J. S. Villarrubia, A. E. Vladár and M. T. Postek: 'Scanning electron microscope dimensional metrology using a model-based library'. In: *Surf. Interface Anal.* **37.11** (2005), pp. 951–958. DOI: 10.1002/sia.2087.
- [245] G. Vineyard: 'Grazing-incidence diffraction and the distorted-wave approximation for the study of surfaces'. In: *Phys. Rev. B* **26.8** (1982), pp. 4146–4159. DOI: 10.1103/PhysRevB.26.4146.
- [246] E. Vogel: 'Technology and metrology of new electronic materials and devices'. In: *Nat. Nano.* **2.1** (2007), pp. 25–32. DOI: 10.1038/nnano.2006.142.
- [247] C. Wang, D. H. Lee, A. Hexemer, M. I. Kim, W. Zhao, H. Hasegawa, H. Ade and T. P. Russell: 'Defining the Nanostructured Morphology of Triblock Copolymers Using Resonant Soft X-ray Scattering'. In: *Nano Lett.* **11.9** (2011), pp. 3906–3911. DOI: 10.1021/nl2020526.
- [248] C. Wang, K.-W. Choi, W.-E. Fu, R. Jones, D. Ho, C. Soles, E. Lin, W.-I. Wu, J. Clarke, J. Villarrubia and B. Bunday: 'Linewidth Roughness and Cross-sectional Measurements of Sub-50 nm Structures Using CD-SAXS and CD-SEM'. In: *Advanced Semiconductor Manufacturing Conference, 2008. ASMC 2008. IEEE/SEMI*. 2008, pp. 142–147. DOI: 10.1109/ASMC.2008.4529019.
- [249] C. Wang, R. L. Jones, E. K. Lin, W.-L. Wu, B. J. Rice, K.-W. Choi, G. Thompson, S. J. Weigand and D. T. Keane: 'Characterization of correlated line edge roughness of nanoscale line gratings using small angle x-ray scattering'. In: *J. Appl. Phys.* **102.2** (2007), DOI: 10.1063/1.2753588.

## References

- [250] J. Wernecke, C. Gollwitzer, P. Müller and M. Krumrey: 'Characterization of an in-vacuum PILATUS 1M detector'. In: *J. Synchrotron Rad.* **21.3** (2014), pp. 529–536. DOI: 10.1107/S160057751400294X.
- [251] J. Wernecke, M. Krumrey, A. Hoell, R. J. Kline, H.-k. Liu and W.-l. Wu: 'Traceable GISAXS measurements for pitch determination of a 25 nm self-assembled polymer grating'. In: *J. Appl. Cryst.* **47** (2014), pp. 1912–1920. DOI: 10.1107/S1600576714021050.
- [252] J. Wernecke, H. Okuda, H. Ogawa, F. Siewert and M. Krumrey: 'Depth-Dependent Structural Changes in PS-b-P2VP Thin Films Induced by Annealing'. In: *Macromolecules* **47.16** (2014), pp. 5719–5727. DOI: 10.1021/ma500642d.
- [253] J. Wernecke, F. Scholze and M. Krumrey: 'Direct structural characterisation of line gratings with grazing incidence small-angle x-ray scattering'. In: *Rev. Sci. Instrum.* **83.10** (2012), p. 103906. DOI: doi:10.1063/1.4758283.
- [254] J. Wernecke, A. G. Shard and M. Krumrey: 'Traceable thickness determination of organic nanolayers by X-ray reflectometry'. In: *Surf. Interface Anal.* **46.10-11** (2014), pp. 911–914. DOI: 10.1002/sia.5371.
- [255] R. Wernecke and J. Wernecke: *Industrial Moisture and Humidity Measurement: A Practical Guide*. Wiley-VCH, Weinheim, 2014. 520 pp.
- [256] K. L. Westra, A. W. Mitchell and D. J. Thomson: 'Tip artifacts in atomic force microscope imaging of thin film surfaces'. In: *J. Appl. Phys.* **74.5** (1993), pp. 3608–3610. DOI: 10.1063/1.354498.
- [257] D. L. Windt: 'IMD - Software for modeling the optical properties of multilayer films'. In: *Comput. Phys.* **12.4** (1998), pp. 360–370. DOI: 10.1063/1.168689.
- [258] H. Winick and S. Doniach, eds.: *Synchrotron radiation research*. Plenum Press, New York, 1980. 754 pp.
- [259] W.-l. Wu: 'Off-specular reflection from flat interfaces with density or compositional fluctuations'. In: *J. Chem. Phys.* **98.2** (1993), p. 1687. DOI: 10.1063/1.464284.
- [260] W.-l. Wu: 'Off-specular reflection from flat interfaces'. In: *J. Chem. Phys.* **101.5** (1994), p. 4198. DOI: 10.1063/1.468464.
- [261] A. Yacoot and L. Koenders: 'Recent developments in dimensional nanometrology using AFMs'. In: *Meas. Sci. Technol.* **22.12** (2011), p. 122001. DOI: 10.1088/0957-0233/22/12/122001.
- [262] M. J. Yaffe and J. A. Rowlands: 'X-ray detectors for digital radiography'. In: *Phys. Med. Biol.* **42.1** (1997), p. 1. DOI: 10.1088/0031-9155/42/1/001.
- [263] M. Yan, J. F. Bardeau, G. Brotons, T. Metzger and A. Gibaud: 'Combined studies of gratings by X-ray reflectivity, GISAXS, and AFM'. In: *KEK Proc.* 2006, pp. 107–116.
- [264] M. Yan and A. Gibaud: 'On the intersection of grating truncation rods with the Ewald sphere studied by grazing-incidence small-angle X-ray scattering'. In: *J. Appl. Cryst.* **40.6** (2007), pp. 1050–1055. DOI: 10.1107/S0021889807044482.
- [265] K. S. Yee: 'Numerical solution of initial boundary value problems involving Maxwell's equations in isotropic media'. In: *IEEE T. Antenn. Propag.* **14.3** (1966), pp. 302–307.
- [266] Y. Yoneda: 'Anomalous Surface Reflection of X Rays'. In: *Phys. Rev.* **131.5** (1963), pp. 2010–2013. DOI: 10.1103/PhysRev.131.2010.

- [267] F. Zhang, J. Ilavsky, G. Long, J. Quintana, A. Allen and P. Jemian: 'Glassy Carbon as an Absolute Intensity Calibration Standard for Small-Angle Scattering'. In: *Metall. Mater. Trans. A* **41.5** (2010), pp. 1151–1158. DOI: 10.1007/s11661-009-9950-x.
- [268] J. Zhang, D. Posselt, A. Sepe, X. Shen, J. Perlich, D.-M. Smilgies and C. M. Papadakis: 'Structural Evolution of Perpendicular Lamellae in Diblock Copolymer Thin Films during Solvent Vapor Treatment Investigated by Grazing-Incidence Small-Angle X-Ray Scattering'. In: *Macromol. Rapid Commun.* **34.16** (2013), pp. 1289–1295. DOI: 10.1002/marc.201300314.